Preparation, Characterisation and Catalytic Properties of Gallium Loaded Molecular Sieves

Graeme Duncan Cruickshank
B.Sc (Hons.) GRSC

A thesis presented for the degree of Doctor of Philosophy at the University of Edinburgh

1994

For Mum and Wend.....

I would like it to be noted that the time of producing this work has seen the passing of the two most influential men in my life. I am forever in their debt and shall always remember them. I would like to take this opportunity to express my appreciation and admiration for the late Dr. B.M.Lowe and Mr. Matthew Duncan.

Barrie was the sole reason for my interest in this field and it was his infectious love of the science that has taken me through to this stage of my studies. His passing in September of 1992 has greatly affected everyone in the group and the zeolite community as a whole. He will be sorely missed by us all. I am angered by my own inability to describe my feelings and regard for Barrie. All I can say to him is ,"Thanks".

" Think about it Graeme, think about it..."

(Dr.B.M.Lowe)

Mathie Duncan was always a tower of strength and I can only hope to follow in his footsteps. Thanks Granda.

"Aye aye Granda, that's me just about finished the school."

Declaration

This thesis was composed by myself, and except where otherwise indicated, describes the work carried out by me at the University of Edinburgh or at the I.C.I. centres at Wilton and Billingham, between October 1991 and September 1994.

Graeme D. Cruickshank

Abstract

The work described in this Thesis is concerned with the preparation, characterisation and catalysis of a range of metal loaded Molecular Sieves and, in particular, gallium containing Zeolite and Zeotype materials. Commercially, the CYCLAR process transforms LPG to aromatics using a catalyst based on gallium and Zeolite ZSM-5. Methods for preparing both this catalyst and related materials employing alternative zeolite structures have been explored and the resulting catalysts studied for their activity in propane conversion.

A range of zeolite molecular sieves and their gallium analogues, with the EUO and MFI framework structures, have been prepared. Attempts to prepare EUO materials with increased metal content yielded the intergrowth material NU-85. The basic physical properties of these materials have been characterised by a variety of techniques including X-ray powder diffraction (XRPD), thermal gravimetric analysis (tga), scanning electron microscopy (SEM), X-ray fluorescence (XRF), neutron activation analysis (NAA) and acidity determinations by ammonia temperature programmed desorption (TPD). X-ray photoelectron spectroscopy (XPS) has shown the isomorphous substitution of gallium into framework sites in these molecular sieves is not homogeneous, with the zeotype crystals having a gallium rich crust and a siliceous core. This technique has also shown the presence of partially reduced gallium species in discharged catalysts.

In catalysis studies all materials exhibited hydrogenolysis, dehydrogenation, oligomerisation activity to varying degrees in addition to the aforementioned CYCLAR aromatisation. Although the commercial preparation displayed the highest activity for aromatisation several of the gallosilicate and gallium doped EU-1 catalysts showed a potentially useful high selectivity for propane dehydrogenation, albeit at low conversion.

Acknowledgments

I am hugely indebted to Dr. G.S. McDougall who has guided me through this work and I also owe a massive debt to Dr.J.L. Casci (I.C.I. Katalco, Billingham) who has dragged me through. Undoubtedly without their help I would have made an even bigger mess!

Dr. Frank Leach deserves thanks for making my life a misery after Scottish defeats. The catalytic work in Edinburgh could never have been undertaken without the fantastic help of Dr. Ron Brown. ("Eh, Ron, I think I've broken it again!"). Some of the catalytic data was obtained with the help of Rachel Duncan and Anya Rayner (4^{th} year project students) and their assistance is gratefully acknowledged. As always, it was the people in the lab who made life bearable and I shall always be in their debt. Jim, Keith and Alister for zeolite boys singsongs and latterly Andrew and Gavin who also sang badly! Anne, Iain, Philip and Peter for Firbush fun. Special mention is due to Richard and Andrew who helped with my myriad of computer foul-ups.

I would like to thank the technical staff of the Chemistry Department, particularly Stuart Mains, Alan King and Robert Wilson who were always there after I'd broken something important.

I would like to thank Barbara Gore for carrying out the MASNMR at UMIST. I am very grateful to Dodie James and Dr. G.Fitton of the Geology Department for their help with XRF analyses and to John Findlay of the University SEM service. They have all assisted me greatly. Irene Brown was responsible for the elemental analyses carried out at I.C.I., Wilton and is due a debt of thanks as is Rob Fletcher, also at I.C.I. Wilton who carried out the micromeritics analyses. Dr. Whitley and Dr. McCartney of the SURRC (East Kilbride) made the NAA available to me and thanks is extended to them also.

The XPS studies could not have been undertaken without the help of Dr. Steve Bailey (I.C.I. Katalco) and Dr. Dale Creaser (I.C.I. C.&P.) and their assistance

in both the running of the experiments and the subsequent spectral analysis is acknowledged and greatly appreciated. Thanks is also due to Dr. Paul Cox (University of Portsmouth), who provided computer modeling output, as did Malcolm Weaver of I.C.I. C.&P., Wilton.

The financial and technical support afforded to me over the past three years by I.C.I. has been greatly appreciated and I wish to extend my thanks to them, in particular John Casci and his group who have assisted me greatly at all stages of the work.

This work has been primarily funded by the Carnegie Trust for the Universities of Scotland, and their financial assistance is gratefully acknowledged along with the assistance they offered which allowed to to attend numerous Meetings and Conferences.

Courses Attended:

Research in Industry: Diffrences with Academia :Dr. D.G.Parker (ICI, Wilton)

Detergent Products from Around the World :Dr. C.J. Adams (Unilever)

Catalytic Reaction Mechanisms :Dr. K.C. Waugh (ICI, Billingham)

Homogeneous Catalysis :Dr. A.C. Lucy (B.P. Chemicals, Sunbury)

Mass Spectroscopy in Action :Prof. J. Monaghan (ICI)
Prof. J. Scrivens (ICI)

Aspects and Applications of NMR :Dr. I. Sadler
Dr. D. Reed

German for Scientists :German Department

LaTeX a document preparation system :M. Ogylvie

UNIX 1 :M.Ogilvie

Physical chemistry evening colloquia

Conferences Attended:

15^{th} Annual Meeting of The British Zeolite Association, Southport, 1992

16^{th} Annual Meeting of The British Zeolite Association, Chiselhurst, 1993

17^{th} Annual Meeting of The British Zeolite Association, Loughborough, 1994

Firbush Catalytic Club Meeting, Firbush Field Centre, May 1992

Firbush Catalytic Club Meeting, Firbush Field Centre, May 1993

Firbush Catalytic Club Meeting, Firbush Field Centre, May 1994

Surcat Ecosse Meeting, University of Stirling, March 1992

Surcat Ecosse Meeting, University of Strathclyde, March 1993

SURCAT '92 Meeting, University of Dundee, April 1992

1^{st} ICI International Symposium on Catalytic Chemistry, Billingham, May 1992

2^{nd} ICI International Symposium on Catalytic Chemistry, Billingham, May 1993

3^{rd} ICI International Symposium on Catalytic Chemistry, Billingham, May 1994

Table of Contents

Chapter 1

INTRODUCTION

1.1 Background to Zeolite Molecular Sieves

Zeolites are crystalline aluminosilicate compounds with rigid, 3-dimensional structures which enclose cavities and channels of molecular dimensions. In conventional zeolite materials the framework silicon and aluminium are tetrahedrally coordinated to four others by bridging oxygen species and are collectively termed T-atoms. Although Si-O-Si bonds are present in a framework, Al-O-Al bonds are forbidden by Lowenstein's rule [1] which means that the framework Si/Al $\geq$1. These microporous materials are *molecular sieves*, [2] which is a broader term used to describe a wide range of materials which are able to differentiate molecules by size *i.e. sieve* them. Although zeolites occur in nature, with some 54 natural zeolites known, many more may be readily synthesised in the laboratory. Indeed, around 150 have already been reported in the literature [3].

Natural zeolites can be separated into two groups, igneous and sedimentary. Igneous deposits are usually small and highly dispersed so, although the crystals are usually large and well defined, commercial extraction is not economically viable. Sedimentary deposits, on the other hand, are found in large localised deposits, however, the crystals are usually very small and of poor morphology. These large deposits are commercially exploited, most notably clinoptilolite for the treatment of nuclear waste cooling water [4].

The term *zeolite* is derived from the Greek *zeein* and *lithos* which literally means "boiling stone". This was based on observations made by the mineralogist

Cronstedt, who discovered what was believed to be the natural zeolite stilbite in 1756 [5], but this find is now thought to have been natrolite [6]. "Boiling stone" refers to the ability of zeolites to release water (reversibly) when heated.

Early zeolite syntheses attempted to simulate the crystallisation processes thought to occur in nature *i.e.* high temperature and pressure. These conditions, however, resulted in the formation of dense phases with little, if any, commercial value. The naturally occurring zeolite Levynite was the first zeolite to be synthesised in the laboratory, in 1862 [7]. Many other reports of early zeolite crystallisations exist [7], however, the lack of reliable identification techniques prevented unambiguous structure determination. Thus many of these early reports remain unsubstantiated. It was not until the advent of X-ray diffraction that a definitive identification technique became available to zeolite chemists and mineralogists.

It was in the 1930's that Barrer began his studies into zeolite crystallisations. His synthesis of the novel zeolites P and Q, reported in 1948 [8], represent the initial attempt to rationalise the crystallisation phenomenon. The development of a low temperature, hydrothermal synthesis technique by workers at Union Carbide [9, 10], using reactive gel precursors, in 1956 allowed the synthesis of a number of novel materials including the commercially important zeolites A and X, under milder conditions, similar to those under which sedimentary zeolites are formed. Such mild synthesis conditions have resulted in the crystallisation of many important zeolite molecular sieves (*eg.* zeolite Y [11]), which unlike early synthesis products have more open, less dense frameworks. The discovery of high silica materials, obtained when an organic reagent is added to the reaction gel, in the early 1960's, further boosted research efforts. Indeed, since the discovery of zeolite A and more especially zeolite Y, with its importance in hydrocarbon conversion reactions, an explosion in research effort has taken place. This has led to the discovery of other families of molecular sieves, most notably the aluminophosphates ($AlPO_4$s) [12], where elements other than Si and/or Al make up the framework structure. The many materials which currently make up the molecular sieve family are shown schematically in Figure 1–1.

The text *Zeolite Molecular Sieves* by Breck provides a splendid introduction to

Figure 1–1: Classification of Molecular Sieves[a]

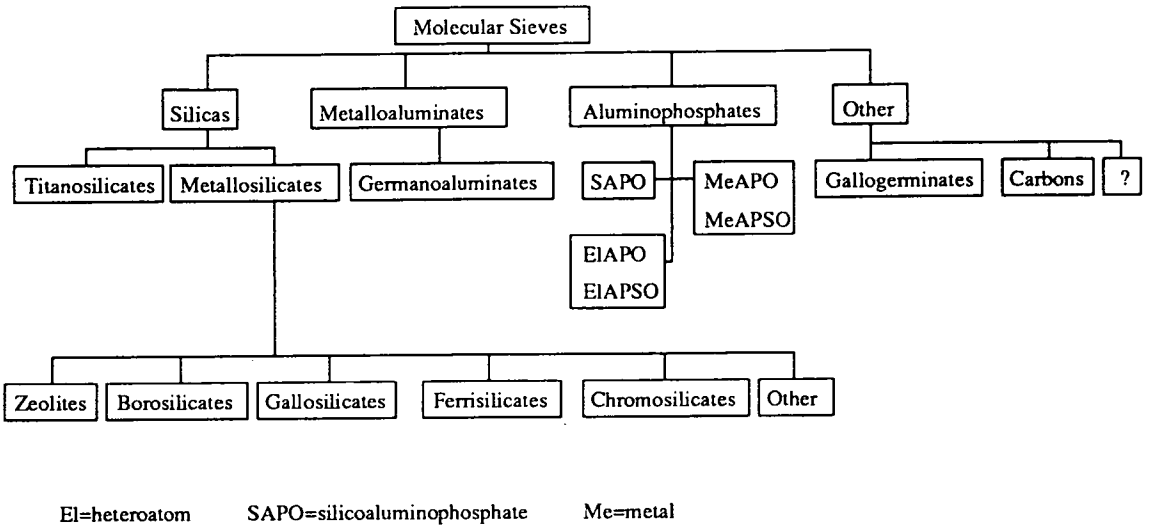

[a]based on reference [3]

these materials, charting the birth and development of zeolite science [7]. Dyer's *An Introduction to Zeolite Molecular Sieves* [13] also provides an excellent background to these materials and their properties.

1.2 Nomenclature

The term *zeolite* is used to describe materials with only aluminium, silicon and oxygen in the framework structure. However, it is sometimes incorrectly applied when used to describe non-aluminosilicate molecular sieves. The substitution of other *heteroatoms* for framework aluminium or silicon atoms results in the formation of materials better described as *zeotypes* [13]. In addition materials which contain *trapped* molecules within the structure (*i.e.* are non-porous) are referred to as clathrasils. The various terms used to describe molecular sieves have been summarised in Figure 1–1. The terms *zeolite* and *zeotype* will be used in this work to describe aluminosilicate and non-aluminosilicate molecular sieves respectively. A

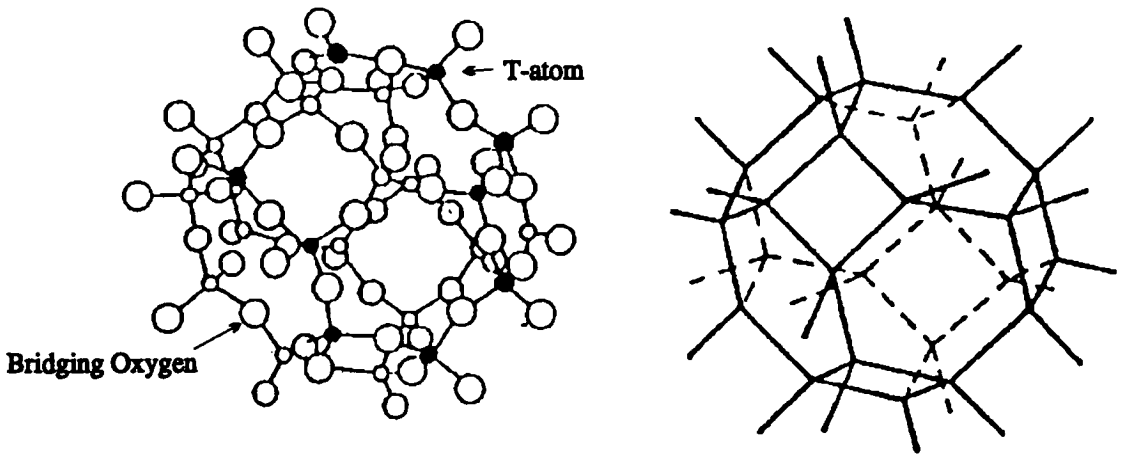

Figure 1–2: Sodalite cage[a], vertices are Si, Al or a heteroatom, *eg.* Ga in zeotype materials. The lines represent T-O-T bonds with oxygen atoms roughly in the middle of each line.

[a] Images modified from ref. [7].

more comprehensive review of nomenclature is provided by Smith [14] and Liebau [15].

1.3 Structure, Properties and Uses of Molecular Sieves

1.3.1 Zeolite Structure

Zeolites possess a unique combination of properties which are a direct consequence of their microporous structure and framework composition. The internal pore system is accessed through *windows* of molecular dimensions (Figure 1–3) which lead to cavities and voids which can be connected by a system of channels.

As has been mentioned, the framework is made up of $(AlO_4)^{5-}$ and $(SiO_4)^{4-}$ tetrahedra which are connected via oxygen bridges. Since tetrahedrally coordinated framework aluminium has an associated negative charge, the framework

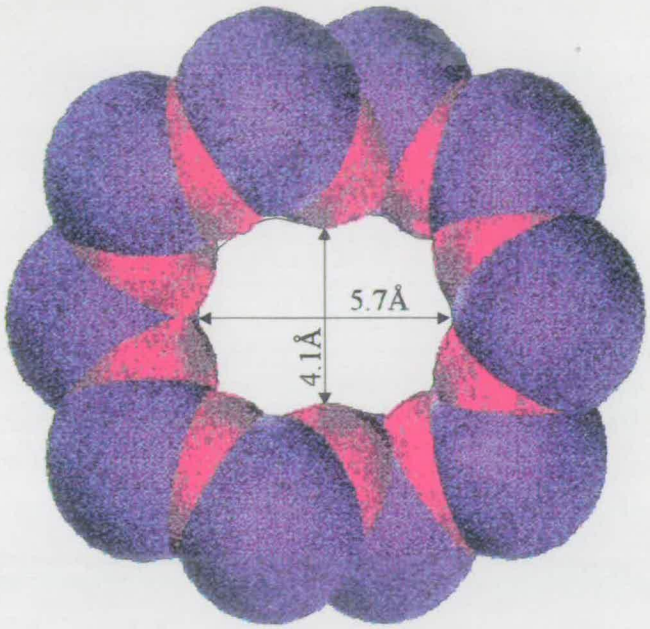

Figure 1–3: A 10 T-atom window at the entrance to the zeolite microporous structure. Image obtained courtesy of I.C.I. C.& P., with the help of M. Weaver using Polygraf 3.1 from Molecular Simulations Software.

carries a negative charge. To compensate for this negative framework, zeolites require charge balancing cations which reside within the cavities and channels. There are also water molecules occluded in the intrazeolitic void space which can also affect zeolite properties. These occluded ions and water molecules are extremely mobile within the porous channel structures and so ion exchange and reversible dehydration of zeolites are readily achieved. Hence, it is the $\frac{Si}{Al}$ ratio of the framework that significantly influences the properties of zeolites. Table 1–1 summarises some of the effects of varying $\frac{Si}{Al}$ ratio on zeolite properties. The negative framework charge is often balanced by alkali or alkaline earth metal cations but may also be balanced by protons to effectively create a solid acid site [16]. These Brönsted acid sites are readily dehydrated at $\approx$ 823 K to create Lewis type sites [17], as is shown schematically in Figure 1–4.

The dimensions of the channel system and the elemental composition of the materials are primarily responsible for the observed properties of the particular zeolite. The size and dimensionality (1, 2 or 3-D) of the microporous channels are crucial to the choice of zeolite for a specific application. The sizes of windows

Figure 1–4: Thermal degradation of Brönsted to Lewis acid sites in zeolites[a].

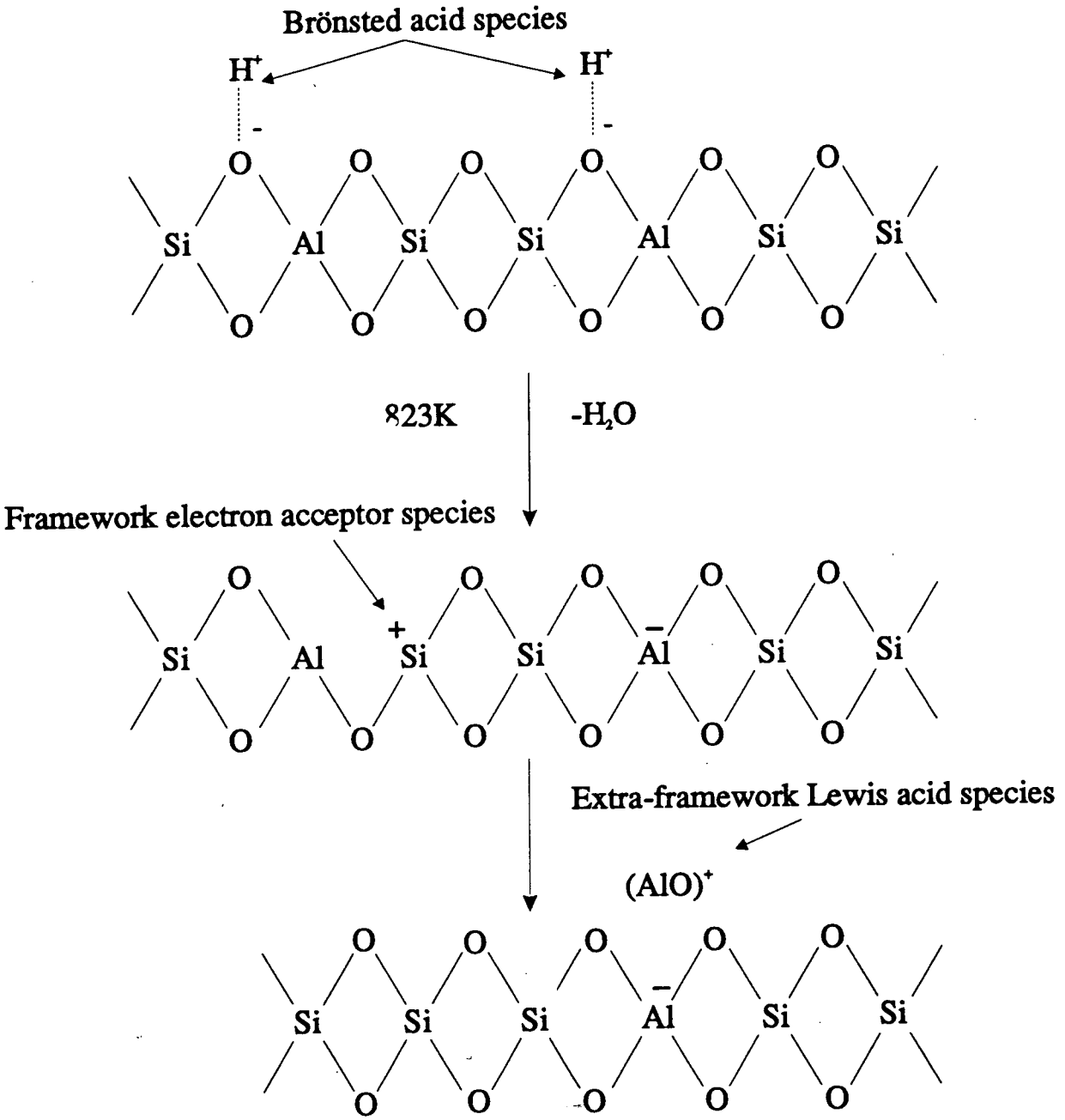

[a] Schematic reproduced from ref. [7].

Table 1–1: Effect of $\frac{Si}{Al}$ ratio on the physical properties of zeolites[a].

High $\frac{Si}{Al}$ ratio	Low $\frac{Si}{Al}$ ratio
increases acid resistance	increases hydrophilicity
increases thermal/hydrothermal stability	increases cation exchange properties
increases hydrophobicity	
decreases affinity for polar adsorbates	
decreases cation content	

[a]from reference [3]

to the channels or cavities can often be "fine tuned" by simply changing the charge balancing cations *eg.* replacing monovalent cations with smaller divalent ones results in an effective increase in window size and void volume as fewer cations are then required to balance the framework charge.

The well characterised channels and cavities allow zeolites to exhibit *shape selectivity.* The presence of Brönsted acid sites in the framework in combination with the well characterised pore system allows zeolites to behave as shape selective catalysts in hydrocarbon transformation reactions, as illustrated in Figure 1–5 (reproduced from ref. [18]).

1.3.2 Structure Classification

Zeolite frameworks can be described in terms of small structural subunits, called secondary building units (SBU) [20]. However, some materials are more readily described by larger polyhedral units such as the sodalite cage (Figure 1–2). This cage can be found in a number of framework structures *eg.* sodalite, faujasite, zeolite A (LTA) and the aluminophosphate $AlPO_4$-20, as illustrated in Figure 1–6.

Zeolites can also be classed according to their properties, which are directly linked to the material's structure and composition. Hence they can be termed

Figure 1–5: The Shape Selectivity exhibited by the rigid zeolite frameworks[a], a) *Reactant Selectivity* where only appropriately sized molecules may enter the porous structure, b) *Product Selectivity* only appropriately sized products can leave the structure and c) *Transition State Selectivity* only certain transition states may be accommodated in the pores.

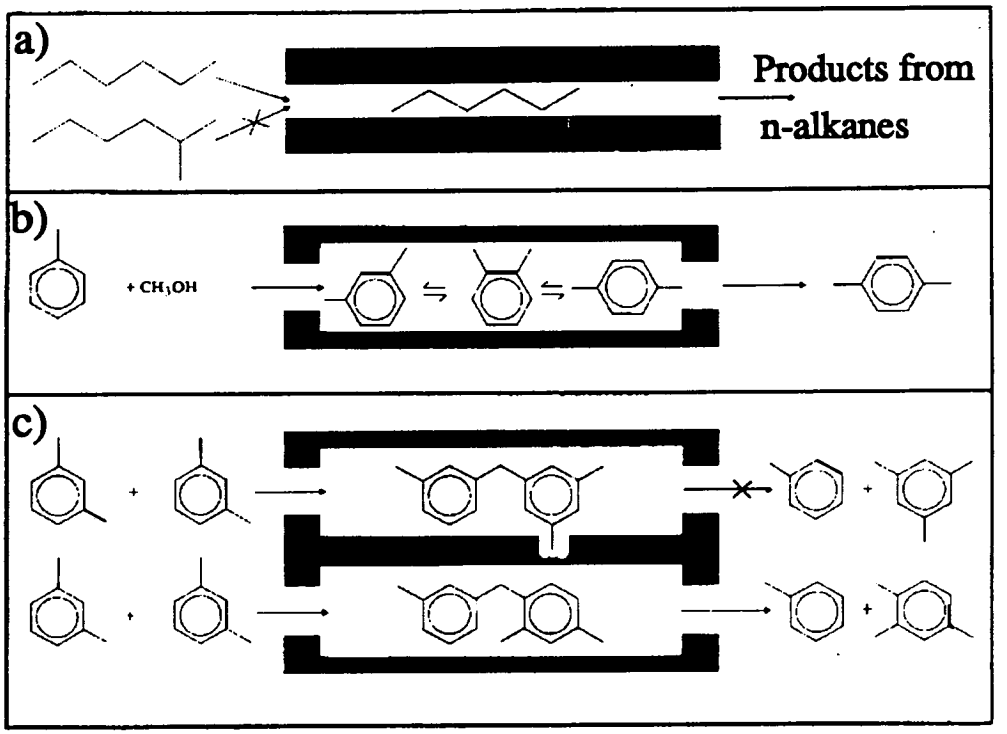

[a]Image reproduced from [18], with modification included in ref. [19].

Figure 1–6: Some of the structures created from the truncated polyhedra of the sodalite cage[a].

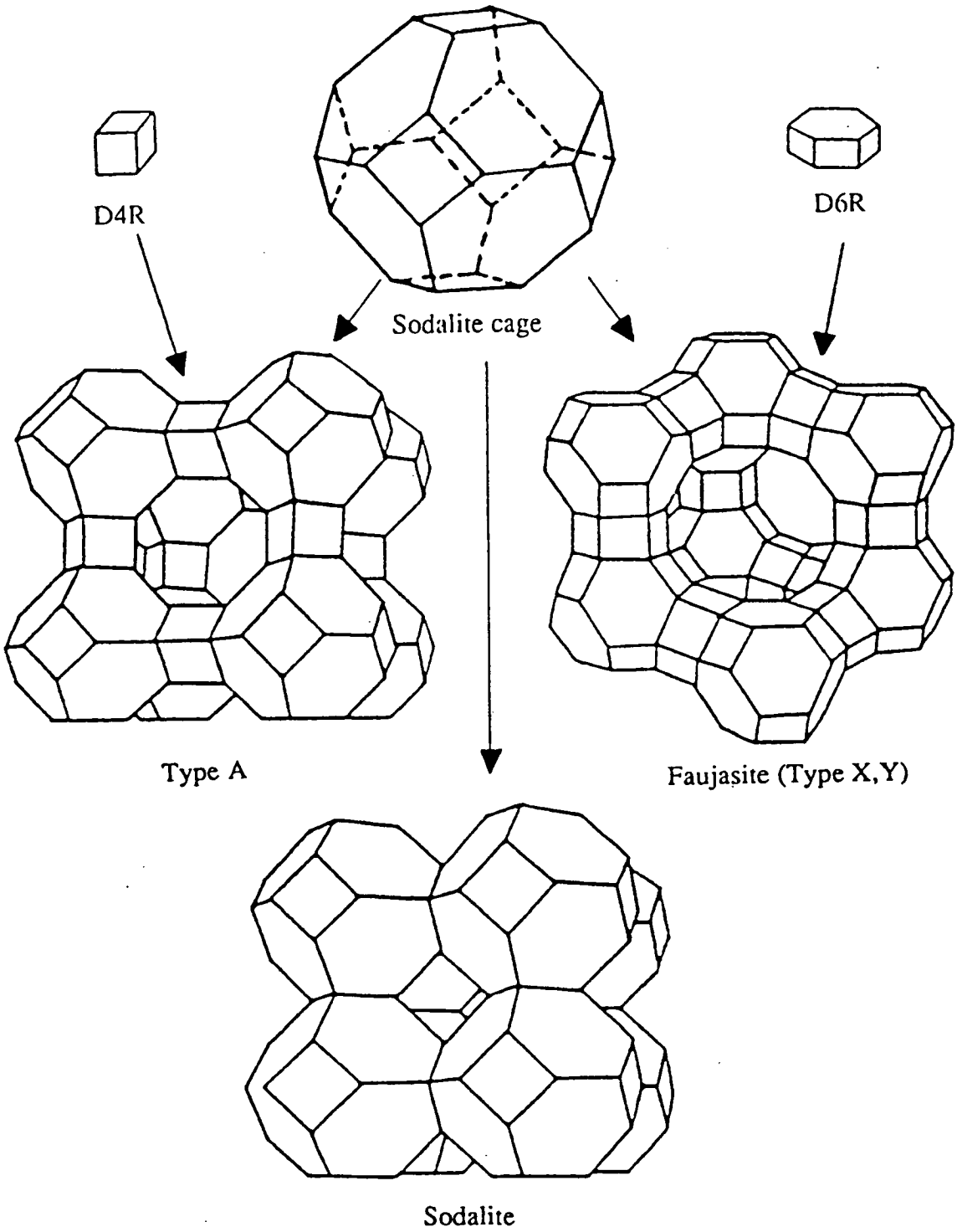

[a] Image reproduced from ref. [7].

as hydrophilic or hydrophobic if they are low silica (aluminous) or high silica (siliceous) respectively. Molecular sieves can be categorised by their pore volume *i.e.* the intracrystalline void space. Similarly they can be classified according to the size of the windows which lead to this internal volume *eg.* sieves are referred to as small, medium or large pore if they contain 8, 10 or 12 T-atom windows respectively. The framework density can also be used to describe zeolite molecular sieves (number of T-atoms/1000Å^3), however, this description gives no indication of the accessibility of the void volume, unlike other classifications based on sorption studies [21, 22].

The Structural Commission of the International Zeolite Association assigns a unique three letter code to each novel framework structure *eg.* the Mobil zeolite ZSM-5 has the classification MFI while the Edinburgh University material EU-1 has the structure code EUO. A comprehensive list of these codes may be found in the *Atlas of Zeolite Structure Types* [23].

1.3.3 Properties and Applications of Molecular Sieves

Introduction

Uses of molecular sieves are extremely diverse although most of their traditional applications are found in the general areas of ion exchange, sorption and catalysis [13]. The ready movement of the charge balancing cations accounts for the ion exchange capability of these materials and the shape selective sorption of small molecules is a consequence of the regular channels and cavities created by the framework structure. The intrinsic acidity of the zeolite framework accounts for much of their catalytic capabilities. A brief description of these properties follows.

Ion Exchange

Ion exchange in zeolites is a consequence of the ready mobility of the charge balancing cations. Commercial applications are essentially limited to zeolites with a high ion exchange capacity *i.e.* low silica (aluminous) materials since they have

the most charge balancing ions available for exchange. Complete exchange is rare, even after successive exchange procedures, since there are often cations in non-exchangeable positions in the void space. Zeolites are able to show a preference for particular cations and so leads to the phenomenon of ion sieving [7].

Zeolites find their largest application (in terms of volume) as builders in washing powders [24, 25]. Their purpose is to sequester Ca^{2+} and Mg^{2+} ions from hard water as these ions inhibit the surfactant's performance. Zeolites have replaced the environmentally unfriendly polyphosphates, which when released into the watercourses support the growth of *algal blooms*. It was discovered that this huge increase in algae depleted the oxygen levels in the water and furthermore, as the algae died, their decomposition products poisoned the water, effectively killing these watercourses.

The use of the natural zeolite clinoptilolite to clean nuclear cooling water ponds [4, 26, 27] is also extremely important with the zeolite showing great selectivity in removing the ^{137}Cs and ^{90}Sr ions from the water. Clinoptilolite is extremely good at retaining such waste products as it is stable to ionising radiation and provides an excellent solid matrix for binding the waste indefinitely.

Sorption

For a zeolite to act as a molecular sieve and so have a sorptive capacity, its microporous structure must first be activated by removal of the water and occluded material from the void space. The size of the windows to be used as a *mesh* can be fine tuned as described previously by ion exchange. Zeolite frameworks are not completely rigid and so factors such as temperature and framework composition can dramatically alter the observed sieving properties. Thermally induced vibrations of the windows can increase the aperture size sufficiently to allow molecules to enter the void space which were excluded at lower temperatures.

Low silica (aluminous) zeolites are hydrophilic and prefer to sorb polar species, whereas high silica (siliceous) zeolites prefer to sorb non-polar, organic species, such that potassium zeolite A is often used as a drying agent for organic sol-

vents and silicalite (all-silica form of MFI) can selectively remove traces of organic molecules from water [28]. Molecular sieves are used industrially in a range of separation processes and as desiccants. The separation of linear from branched hydrocarbons using Ca-A [29] and para-xylene from a mixture of xylene isomers using K-Y or Ba-Y [30, 31] are amongst the most valuable.

Catalysis

The high available reaction area and well defined porous structure of these materials along with their intrinsic acidity make them extremely useful in a wide range of catalytic applications, both as acid catalysts and as highly ordered supports for metals. Since catalysis forms a large part of this work it will be discussed more extensively in Section 1.7.

Recent Applications of Molecular Sieves

Recently, attention has turned to sieves as *filled materials* [32], where they are used as well defined hosts for another component. This results in the properties of either the sieve or filler compound (or both) being altered [33].

The utility of the zeolite ZSM-5, in a very diverse range of applications, has actually been blamed for the lack of investigation of other structure types. However, research has now switched to a wider range of zeolites for use in the production of fine chemicals *eg.* with enantioselective properties [34].

A review of potential high technology applications in the electronic and optical fields is given by Ozin *et al.* [32]. *Molecular wires* are similarly reported with conducting polymers grown inside zeolite frameworks [35]. Such materials have great prospects but, as yet, no commercial applications.

1.4 Large Pore Materials

The molecular sieve with the largest known pore size is JDF-20, an $AlPO_4$, with 20 T-atom windows ($\approx$ 18Å in diameter). However, the channels of this molecular sieve are partially restricted by O/OH groups [36] which protrude into the windows. Large pores are very desirable in separation and catalytic processes since this increases the maximum size of molecules which may enter the porous system. The discovery of molecular sieves such as VPI-5 [37], Cloverite (a gallophosphate) [38] and JDF-20 [36] with significantly larger pore sizes than any zeolite has led to them being termed extra-large pore materials.

It is still difficult to obtain extra-large pore zeolites and faujasite, first synthesised over 30 years ago, remains the largest pore zeolite to date. A major goal in zeolite synthesis has been the crystallisation of aluminosilicate molecular sieves with extra-large pores as these would be extremely valuable in cracking catalysts where conversion of large organic molecules into smaller, more valuable products would be a major advance in catalyst manufacture.

Perhaps the most important recent synthetic preparations are the novel range of inorganic materials, discovered by Mobil, based on a tube like structure, prepared in the presence of liquid crystals [39-42]. These paracrystalline materials have pores in the range of $\approx$15-80 Å (claimed as >100 Å) which represents a massive increase in pore size. It remains to be seen whether these will be classified as molecular sieves or if they are to be regarded as a new type of inorganic oxide material.

1.5 Zeolite Synthesis

1.5.1 Introduction to Synthesis

Zeolite crystallisation is a complicated process and is not fully understood [3, 7, 13, 43]. It is still not possible to design a synthesis to produce a specific novel structure despite the wealth of research and the various mechanisms proposed, but there may well be more than one mechanism in place during the crystallisation of molecular sieves. The use of synthetic zeolites has a number of advantages over the use of natural zeolites, primarily because synthesis allows a much greater degree of control over the quality of material produced. It is possible to crystallise pure sample of zeolite which may be novel *i.e.* unknown in nature. A number of novel zeolites have found wide application. Synthesis also allows control over the morphology and the $\frac{Si}{Al}$ ratio of the materials prepared which is important if these materials are to perform their tasks efficiently.

The basic synthesis procedure for molecular sieves is shown schematically in Figure 1–7 although in some syntheses a delay between gel preparation and reaction (*aging*) has been found to be particularly important [44, 45]. The synthesis essentially involves the reaction of a reactive silica and an alumina source in a hydroxide solution at high pH and elevated temperatures. To increase the $\frac{Si}{Al}$ ratio of the sieve, organic reagents may be added to the reaction gel, the role of which will be discussed in Section 1.5.2.

Zeolites are metastable phases and if they remain in contact with their mother liquor they will eventually transform to more thermodynamically stable phases such as quartz. Hence, in crystallisation there is a danger of reaction over-run to these dense phases, particularly if organic void fillers are not included in the reaction mixture. Therefore, sampling is carried out during synthesis and crystallisations are terminated after the appearance of the desired product. After the solid zeolite has been removed from the mother liquor it remains stable indefinitely.

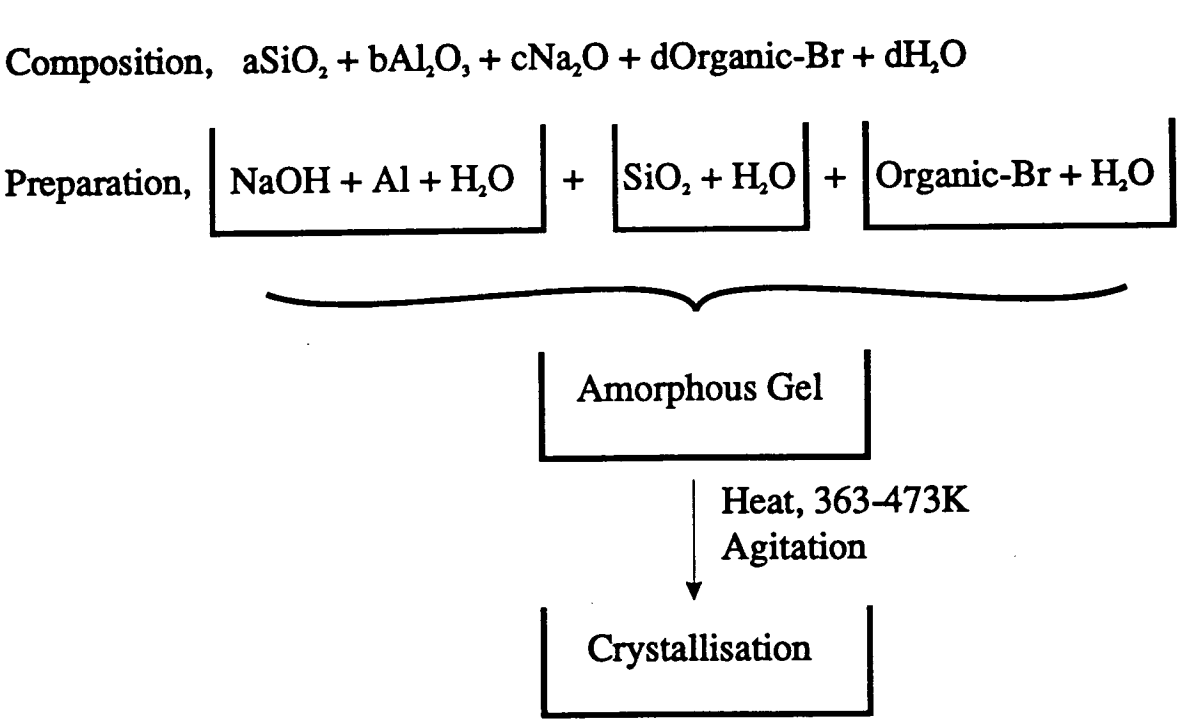

Figure 1–7: A schematic of the general preparation procedure adopted for zeolite synthesis.

1.5.2 The Role of the Organic Component

The role of the organic component in molecular sieve synthesis remains uncertain. It is possible that the organic's role varies between syntheses. Initially the idea of the organic's shape controlling the type of framework created led to these organics being known as *templates* [46] where the organic component was thought to behave as a template [47] around which the molecular sieve structure was built. Similarly, in an attempt to rationalise the effect of inorganic cations in zeolite synthesis Flanigen proposed a *Templating Theory* [48]. However, there are a number of anomalies *eg.* one organic species such as tetramethylammonium cations (TMA^+) can be used in the synthesis of a range of structures and a structure such as MFI may be produced from a number of different templates [47]. Indeed, MFI may be synthesised from an organic free system, although the compositional range from which it can be formed is much reduced.

It has been observed that many organic components do not behave as true

templates *i.e.* where the shape of the channels or cavities is directly related to the structure of the organic present. However, good examples where the organic does appear to act in such a way is that of TPA-ZSM-5, with the tetrapropylammonium (TPA^+) fitting neatly in the channel intersections and the propyl chains extended into the intersecting channels and also TMA^+ in a sodalite cage, where the TMA^+ is too large to have entered the cage after crystallisation, but fits closely inside the cage itself. A similar closeness of fit has been suggested for the hexamethonium cations employed in synthesis of EU-1 [49]. Many studies have been carried out on the role of the organics in zeolite synthesis and Lowe and Araya [50] suggest that many are merely void fillers rather than true structure directors. This has also been demonstrated by the very recent work of Lowe, Nee and Casci [51].

As has already been mentioned zeolite frameworks contain a negative charge associated with the framework aluminium which is balanced by extra-framework cations. The $\frac{Si}{Al}$ ratio can be increased by using organic cations as charge balancing species. Since the pore system can accommodate fewer bulky cations than inorganic cations, the amount of Al that can be incorporated into the framework is reduced. (TMA^+) was the first quaternary amine to be employed in zeolite synthesis, producing the zeolite A (LTA) structure (known as N-A, where N denoted a quaternary amine had been used), with increased $\frac{Si}{Al}$ ratio [52]. Although TMA^+ may readily fit into a sodalite cage, it was found that Na^+ ions were also required in this system. The advantage of TMA^+ in LTA synthesis, is that one ion is occluded per cage, as opposed to 3 Na^+ ions. This allows a higher $\frac{Si}{Al}$ ratio in the product. Subsequently, other quaternary ammonium cations have been used to produce a wide range of high silica materials. These quaternaries are located in the large zeolitic voids, (cages, channels, and intersections) and indeed many structures can not be obtained in the absence of such organic components.

Clearly, the organic component plays a crucial role in zeolite synthesis. A complete understanding of this role would significantly advance research towards the goal of engineering specific new structures. The use of organics in zeolite synthesis is discussed in a review by Davis *et al.* [53]. The role of the organic component is possibly best described as one of structure director rather than as a

template. It should also be noted that the organic can influence the gel chemistry where it may modify the distribution of silicate and/or aluminate precursors in the system, buffer the pH by interaction with other components of the gel and also modify the gelation process itself.

1.5.3 Factors Affecting Crystallisation

Crystallisation can be separated into two processes, initial nucleation followed by crystal growth which when represented as a plot of the amount of zeolite crystallised versus time appears as a characteristic *s-shaped* curve. Nuclei continually form and disappear until they reach a critical size (the *critical nucleus*) and are able to support crystal growth. This growth is thought to occur via condensation-polymerisation of aluminate/aluminosilicate/silicate species at the growing crystal surface [43, 54]. This nucleation depends on the degree of supersaturation *i.e.* if there are high levels of supersaturation, many nuclei will form leading to smaller crystals, whereas, at low levels there will be fewer nuclei and thus larger crystals are obtained. Crystallisations are affected by a number of factors including; temperature, pH, the gel composition and a range of history dependent factors *eg.* aging, the nature of the reaction vessels and potential seeding of the reaction.

Effect of Temperature

As the temperature of the crystallisation is increased this usually leads to an enhancement in growth rate and reduction in nucleation time. However, at very high temperatures dense phases are often observed, partially due to over-run of metastable phases. This over-run is suppressed in high silica zeolite syntheses where the organic present in the reaction mixture helps to stabilise the less dense, porous zeolite structure.

Effect of Gel Composition

The gel composition is the primary factor governing the type of zeolite crystallised, hence, variations in any of the components can have significant effects upon the

zeolite formed. The $\frac{SiO_2}{Al_2O_3}$ ratio determines the framework composition and it is common to obtain different phases upon changing this parameter [55]. The $\frac{Si}{Al}$ ratio of the product is usually less than that of the reaction gel as all of the Al is consumed in the crystallisation, however, significant amounts of Si may remain in the liquor. For high silica zeolite crystallisations, an increase in $\frac{Si}{Al}$ ratio increases the rate of crystallisation as the incorporation of Al into the framework is energetically less favourable than that of Si. This may be because the Al-O bond is longer than a Si-O bond and so disrupts the crystallisation process or because Al goes into specific locations within the framework structure and so introduces steric constraints.

An increase in pH of the gel has (directionally) a similar effect to an increase in temperature, *i.e.* a decrease in the nucleation time and increase in growth rate. This can also result in a decrease in the $\frac{SiO_2}{Al_2O_3}$ ratio of the product as more Si remains in the liquor and consequently an increase in pH usually leads to a reduction in yield.

Water is important in the synthesis of zeolites where it may participate in structure direction as well as provide a medium for nutrient transport. An increase in the water content would dilute the system and so reduce both nucleation and growth rates.

History Dependent Factors

It is not uncommon to obtain "unexpected" products from a zeolite synthesis. However, in many cases this may be attributed to apparently trivial things, such as the history of the reaction vessel and the order of reagent mixing. The agitation of the reaction vessel and the source of the starting materials are also important variables in the synthesis of zeolites and so it is essential to maintain high standards of cleanliness in the preparative laboratories and to be consistent in the reagents used in comparative series of syntheses.

1.5.4 High Silica Zeolites

High silica zeolites are very valuable to the oil and petrochemical industries (Table 1–2). Their high degree of organophilicity and thermal/hydrothermal stability make them ideal as shape selective catalysts. Consequently, the drive to produce high silica materials, of desired structure types is very strong (particularly FAU types). Zeolite Y is the most widely used zeolite in catalytic cracking and typically has a framework $\frac{Si}{Al} \approx 2.5$. This high aluminium content means that zeolite Y may be liable to degradation, particularly by acid attack and in the presence of steam and high temperatures. Therefore, in order to improve the stability of this zeolite various methods of dealumination have been devised. Paradoxically one of the most common ways of stabilising zeolite Y is *steaming* [56] under controlled conditions: mild treatments with steam can improve the material's stability. Another method of stabilisation comes from reaction with ethylenediamine tetra-acetic acid (EDTA) [57] where both of these approaches remove aluminium from the framework structure. Treatment with $SiCl_4$ replaces framework aluminium with silicon [58] and similarly stabilises the material. Similar stabilisation effects are observed by "partially removing" the Al from the synthesis gel by complexing some of the Al as a soluble aluminium phosphate [7].

1.6 Zeolite EU-1

1.6.1 Introduction

While a large number of structure types have been prepared, relatively few have been studied extensively. One such material is EU-1. This was the first novel material to be prepared in the laboratories of Edinburgh University, hence Edinburgh University One, and has been assigned the three letter code EUO. EU-1 has a novel structure type, combining both 10 and 12 T-atom windows, which is potentially very interesting and so is worthy of further study. A brief description of the structure and properties of EU-1 follows.

1.6.2 Synthesis of EU-1

Zeolite EU-1 is a synthetic, high silica zeolite. It was the first novel material reported to have been synthesised using a bis-quaternary ammonium ion (Hexamethonium, hexane-1,6-bis(trimethylammonium)) [49]. This zeolite was also obtained by Rao *et al.* [59] from a mixed template system (benzyl dimethylamine and benzyl chloride were used to make dibenzyldimethylammonium *in situ*) and this procedure produced crystals with $\frac{Si}{Al}$ ratios of up to 525, somewhat higher than the original preparation, where 120 was the maximum reported ratio. Sand *et al.* [60] found that by the use of ammonium ions, rather than sodium ions, in conjunction with hexamethonium, alkali-free EU-1 could be prepared. Similarly tetramethylammonium hydroxide can be used with hexamethonium bromide to afford the alkali-free EU-1 product [61]. Such alkali-free preparations are useful since an ion-exchange step is no longer required after removal of occluded organic by calcination, so a one step calcination is sufficient to prepare the acidic form of EU-1. Sand *et al.* observed that an increase in ammonium content increased the size of the crystals produced, control of which is important for zeolite catalysts.

1.6.3 Structure of EU-1

EU-1 has a novel pore structure as shown in the pore map in Figure 1–8. This pore map is a representation of the van der Waals' surface of the channels. It shows clearly the porous structure, indicated by the *contour* lines, comprising of long, straight, unidimensional channels with large side-pockets (12 T-atom windows) exiting from them. Shannon *et al.* [62] concluded that the framework symmetry was Cmma with lattice parameters of a=13.695, b=22.326 and c=20.178 Å, and the unidimensional channel in the (100) direction. This structure is closely related to that of the NU-87 [63] material (Figure 1–9) since a displacement along the unidimensional channel direction in the EU-1 structure leads to a cross-linking of the side-pockets to form a 2-dimensional channel structure. The zeolite NU-85 is an intergrowth [64], composed of both of these channel structure types in the same crystallite.

Figure 1–8: Pore map of the EUO framework channel structure with the contours outlining the internal void space. This image was obtained with the help of M. Weaver and is included courtesy of I.C.I.

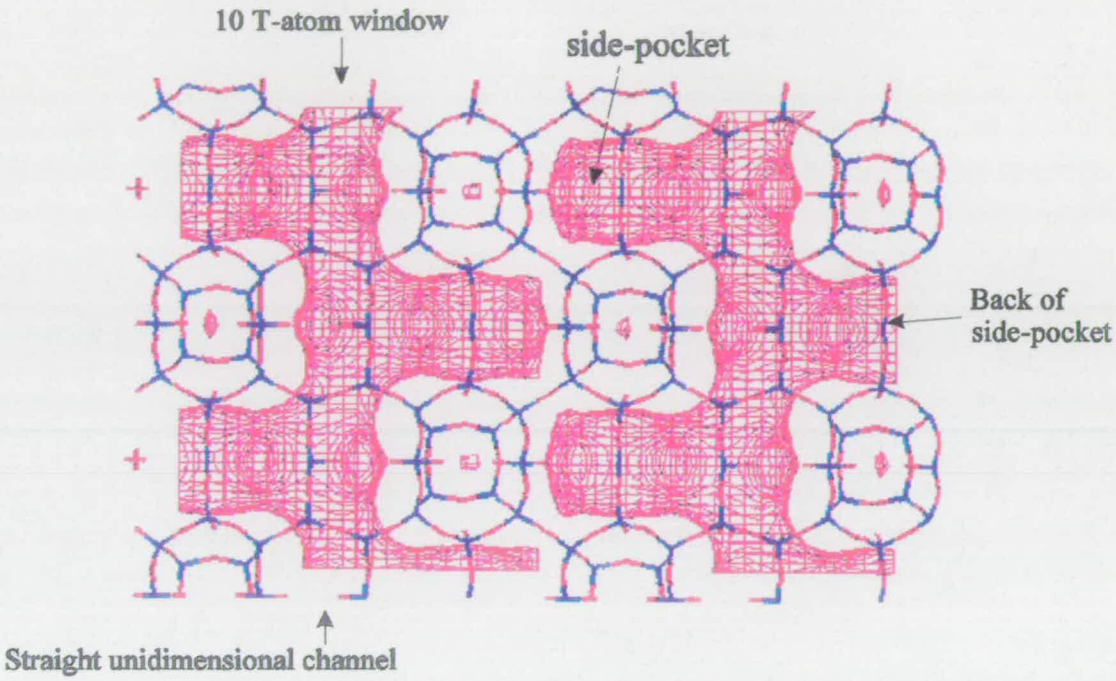

Figure 1–9: Pore map of the 2-D NU-87 (NES) framework channel structure. Obtained courtesy of I.C.I. C. & P., Ltd.

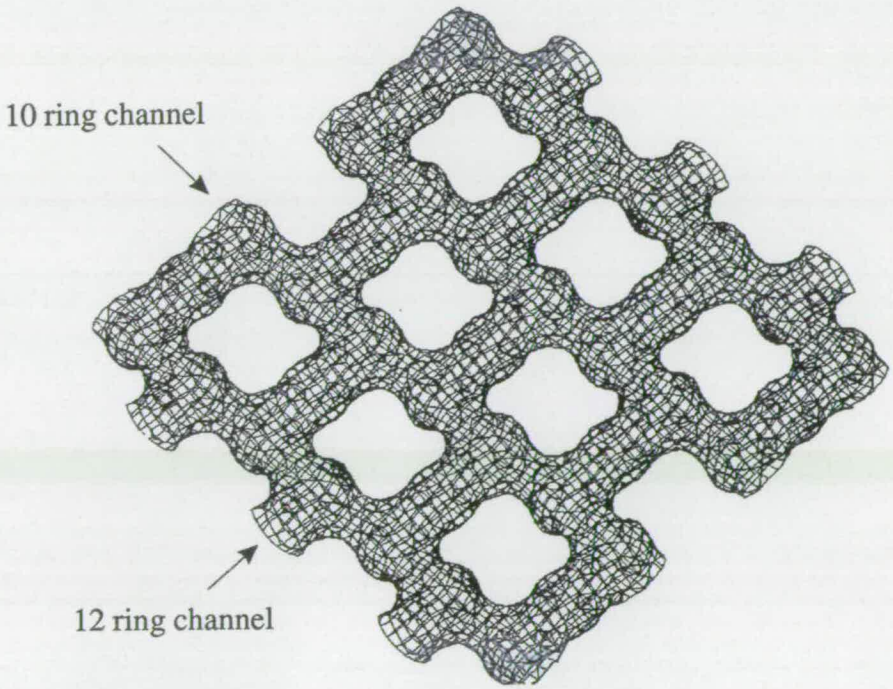

EU-1 has a unique X-ray powder diffraction pattern (XRPD) which alters on calcination [49] with the low angle peaks observed to increase in intensity with respect to the higher angle peaks. This behavior is characteristic of high silica zeolites. This has been suggested to be due to a combination of effects associated with the removal of the organic from the intracrystalline space [65]. Peak intensities are a function of all the atoms present in the unit cell and also their degree of ordering. The occluded organic has a disruptive effect on the crystallites and so its removal has an increase in the long range order of the unit cell and an associated increase in peak intensity is observed. This is most apparent for the peaks at low angles of 2θ. The occluded organic species can also distort the structure and its removal can result in a change in the crystal symmetry

Scanning Electron Microscopy (SEM) showed the original hexamethonium EU-1 crystals [49, 66] to be ellipsoidal agglomerates. Sorption studies with a range of sorbates of different diameters demonstrated [66] that the EU-1 framework has a pore volume of around 14 $cm^3/100g$, with windows $\leq$0.6 nm *i.e.* 10 T-atom rings, which is consistent with the structure proposed by Shannon *et al.* .

1.6.4 Properties of EU-1

EU-1 has a high degree of hydrophobicity as expected for high silica zeolites [66]. Thomas *et al.* [67] simulated the adsorption and diffusion of benzene in EU-1 and related structures. It was concluded that two modes of diffusion were probable in EU-1; a) diffusion only along the straight channels and b) diffusion both along the channels and also into the side-pockets where a global energy minimum was predicted. In essence this means that molecules diffusing through the channels would preferentially reside in the side-pockets since the entrance to the side-pockets is through 12 T-atom windows and so presents a smaller energy barrier to diffusion than along the 10 T-atom channel. This preferential siting could have profound implications for the catalytic capabilities of materials with the EUO structure. Until now, little work has been reported on the catalytic capabilities of EU-1. It has been shown to be a useful catalyst for the isopropylation of benzene [68]

and the original patent [49] claimed significant activity in the xylene isomerisation reaction.

Analogy to ZSM-5

The most versatile zeolite catalyst presently available is ZSM-5 [69] which has the structure code MFI. The long straight channels of EU-1 and its high silica composition are similar to those of ZSM-5 [23] (Figure 1–10) and so it is reasonable to assume that EU-1 may also be a valuable catalyst in a number of different reactions, particularly in reactions where a metal might reside in the side-pocket providing an active centre for reaction. ZSM-5 has a 3-D pore structure as shown in Figure 1–10. This structure is composed of two different types of interconnecting channels, straight 10-ring channels which are elliptical (5.6 Å × 5.1 Å in diameter), and 10-ring sinusoidal channels which are almost circular (5.4 Å × 5.6 Å). The unit cell composition is $Na_y[Al_ySi_{96-y}O_{192}]$. zH_2O, where $y \leq 8$ [70]. ZSM-5 may be produced over a relatively large compositional range and so the framework charge can be varied and tailored to specific applications. There is an all-silica MFI material, Silicalite [71], the proprietal rights to which have been the focus of much legal wranglings.

The active centres of the protonated form of ZSM-5 (H-ZSM-5) have been extensively studied *eg.* [72] where a correlation between the concentration of surface hydroxyls, acidic sites and the turnover of a test reaction (isomerisation of o-xylene) has been found. This isomerisation reaction was chosen as a test reaction as it is known to be catalysed by Brönsted rather than Lewis acid sites. These Brönsted sites may be visualised as proton donors, with the Lewis acid sites being thought of as hydride abstractors. Studies using Temperature Programmed Desorption (TPD) of ammonia revealed the existence of three distinct types of acid sites; strong, medium and weak. The adsorption data suggested the active sites for isomerisation to be the strong acid sites which are located, at the channel intersections.

Figure 1–10: A schematic of the ZSM-5 structure type with long, straight channels interconnected orthogonally by elliptical, sinusoidal channels[a].

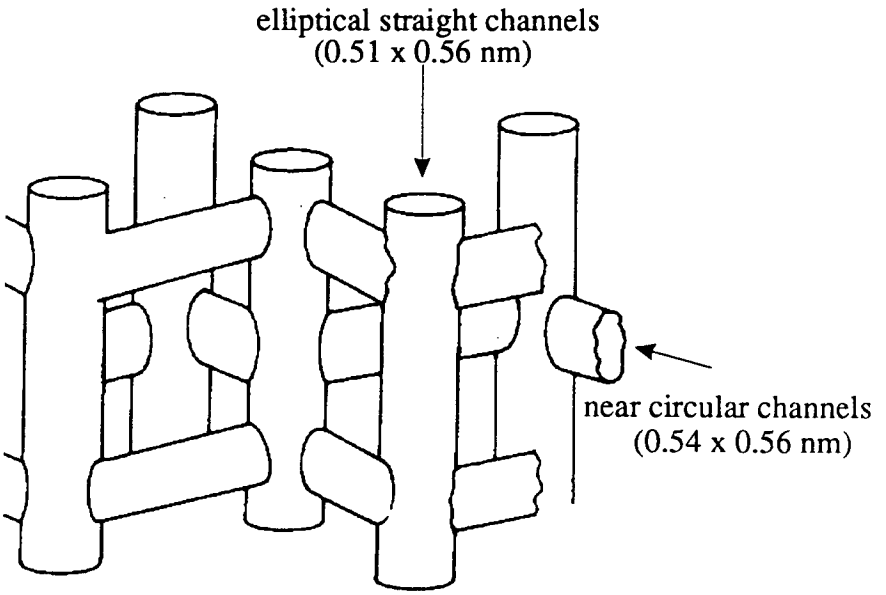

[a] Image modified from ref. [19].

1.7 Introduction to Catalysis and Bifunctional Catalytic Systems

Berzelius [73] was first to offer a definition of catalysis,

> Many bodies...have the property of exerting on other bodies an action which is very different from chemical affinity. By means of this action they produce decomposition in bodies, and form new compounds into the composition of which they do not enter. This new power, hitherto unknown, is common in both organic and inorganic nature...I shall... call it *catalytic power*. I shall also call *catalysis* the decomposition of bodies by this force.

Catalysis essentially involves the addition of a substance (catalyst) to a reaction which increases the rate of attainment of chemical equilibrium without the catalyst itself being consumed in the process.

Table 1–2: Summary of some of the industrially used zeolite catalysts[a].

Process	Catalyst
Cracking	Rare earth exchanged X and Y
Hydrocracking	X and Y, erionite and mordenite, loaded with Co, Mo, W and Ni
Selectoreforming	Ni-erionite, Ni-erionite/clinoptilolite
Hydroisomerisation	Pt-mordenite
Dewaxing	Pt-mordenite, ZSM-5
Benzene Alkylation	ZSM-5
Xylene Isomerisation	ZSM-5
Methanol to Gasoline	ZSM-5
NO_x Reduction	H-mordenite

[a] summary reproduced from ref. [77].

It was the commercial application of zeolites X and Y in the 1960's as hydrocarbon conversion catalysts [74] which led to the huge research thrust in zeolites which has since followed. The Mobil Oil Company lays claim to many of the utilised materials. The most notable are the ZSM series, of which ZSM-5 is possibly the most versatile. The field of zeolite catalysts is extensively reviewed *eg.* [74-76] and some of the industrial applications are summarised in Table 1–2.

Zeolites are particularly suitable as catalysts as they offer extremely high reaction surface area, within well defined shape selective environments where there is the possibility of selective cracking. The 3-D channels of ZSM-5 are particularly useful in catalytic applications as pore blockage *eg.* by coking, does not immediately lead to catalyst deactivation as alternative, *by-pass*, routes are available around any blockage. This is a much more significant problem in zeolites of lower dimensionality *eg.* EU-1 and ZSM-12. The 10 T-atom windows lend themselves very well to molecular sieving of hydrocarbon molecules and so lead to applications in a large number of hydrocarbon conversion reactions.

1.8 Catalyst Preparation

The catalytic capabilities of a number of metals is well known and so their incorporation into a zeolite host is extremely desirable for certain applications. The combination of these two catalytic systems leads to the production of bifunctional catalysts which contain highly dispersed metals, able to catalyse a wide range of reactions, supported in a shape selective and acidic environment.

Preparation of such bifunctional catalysts can be achieved by a range of wet impregnation and physical mixing techniques [75, 76] and a critical examination of some of these procedures follows.

1.8.1 Ion Exchange

The zeolite host is ion exchanged in a solution of a salt of the desired dopant metal. After equilibrium is reached the solid zeolite is removed by filtration and dried, although this exchange can be repeated as often as is required to obtain the desired degree of metal incorporation. This technique is obviously limited to use with zeolites which have a significant ion exchange capacity, otherwise apparent metal incorporation would simply be metal deposited on the external surface of the zeolite crystallites. For sieves with a high exchange capacity excellent dispersion can be achieved with individual metal ions located in the channels and cavities. The apparent size of the ions to be exchanged into the sieve is important as entry to the porous network of channels is limited by the size of the sieve window. Hence, some hydrated ions may be too large to to introduced by such ion exchange. A drawback of this doping technique is that it leads to a reduction in Brönsted acidity of the zeolite as some H^+ ions of the H-form may be irreversibly lost in the exchange process. However, for materials with high ion exchange capacities this is a very useful and reproducible method for the incorporation of metal species into zeolite hosts.

1.8.2 Incipient Wetness Impregnation

The desired amount of dopant metal salt is dissolved in the minimum amount of water required to turn a known amount of dried zeolite powder into a paste-like consistency. This paste is then allowed to dry slowly and it is the zeolite's desire to be hydrated that effectively "pulls" the solvated metal ions into the microporous channels and cavities of the zeolite crystallites. This can however, lead to a very inhomogeneous metal dispersion with the majority of the metal ions deposited on or near the external surface of the crystallites, deposited "like stones from a river" as the solvation front progresses through the channels. This can negate the potential molecular sieving effects of the zeolite host. In this approach complete dehydration is required to achieve successful impregnation. A degree of ion exchange can also be observed with ions transported in the aqueous medium. Such a technique is notoriously difficult to reproduce since the metal species are not homogeneously dispersed.

1.8.3 Physical Mixtures

Intimate mixtures of zeolite and catalytically active metals, usually as oxides, are employed in some catalytic applications. The mixing process is often incomplete and although the use of extensive ball-milling allows a greater degree of mixing there is no deliberate attempt to insert metal species into the zeolite micropores.

There has been a great deal of interest in the application of solid state ion exchange in the preparation of metal loaded zeolite catalysts. Studies led by Beyer and Karge [78-80] have concluded that at elevated temperatures mixtures of metal halides (primarily chlorides) and zeolites in their H or NH_4-forms results in an ion exchange with metal ions entering the zeolite void space and the replaced H species released as volatile gases *eg.* HCl. It has been suggested that the interaction of the zeolite external surface with the metal salt results in a lowering of the lattice energy of the salt such that molecules of the salt are able to migrate into zeolite cavities and react with the protons which are there. This mode of exchange is potentially more useful than solution phase exchange processes as the exchanging ions do

not have associated solvation spheres and so larger ions can enter the zeolite void space unencumbered by a solvation shell. Physical mixing is a relatively cheap and simple preparation procedure.

1.8.4 Isomorphous Substitution

R.M. Barrer proposed [81] that one of the most important properties of zeolites is that a number of elements can be isomorphously substituted into the framework. He suggested four ways by which substitutions can occur and so the properties of the molecular sieves can be modified.

(i) Isomorphous replacement of intracrystalline salts or molecular water by other salts or guest molecules. This is often regarded as creating a different mineral even although the framework topology is unaltered *eg.* Sodalite ($Na_6[Al_6Si_6O_{24}]2NaCl$) and Nosean ($Na_6[Al_6Si_6O_{24}]Na_2SO_4$).

(ii) Cation exchange is facile and normally achieved by direct treatment with aqueous solutions.

(iii) Replacement of framework oxygen by its isotope ^{18}O at high temperatures and pressures.

(iv) Replacement of framework Si and/or Al. This is possible with a number of elements which are close to Si and Al in the periodic table and is usually achieved during synthesis. However, post synthesis isomorphous substitution is possible and is best illustrated by the replacement of framework Al with Si by using $SiCl_4$ *eg.* Na-Y may be heated in a stream of $SiCl_4$ producing a silica rich material. The reverse procedure of Al insertion has also been achieved with aluminium halides [82]. The introduction of Si by such gas phase procedures is very useful provided, the windows in the molecular sieve are large enough to allow access for the $SiCl_4$ to the internal surfaces and that the channels do not become blocked by reaction products (*eg.* $AlCl_3$).

The incorporation of metals such as gallium [83-91] and iron [92-94] into the framework during zeolite crystallisation is well known and is often achieved by simply substituting all or part of the aluminum source in the reaction gel with

the appropriate metal source *eg.* it has been suggested that the substitution of gallium into a zeolite framework may be achieved [95-98] by simple replacement of Al_2O_3 by Ga_2O_3 in the synthesis gel. This procedure has been extensively employed in this work to insert gallium, of a range of levels into the framework of two structure types: EUO and MFI.

A number of workers have confirmed isomorphous substitution [99] by EXAFS in tandem with MASNMR, thermal analysis and XRPD [93]. Isomorphous substitution potentially results in the metal being very highly dispersed in the metallosilicate or metaloaluminosilicate framework. Thus high dispersion of the active metal is readily achieved; however, as tetrahedrally coordinated framework species, the metal is unlikely to be in a catalytically active form [95, 100-103]. Furthermore, this zeotype will now have different properties to the structurally analogous zeolite and catalytically important features *eg.* acidity, may be dramatically different. Extra-framework metal species can be obtained by post synthesis activation, which is usually carried out at elevated temperatures in a variety of atmospheres [104]. These reaction conditions are critical if the dispersion of the ejected metal species is to be controlled, however, the metal component is liable to sinter and migrate to the external surface of the crystallite. This significantly inhibits the shape selective properties of the molecular sieve's microporous structure.

1.8.5 Gas Phase Deposition

The use of gas phase metal species (usually at temperatures above ambient) has become increasingly popular as a novel route to achieving highly dispersed metal species inside the channels and cavities of zeolite molecular sieves [82, 105-107]. Such methods are potentially zeolite composition insensitive *i.e.* work equally well in high and low silica sieves, which is a great advantage over the traditional *wet techniques.* However, such gaseous procedures often require expensive and intricate apparatus would be extremely difficult to scale-up to a commercially viable process. The metals able to be doped are also limited to those which are available as volatile compounds and are small enough to enter the microporous system,

eg. trimethylgallium (TMG) or $Pt(acac)_2$ (platinum acetylacetonate). Combination of the gas phase dopant and zeolite can be achieved in either a static or a dynamic system. If the organometallic is a solid, with a sufficiently high vapour pressure at relatively low temperatures, a static approach can be adopted. The zeolite and the solid organometallic could be physically mixed, then evacuated and maintained in a sealed system, at a suitable temperature to allow gas phase molecules to diffuse into the intracrystalline void space. If the organometallic is already a gas at ambient temperatures the doping can be carried out as a simple pulsed reaction with the dopant pulsed into an inert gas stream which flows through the molecular sieve, supported in a suitable vessel. Most of the metals deposited are in a form not suitable for direct catalytic application and so require degradative pretreatment *eg.* $Pt(acac)_2$ requires a thermal treatment to degrade the organic component and deposit oxidised Pt species [107] in the micropores of the sieve. In addition to the restricted availability of suitably sized organometallic compounds, many of these materials cannot be readily handled or disposed of, as many are pyrophoric, explosive or poisonous. This makes such impregnations very difficult and hazardous to perform, although, the technique is potentially the ideal impregnation procedure.

1.8.6 Appraisal of Doping Techniques

An appraisal of the techniques described above is summarised in Table 1–3.

In practical terms, the physical mixing of metal oxides with zeolite powders is the simplest and cheapest method for the preparation of a bifunctional catalyst. However, the low concentration of active metal sites close to the internal Brönsted acid sites of the zeolite renders this technique inadequate for the direct preparation of a shape selective, bifunctional catalyst. Repeated ion exchange procedures are more labour intensive than a wet impregnation approach, however, for a material with a high ion exchange capacity this allows for a more homogeneous and reproducible distribution of occluded metal species. Incipient wetness impregnation is very simple to perform, however, the deposited metal species tend not to be

Table 1–3: Summary of the advantages and disadvantages of the methods used to incorporate metals into zeolite molecular sieves.

Ion Exchange (IE)	
Advantages	Disadvantages
High dispersion for sieves with a high exchange capacity	Low Loading and Dispersion for sieves with low exchange capacity. Multistep, hence more expensive and often requiring several treatments
Incipient Wetness (IW)	
Advantages	Disadvantages
Cheap, Simple	Inhomogeneous deposition. Deposits primarily on the external surfaces and at pore mouths
Physical Mixtures	
Advantages	Disadvantages
Cheap, Simple	No attempt to introduce metal to zeolite channels and cavities
Gas Phase Deposition	
Advantages	Disadvantages
Highly dispersed metal	Limited number of suitable dopants. Materials are often hazardous.
Hydrothermal Synthesis	
Advantages	Disadvantages
Simple to perform during synthesis. High dispersion of metal	Post synthesis treatments may not produce reproducible catalysts

homogeneously distributed between the crystals as complete mixing is usually not achieved. Wet impregnation, however, may give better dispersions when low silica (aluminous) zeolites are impregnated as the more highly charged internal surface readily accepts the solvated dopant species. However, in the case of a high silica zeolite, both these *wet* techniques *i.e.* ion exchange and wet impregnation, would result in primarily externally hosted metal species. Post synthesis treatments of zeotype materials offers a potentially excellent route to a highly dispersed metal system, however, subsequent thermal activation treatments may not afford reproducible catalysts. Gas phase deposition techniques may offer an ideal mode of metal introduction, however, this is greatly limited by the availability of suitable dopant materials. The reactivity of these organometallic materials makes them difficult and hazardous to work with in the laboratory and so would be many times more difficult to employ on an industrial scale. Clearly, all these routes have their limitations; however, it was decided to use ion exchange, incipient wetness impregnation and isomorphous substitution to prepare bifunctional catalysts in the present study. Gas phase deposition was also examined; however, the practical difficulties of this approach prevented a suitable catalyst being prepared and examined.

1.8.7 Zeolite Catalyst Deactivation

Zeolite catalysts are readily deactivated in hydrocarbon conversion processes by the formation of large organic molecules (coke) which block the zeolite channels or the active site where reaction takes place [108-110]. It has been proposed [111] that for catalyst systems based on high silica zeolites, coking can be retarded if small crystals, of diameter 0.05-0.1 μm, are used (industrially this is a problem as centrifugation and specialised filtration is required to recover these small crystallites). It is proposed that zeolite molecular sieves will always deactivate with time on stream and the industrially important factor is the rate of this deactivation [112]. The problem of coking due to the formation of hydrogen deficient carbonaceous deposits is often encountered as a consequence of the higher dehydrogenation rates produced by an active catalytic system. Although, deactivation

can also be attributed to the formation of large species in the cavities which are unable to be expelled through the channel windows. It appears that simple combustion in flowing oxygen is sufficient to remove the majority of carbonaceous deposits *i.e.* regenerate the catalyst. This, however, may not return the catalyst to its original state as a residual hydrogen pool and some organic fragments may remain and the dispersion and state of any occluded metal species is likely to have been altered. These effects may dramatically alter the activity and selectivity of the catalyst in further reactions.

The metal component of the bifunctional catalyst can also lose its activity. This activity is much less likely to be recovered by traditional regeneration treatments *i.e.* calcination. The metal can be partially lost (leached) from the system at high reaction temperatures where more volatile metal components can be sublimed into the gas phase and carried away from the catalyst. This is particularly true of metal oxide species [113, 114]. Furthermore,the metal often migrates to the external surface of the crystallites where agglomeration of the metal particles (sintering) can occur [103, 104, 115]. It has also been proposed [116] that sintering can occur within the crystals which leads to a degradation of the zeolite structure. Redispersion of the metal is then extremely difficult. The oxidation state of the metal component is usually altered under reaction or regeneration conditions [117]. However, this can often be redressed by suitable oxidative or reductive treatments.

1.8.8 Aromatisation of Short Chain Alkanes

Hydrocarbon conversion reactions are hugely important in the petrochemical industry and as such a great deal of research in particular conversion processes has been carried out. One relatively new and potentially valuable conversion process is that of propane aromatisation. There follows a brief review of the current knowledge of the propane aromatisation process.

The conversion of low value, short chain alkanes (Liquid Petroleum Gas, LPG) to higher value aromatics (BTX *i.e.* benzene, toluene and xylenes) is an extremely desirable process [82]. Much interest has been shown in this conversion and has

led to a variety of industrial processes *eg. Cyclar*, jointly developed by BP and UOP [118, 119], *M-2 Forming* (Mobil)[120, 121] and *Aroforming* (IFP-Salutec) [120, 122]. These processes use a zeolite catalyst with a gallium component and a large amount of effort has been invested in the study of this catalyst system. Many literature reports offer different rationale for similar catalytic observations and so no complete consensus has been reached on the reaction mechanism or on the active species involved. The Cyclar process is based on continuous catalyst regeneration (CCR) technology from UOP and a gallium doped ZSM-5 zeolite catalyst supplied by BP which were combined in a demonstration unit [118, 119]. This unit showed that LPGs could be converted into aromatics and hydrogen on a commercial scale, however, the large fuel gas production from cracking remained a problem. Thus research has centred on catalyst formulations which reduced this cracking activity.

Propane Aromatisation Catalysts

Propane transformation over a metal-free, acid form of MFI (H-ZSM-5) results primarily in the production of propene, ethene and methane by protolysis of C-H and C-C bonds with carbocation formation being the rate limiting step. The observations of many authors [100, 123, 124] have lead to a general agreement that the reaction over the acid form of MFI with an added dehydrogenation component *eg.* gallium, follows the pathway illustrated in Figure 1–11.

Since the initial dehydrogenation is assumed to be the rate determining step, the incorporation of a dehydrogenation component was reasoned to be of significant value. Thus, platinum was initially introduced into the zeolite catalyst. However, the stability and selectivity of these catalysts was not satisfactory. Although activity was significantly increased *cf.* H-ZSM-5 the deactivation rate also increased markedly. This deactivation was primarily associated with the formation of hydrogen deficient carbonaceous deposits formed as a byproduct of the dehydrogenation and acid catalysed reactions. A reduction in metal dispersion at these high reaction temperatures may also have contributed to the loss in activity. It was reasoned that platinum may be more effective when used together

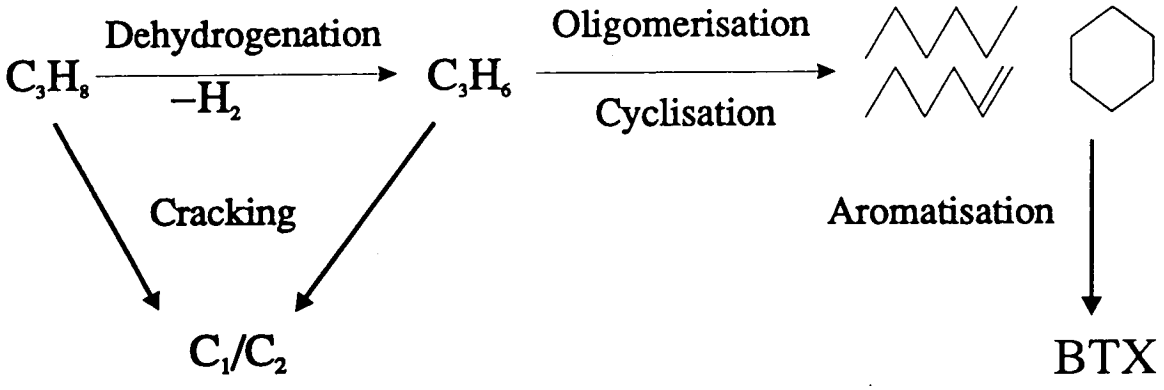

Figure 1–11: Schematic of the suggested reaction pathway for propane aromatisation over H-ZSM-5.

with a second metal *eg.* copper [125] or gallium [113, 114, 125], as was indeed the case, however, other potential dehydrogenation components were also investigated. When gallium and zinc [126] were examined it was observed that zinc was extremely volatile and so was too readily lost from the catalyst [113, 114]. As a result zinc was discarded and gallium remained as the most effective dehydrogenation component for the bifunctional catalyst required for this aromatisation reaction.

Gallium has been found to be active, to a greater or lesser degree, regardless of its method of introduction *i.e.* ion exchange [124, 127-129], incipient wetness impregnation [102, 125, 129-135], physical mixtures [131, 136-140] or as framework gallium species [95, 100, 110, 134, 135, 141-143]. However, it was suggested that the close proximity of gallium species to the acid sites of the zeolite was essential for efficient conversions in this reaction [100, 135, 142].

Work on highly dispersed gallium systems has been extended to materials with tetrahedrally coordinated framework gallium, since these potentially offer a per-

fectly dispersed metal component in the catalyst. The protonic forms of these, produced by ion exchange with ammonium nitrate solution followed by calcination, were observed to have a higher activity for the aromatisation of hexane [136] compared to the Ga^{3+} exchanged form of H-ZSM-5 or Ga_2O_3 physically mixed with H-ZSM-5. However, a gallosilicate exchanged with HCl showed lower aromatisation activity [136], although this was improved by the addition of a small amount of Ga^{3+}. The conclusion drawn from this was that the active gallium species were not tetrahedrally coordinated framework species but were extra-framework species occluded in the zeolite channels and cavities [95].

Gnep *et al.* [123] suggested that zeolite hosted gallium exhibited bifunctional catalysis whereby the gallium species dehydrogenated the alkanes to alkenes and also naphthene intermediates to aromatics while the acid sites catalysed oligomerisation of the alkenes and cyclisation of the oligomers produced. In other studies this group [144] suggested that pure Ga_2O_3 could dehydrogenate propane but was incapable of cyclising hexene, thus concluding that the sole function of the gallium was one of dehydrogenation.

The main difference between the suggested mechanisms was, the mode of formation of the olefinic carbocation which could be readily cyclised over Ga-ZSM-5, *i.e.* either by hydrogen transfer on acid sites or dehydrogenation on gallium species followed by protonation by an acid site. However, it was accepted that both are operable in the Ga-ZSM-5 system. It must be noted that the bifunctionality requires not only these two reaction components but ready mobility between these two active sites. This led to the suggestion that the dehydrogenation function and acid sites must be in close proximity. IR spectroscopy [145] was used to examine the mobility of Ga_2O_3 species supported on H-ZSM-5. After successive treatments with either hydrogen or oxygen, a decrease in the number of acidic OH groups was observed. The conclusions drawn from this were that a semi-reduced form of gallium oxide migrated within the zeolite, thus an interaction between Ga_2O_3 and H^+ may occur which may be represented as follows:

$$Ga_2O_3 + 6\ SiOH \longrightarrow 2\ Ga(OSi)_3 + 3\ H_2O$$

This gallium surface migration would effectively result in an ion exchange between Ga^{n+} and H^+.

A separate observation was made which suggested that the gallium species could act in a completely different manner, not as a dehydrogenation component, but as a catalyst "surface cleaner" [130]. Here gallium species were thought to remove surface hydrogen by a reverse spillover effect *i.e.* allow ready recombination of chemisorbed surface hydrogen atoms (adatoms) to form diatomic hydrogen which could be desorbed into the gas phase and take no further part in the reaction. This reduced rehydrogenation of the alkenes which are required for aromatisation.

These authors also found [129] that in the ZSM-5 system the formation of aromatics could be enhanced by simple treatment with oxygen. They claimed the oxygen was able to selectively react with surface hydrogen and thus provide another route to hydrogen removal, as water. This decrease in surface hydrogen concentration enhances aromatic formation. It may, however, simply be that this treatment also increased the metal dispersion, so increasing the activity.

It was noted that the dehydrogenation ability of gallium species was dramatically increased by the Brönsted acid sites of H-ZSM-5. Thus a mechanism of dissociative adsorption of propane was suggested [123, 144]:

$$Ga^{x+}\text{–}O^{-}\text{–}Ga^{x+} + C_3H_8 \longrightarrow (H^{-})\text{-}Ga^{x+}\text{–}(C_3H_7^{+})\text{-}O^{-}\text{–}Ga^{x+}$$

These surface propyl carbocations formed can then rapidly exchange with zeolite protons by surface migration and then desorption of propene follows with the restoration of the zeolite acid site.

Another proposed mechanism [135] involves gallium Lewis acid sites (L) which are able to hydride-abstract from the propane. These H^- species are able to react with Brönsted acid sites to form diatomic hydrogen and the carbocation again replacing the proton *i.e.*

$$C_3H_7^{+} + H^{+}Z^{-} + \text{L-H} \longrightarrow C_3H_7^{+}Z^{-} + H_2 + \text{L}$$

However, it has also been suggested [131] that a concerted process could occur between gallium species and the Brönsted acid sites for the initial C-H bond cleavage and this would be the rate determining step for dehydrogenation.

Thus, gallium is deemed the best second component for the ZSM-5 bifunctional system since it has a lower rate of deactivation than Pt doped materials and has higher selectivity towards aromatics and lower hydrogenolysis rates which would lead to the formation of methane/ethane. The increased selectivity to aromatics is at least partially due to the reduction in hydrogenation of the alkene intermediates and low rates of hydrogenolysis of alkanes. However, the nature of these active gallium species has yet to be resolved.

1.8.9 Nature of the Gallium in the Bifunctional Catalyst

The gallium species introduced into zeolite catalysts are exposed to oxidising conditions, prior to reaction, and consequently are likely to be in the form of a gallium oxide species (*eg.* Ga_2O_3) deposited in the pores and on the outer surface of the crystallites. Hence most catalysts differ only in the dispersion of Ga_2O_3 and the proximity of gallium species to the acid sites. It has been reported [146, 147] that the order of activity observed for these catalysts is;

Ga doped H-ZSM-5 > H-ZSM-5 > [Ga,Si]-MFI

Although elevated thermal treatments were observed to increase the activity of [Ga,Si]-MFI materials, attributed to the formation of active extra-framework gallium species, it was also noted that framework gallium species are much poorer dehydrogenation centres than extra-framework species [95, 135]. Consequently extra-framework gallium species are required for effective aromatisation reactions.

The influence of the activation procedure is crucial to the investigation of zeolite catalysts. Since conversion in a propane aromatisation reaction leads to significant hydrogen production studies were carried out to examine the effect of these reductive conditions on the catalyst. Consequently, it was found that

reaction in the presence of hydrogen resulted in an increase in the activity of the catalyst. Indeed, a simple thermodynamic investigation of the required reduction temperature of Ga_2O_3 using ΔH_f of 1078.5 $kJmol^{-1}$ and ΔS_f of 85 $JK^{-1}mol^{-1}$ and a Hess's Cycle suggests that,

$Ga_2O_3 + 3\ H_2 \longrightarrow 2\ Ga + 3\ H_2O$

would occur at $\approx$ 1170 K. However, this approach is not applicable in a dynamic reactor system and it has been reported [104, 115, 117, 134, 148] that a partial reduction in the oxidation state of Ga_2O_3 occurs at $\approx$ 873 K.

In summary, gallium loaded MFI catalysts are active for the production of aromatics and hydrogen from alkanes; however, a reduction in fuel gas make would be required for this to become an economically viable process. A bifunctional pathway has been broadly agreed with gallium species able to dehydrogenate alkane and naphthene intermediates and acid sites able to oligomerise and cyclise the alkenes produced. The balance between these functions and the distance between the sites are vital parameters in catalyst performance. The actual state of the gallium remains unresolved although a partial reduction of the gallium from Ga_2O_3 under the reductive reaction conditions is suspected [104, 115, 117, 148]. A number of splendid reviews on aromatisation processes are available in the open literature *eg.* [120, 149].

1.9 Aims of This Work

1.9.1 Introduction

It has already been stated that propane aromatisation is potentially of great importance to the chemical industry. It is appropriate to extend the study of bifunctional catalysts to other high silica zeolite/gallium combinations *eg.* EU-1, NU-85 and NU-87 but more importantly to further rationalise the mechanism of the reaction and attempt to identify the individual components required for successful aromatisation. In the present work a range of gallium containing zeolite and gallosilicate zeotype catalysts were investigated under propane aromatisation conditions. The

presently employed MFI based materials were also examined. As has been mentioned, the EUO structure potentially offers exciting new shape selective reaction conditions. The materials prepared in this work have been characterised by a variety of techniques in an attempt to rationalise the catalytic observations made and so propose criteria required for the successful conversion of LPG feedstock to more valuable aromatic products.

1.9.2 Outline of this Thesis

This first chapter gives a brief introduction to zeolites and the properties of molecular sieves. The concept of catalysis is discussed and the present understanding of the chemistry related to propane aromatisation is summarised.

This is followed by a chapter in which the procedures for the preparation of the molecular sieve catalysts used in this work are described. Chapter 3 then briefly describes the techniques used to characterise these molecular sieves as well as the experimental procedures used in the characterisation experiments. The results of these characterisation techniques are then presented in Chapters 4 and 5. Chapter 4 contains the general characteristics of the molecular sieves themselves including; crystal structure, size and morphology along with the unit cell compositions and acidity determinations. Chapter 5 relates specifically to the location and form of the gallium species, using a range of techniques which include ^{71}Ga NMR, refinement of XRPD data to examine unit cell parameters and also an extensive X-ray Photoelectron Spectroscopic (XPS) study of some of the gallium containing materials.

Two separate series of catalytic experiments are described in Chapter 6 together with the results of each. These are then discussed in conjunction with observations made in the characterisation procedures in an attempt to rationalise the catalytic observations made. Finally, Chapter 7 attempts to draw together the various parts of this work and highlights features worth further study.

Chapter 2

Molecular Sieve Preparation and Activation

2.1 Introduction

An aim of this work was to prepare a range of materials with EUO, and MFI structure types, as aluminosilicates, galloaluminosilicates and gallosilicates. This Chapter details the preparation and synthesis procedures employed in this study.

2.2 Reagents

The reagents used in this work are summarised in Table 2–1 and were used without further purification.

2.3 General Description of Autoclaves

Two different sets of crystallisations were carried out in autoclaves. In the first set, a 1l stainless steel autoclave (designed by Baskerville and Lindsay Ltd., Manchester) designated as autoclave D, was used. The others were carried out in three 500 cm^3 stainless steel autoclaves (also designed by Baskerville and Lindsay Ltd., Manchester), designated A, B, and C. These 3 autoclaves are essentially identical, and a schematic of such a vessel is included as Figure 2–1.

Figure 2–1: 500 cm^3 stainless-steel autoclave.

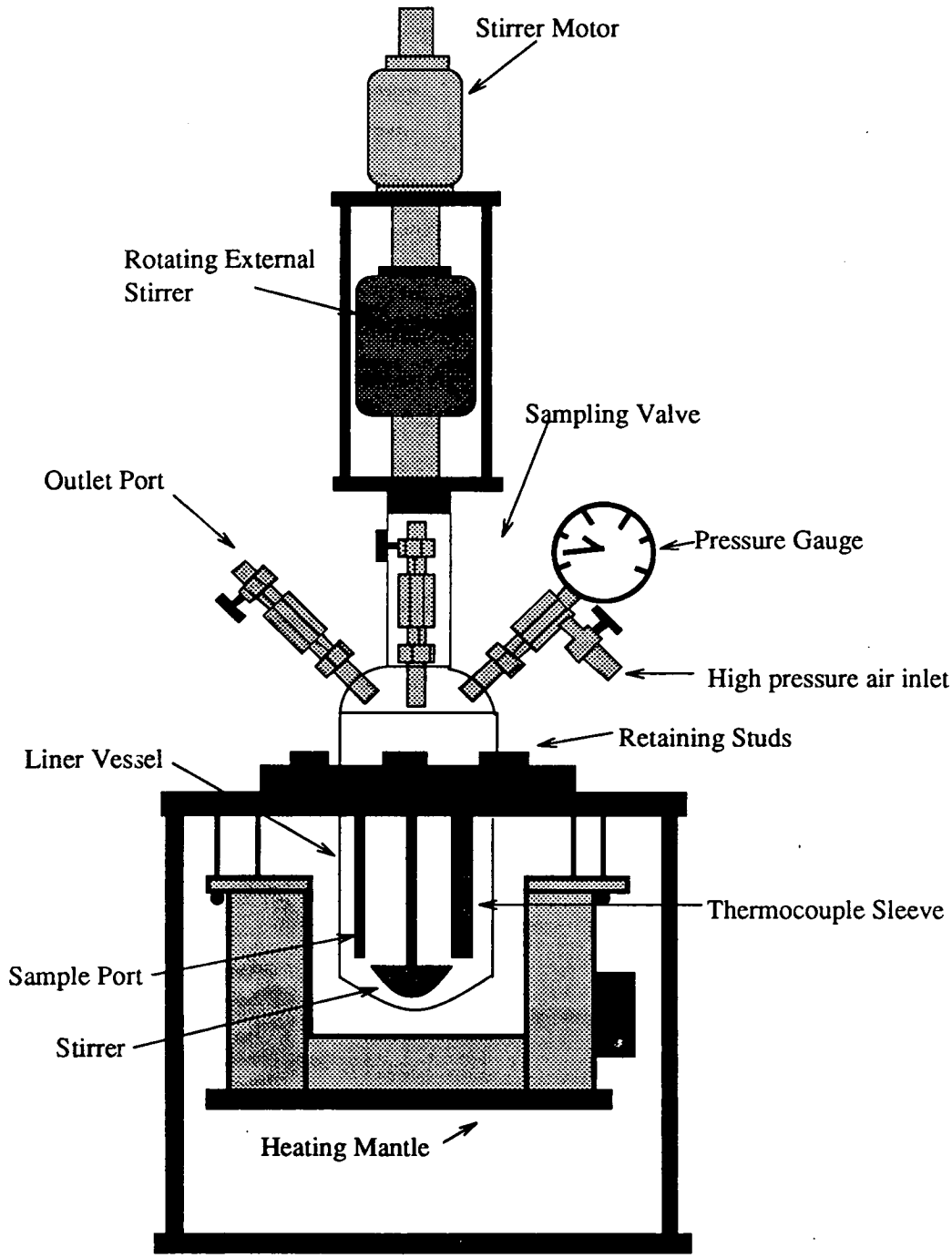

Table 2–1: Reagents used in synthesis procedures

Reagent	**Supplier**	**Grade/Purity**
Tetrapropylammonium bromide (TPABr)	Aldrich	98%
Hexamethonium Bromide ($HexBr_2$) Monohydrate	Aldrich	97%
Sodium Hydroxide (NaOH)	BDH	Aristar
Gallium Oxide (Ga_2O_3)	Aldrich	99.99+%
Aluminium wire	Aldrich	99.999%
Fumed Silica CAB-O-SIL M-5	BDH	-

All autoclaves were stirred by magnetically driven paddle stirrers (300 rpm). These were frequently calibrated using a RS Model TM 2011 optical hand held tachometer (± 5 rpm). A Gu lton-West MC36 temperature controller was used and the temperature monitored by a thermocouple housed inside the vessel along with a thermal trip (usually set 20 K above reaction temperature). A pressure trip was also incorporated into each autoclave which cut the heater power when the pre-set maximum pressure was exceeded. The autoclaves took ≈ 50 minutes to reach 433 K, and the reaction starting time (t_o) was noted as the time when the gel reached the reaction temperature. Reactions in the 500 cm^3 autoclaves could be sampled by means of a dip-tube which allowed aliquots to be removed as the reaction progressed without disturbing the synthesis. The first few cm^3 of samples were discarded to avoid cross sample contamination (samples ≈ 8 - 10 cm^3). The 1l vessel (D) could not be sampled as a dip tube facility was not available.

The autoclaves were leak-tested prior to each run by pressurising the vessel to ≈ 6 atm with air from a high pressure inlet and left for ≈ 20 minutes. If any major pressure loss was detected, remedial action was taken.

Mass balancing was used for all reactions to check that material had not been lost from the reaction as a result of leakage. All material sampled (including waste material collected between samples) was weighed together with the final contents

of the autoclave. The reaction was discarded and the product disposed of if more than 5% of the original charge was lost.

2.3.1 Cleaning Autoclaves

The reaction vessel, dip tube, thermocouple sheath and paddle were washed with water and all visible material carefully removed. Vessels were then charged with ≈ 4 % (wt/wt) solution of Aristar sodium hydroxide and heated to 373 K (at which point the autoclave was set to trip). Hot caustic was sampled to remove trapped material from the sampling port. Once cooled, the solution was discharged and the vessel, dip-tube, paddle and thermocouple sheath were washed thoroughly with tap and then distilled water.

2.4 Sample Nomenclature

Samples obtained from the limited number of syntheses carried out in the 1l autoclave are given the prefix D, followed by a number which indicates the order in which these early synthetic attempts progressed. Materials prepared in the 500cm^3 vessels have a four letter code terminated with a number. The first letter refers to the actual autoclave used (A, B or C) and since the autoclaves were dedicated to one metal type the metal content of the sample may be deduced from this part of the name (A = Al, B = Al + Ga and C = Ga). The next three letters are the notation for the desired structure type, as approved by the IZA Structure Commission *i.e.* EUO or MFI. The names terminate with the experimental number, 1 to 4 which gives an indication of the amount of metal used in the synthesis *i.e.* 1 = lowest amount used while 4 = the highest. For example AEUO1 is the reaction carried out in autoclave A, with Al as the metal type, in an attempt to prepare zeolite EU-1 (structure code EUO) with the lowest in a series of Al contents in the synthesis gel.

Table 2–2: Reaction Gel Compositions[a] for Autoclave D Syntheses (453 K, stirred at 300rpm)

Reaction Number	$ySiO_2$	xM_2O_3	Reaction time/d
D1[b]	60	1 Al	5
D2	60	1 Ga	7
D4	50	1 Ga	5
D6	60	2 Ga	5
D7	60	0.5 Ga	4.5
D8	60	1 Al	5
D9	60	2.5 Ga	6

[a] Composition based on: $10HexBr_2.10Na_2O.xM_2O_3.ySiO_2.3000H_2O$

[b] Reaction carried out at 477 K

2.5 Synthesis of Molecular Sieves

The molar compositions of the gels prepared for the series of reactions carried out in autoclave D are shown in Table 2–2 and for the comparative EUO and MFI series carried out in autoclaves A and C the compositions are shown in Tables 2–3 and 2–4. The gel preparation procedures were effectively identical except for the actual weights of reagents used. The weights of reactants required for the synthesis, which correspond to these molar compositions, were obtained using a programme written by Dr. B.M. Lowe for a BBC microcomputer but were routinely checked manually. The $500cm^3$ autoclaves were charged with 350g of gel and the 1l vessel with 600g.

In each preparation, the metal source (Al wire or Ga_2O_3) was dissolved in a concentrated solution of sodium hydroxide (Solution A). This was carried out in a polypropylene bottle which could be left in an oven at 363 K overnight. This rather rigorous treatment was required to dissolve the gallia or aluminium, which on cooling produced the clear sodium gallate or aluminate solution. The fumed

Table 2–3: Reaction Gel Compositions[a] for the Preparation of MFI Materials at 433 K (stirred at 300rpm)

Reaction Number	xM_2O_3	Reaction time/d
AMFI1	1 Al	1
AMFI2	1.5 Al	1
AMFI3	2 Al	1.2
AMFI4	3 Al	2
CMFI1	1 Ga	2
CMFI2	1.5 Ga	4
CMFI3	2 Ga	3
CMFI4	3 Ga	3

[a] Composition based on: $10TPABr.10Na_2O.xM_2O_3.60SiO_2.3000H_2O$

Table 2–4: Reaction Gel Compositions[a] for the Preparation of EUO Materials at 433 K (stirred at 300rpm)

Reaction Number	xM_2O_3	Reaction time/d
AEUO1	0.5 Al	3
AEUO2	1 Al	3
AEUO3	1.5 Al	3.5
AEUO4	2Al	4
CEUO1	0.5 Ga	4
CEUO2	1 Ga	4
CEUO3	1.5 Ga	4.5
CEUO4	2 Ga	4

[a] Composition based on: $10HexBr_2.10Na_2O.xM_2O_3.60SiO_2.3000H_2O$

silica was weighed into a large beaker and distilled water was added to produce a silica slurry (Solution B). The organic component was dissolved in a small amount of distilled water and added to the silica slurry (B) with thorough mixing using an electric hand blender (Braun Multipractic MR300). The caustic solution (A) was then added together with the rest of the water required to bring the weight of the reaction mixture to the desired amount (350g or 600g). The white gel was thoroughly mixed with the blender for several minutes before it was transferred to the appropriate autoclave.

The B series of syntheses were not completed because of a series of major faults with the autoclave vessel which has since been decommissioned and consequently the series of materials was never completed. Several syntheses with both gallium and aluminium sources in the reaction gel were attempted and some crystalline products were obtained. However, a systematic series of materials could not be prepared. XRPD of the mixed metal materials prepared were somewhat ambiguous and the syntheses were not reproducible and so these materials were not pursued to any great length and are not mentioned hereafter.

2.6 Sample Activation

The autoclave discharges were filtered through 2μm membrane filters under reduced pressure and were washed with copious amounts of distilled water to constant pH ($\approx$9). The washed products were then dried on the filter paper in an oven at 368 K overnight. The as-made materials were first calcined in a static furnace at 773 K for 16 hours, then converted to their *active* acid form by repeated ion exchange with a 1M HCl solution at 313 K. This was routinely achieved with sample and acid (10 cm^3g^{-1} zeolite) in plastic bottles, rotated constantly for 16 hours, in a water bath. The acid was then decanted and the exchange repeated four times in total. After the final exchange the sample was filtered and washed with distilled water before drying overnight at 368 K.

Table 2–5: EU-1 Samples Prepared by I.C.I. C. & P., Wilton

Material	$\frac{SiO_2}{Al_2O_3}$
ZP1	27
ZP2	35
ZP3	49
ZP4	74
ZP5	121
ZP6	712

2.7 Preparation of Gallium Doped Zeolites

Gallium was introduced into the sieves by either Incipient Wetness Impregnation (IW) or Ion Exchange (IE).

A series of EU-1 samples with a range of $\frac{SiO_2}{Al_2O_3}$ ratios were obtained from ICI Chemicals & Polymers Ltd., Wilton. These zeolites were generically named. This zeolite batch was denoted ZP, with this stock name followed by a number (1 to 6) which increases with increasing $\frac{SiO_2}{Al_2O_3}$ ratio, as shown in Table 2–5. These zeolites were then doped with gallium. In addition to these materials I.C.I. also supplied a sample of gallosilicate NU-87 (referred to as [Ga,Si]-NU-87).

2.7.1 Incipient Wetness Impregnation

A known amount of gallium nitrate was dissolved in 10ml of deionised water. This solution was sufficient to turn 10g of zeolite powder into a paste-like consistency. The zeolite was weighed into an evaporating basin and dried at 383K for 16 hours before impregnating with the gallium nitrate solution. The paste was thoroughly mixed with a glass rod and allowed to dry slowly, at ambient temperature.

Figure 2–2: A schematic of the proposed titration of acid sites in zeolites with TMG.

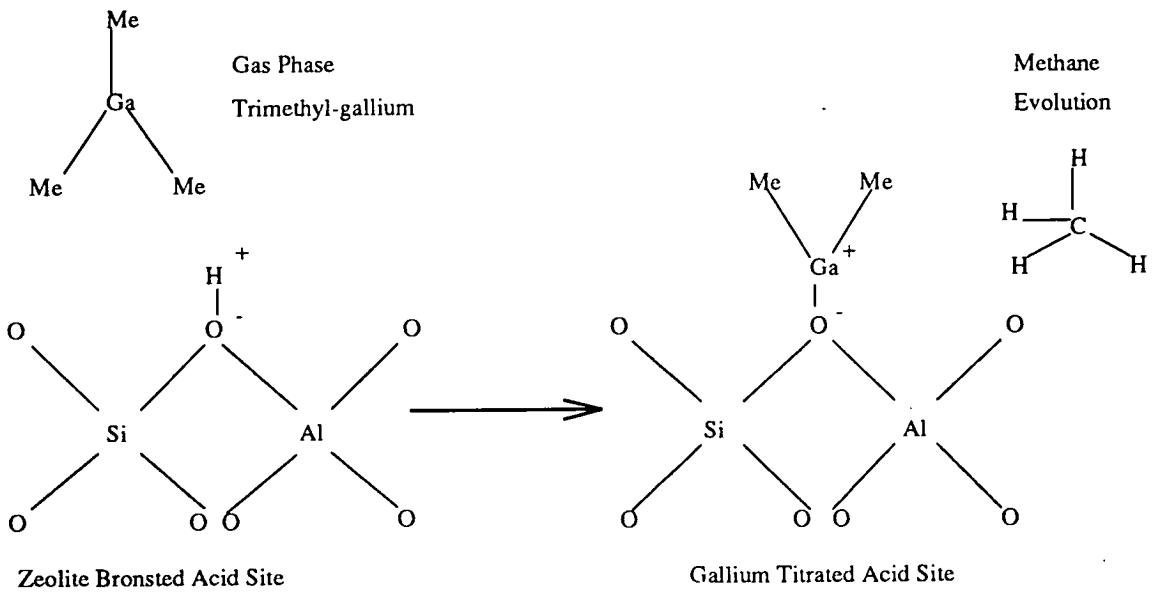

2.7.2 Ion Exchange-Deposition

The zeolite to be doped was placed in a round bottomed, Quickfit flask with a solution of known concentration of gallium nitrate. This was stirred in an oil bath at 313 K for 16 hours before the excess water was removed, on a rotary evaporator, to deposit any unexchanged gallium species on the external surface of the crystallites.

2.7.3 Chemical Vapour Deposition of Trimethyl gallium (TMG)

It has been reported that TMG can be deposited in the zeolite channels by a chemical vapour deposition technique [106]. It was suggested [150] that the TMG was able to titrate the Brönsted acid sites to become incorporated in the framework structure and liberate methane in the process, as represented schematically in Figure 2–2. Such gas phase deposition techniques have been the focus of a great deal of research [105] since they offer a mode of deposition which is potentially

unaffected by the $\frac{Si}{Al}$ ratio of the zeolite being doped. This is unlike the wet techniques, which as previously mentioned, do not offer homogeneous distribution of metal species in high silica zeolites. In the gas phase impregnation experiments carried out in this study, the adsorption process was followed directly by analysis of the methane production using on-line mass spectrometry.

Experimental Approach

A schematic of the experimental apparatus is shown in Figure 2–3. The zeolite ($\approx$ 0.5 g) was held in a stainless steel U-tube supported in a furnace. This was dried under flowing N_2 for at least 4 hours at 473K before adding a pulse of TMG to the carrier stream from the Carle valve. The valve was then evacuated before refilling the 0.2ml loop with TMG for the next pulse to be introduced into the stream of N_2. The TMG was stored in a stainless steel pressure vessel and was egged into the loop by simple diffusion since TMG has a vapour pressure of $\approx$ 200 torr at 298 K. Once the TMG was introduced into the stream of carrier gas it passed over the zeolite sample. Any unreacted TMG was trapped in a stainless steel vessel maintained at 178K (dry ice in alcohol slurry) and the stream was then split between the mass spectrometer and the exhaust flow to vent. The mass signal at 16 a.m.u., for methane, was monitored and the data collected using a BBC Archimedes computer.

This approach to gallium deposition was hoped to allow monatomic deposition of gallium species in selective sites inside the micropores of the zeolite molecular sieves. However, the TMG was so reactive in the presence of water vapour that it decomposed inside the apparatus, before reaching the zeolite substrate. It was not possible to obtain a sufficiently "dry" system during the course of this work and so this approach was abandoned at an early stage. It is proposed that even if a suitable doping apparatus was available the nature of the external surface of molecular sieve crystallites is such that deposition would be primarily on the external surface of crystallites rather than in the channels of the sieves. The TMG was proposed to react with OH species and so the external surface of the crystallites, covered in Si-OH species, would be an extremely reactive substrate for the

Figure 2–3: A schematic of the apparatus used to dope gallium into zeolites by CVD.

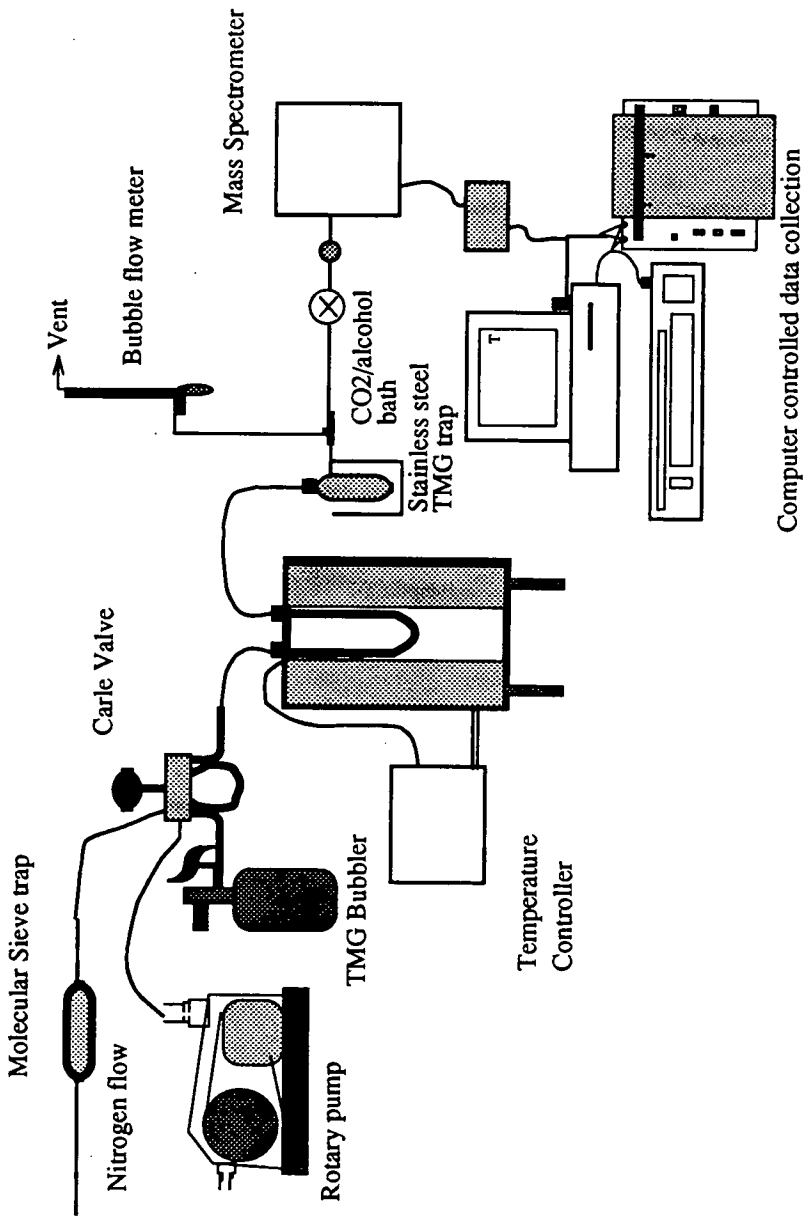

TMG. The probability of a gas phase TMG molecule colliding with the external surface of the crystallites is much greater than the probability of it entering the microporous space and so it is likely that the TMG will decompose on the external surface of the crystallites. Other workers in this field have claimed to have successfully deposited gallium into zeolite hosts [106] by using a flow of TMG. However, it is suggested that the approach employed in their work, exposing the zeolites to flows of the TMG, effectively saturated the external surface of the molecular sieve crystallites with gallium species. These gallium species were not selectively deposited in the zeolite channels, monatomically dispersed, but it is believed that they were simply deposited on the external surface of the crystallites, in a manner similar to IW.

Chapter 3

Analytical Methods

3.1 Introduction

Synthetic zeolites are often prepared as microcrystalline powders (0.1 - 5 μm) which are too small for single crystal X-ray diffraction analysis, which usually would allow elucidation of the structure. However, it is possible to derive a great deal of information from a range of other analytical techniques. The following is a brief account of the principles of each of the techniques used in this work together with the experimental procedures adopted.

3.2 X-ray Powder Diffraction

X-ray powder diffraction (XRPD) is the fundamental analytical technique used in the identification and characterisation of crystalline molecular sieves. The primary function is to determine the nature of crystalline phases present within a sample. Each material generates a unique X-ray diffraction pattern based on the spacings of the atomic planes in the crystallites. These *fingerprints* allow ready identification of a known material, provided a pattern is already available in the literature. A collection of simulated XRPD patterns, prepared by Von Ballmoos and Higgins [151], contains patterns for most of the known structure types and this serves as a starting point for molecular sieve identification.

Great care is required in the interpretation of XRPD patterns since it is quite common for several crystalline phases to be present simultaneously. In addition

to this, the pattern itself can be altered by a number of effects; the most common of which are discussed below. The degree of crystallinity of a sample can only be obtained from XRPD when the pattern is compared to an appropriate reference material.

XRPD patterns can change dramatically on post synthesis treatment *eg.* ion exchange, de-alumination and calcination can modify peak intensities and positions. The degree of hydration of the sample and the geometry of the sample holder itself can also affect the XRPD pattern. Crystal size and morphology can dramatically alter the appearance of the XRPD pattern [152]. XRPD relies on a random distribution of all crystal orientations present in the sample. Small crystals can result in peak broadening and plate-like crystallites can cause *preferred orientation effects.* This is where diffraction at some preferred angles occurs with unusually high intensity, since the crystallites are not randomly orientated in the sample holder and so do not offer a homogeneous distribution of crystal faces to the analysis beam.

Diffraction is observed from a sample when the well known Bragg expression 3.1 is satisfied.

$$n\lambda = 2dsin\theta \tag{3.1}$$

Where λ is the wavelength of incident X-rays, θ is the angle of incidence of the X-rays to the plane, d the distance between atomic planes and n the reflection order.

Figure 3–1 shows that when the path difference is an integer number of wavelengths, constructive interference of the X-rays is observed. This corresponds to a peak in the plot of intensity against diffraction angle, 2θ *i.e.* the XRPD pattern.

3.2.1 Analysis and Instrumentation

Diffraction patterns were obtained using a Philips Powder Diffractometer equipped with an automatic sample changer (type PW1170/02). The goniometer (PW1050/80) was mounted on a stabilised X-ray generator (PW1730/10) which emitted Cu-K_α

Figure 3–1: Schematic of X-ray diffraction conditions.

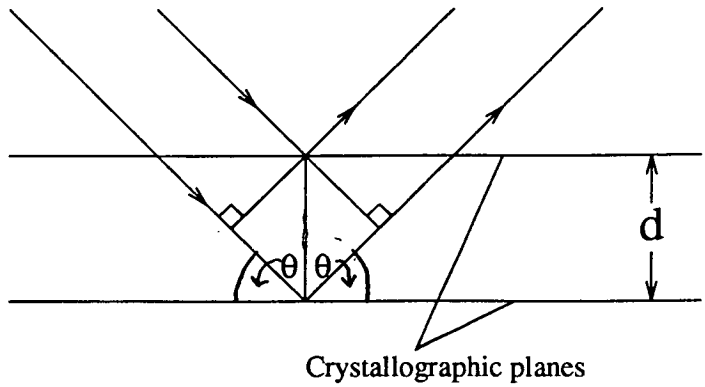

radiation of wavelength 1.5418 Å. The instrument had a PW1390 motor control unit and an AMR focusing monochromator (AMR 3-202E) was fitted in front of the PW1965/60 detector.

Unless otherwise stated, the running conditions were as follows:

Tube voltage	40 kV	Tube current	30 mA
Scanning angle	40 to 3°2θ	Time constant	2 s
Range	4×10^3 cts s^{-1}	Step angle	1° 2θ min^{-1}
Chart speed	1cm min^{-1}	Divergence slit	fixed

Samples were allowed to become hydrated in the laboratory before being carefully ground to a fine powder. They were then packed into aluminium sample holders and the surface carefully flattened with a glass microscope slide, avoiding any shearing action. These filled sample holders were then stored in a desiccator overnight over a saturated solution of NaCl ($\frac{p}{p_o} = 0.735$) prior to analysis. Errors from preferred orientation effects may be minimised by avoiding orientation-sensitive peaks in crystallinity calculations *eg.* in MFI materials the peaks at 23.0°, 23.8° and 24.4°2θ are relatively insensitive to the way in which the powder is packed [61].

3.3 pH Measurement

3.3.1 Introduction

In any synthesis an indication of reaction progress is essential. In zeolite synthesis it was noted that reactions could be followed using pH measurements [153] carried out on samples drawn from the autoclaves during the reaction. Crystallisation is known to be accompanied by a significant rise in pH, attributed to a combination of the occlusion of the organic component of the reaction mixture into the solid product and the incorporation of silica units into the framework produced. The reduction in the amount of silica in the solution phase, results in an increase in the amount of free base in the system, hence the sharp rise in pH. This simple technique is relatively accurate. However, in aluminous systems, where the pH of the reaction mixture is very high the use of pH measurements to follow crystallisations is far less accurate [61].

3.3.2 Analysis and instrumentation

Measurements were carried out as described by Casci and Lowe [153] using a Philips type PW9422 digital pH meter fitted with an EIL type 1180/200/BNC/UKP combination electrode. The meter was calibrated with buffer solutions of pH 7 and 9.2. Samples were allowed to cool for at least 24 hours prior to analysis but were usually analysed in batches after completion of the reaction. Measurements were made on unfiltered samples and the pH values recorded after 10 minutes. The electrode was rinsed thoroughly with distilled water and wiped dry with a tissue between measurements. Plots of pH against reaction time then provided useful information about the successive transformations in the gel.

3.4 Thermal Analysis

3.4.1 Introduction

Thermal analysis is particularly useful in zeolite characterisation. The process simply involves heating a small sample (either statically or in a flow of gas *eg.* air) from ambient temperatures to $\approx$ 1173 K. Thermal Gravimetric Analysis (TGA) gives total weight loss from the sample on heating while Differential Thermal Analysis (DTA) provides information on the thermodynamics of the processes which occur on heating. DTA and TGA can be measured simultaneously *i.e.* simultaneous thermal analysis (STA), so thermal events can be identified and quantified. The sample is weighed into a small platinum pan attached to a very accurate balance along with a reference sample pan which contains a standard material, usually alumina. The samples are enclosed in a furnace and heated, with any weight changes recorded. Any difference in temperature between the two pans at a given point in time is recorded in a Differential Thermal Analysis trace (DTA). This temperature difference can be assigned to either exothermic or endothermic events. In a typical high silica zeolite sample dehydration is represented by an endotherm (usually <473 K). Combustion of any occluded organic molecules is seen as an exotherm usually in the range of 623 K to 873 K. Organic removal usually occurs over a range of temperatures, depending on the location of the occluded organic in the framework and strength of its interaction with the framework.

Samples were routinely examined in flowing air, however, nitrogen or other inert gases may be used where the removal of occluded organics becomes a pyrolysis rather than combustion process. Some instruments also allow differentiation of the TGA. This Differential Thermal Gravimetric analysis (DTG) shows the rate of change of weight loss in the sample. This often reveals events not readily detected in the TGA trace.

3.4.2 Analysis and Instrumentation

A Stanton-Redcroft STA-780 Series Simultaneous Thermal Analyser was used for simultaneous analyses of samples (≈15mg), with a heating rate of 10 $Kmin^{-1}$ in a flow of air (30 cm^3min^{-1}). The data for the analyses were collected on a BBC microcomputer [154].

A Stanton Redcroft TG750/770 thermal analyser was also used to obtain thermal gravimetric analyses only. Samples (≈8mg) were heated at 10 K min^{-1} in platinum pans under flowing air (15 cm^3min^{-1}). The temperature and weight loss signals were displayed on a Kipp and Zonen BD9 dual channel chart recorder. This apparatus was used initially because of the unavailability of the simultaneous apparatus and the TG750/770 allowed more rapid analysis, with a shorter set-up time between samples.

The degree of hydration of all samples was standardised by equilibration, in a dessicator, overnight, over a saturated solution of sodium chloride ($\frac{p}{p_o} = 0.735$), prior to analysis.

3.5 Microscopy

3.5.1 Introduction

Both optical and electron microscopy are extremely useful in sample identification and characterisation. Important kinetic information can also be obtained by simply measuring crystal size as a function of crystallisation time. Impurities that may not be readily detected from XRPD patterns can often be detected by microscopy. The following briefly describes optical and scanning electron microscopies.

3.5.2 Optical Microscopy

This may be used as a first means of determining if crystallisation has occurred; however, only crystals > 5 μm may be observed. In this work crystal sizes were very often smaller than this, hence this technique was not extensively used.

Analysis and Instrumentation

A Vickers model M41 Photoplan microscope was used to examine the samples. Very small amounts of sample were placed on a glass microscope slide with a drop of water and a cover-slip placed over the sample. The images obtained could be recorded by a camera attached to the apparatus.

3.5.3 Scanning Electron Microscopy (SEM)

Introduction

The resolution afforded by optical systems is limited to $\frac{\lambda}{2}$ of the radiation source (≈ 0.5 μm). Substantially better resolution is obtained when accelerated electrons are used as the radiation source. Resolution in SEM is limited by the detection system and the image processing rather than the incident radiation. This greater

resolution coupled with increased depth of field allows detailed surface and structural analyses to be performed. This technique allows study of crystal morphology and crystal size distribution.

Principles

The sample surface is scanned with a very fine high energy electron beam in a pattern of parallel lines (rastor). This causes low energy secondary electrons to be emitted from atoms at the surface. The emitted electrons are collected in the detector, amplified and displayed on a cathode ray tube (CRT) which synchronously scans with the incident beam. Magnification is altered by varying the rastor size on the sample. Resolution may be increased by narrowing the electron beam. However, this usually results in a loss of signal which requires an increase in the accelerating voltage. This, however, can lead to a build up of electrons on the surface of non-conducting samples which causes image distortion and may damage the sample. To counter charge build up and improve the image resolution the sample is coated with a thin conductive layer of gold (≈ 0.01 μm).

Analysis and instrumentation

Scanning electron photomicrographs were obtained using a Cambridge Instruments Stereoscan 250 scanning electron microscope. Mr. John Findlay of the Faculty of Science SEM Unit was responsible for apparatus calibration, sample coating and film processing.

Samples were prepared as follows. A small amount of ground sample was suspended in acetone and transferred dropwise onto an aluminium stub using a Pasteur pipette. The acetone was allowed to evaporate to leave a white residue on the stub. The samples were then gold coated in an argon atmosphere before being transferred to the vacuum chamber of the microscope for examination.

3.6 Elemental Analysis

3.6.1 Introduction

Throughout the course of this work a number of elemental analysis techniques have been used. Initially, the lack of ready in-house elemental analyses prompted the search for a suitable analysis technique. The gallosilicate molecular sieves prepared first (D series of syntheses) proved extremely difficult to dissolve and so the atomic absorption spectroscopy available in the Chemistry Department of the University of Edinburgh was unable to give complete elemental analyses for the materials. It was then suggested that the non-destructive, neutron activation analysis (NAA) was a novel and interesting avenue to explore. This technique was used to determine the gallium content of the D series of gallosilicate molecular sieves prepared. However, this was not a suitable technique for the large number of elemental analyses required in this work. The availability of X-ray fluorescence spectroscopy was then recognised and subsequent analyses were carried out using this technique. A brief description of each technique follows and is concluded with an evaluation of their relative merits.

3.6.2 Atomic Absorption/Emission Spectroscopy

There are a variety of emission techniques *eg.* plasma and flame. The essential difference between them is the atomisation temperature. Samples are atomised at temperatures of 2000 - 3500 K in flame methods compared to 6000 - 8000 K in inductively coupled argon plasma (ICP) spectroscopy. The higher temperature allows analysis of heavy elements and refractory materials with increased sensitivity.

In Atomic Emission Spectroscopy (AES) the flame or plasma acts as the source of radiation. The sample (in solution) is aspirated into the flame or plasma through a capillary tube, where it is atomised. The metallic constituents are reduced to

gaseous atoms which emit characteristic radiation at wavelengths (λ) corresponding to valence electron transitions. However, considerable ionisation may occur at high temperatures which interferes with the observed signal. This may be suppressed by the addition of caesium salts to the sample solution where the Cs is preferentially ionised.

All analyses were carried out by Ms. I. Brown at I.C.I. C.&P. Ltd., Wilton. Analyses were carried out for Si, Al, Ga and Na. Samples ($\approx$ 100 mg) were dissolved in hydrochloric or hydrofluoric acids before dilution with deionised water (100 cm^3).

3.6.3 Neutron Activation Analysis

Introduction

Neutron activation uses artificially induced radioactivity to *tag* elements by a simple neutron capture [155]. The rate of production of activated atoms, **P** is dependent upon the flux of neutrons **f** ($ncm^{-2}s^{-1}$), reaction cross-section σ (cm^2 or barns) and the abundance of the target nuclei, **N** (number/g).

$$P = f \times \sigma \times N \tag{3.2}$$

The flux depends upon the characteristics of the neutron source as does the σ, since this depends upon the kinetic energy of the neutrons relative to the target nuclei and **N** is the desired quantity. With the operation of a conventional *thermal reactor* the primary fission spectrum must be transformed into one with a thermalised neutron distribution with the kinetic energies comparable to a Maxwellian distribution (average E_k = 0.025 eV). The main advantage of neutrons as nuclear projectiles for activation analysis is that they are able to penetrate deeply into a wide variety of matrices without substantial flux gradients, such that matrix effects are minor and are usually negligible. Nuclear decay is a first order process and the decay of product nuclei during irradiation must be taken into account. The familiar integrated rate law is given by 3.3.

$$N_t^* = N_o^* \, e^{-\lambda t} \tag{3.3}$$

where N* is the number of activated nuclei at various times and λ is a decay constant related to the $t_{\frac{1}{2}}$ by $\lambda = 0.693/t_{\frac{1}{2}}$. The combined equation to account for the production and decay of the activated nuclei is expressed as 3.4

$$N_t^* = (f\sigma N/\lambda)(1 - e^{-\lambda t}) \tag{3.4}$$

The general experimental procedure is to remove irradiated samples and observe the nuclear radiations produced either directly with suitable instrumentation or after chemical processing.

It is not usual to attempt to obtain absolute decay rates but rather to compare samples with standards. This comparative method has many advantages over an absolute determination. If a sample and a suitable standard were irradiated for the same length of time in the same neutron flux the ratio of observed activities depends only on the difference in time of analysis and the concentrations of the target nuclei.

Experimental Procedure

Samples were calcined at 823 K for 16 hours and were then thoroughly ion-exchanged with 1M HCl to remove sodium from the samples. Sodium is a very active nuclei and the intense signal it generates masks other signals. Standards were made up from commercially available gallium nitrate atomic absorption standard solution (1010μg/ml of Ga in 1wt.% HNO_3(Aldrich)) and ultrapure water. Accurately weighed samples were placed in plastic vessels (eppudorfs) and sealed with a hot spatula to prevent any spillage of radioactive material. The samples and standards were loaded into a plastic container (known as a *rabbit*) and conveyed into the reactor for the desired exposure time. After exposure the samples were discharged into the laboratory (*hot-lab*). The external surface of the eppudorfs were cleaned with water to remove any contamination before transferring the eppudorfs to a separate laboratory (*clean room*) for analysis. Measurements were made by computer controlled high resolution (Ge) gamma ray detectors. Analyses were carried out with the help of Dr. J.E. Whitley and Dr. M. McCartney of the Scottish Universities Research and Reactor Centre (SURRC) at East Kilbride.

3.6.4 X-ray Fluorescence Spectroscopy (XRF)

When X-rays are incident upon a sample, these primary photons may be of sufficient energy to remove an electron from the inner shell of an atom *i.e.* a photoelectron. The atom is now excited and examination of the resultant relaxation, by fluorescence, forms the basis of this well established technique for elemental analysis [155].

X-ray spectra are usually simple and lines can generally be unambiguously assigned to specific elements. To measure concentrations, a calibration curve is obtained by analysis of standard samples of known composition. The concentration range of the standards should bracket the anticipated concentrations in the unknowns. The matrices of the standards and unknowns should also be similar. These calibration curves are usually simple linear correlations between signal intensity and element concentration. Sample interrogation is not only of the surface but also below this into the near-surface bulk of the sample where scattering and absorption occur. In a multicomponent sample this could hinder quantitative elemental analysis. These *matrix effects* [156] may cause huge distortions of the observed signal. The extent of these effects depends on the medium which the X-rays must pass through and so depends on the absorption coefficients of all the elements present in the sample. These effects are readily accounted for by matrix matching with appropriate standards and so elemental analysis is achieved with a high degree of accuracy.

Experimental Procedure

Since this is essentially a surface sensitive technique it is important to prepare reproducible surfaces if reliable quantitative data is to be obtained. The *glass technique* used for sample preparation involved accurate measurement of $\approx$ 1g of dried sample into a Pt/5% Au crucible with subsequent addition of exactly five times the sample weight of a suitable flux (Johnson Matthey, Spectroflux 105). The crucible, with lid, was placed in a furnace at 1373 K and allowed to fuse for $\approx$ 1 hour. The molten sample was then removed from the furnace and allowed

to cool before the weight loss, caused by removal of moisture in the flux, was replaced by the addition of the same weight of extra flux. The mix was then remelted on a Meker burner, poured onto a graphite disc mould surrounded by a collar and pressed down with a plunger to obtain a suitable surface for analysis. This disc was allowed to cool gradually on a hotplate before being analysed in the spectrometer. This procedure is well known to workers in the field and is that described by Norrish and Hutton [157].

This approach produces a deliberately roughened surface with a texture which resembles an *orange peel* and is deemed to be reproducible. Analyses were carried out by Dr. J.G. Fitton and Mrs. D. James of the Grant Institute of Geology at the University of Edinburgh on a Philips PW1480 wavelength-dispersive sequential X-ray fluorescence spectrometer. The inter-elemental (*matrix*) effects were corrected by online Philips X40 software which produced theoretical *alpha* values to account for these effects. These alpha values correspond to the combined correction factors which account for both primary and secondary absorption coefficients as well as apparatus specific parameters. Calibration curves for Si, Al and Na were already available online and calibration for Ga was achieved by synthetic standards prepared from mixtures of Ga_2O_3 (Aldrich, 99.99+%) and EU-1 zeolite (I.C.I., ZP6). Analysis of these standards is summarised in Table 3–1

Analysis for gallium was simplified by the absence of any spectral line overlap effects or similar interferences. An estimate of instrumental precision is obtained from the spread of observed analyses of the same sample. This was found to be negligible compared to the accuracy, which corresponds to the experimentalist's error in sample preparation. In this work, a total error in analysis, or root mean squared deviation (σ), of 0.11446 wt% was observed.

3.6.5 Appraisal of Techniques

A summary of the advantages and disadvantages of these techniques is shown in Table 3–2.

Table 3–1: Calibration data for the gallium analyses carried out by XRF

"True" wt% Ga_2O_3	Observed wt% Ga_2O_3
0.00	0.00
2.78	2.61
4.05	4.29
4.27	4.31
5.38	5.33
6.72	6.71
Alpha	0.10327
Std Dev σ	0.11446

Of the three elemental analysis techniques examined, XRF was by far and away the most suited to this work and was therefore used for the majority of the elemental analyses. This was primarily because of the ready access to the facility and the rapid and simple sample preparation procedure. This, in conjunction with the reliable and reproducible results obtained made XRF an extremely useful tool. NAA, although non-destructive in principle, was only offered as a service facility and consequently was not available on a regular basis. This is also an expensive and time consuming technique which could only analyse for the gallium contents of the materials when a full elemental analysis was required. The ICPAES was similarly run as a service courtesy of I.C.I. C.&P. and so was not readily at hand. This technique is also notorious for giving low silicon values because of the loss of volatile silicon halides during the dissolution process, in sample preparation.

Table 3–2: Summary of the advantages and disadvantages of the elemental analysis techniques used.

X-ray fluorescence analysis (XRF)	
Advantages	Disadvantages
Readily available facility. Reproducible data. Samples available for reanalysis. Rapid and simple sample preparation. Sensitive for all the elements under examination.	Destructive technique. Requires $\approx$ 1 g of sample.

ICPAES	
Advantages	Disadvantages
Reproducible data. Only small sample required.	Notoriously poor for Si analysis as volatile silicon halides are lost during dissolution. Restricted availability (Service from ICI).

Neutron activation analysis (NAA)	
Advantages	Disadvantages
Non-destructive technique.	Extremely expensive. Not readily available, only offered as a service by SURRC. Sample preparation difficult. Only Ga analysis.

3.7 Pore Volume Determinations

3.7.1 Micromeritic Studies

Adsorption isotherm data may be interpreted in a number of ways, most notably by the BET expression or by the Langmuir approach. However, neither of these are suitable for the examination of zeolite systems, although it is generally accepted that the Langmuir interpretation is more appropriate [158]. This is because the isotherms rely on a number of assumptions which are invalid for microporous zeolites. For example in the BET approach it is assumed that each adsorption site is able to accommodate only one sorbent molecule, the occupancy of each site is equally likely and sorbed molecules have no interactions with other sorbed molecules. These models were essentially designed for flat surfaces and not the microporous structure of zeolites. When the sorbent gas (usually N_2) enters the microporous structure it condenses to effectively behave like a liquid and so from the uptake of N_2 liquid, pore volumes may be determined. Although pore volume offers a more meaningful value for zeolite investigation than surface areas, even these involve the assumption that the N_2 is present as a liquid and so may be misleading. Initial studies of BET surface areas were carried out with a traditional glass vacuum line with mercury diffusion pumps. However, it was soon realised that the lack of reproducible data was most likely a consequence of residual vapour in the apparatus which would be readily taken up by zeolite samples so rendering the analyses meaningless. This vapour could come from a number of sources with mercury from the diffusion pumps and residual water vapour being the most likely. Consequently pore volume determinations were carried out as a service by Mr. R.S. Fletcher of I.C.I. C.&.P, Wilton, on a MICROMERITICS ASAP2400 nitrogen adsorption apparatus.

Figure 3–2: Schematic of typical Isotherm for micromeritic studies, a) Uptake by External Surfaces, b) Zeolite Microporous Uptake and c) Total Uptake.

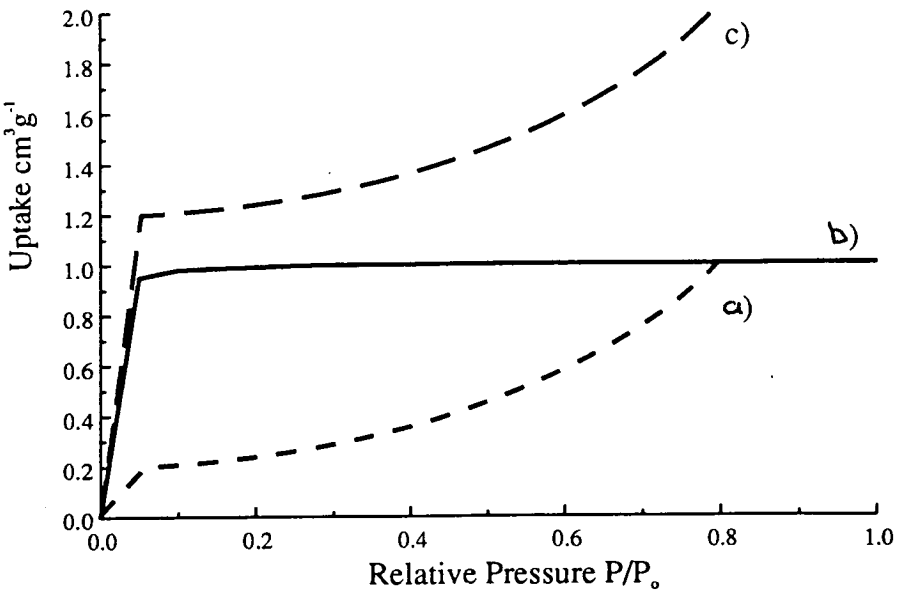

Experimental Procedure

Samples were outgassed offline in an oven at 723 K for 16 hours under a flow of nitrogen. The samples were then transferred to the automated apparatus which weighed the samples before and after adsorption. After the pressure transducers were reset to zero, the sample information was entered into the computer system which allowed generation of void volume data and alpha plots.

Zeolites with little mesoporous or external-surface adsorption exhibit isotherms typical of plot b in Figure 3–2. For most zeolites, the micropores are saturated at $p/p_o = 0.1$; at higher pressures the uptake (u_p) is constant and is equal to the pore volume(**pv**).

The isotherm of a non-microporous material with substantial external surface area is shown as plot a in Figure 3–2. Most zeolites are composed of small (submicron) crystallites and therefore contain both zeolitic micropores and a high external surface area associated with the mesoporous structure formed by crystallite agglomerates. Thus zeolitic isotherms reflect both these features and appear similar to plot c in Figure 3–2.

The uptake $\mathbf{U}_p$ at a pressure **p** relative to the uptake of a standard at the same pressure, $\mathbf{R}_p$, is given by 3.5.

$$U_p = R_p \times S \tag{3.5}$$

where **S** is the relative surface area of the two materials. For a zeolitic material composed of small crystals with mesopores, the uptake at any pressure is the sum of the two components described by 3.6.

$$U_p = R_p \times S + u_p \tag{3.6}$$

At pressures above saturation of the micropores this simplifies to 3.7.

$$U_p = R_p \times S + pv \tag{3.7}$$

Conventionally the uptake of the standard is quoted relative to its uptake at $\frac{p}{p_o} = 0.4$ such that this becomes 3.9.

$$A_p = \frac{R_p}{R_{\frac{p}{p_o}=0.4}} \tag{3.8}$$

Equation 3.7 becomes 3.9

$$U_p = A_p \times S \times R_{\frac{p}{p_o}=0.4} + pv \tag{3.9}$$

This is of the form y = m.x + c, hence, a plot of **Up** against **Ap** should yield a straight line, from which micropore volume and surface area of the unknown material may be determined. This is commonly known as the alpha plot method. Note nitrogen is assumed to adsorb as a liquid, although it is gas uptake which is measured. To accommodate this, the ratio of the densities of the gas to the liquid (0.0015468) must be used to covert the value obtained to one of cm^3g^{-1}.

The micropore volume (pv) is the intercept (c), gradient (m) = $S.R_{\frac{p}{p_o}=0.4}$ and therefore, $S = m/R_{\frac{p}{p_o}=0.4}$. TK800 was the silica standard used for zeolite analyses and has a surface area of 144.9 m^2g^{-1} hence,

$$\frac{S_z}{S_{TK800}} = \frac{m}{R_{\frac{p}{p_o}=0.4}} \tag{3.10}$$

therefore the expression becomes 3.11

$$S_z = \frac{m \times S_{TK800}}{R_{\frac{p}{p_o}=0.4}} \tag{3.11}$$

where S_z is the zeolite surface area.

3.8 NMR Studies

Some nuclei possess intrinsic angular momentum of magnitude $\frac{h}{2\pi}[I(I+1)]^{1/2}$ [156, 159], where I is the nuclear spin quantum number which is quantised into 2I+1 equivalent spin states, each with an associated magnetic moment (μ). In the presence of an applied magnetic field ($\mathbf{B}_o$) the degeneracy of these states is lifted (known as the Zeeman interaction). Moments aligned parallel to the applied field will be of lower energy than those aligned against the field. The energy difference between these levels is small and irradiation with radio frequency stimulates transfer between these levels with a net absorption which occurs when the radio frequency (ν) satisfies ν=ΔE/h, where h is Planck's constant and ΔE is the energy difference between levels. This ΔE is characteristic of a particular nuclei in a particular environment. The NMR spectrum is effectively a plot of radio frequency absorption against radio frequency with the intensity of the absorption directly proportional to the number of absorbing nuclei. The appearance of this plot may alter as the chemical environment of an atom changes with this alteration known as the chemical shift, usually related to some standard *eg.* Tetramethylsilane (TMS) for ^{1}H NMR.

The local magnetic field observed at the nucleus $\neq B_o$ since it is affected by the field created by the local electron density. The Zeeman interaction has the greatest effect on nuclear spin but there are also through space interactions with nearby nuclear magnetic moments. In liquids, however, the rapid, random, rotations average these fields to zero. These tumblings also average the chemical shift effect, observed as the orientation of the molecule changes, with respect to B_o, to zero.

3.8.1 Solid State NMR

NMR in solids [159-163] suffers three major problems:

i) the through space interactions (dipolar couplings) are not averaged to zero by molecular tumbling and long range couplings are also important, which leads to

very broad resonances (tens of kHz).
ii) chemical shifts of a nucleus depend on the orientation of the molecule with respect to the magnetic field and in solids the chemical shift anisotropy is not averaged by molecular tumbling.
iii) since the nuclei are fixed they have very long relaxation times (T_1).

In examining powders (*eg.* zeolites) all possible orientations of crystallites are present so many frequencies are observed, resulting in broad NMR spectra. Therefore a line narrowing technique is required. One such technique is Magic Angle Spinning (MAS) where the sample is rotated rapidly while inclined at an angle of 54° 44′ to the applied magnetic field. The truncated Hamiltonian which describes the dipolar interactions contains a term ($3\cos^2\theta$ - 1) which if zero narrows the line observed. This can occur naturally by random rotations of adsorbed liquid within the zeolite pores *eg.* water where the isotopic average $\cos^2\theta_{ij} = \frac{1}{3}$. The experimentalist may manipulate the sample to a similar state by rapid rotation (frequency ν) inclined to the field at an angleΘ. This causes the Hamiltonian to split into two separate components, a mean value which is independent of time and a time dependent component. Spinning at the magic angle causes $\cos^2\Theta = 1/3$ and so the time dependent component is removed. In some cases multiple pulse methods are able to afford a similar effect [159, 160]. MAS also eliminates chemical shift anisotropy and so removes chemical shift broadening, however, the quadrupole interaction is not of the form ($3\cos^2\theta$ - 1) and so is not entirely eliminated. Consequently samples which have quadrapolar moments are notoriously difficult to examine by such techniques and this problem is not readily overcome.

MASNMR affords information on the environment of a particular atom *eg.* Si connected to 0, 1, 2, 3 or 4 Al in a zeolite structure are distinguishable by their different chemical shifts [163].

3.8.2 ^{71}Ga NMR

Location of the gallium species in the gallium containing molecular sieves was extremely important for rationalisation of observations made in this work. The sim-

plest method for the determination of gallium coordination comes from ^{71}Ga NMR which clearly distinguishes between octahedral and tetrahedral gallium species *i.e.* framework or non-framework gallium [164, 165]. It is conceivable that gallium species could exist in a tetrahedral environment which is not in the molecular sieve framework; however, it is accepted that tetrahedrally coordinated gallium is most likely to form part of the molecular sieve framework. Consequently workers in this field generally assign signals in ^{71}Ga NMR at $\approx$150 ppm to tetrahedral/framework gallium species and at $\approx$0 ppm to octahedral/non-framework gallium species [141, 166, 167]. The technique allows determination of the number of structurally inequivalent types of Ga (or Al, Si *etc.* if under investigation) and from the normalised areas under these peaks a semi-quantitative determination of the Ga content can be obtained [164, 168]. It has been reported that semi-quantitative information has been obtained for tetrahedrally coordinated gallium species in gallosilicate molecular sieves, however, the signal derived from octahedral gallium species appears to be ambiguous and irreproducible and so no quantitative analyses have been successfully completed [164, 169]. Attempts to quantify Ga in gallosilicate molecular sieves have led to the suggestion that Lowenstein's rule applies to gallosilicate zeotypes as it does to zeolites [166], although this remains unconfirmed. However, Ga, like Al, has extremely strong quadrupole interactions and this can cause lines to be broadened beyond detection [163, 167] (apparently invisible Al/Ga). Gallium has nuclear spin quantum number $I=\frac{3}{2}$ which results in much broader lines than Al ($I=\frac{5}{2}$), when the second order quadrapolar interaction is dominant and so experimentally, ^{71}Ga NMR is expected to be more difficult than ^{27}Al NMR because extreme conditions *i.e.* much higher spinning speed and shorter 90 ° pulses are required. As B_o increases so does the intensity of spinning side bands which are a consequence of observations which are separated in time by the rotational period of the sample. These bands can interfere with signals to make quantitative analysis impossible without further experiments designed to remove or discriminate these features. The problem of *invisible* octahedral Al/Ga is well known and it had been suggested that sample equilibration with acetylacetonate (acac) [168] was required to observe a signal from octahedrally coordinated gallium species. However, this was rejected by some workers [169] who suggested

that hydration eased sample analysis and this has been supported by other workers [167]. It is possible that it is the molecular tumblings of these water molecules in the channels of the molecular sieves which reduces the broadening observed, however, this remains unconfirmed.

All MASNMR studies included in this work were carried out by staff at the SERC facility at the University of Manchester Institute of Science and Technology (UMIST). Analyses were carried out on a Bruker MSL 400 spectrometer at a frequency of 122 MHz with a 4mm double bearing probe designed for Magic Angle Spinning. The sample was spun at speeds of > 10,000 Hz in a Zirconia rotor. The experiments were all one pulse with a pulse length of 0.6 μs, a 15 ° flip angle and a 0.5 s repetition time. The Chemical shifts were measured against hexa-hydrated gallium (Ga^{3+}) from a standard gallium nitrate solution. Such experiments are extremely time consuming (≈6h/spectrum) and so very few analyses were obtained in the limited time available to this work.

3.9 Acidity Determinations

3.9.1 Introduction

The use of zeolites as catalysts is primarily due to the presence of two types of acid sites associated with zeolite framework structures, *i.e.* Brönsted and Lewis sites [170]. These may be considered as proton donors or electron acceptors respectively. The nature of these sites has been the subject of a great deal of research effort, much of which is reviewed by Rabo *et al.* [171]. Thermal desorption has long been used to study catalyst surfaces. The review by Cvetanovic and Amenomiya [172] forms the basis of most of the temperature programmed desorption studies undertaken in the last three decades. Acid sites may be most readily investigated by employing a basic probe molecule *eg.* ammonia [173], the temperature programmed desorption (TPD) of which yields information about the strength of the acid sites present and the number of ammonia molecules desorbed indicates the

number of acid sites in the sample. Such probe molecules are often used with a variety of techniques such as, calorimetry [174], ^{1}H NMR [147], X-ray photoelectron spectroscopy (XPS) [175] and most especially IR spectroscopy [146, 173]. There are also many test reactions used to determine the acidity of such solid catalysts *eg.* hexane cracking [176, 177], xylene isomerisation [72] and also the isomerisation of cyclopropane [178, 179].

3.9.2 Cyclopropane Isomerisation

The ring opening of the cyclopropane system to form propene is well known and has been proposed to be a Brönsted acid catalysed reaction [178, 179]. The recirculating reactor used for catalysis studies (described in Chapter 6) was also used for this study with the only modification being the use of a U-shaped glass reaction vessel instead of a stainless steel one. The steel vessel was added after completion of these studies to allow catalytic investigations at temperatures >773 K.

The H-exchanged ZP samples (obtained from I.C.I.) and D series samples were pressed, crushed and sieved (300-500 μm granules). Around 0.1g of the pelletised sample was held in the Pyrex U-shaped reaction vessel and outgassed overnight at 523 K. The samples were then pretreated with flowing hydrogen (15 ml min^{-1}) for 2 hours and then outgassed at 473 K at which temperature the reaction was carried out. The samples were then exposed to cyclopropane at a pressure of 500 torr and the recirculating gases analysed as described in Chapter 6.

3.9.3 Temperature Programmed Desorption of NH_3

Temperature programmed desorption is a widely used technique and a traditional desorption apparatus [72, 177, 180-183] was constructed as shown schematically in Figure 3–3. Around 0.4g of material was weighed into the stainless steel reactor vessel which was then fitted inside the oven. The oven temperature was then raised from room temperature to 473 K and maintained there for $\approx$ 2 hours under a flow of 25 ml min^{-1} of dry helium, to completely dry the sample. This flow was

then switched to a flow of He with 5% NH_3 for $\approx$ 15 minutes to saturate the acid sites in the sample before purging the system with pure He for a further 2 hours (473 K), which is sufficient [184] to drive away any weakly physisorbed ammonia. The temperature was then ramped at 10 K min^{-1} to 823 K and the output from the thermal conductivity detector (TCD) recorded on a chart recorder. This TCD output was also sent to a BBC Archimedes computer where the data was stored and examined using software written in collaboration with Mr. A. King and Sen. C. Alvarez. The samples were routinely maintained at 823 K until data collection was stopped manually.

3.9.4 Quantitative Evaluations

Quantitative analysis of heats of desorption from TPD data is extremely difficult and must always be treated with great caution [176]. Many theories aimed at rationalising the processes which govern ammonia desorption from zeolites have been offered [185-187] although these are generally derived from the Cvetanovic and Amenomiya propositions of desorption controlled by one of three separate processes [172]; (i) desorption can occur without significant readsorption, (ii) with significant readsorption or (iii) the desorption process can be controlled by intracrystalline diffusion. Mathematical expressions, derived for each of these possible processes, have been compared to experimental data [181, 184] and it has been suggested that for microporous molecular sieves the desorption of ammonia is controlled by the intracrystalline diffusion [184]. However, the rigorous data treatments carried out by these workers required extensive analysis by computer software packages not available for this work.

Determination of the heats of adsorption of ammonia in a number of zeolites have been obtained by several workers [177, 185] employing a graphical analysis method derived from the relationship 3.12,

$$2\ ln\ T_{max}\ -\ ln\ \beta\ =\ \frac{\Delta\ H}{R\ T_{max}}\ +\ C \qquad (3.12)$$

where T_{max} is the desorption peak maximum, β the heating rate, Δ H the heat of desorption, R the gas constant and C is a constant derived experimentally.

Figure 3–3: Apparatus used for NH_3 tpd studies.

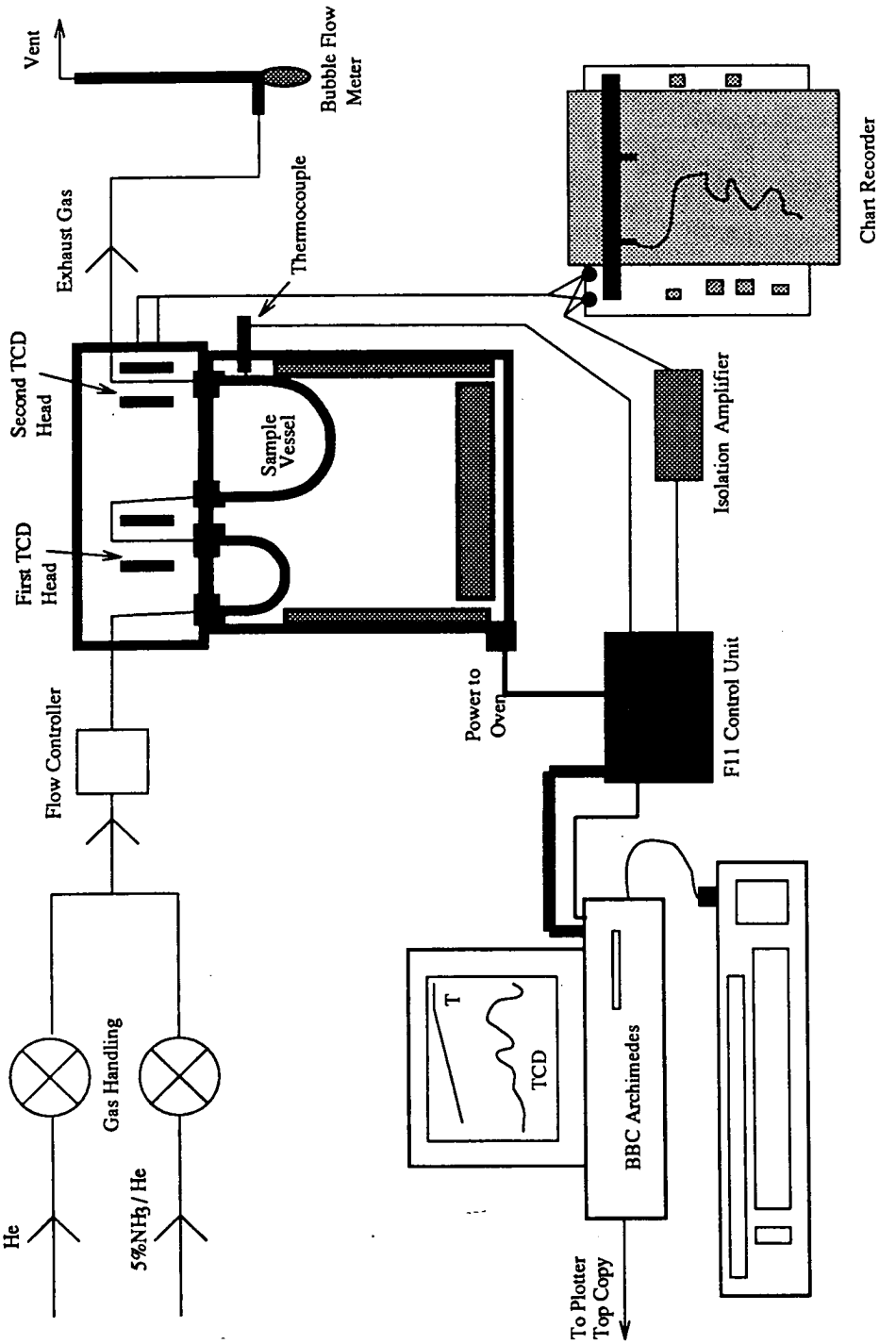

However, this approach requires a sample to be studied with a range of heating rates (β) to obtain Δ H from a plot of (2 ln T_{max} - ln β) v $1/T_{max}$. It has been suggested [188] that β should vary by 2 orders of magnitude to obtain a more reliable analysis; however, experimentally this is extremely difficult. In this work the large number of samples to be investigated made such an approach inappropriate. Many workers have also preferred to adopt a more qualitative approach to characterising zeolites [146, 176, 189] and avoid determination of the heat of desorption entirely.

The ideal analytical approach would be to obtain heat of desorption data directly from a single TPD profile, which is possible with the Redhead approach [188], common in surface science. The Redhead equation (equation 3.20) is very simple and as such extremely useful; however, it does require a constant (ν) which is not readily measurable and must therefore be assumed. This is a major source of variance when this approach is applied to different systems but since a range of materials were to be studied in the present work it potentially offers a convenient method for analysing TPD data. A simplified derivation of the Redhead expression follows [190].

The Redhead Expression

Analysis of data obtained from temperature programmed desorption studies is routinely achieved by inspection of a simple Arrhenius type equation which describes the rate of change of surface coverage ($\frac{-dn}{dt}$) in terms of the order of the desorption process (a), the activation energy of desorption (E_d), the surface coverage (n in Number cm^{-2}) and a pre-exponential, or frequency, factor ν (s^{-1}).

$$\frac{-dn}{dt} = \nu_a \, n^a \, exp \, \frac{-E_d}{R \, T} \tag{3.13}$$

Such analyses are simplified if a linear heating rate (β) such as $T=T_0 + \beta t$ is adopted. The signal or peak detected is at its maximum when $\frac{d^2n}{dt^2} = 0$ *i.e.* for a linear heating rate $\frac{d^2n}{dT^2} = 0$. Differentiation of the expression for the linear heating rate, with respect to time (t), gives $\frac{dT}{dt} = \beta$ and so $\frac{dn}{dt} = \beta\frac{dn}{dT}$ and so substitution into equation 3.13 leads to the expression 3.14

$$-\beta \frac{dn}{dT} = \nu_a \, n^a \, exp^{\frac{-E_d}{R\,T}} \tag{3.14}$$

which is more simply expressed by 3.15,

$$-\frac{dn}{dT} = \frac{\nu_a \, n^a}{\beta} \, exp^{\frac{-E_d}{R\,T}} \tag{3.15}$$

differentiation of this leads to ,

$$-\frac{d^2n}{dT^2} = \frac{\nu}{\beta}\left(an^{a-1}\frac{dn}{dT}\, exp^{\frac{-E_d}{R\,T}} + \frac{n^a\, E_d}{R\,T^2}\, exp^{\frac{-E_d}{R\,T}}\right) \tag{3.16}$$

Since at a peak maximum $\frac{d^2n}{dT^2} = 0$, this simplifies to equation 3.17,

$$an^{a-1}\frac{dn}{dT} = \frac{n^a\, E_d}{R\,T_{max}^2} \tag{3.17}$$

$\frac{dn}{dT}$ can be replaced by substitution of equation 3.15 such that,

$$an^{a-1}\frac{\nu_a\, n^a}{\beta}\, exp^{-E_d/R\,T_{max}} = \frac{n^a\, E_d}{R\,T_{max}} \tag{3.18}$$

and if the assumption is made that the desorption process is first order then $a = 1$ and so simplifies to 3.19. First order processes are indicated by a peak in the desorption profile which is independent of surface coverage for a constant activation energy and this has been assumed to be the case with ammonia desorption from a zeolite.

$$\frac{\nu}{\beta}\, exp^{\frac{-E_d}{R\,T_{max}}} = \frac{E_d}{R\,T_{max}^2} \tag{3.19}$$

Therefore, the temperature of the signal maxima in the desorption profile (T_{max}) is independent of the initial surface coverage for a first order process with a constant activation energy. This particular relationship was further simplified by Redhead who found that the relationship between E_d and T_{max} was almost linear $\pm 1.5\%$ and given by 3.20,

$$\frac{E_d}{R\,T_{max}} = \ln\left(\frac{\nu\, T_{max}}{\beta}\right) - 3.64 \tag{3.20}$$

for

$$10^{13} > \frac{\nu}{\beta} > 10^{8}\ \mathrm{K}^{-1}$$

where, ν, the frequency constant $\approx 10^{13}$, β the heating rate (K min^{-1}) and T_{max} in K. Justification of the value used for ν is derived from the physical process of vibration. This physical motion is a prerequisite of the desorption process and since the frequency of vibrations are of the order of 10^{13} s^{-1}, this is a reasonable constant. When the heating rate is β=10 K min^{-1}, as was the case in this work, the Redhead equation further simplifies to equation 3.21

$$E_d = R\,T_{max}\left(\left[\ln T_{max} \times 10^{12}\right] - 3.64\right) \tag{3.21}$$

This simplified approach has some value to studies of molecular sieves; however, there are systematic overestimations in these calculated heats, associated with the diffusional constraints imposed upon the base molecules *i.e.* the time and consequently temperature differences between the physical desorption of the basic probe molecule and its subsequent evolution from the porous structure and analysis. However, as a qualitative approach it is applicable to the systematic ranges of materials examined in this work. The nature of the experimental approach adopted in this work was such that precise identification of T_{max} was not readily achieved and so consequently most of the analyses were derived from investigation of temperature ranges, rather than precise T_{max} measurements.

3.10 X-ray Photoelectron Spectroscopy (XPS)

3.10.1 Introduction

It is accepted that the nature of a surface (including macrodefects *eg.* grain boundaries and dislocations) is influenced by sample history more than bulk composition and so information on the surfaces of solid samples is vital for rationalisation of their properties. XPS has become an excellent tool for the investigation of

solid surfaces. It was first utilised in the 1950's by Siegbahn [191], however, its fundamental principles were established a century before by Hertz [192] in his examination of the photoelectric effect. Einstein [193] rationalised those observations by proposing electromagnetic radiation to be a cascade of massless particles (quanta). These quanta could have sufficient energy to remove a bound electron from an atom imparting a kinetic energy (E_k) (equation 3.22).

$$E_k = h\nu - E_b - \phi \tag{3.22}$$

E_b = electron binding energy

ϕ = work function of the material

The technique stagnated until the instrumentation was available to reproducibly examine and detect such electron emissions. It was found that the binding energies of electrons were affected by the chemical environment such that *shifts* in spectra could be observed. This *chemical shift* allows differentiation between chemical states of an element. Siegbahn originally called the technique ESCA (electron spectroscopy for chemical analysis). Although initially an academic tool, the advent of commercial spectrometers mean that it is now also a key industrial technique.

3.10.2 Principles of XPS

A schematic of the idealised process is shown in Figure 3–4. The *binding energy* of a core electron (*i.e.* ionisation energy minus the spectrometer and material workfunction contributions) is characteristic of that element. Thus qualitative elemental analysis is readily achieved and with chemical shifts of up to 10eV observed, qualitative evaluation of chemical environments can also be achieved by reference to known data values [194].

Experimentally, the sample was irradiated with low energy X-rays ($AlK\alpha_{1,2}$ = 1486eV in this work) in high vacuum conditions (10^{-8} - 10^{-11} torr). This causes photionisation, with the ejected electrons having a kinetic energy, given by the Einstein Equation, 3.22. The *shell* nature of atoms results in discrete bands of photoelectrons with an E_k distribution of N(E). The photoelectron spectrum recorded is a plot of this distribution N(E) versus E_k *i.e.* the number of electrons

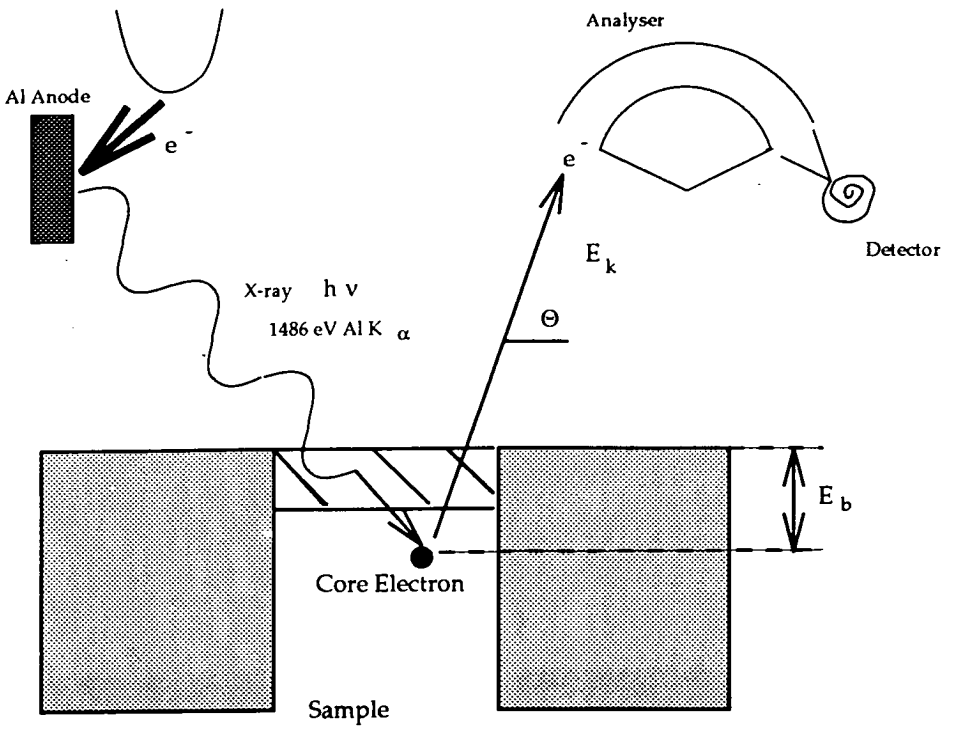

Figure 3–4: Schematic of the processes in photoelectron spectroscopy.

with a specific E_k against the range of energies. The sample atoms are now excited and to relax can either fill this core level hole with another electron and release the excess energy by emission of an X-ray photon or donate this energy to a third electron which is also ejected (Auger emission). These Auger electrons are detectable and give further surface information. Auger spectroscopy is a surface analysis technique in its own right but is not examined further in this work.

Continued bombardment of the sample results in an accumulation of a positive charge on the sample and this can dramatically alter the appearance of the spectra obtained, by both broadening signals and shifting their positions. This is an extremely important effect which must be considered when examining insulating samples. This charging must be countered and is most readily achieved by charge neutralisation with a low-energy electron flood gun (typically operated at ≈ 1 eV). This stabilises the static charging of insulators examined by XPS by supplying a constant flux of low energy electrons to neutralise the accumulating positive charge. Optimum conditions, *eg.* sample position, must be user defined to best suit the particular experimental configuration.

3.10.3 Instrumentation

As illustrated in Figure 3–9 when X-rays impinge upon a sample, electrons can be ejected which can be energy dispersed and subsequently detected. Hence, experimental apparatus requires a source of X-rays, analysis and detection hardware all of which must be enclosed within a vacuum system.

Vacuum System Required for XPS

High levels of vacuum are required in XPS studies for two reasons. Firstly the quantity under examination is the kinetic energy of the ejected photoelectrons and so the emitted electrons must collide with as few gas molecules as possible before analysis *i.e.* the mean free path of the ejected electrons must be much greater than the dimensions of the spectrometer. Experimentally, pressures of 10^{-5}-10^{-6} torr are sufficient for adequate analyses. However, the second requirement enforces much more stringent pressure conditions. Since XPS is surface sensitive, the technique is very sensitive to surface contamination and must therefore operate in a pressure regime where the rate of accumulation of contaminant is negligible. It is known that contaminants accrue at 1 monolayer s^{-1} at pressures of 10^{-6} torr. Hence, to maintain a *clean* sample surface, working pressures of 10^{-9} torr are required. Such pressures are achievable in stainless steel apparatus which can reach such levels of vacuum in a reasonable time by removing the adsorbed gases in a *bakeout* at 473 K. This procedure involves heating the entire apparatus to elevated temperatures to increase the rate of degassing. Since the entire apparatus must be exposed to this temperature regime no materials of fabrication can be employed which would deteriorate under these conditions, *i.e.* stainless steel is preferred for all the components of the apparatus. The vacuum required in an XPS apparatus can be maintained by pumping from a combination of diffusion, ion, cryostatic or turbomolecular pumps.

Figure 3–5: Schematic representation of a X-ray Source[a]

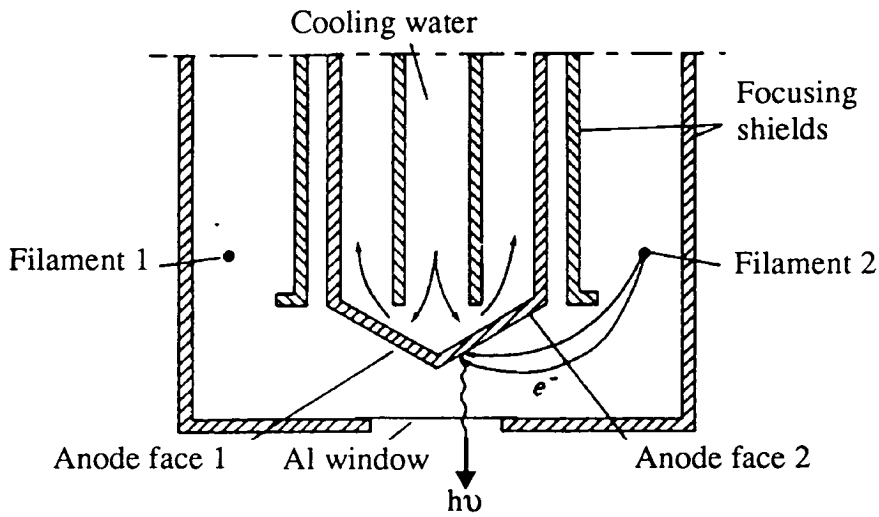

[a]from ref. [195]

X-ray Source

Some X-ray techniques use high energy photons, however, XPS requires only soft excitations (1-2 keV *cf.* XRPD CuK_α = 8.2 keV). Commercial instruments have a variety of sources (*eg.* Al and Mg anodes), as shown schematically in Figure 3–5. XPS sources have an unusual configuration with the filament maintained at around earth potential and the anode maintained at a high positive potential in an attempt to prevent the electrons bombarding the window or other parts of the vessel but to draw them directly to the anode. The anode material is also very important if well resolved spectra are to be obtained. The linewidth of the E_k detected depends upon the linewidth of the exciting photon ($h\nu$) *i.e.* Full Width at Half Maximum (FWHM). For an instrument to have an intrinsic resolution of *circa* 1-2 eV the anode source must have a linewidth of less than 1 eV and yet produce a flux of photons which are sufficiently energetic to probe a large range of core electrons. As such the two most suitable materials are Mg and Al which have the following characteristics.

Anode Material	Energy (eV)	Linewidth (eV)
Mg K_α	1253.6	0.7
Al K_α	1486.6	0.85

Efficient production of these X-rays requires excited electrons with energies an order of magnitude higher ($\approx$15 keV). It is also desirable to bombard the anode with as high an electron flux as possible as photon flux $\propto$ current applied. The necessity to generate as high a photon flux as possible is due to the rapid loss in intensity of the flux through space *i.e.* irradiation flux $\propto 1/d^2$, where d is the distance between the anode and the sample surface. The high power dissipated in this process (around 1kW) means that the anode block must be made of a material which can be readily cooled and so Cu is used with extensive water cooling.

Two anodes are often found in modern XPS spectrometers since it is sometimes essential to have the better inherent resolution afforded by a Mg anode (*cf.* an Al anode) and also changing between these anodes can enable the identification of Auger features. This differentiation between Auger and XPS features arises because when the sources are changed, different energies are supplied to the sample surface, however, similar core electrons will be ejected. The difference between the anodes is apparent in the kinetic energies (E_k) of the ejected electrons *i.e.* the higher the energy imparted to the sample the greater the kinetic energy of any given photoelectron. The XPS binding energies are constant for a particular core electron and so their escape velocities (or kinetic energies) will differ when different anodes are used. However, Auger emissions are a direct result of internal atomic transitions and so are independent of the incident energy *i.e.* the change in incident radiation has no direct effect upon them. Thus XPS and Auger features can be differentiated by changing the energy of the incident X-rays with Auger features apparently unchanged and XPS features showing different kinetic energies (E_k) of photoelectrons.

Windows

The incident X-rays pass through thin aluminium windows, into the UHV spectrometer chamber and irradiate the sample surface. The window provides a physical barrier between the source and sample and so reduces cross contamination of the sample and source material. The window also insulates the sample from the high potential of the anode and any stray electrons from the electron gun used to generate the X-rays. The window itself must be transparent to the primary X-ray photons. It is convenient and practicable to use Al foil (≈ 2 μm), although this attenuates the Al Kα flux by ≈ 15 %. This flux loss is sufficiently small for this window arrangement to be experimentally practical.

X-ray Monochromatisation

Emission from any material is complex and consists of a broad background (known as a Bremsstrahlung) with the narrow characteristic lines of the material under investigation superimposed on this. Removal of this Bremsstrahlung radiation, satellite interference and an increase in the signal-to-noise are all extremely desirable and are achievable by monochromatisation of the emitted X-rays. This is best done by dispersing the X-ray energies by diffraction in a crystal of known d-spacing. Quartz has been found to be particularly suitable as it is simple to produce perfect, large, crystals which may be bent elastically and are stable to *bakeout* conditions. It should be noted, however, that monochromatisation only allows the transmission of a part of the incident flux and so attenuates the photon flux which is not desirable experimentally.

Energy Analyser

The most commonly used analysers are electrostatically dispersive *i.e.* they rely on the action of an electrostatic field to disperse the electrons and separate them by energy so that in any given field only those in a particular, narrow energy range are measured.

Resolution

Analyser resolution is of key importance, however, many terms are used to describe this quantity and confusion often arises. Absolute Resolution (ΔE) is usually the full width at half maximum (FWHM) or may be described as ΔE_B, the width at the base of the peak. Ideally $\Delta E_B = 2 \times \Delta E$.

The Relative Resolution, R, is given by $R = \Delta E/E_o$, where E_o is the kinetic energy at a particular peak position. R is usually expressed as a percentage or as a Resolving Power (ρ), $\rho = 1/R = E_o/\Delta E$. Therefore, absolute resolution is specified independent of actual peak position but relative resolution is applicable only at a specified E_k.

To obtain a resolution similar to the natural linewidth of Al Kα (0.85 eV) requires $R \approx 6\times10^{-4}$. This is only achievable with an unacceptable loss of sensitivity. Hence, it is standard practice to retard the E_k of the photoelectrons, either to a chosen energy (pass energy) or a chosen ratio which is fixed during an experiment. If a pass energy of 50 eV is set and $\Delta E = 0.7$eV was desired a $R \approx 10^{-2}$ would be required and so retardation allows the same absolute resolution to be obtained with lower relative resolution.

Analysers

Cylindrical mirror analysers (CMA) and concentric hemispherical analysers (CHA) sometimes referred to as spherical sector analysers (SSA) are most commonly found and although both have a wide range of operation the CMA performs better under high resolution conditions. Consequently, the CMA has found favour with most manufacturers and is recommended by Siegbahn [196], the founder of XPS. A schematic is shown in Figure 3–6. Here two concentric hemispherical surfaces are used with a potential difference between them, outer surface negative and inner positive. Consequently there is a median equipotential surface between the hemispheres, ideally $R_o = (R_1 + R_2)/2$. The specimen is earthed while the whole analyser floats, isolated from ground potential and so scanning is carried out by varying the potential (or pedestal) the analyser sits on. Generally a large slit

Figure 3–6: CMA Analyser[a]

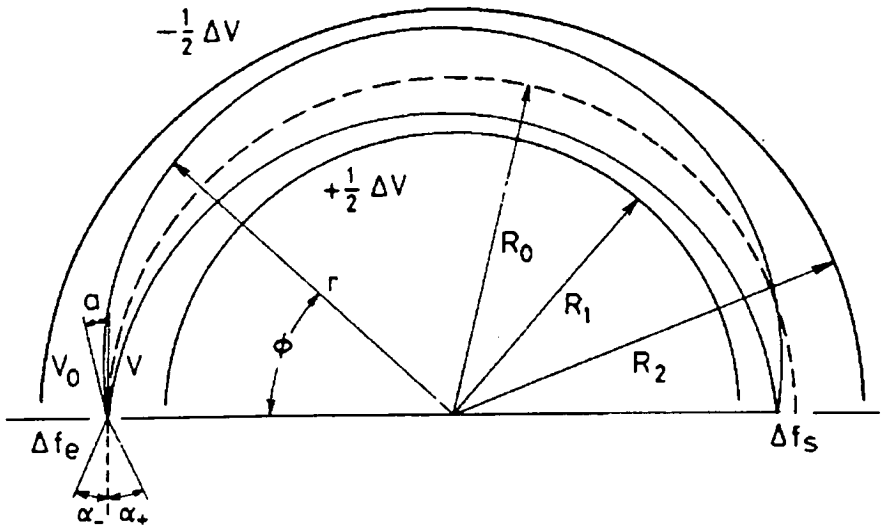

[a] from ref. [195]

entrance (w) is chosen for increased sensitivity and with a compromise between resolution and sensitivity required, it is usual for $\alpha = w/2R_o$ which leads to $\Delta E/E = 0.63\ w\ /\ R_o$. Thus if R_o and ΔE are set, the pass energy $\propto 1/w$. When electrons are decelerated to a constant pass energy there is constant absolute resolution and with a constant analyser transmission (CAT) quantification is easier but signal-to-noise is worse at low E_k. Such retardation is accomplished by planar grids across the entrance to the slit although a similar effect is possible with a lens arrangement. A lens allows the sample to be moved further from the entrance of the analyser and project the analysed area onto the entrance slit so generating a greater working distance below the lens. The dispersed electrons then enter an electron multiplier/detector which operates on a pulse-counting mode (rates of $3x10^5\ s^{-1}$).

3.10.4 Composition Determined at Different Depths

X-rays penetrate deeply into solid samples, however, ejected electrons come from the outermost layers of a sample, their mean free path (λ) being a function of the kinetic energy (E_k) they possess [197]. The analysis volume of samples can vary dramatically, depending on the matrix that the photoelectrons must pass through. It is known that the inelastic mean free path (IMFP), λ, is usually in the range of $\approx$ 1nm in metals to $\approx$ 10nm in organic polymers. The majority of the XPS signal detected originates in the outer surface of the sample, however, statistically it is known that the intensity of the emitted electrons decreases dramatically through the solid matrix, such that 95% of the detected intensity has been emitted from the first 3 λ (IMFP) of the sample (*i.e.* ranging from values of $\approx$3nm for the most energetic photoelectrons from metal samples up to $\approx$30nm for the energetic photoelectrons from organic polymers). The key to the actual examinable volume of the sample is the nature of the sample matrix. Consequently, XPS provides information averaged over the first 3λ (IMFP) of the photoelectrons emitted from the sample. However, it is possible to examine compositional changes, with depth in the sample, in a variety of ways, some of which are destructive to the sample and some non-destructive.

Depth profiling using destructive techniques is notoriously erroneous because of the severe limitations in depth resolution *i.e.* it is extremely difficult to obtain a *clean cut* through the sample, parallel to the original surface. The most successfully employed technique for this *sectioning* of the sample is surface erosion by ion sputtering or ion etching [195]. The sample is bombarded with accelerated ions (*eg.* Ar^+) and a fraction of the ion's energy may be imparted into sample atoms, causing them to be ejected from the sample and so the surface is successively decomposed. However, it is known that ejection of surface atoms is not equally likely for all atoms and so ejection can occur which leads to an apparent enrichment of the surface with atoms which are not so readily ejected. The freshly exposed surface is then analysed.

Non-destructive techniques are obviously more useful since the sample remains

Figure 3–7: Relationship between escape depth λ and energy[a] E_k.

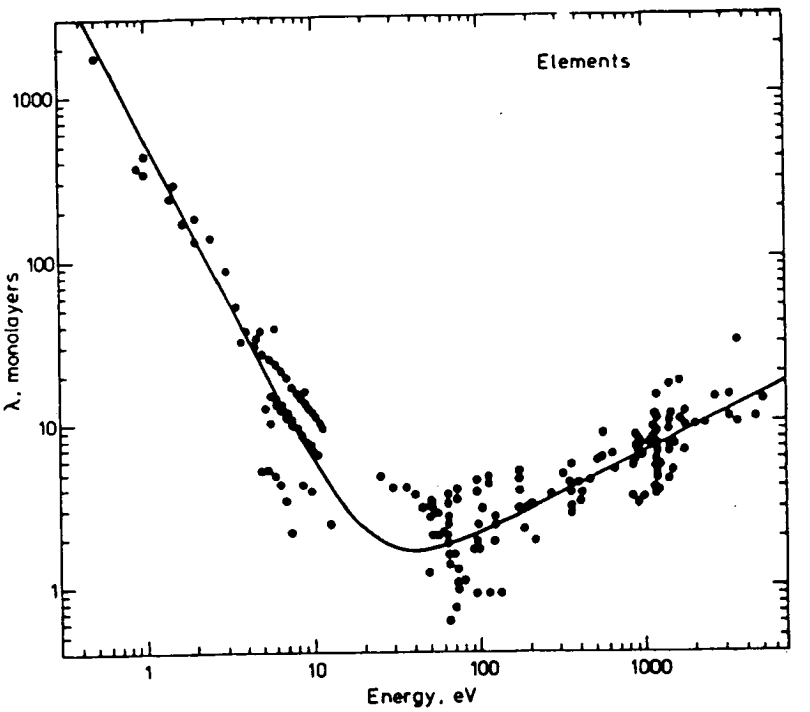

[a] from ref. [195]

intact. Such non-destructive approaches include, analysis of different core levels of the same element, analysis with different X-ray energies and analysis with different take-off angles (θ). The first of these was used extensively in this work. This technique relies upon the fact that photoelectrons from a particular element (but from different core levels) have different binding energies and consequently different kinetic energies upon ejection. These ejected electrons have different inelastic mean free paths (λ) *i.e.* different sampling depths because sampling depth and kinetic energy are known to be directly related *i.e.* $\lambda \propto E_k$ as illustrated in Figure 3–7, a function known as the *Universal Curve.*

Hence, it is possible to determine from a single XPS spectrum if a particular species is enriched or depleted at the *surface*, relative to the *near-surface*, if there are two suitable pairs of signals from photoelectrons sufficiently different in E_k to infer that they have been ejected from atoms of significantly different depths within the sample.

The *Universal Curve* is a collection of observations made by a number of work-

ers who have examined a wide range of samples. It is proposed that the molecular sieve materials examined in this work would follow a similar relationship, in a qualitative manner, but not necessarily through the same absolute range of λ values as depicted in Figure 3–7. Recently a number of workers have tried to obtain a more quantitative estimate for this IMFP value in metal oxide materials [198-200] and they have concluded that precise quantification is extremely difficult, with variances of ≈20% between theoretical models. The TPP-2 approach of Tanuma *et al.* [198] has received widespread acceptance and its use in studies of a range of elements and inorganic compounds has led to the proposition that the IMFP (λ) for Si (2p/2s) in SiO_2 is ≈3.5nm. This approach for a range of inorganic compounds, including, Al_2O_3, has been summarised in a schematic which is very similar to the *Universal Curve*, however, the gradient of the function between 100eV and 1200eV (the operational range in this study) is much greater for these less dense oxide materials. This is as would be expected and qualitatively this means that photoelectrons with very different E_k *eg.* 300eV *cf.* 1300eV, have emerged from very different depths in the sample. Thus a compositional analysis of the sample at different distances into the sample can be obtained from a single experiment.

It has been proposed that the less dense metal oxide matrices have a larger IMFP than those observed for metal samples [198, 199, 201]. This has been partially explained by the suggestion that the photoelectrons are attenuated by a slightly different mechanism in oxides, since there is a reduced propensity for plasmon losses in the oxide matrix compared to that of the metal. This has not been rigorously quantified, however, it is proposed that the most energetic photoelectrons from a metal oxide sample would have an IMFP up to ≈8nm. It is therefore proposed that in microporous molecular sieves, which have huge void volumes, that the IMFP would be significantly increased up to ≈10nm. Consequently, if one considers the two gallium signals, which are of great interest in this work, then clearly there is a significant difference in their binding energy (BE) which would allow them to be used in such an analysis comparing composition at different depths in the sample. The Ga $2p_{3/2}$ has a BE of ≈1118eV which means that the

photoelectrons ejected from this level would have a kinetic energy (E_k) of ≈360eV (using an Al K_α source), compared to the Ga 3d which has a BE of ≈18eV and so an E_k of ≈1460eV. Hence, it is proposed that the analysis depth for photoelectrons from the Ga $2p_{3/2}$ level to be of the order of 10nm and those from the Ga 3d to have an analysis depth (*i.e.* 3λ) of around 25nm. These values have been crudely determined from the TPP-2 relationship proposed by Tanuma *et al.* [198]. Thus, if one considers a spherical crystallite of 1μm diameter, as represented in Figure 3–8, then these analysis volumes represent only the outer shell of the sample particle. The very thin shell which can be analysed by the Ga $2p_{3/2}$ photoelectrons corresponds to only 11.5% of the total volume of the 1μm particle and the deeper analysis offered from the Ga 3d signal which is termed *near-surface* represents only an analysis of 27% of the total volume of the particle, which shows that even the most energetic photoelectrons (*i.e.* those with extremely low BE, like the Ga 3d) are only able to emerge from 5% of the way to the center of this spherical particle. Consequently, the analyses which are described as *surface* in this work represent analyses averaged through a volume which represents a profile 2% of the way to the center of these 1μm particles (analysing 11.5% of the volume of the particle) and those described as *near-surface* analyse a volume which extends 5% of the way to the centre of this spherical particle, analysing 27% of the volume of the particle. These estimates are extremely crude, but do serve to highlight the suggestion that such analyses using different photoelectrons do represent a realistic investigation of the composition of the sample at different depths.

XPS analyses are therefore confined only to the outer surface of the samples under investigation. However, gallium lends itself to such a non-destructive depth analysis since it has two signals which are extremely different E_k and so analyse different depths. The molecular sieve material examined in this work are very suitable for study by such a technique since the analysis depths, defined as 3 IMFP, for the gallium and oxygen signals are significantly different (determined by Tanuma *et al.* [198]) and consequently differences in quantitative analyses can be related to physical differences, in the elemental composition, with depth of the samples. Hence, investigation based on observation of the Ga $2p_{3/2}$ signal can be

Figure 3–8: Schematic representation of a spherical sample particle, 1μm in diameter, with the two analysis volumes described as *surface* and *near-surface* marked for the Ga $2p_{3/2}$ and Ga 3d photoelectrons respectively[a].

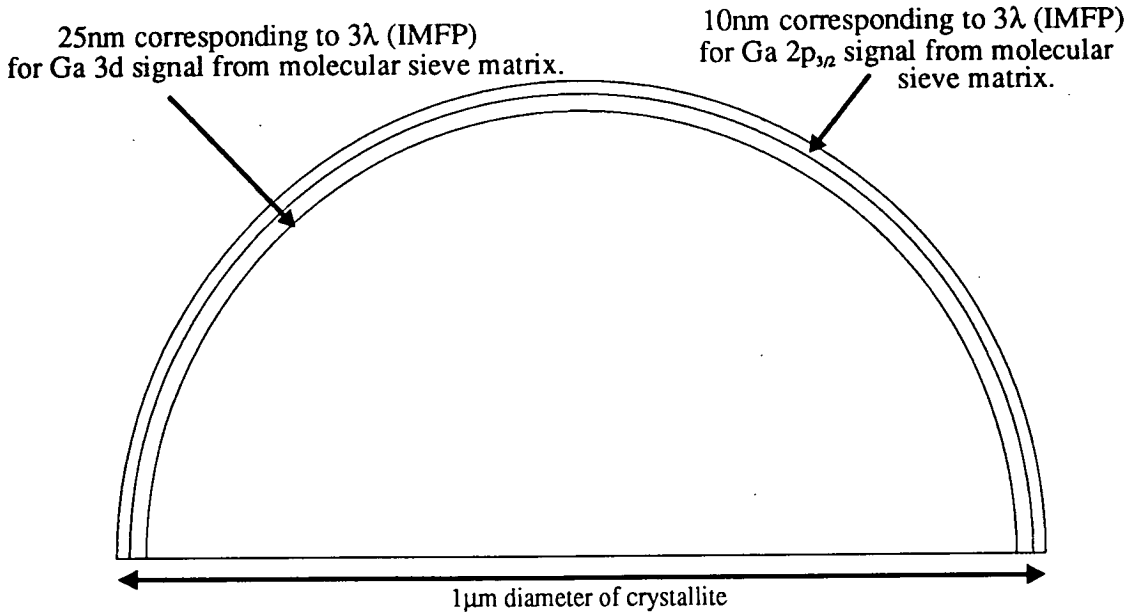

[a]Model dervied from predictions made by Tanuma *et al.* [198].

proposed to be solely of the outer *surface* (extending to a depth of around 10nm into the sample), however, analyses based on the Ga 3d signal can be considered to be analyses averaged over a much greater volume, penetrating to a depth of ≈25nm into the sample and so is considered as *near-surface.*

3.10.5 Experimental Procedure

XPS studies were undertaken on a Surface Science Instruments M-probe Photoelectron Spectrometer at the ICI Katalco facility in Billingham. The basic apparatus configuration is shown schematically in Figure 3–9. This shows the analyser chamber in a simplified form and indicates the close proximity required between sample, X-ray source and the hemispherical analyser and detection system. The sample holder was readily manipulated in all three directions and it should be noted that the ion gun and monochromator facilities were not utilised in this work. A more detailed representation of the M-probe apparatus is included in Figure 3–10. This clearly shows the positions of the flood gun and 2^{nd} X-ray source (non-monochromatised). The sample handling arrangement is shown in Figure 3–11. This separately pumped sectioning allowed very rapid *turnaround* time on the instrument as the analyser chamber did not need to be exposed to atmosphere and so did not require lengthy re-evacuation. This saved experimental time and so increased the rate of sequential sample analysis.

Figure 3–9: A Schematic of the basic configuration of an X-ray Photoelectron Spectrometer[a].

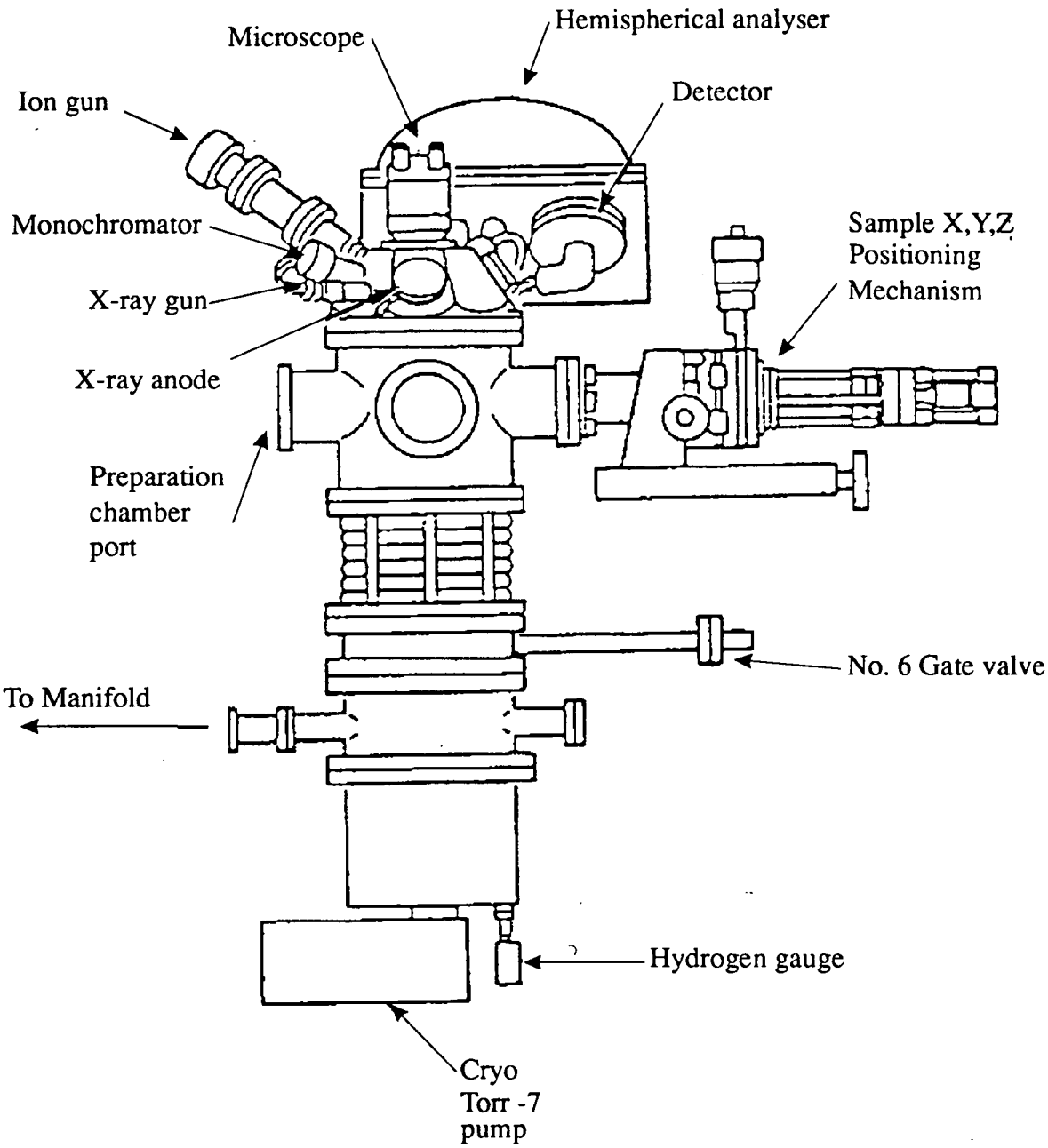

[a] Annotated from a drawing obtained courtesy of I.C.I. Katalco.

Figure 3–10: The X-ray Spectrometer (M-probe)[a].

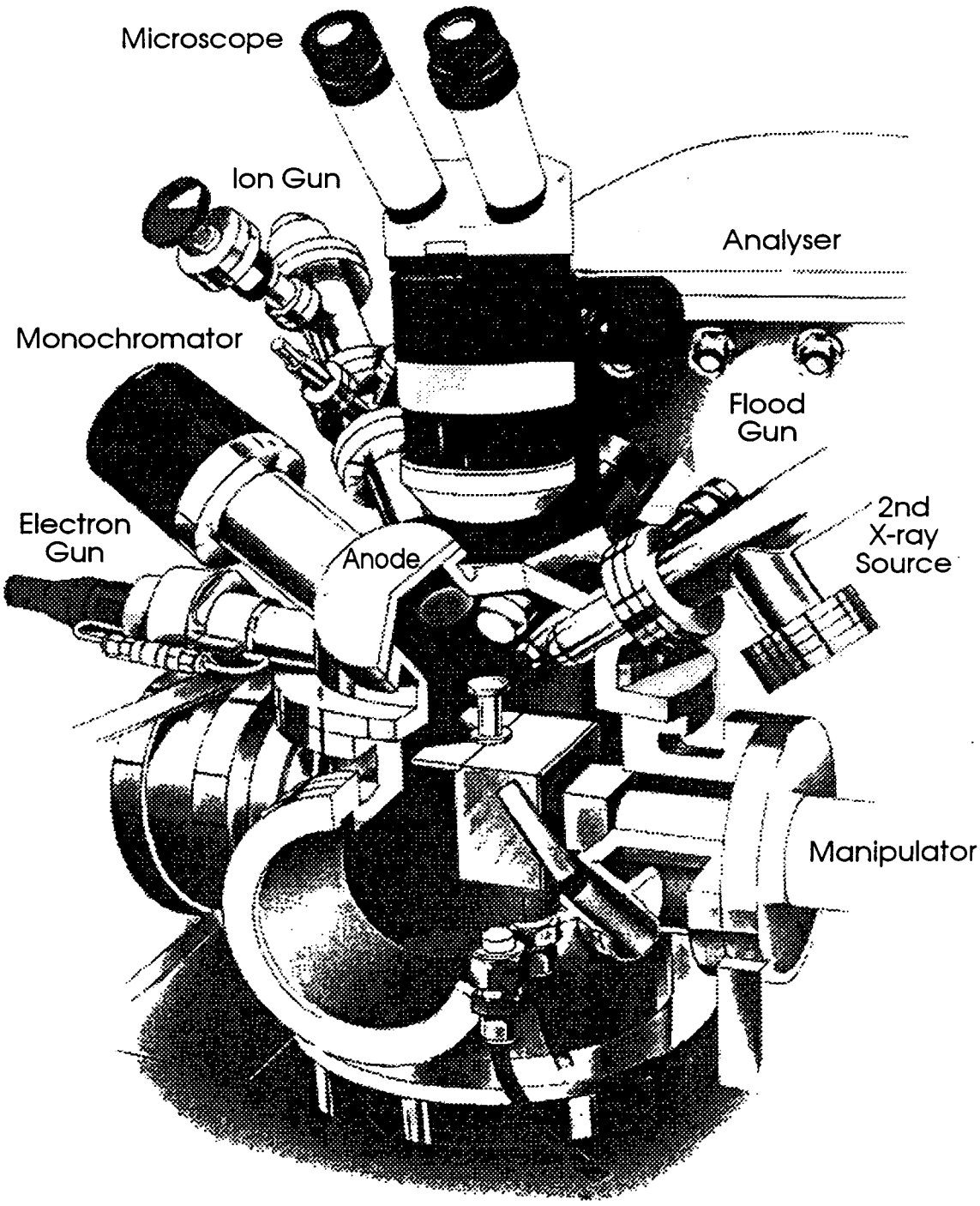

[a]Annotated from a photograph obtained courtesy of I.C.I. Katalco.

Figure 3–11: Sample handling arrangement[a].

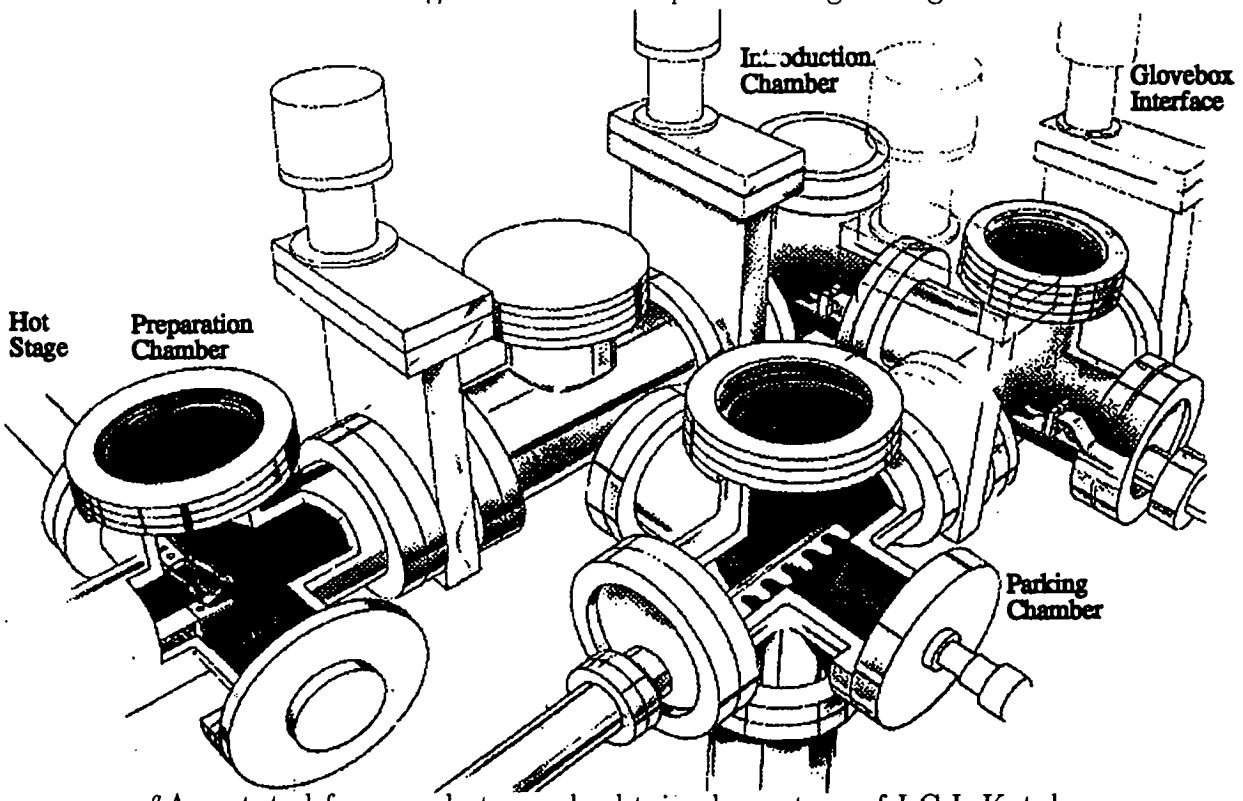

[a]Annotated from a photograph obtained courtesy of I.C.I. Katalco.

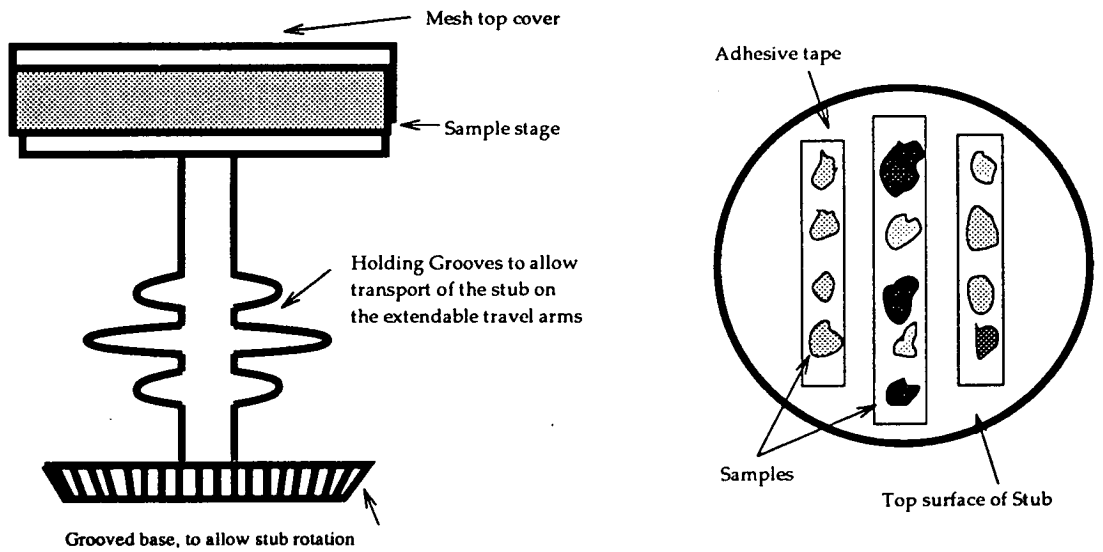

Figure 3–12: Sample mounting on the stub.

3.10.6 Sample Handling

The samples ($\approx$ 10-15mg) were loaded onto the host stub by deposition of the powdered samples in discrete piles onto double-sided adhesive tape, followed by gentle pressing to ensure they were secure. The stub and sample location is shown schematically in Figure 3–12. A mesh cover plate was then fitted above the samples. This was not merely to prevent spillage during the experimental procedure but essentially forms a Faradaic cage around the sample, preventing the build up of a heterogeneous field around the samples. The stub was placed in the UHV system at atmospheric pressure on a traveling arm in the introduction chamber in the sample handling system (Figure 3–11). This chamber was then evacuated and the stub transferred to a rear parking chamber were it was evacuated for 18 hours at room temperature. The stub was then transferred to the spectrometer chamber (pressure $\approx 10^{-9}$ torr). Samples were manually positioned under the beam by moving the stub with the positioning mechanism while viewing the operation through the microscope. The focal point of the microscope was the same as that of the analyser and the optimum position for each sample was selected when the detection count rate was at its highest. The computer control facility was able to record these polar coordinates so that in the automated procedure, for sequential analysis, the stage could be returned to precisely this position and optimum analyses obtained. The entire experimental procedure for sample positioning and data collection was computer controlled and operated by means of the associated M-probe ESCA software. The regions to be scanned *i.e.* the energy envelopes to be more closely scrutinised and all run parameters were initially entered in the Windows driven software and these are shown in Table 3–3.

The samples were irradiated with non-monochromatised Al $K\alpha_{1,2}$ X-ray photons with the anode at 10 kV and were charge neutralised with a flood gun operated at $\approx$ 1 eV with an analysis spot size of 800 μm.

Table 3–3: The standard run parameters used in the XPS investigations.

High Binding energy	Low Binding energy	Number of scans	Resolution (eV)	Species Examined
1160.0	0.0	5	4	Broad Scan
1125.0	1100.0	200	2	Ga $2p_{3/2}$
540.0	520.0	5	2	O $1s_{1/2}$
290.0	275.0	5	2	C 1s
160.0	140.0	20	2	Si $2s_{1/2}$, [a](Ga $3s_{1/2}$)
110.0	85.0	20	2	Si $2p_{1/2}$, [a](Ga $3p_{3/2 + 1/2}$)
35.0	10.0	200	2	Na 2p, O $2s_{1/2}$, Ga 3d

[a]Main "contaminant" interference.

3.10.7 Data Manipulation

Photoelectron spectra may be examined on a number of different levels. Assignments of the peaks observed allows a qualitative elemental analysis to be carried out and this can be made quantitative by examination of the relative peak intensities, given that the sensitivity factors for the elements under investigation are known [202]. The apparatus had been previously calibrated by Dr. S. Bailey (I.C.I. Katalco) using a clean copper calibrant (Cu $2P_{3/2}$ and Cu $3S_{1/2}$). Peak assignment was readily achieved by reference to the literature values known for various gallium species of interest [117, 203-207] after the XPS spectra had been themselves internally standardised by referencing the binding energies (BE) of the signals to that of the C 1S signal at 285 eV. It is by the use of such an internal reference that unambiguous qualitative analysis was achieved. To determine absolute binding energies (BE) more sophisticated investigation was required in which high resolution spectra of specific peak envelopes were obtained and then those envelopes had their BE referenced to the standard C 1S peak position.

Data handling and spectra manipulation was achieved with the on-line *ESCA M-probe* software. The peak fitting and area determination functions were used to

quantify the peak areas and positions of interest in the samples after they had been referenced to the adventitious carbon signal at 285 eV. These peak manipulation procedures all employed a Shirley background function [195, 208, 209] rather than a straight line approach. This has been shown to give more accurate interpretation of experimental data. The Shirley approach determines the background for the base of any peak of interest for each of the points individually. It determines the background by an iterative approach and where the background is proportional to the peak area above that point on the baseline and also to higher energy. This gives a curved background but the end points must always be chosen very carefully (particularly if the data is relatively noisy). The peak areas determined were then manually entered into a separate package (developed internally by I.C.I. Katalco) to determine the atomic composition ratios in the materials. These ratios were produced for only two elements at a time, thus for gallosilicates three ratios were determined *i.e.* Ga:O, Si:O and Ga:Si and by use of the different signals detected for these materials an investigation of the composition at different depths was achieved. This data manipulation programme involves the assumption of a model for the surface under examination and several such models are available within the software *eg.* an alloy or a substance deposited above a substrate. The model then corrected the measured photoelectron intensities (areas) to account for atomic photoionisation cross-sections, analyser and X-ray source geometries and the analyser transmission.

It is common to use peak areas to estimate the surface coverage and material compositions with the majority of workers opting to use tabulated sensitivity factors [210] to correct their raw experimental data. However, this approach is an oversimplification of the situation since there are apparatus dependent quantities (analyser and source geometries *etc.*) which must be considered. In the software package obtained from I.C.I. the chosen model automatically adjusted the raw input data with the appropriate sensitivity factors for the photoionisation cross-sections with,

$$\frac{N_A}{N_B} = \frac{I_A C_B T_B L_B}{I_B C_A T_A L_A} \tag{3.23}$$

N_i = atomic concentration of component i

I = photoelectron peak intensity (area)

C = atomic ionisation cross-section

T = transmission probability (into the analyser)

L = geometric term

The ionisation cross-sections (S_f) are those derived by Schofield [205] and these have been generally accepted and successfully employed [211]. The value of $T \propto 1/E_k$ of the photoelectrons to be analysed [212]. The angular asymmetry factor, L (equation 3.24) was obtained from [213], where β is a factor which depends on the core level [213] under analysis and ϕ is the angle between the analyser and the X-ray source.

$$L = 1 + 0.5\beta(1.5\sin^2\phi - 1) \tag{3.24}$$

Thus an atomic ratio is derived for any two elements, A and B, within the analyte, within the volume defined by the incident radiation and the escape depth of the subsequently analysed photoelectrons. It is essential to choose a good model to represent the sample as XPS intensities reflect the *surface structure.* The model chosen to represent the samples in these studies examines the ejection of an electron corresponding to a signal such that,

$$I = I_o exp - d/\lambda\cos\phi \tag{3.25}$$

I = the signal detected at the surface from a material at a depth d

I_o = the signal from the material at the outermost surface

λ = escape depth or inelastic mean free path

ϕ = angle between the surface normal and the analyser

If all elements had the same cross-section and the X-ray intensity was invariant then I would be equal to C. Here the major assumption is that the X-ray flux variation with depth is negligible and since X-ray penetration is $\gg$ photoelectron escape depths this assumption is justified. The escape depth profile may then be modeled mathematically by an equation which does fit the depth model of Figure 3–7.

$$\lambda = 0.41 \times a^{1.5} \times E^{0.5} \tag{3.26}$$

a = atom size

E = E_k of the photoelectron

However, the approach used by Tanuma *et al.* [198] has suggested that an $E^{0.75}$ relationship is more representative for the less dense oxide type materials. The major problem with such analyses relates to the fact that the approximations made are less accurate as the ratio of E_k to Pass Energy increases. Another source of potential error arises from the relationship between the surface normal and the analyser, however, it has been suggested [214] that assuming the angle between them to be 45° gives a good representation of surface roughness.

In mixed compounds and interdispersed components the major concern is that photoelectrons from different atoms have to escape past regions containing both the analyte species and matrix species. Rather than solve all the simultaneous equations exactly, it is more practical to use numerical integrations to from a model. Here layers from zero depth *i.e.* the topmost surface, to a depth where the intensity observed would be $1/1000^{th}$ of the intensity from the topmost surface, are considered in turn. Then for each of these layers the attenuation of the signal from that atom type is simulated, through a fraction of the surface consisting of the atomic ratio of that type, which was the initial guesstimate the user enters into the programme, and the atomic ratio of the other component is then calculated. This procedure is then repeated for the other atom type. The total signal measured is the sum of these contributions and so escape depths for different atoms may be taken into account. An iterative procedure is adopted until the estimated atomic fractions closely resemble the modeled signal in a sample from the topmost layer to the deeper layer described with that composition.

Chapter 4

Characterisation of Molecular Sieves

4.1 Introduction

In this Chapter the results of a variety of analytical techniques are discussed. This Chapter is composed of three main sections which discuss the nature of the molecular sieves, their elemental composition and the nature of the acidic sites in these materials. Each section sets out the experimental results obtained from each of the various analytical techniques described in Chapter 3 and these results are then discussed.

4.2 Crystal Structure, Size and Morphology

4.2.1 X-ray Powder Diffraction

Only materials which were found to be highly crystalline by XRPD are presented in this work. The powder patterns for the as-made and calcined forms of AMFI2, AEUO2 and AEUO4, are shown in Figures 4–1 and 4–2, with the d-spacing and intensity data (ds and Is) for these patterns summarised in Tables 4–1 to 4–3.

Upon calcination, the samples exhibit the characteristic phenomenon of intensity increase in the low angle peaks with respect to the high angle ones [3, 49]. This observation has not been fully rationalised but a number of factors are thought to contribute [65, 215], the most important of which are the net long range ordering effect within the crystallites after the removal of the organic void fillers and

Figure 4–1: X-ray powder diffraction patterns for a) as-made AMFI2 and b) calcined AMFI2.

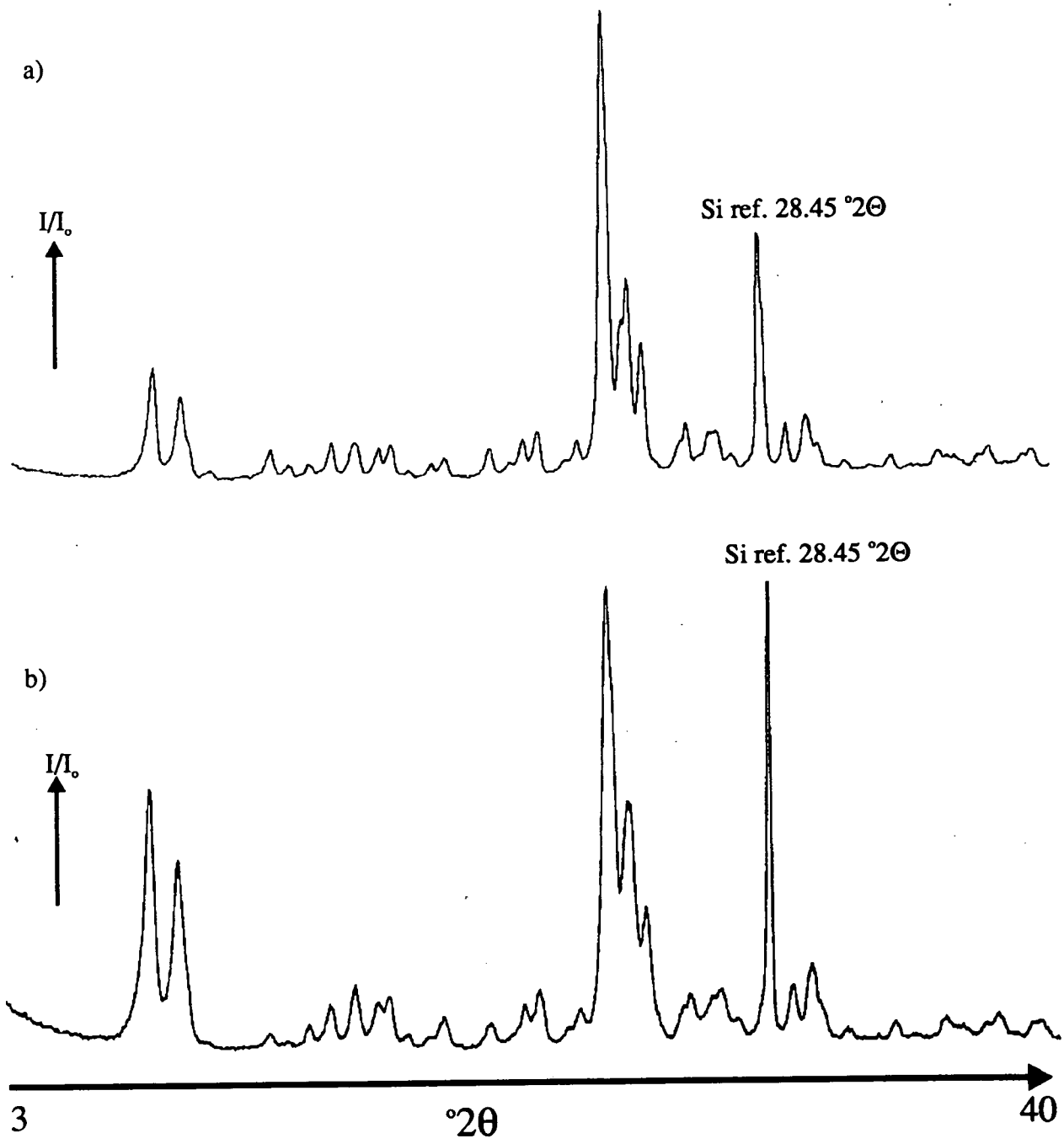

Figure 4–2: X-ray powder diffraction patterns for a) as-made AEUO2, b) calcined AEUO2, c) as-made AEUO4 and d) calcined AEUO4.

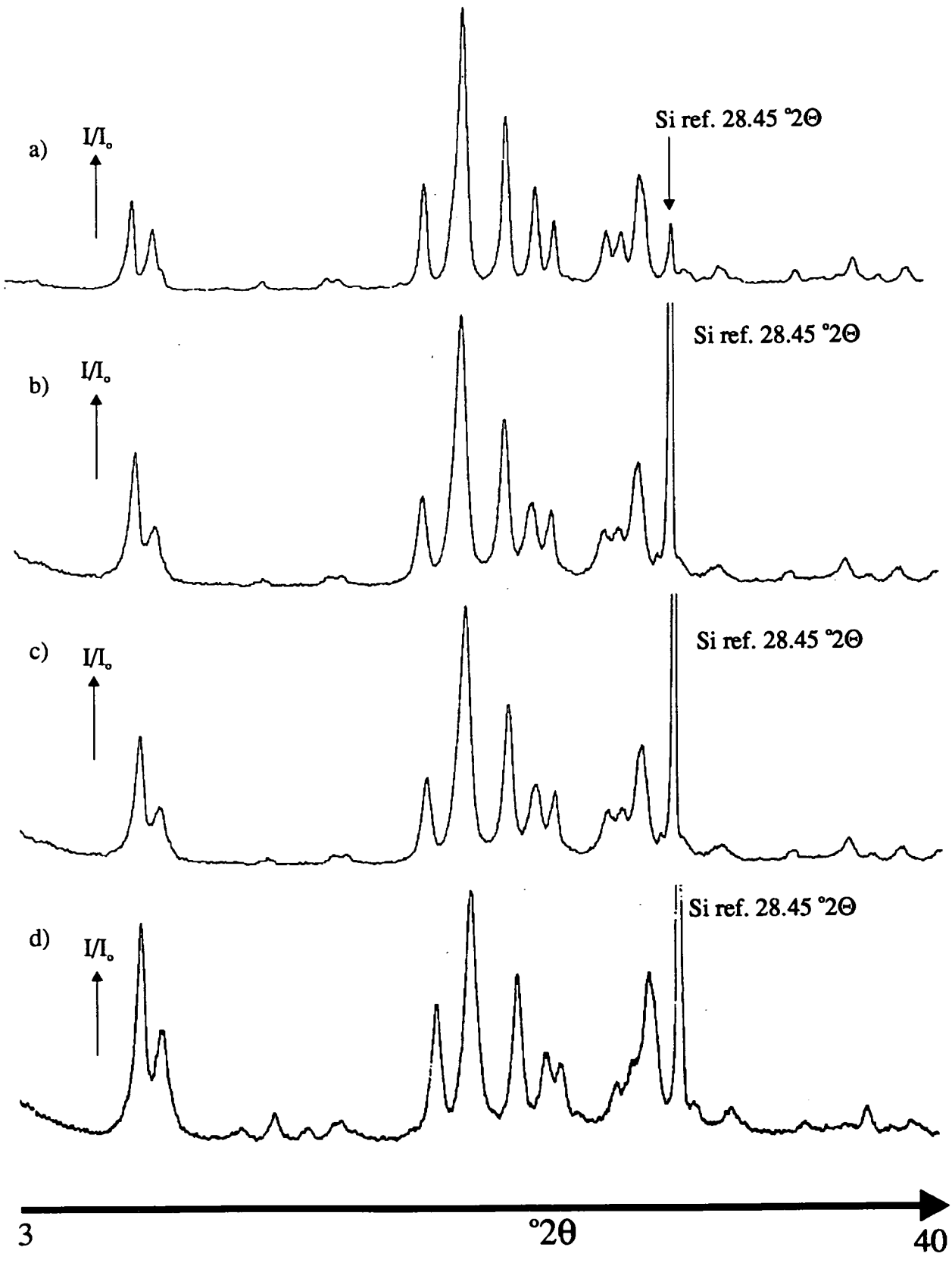

Table 4–1: d-spacing and Intensity data for MFI materials prepared.

MFI[a]		AMFI2		AMFI2C[a]		Est.
d (Å)	I/I_o	d (Å)	I/I_o	d (Å)	I/I_o	Error (d)
11.13	s	11.12	s	11.12	vs	0.07
10.01	m	9.94	m	10.11	s	0.06
9.71	m	9.72	sh	9.75	sh	0.05
7.44	vw	7.44	vw	7.44	vw	0.03
7.06	vw	7.05	vw	7.08	vw	0.03
6.69	vw	6.68	vw	6.76	vw	0.03
6.35	w	6.35	w	6.39	w	0.02
5.97	w	5.99	w	6.03	m	0.02
5.70	w	5.68	w	5.72	w	0.02
5.55	vw	5.54	w	5.61	w	0.02
5.35	vw	5.34	vw	5.40	vw	0.02
5.01	vw	5.00	vw	5.04	w	0.02
4.60	vw	4.60	vw	4.65	w	0.01
4.35	vw	4.35	vw	4.37	w	0.01
4.26	vw	4.25	w	4.29	w	0.01
4.08	vw	4.07	vw	4.11	w	0.01
4.00	vw	4.00	vw	4.04	w	0.01
3.84	vs	3.84	vs	3.87	vs	0.01
3.82	vs	-	-	-	-	0.01
3.75	m	3.75	m	3.75	s	0.01
3.71	s	3.72	s	-	-	0.01
3.64	s	3.65	s	3.66	s	0.01
3.43	w	3.43	w	3.49	w	0.01
3.48	vw	3.47	w	3.46	m	0.01
3.35	vw	3.34	w	3.35	w	0.01
3.30	w	3.30	vw	3.33	w	0.01
3.04	w	3.05	w	3.06	w	0.01
2.98	vw	2.98	w	3.00	m	0.01
2.97	vw	2.96	vw	2.96	w	0.01
2.94	vw	2.87	vw	2.88	vw	0.01
2.72	vw	2.73	vw	2.75	w	0.01
2.61	vw	2.61	vw	2.63	w	0.01
2.49	vw	2.49	vw	2.50	w	0.01
2.41	vw	2.42	vw	2.42	vw	0.01

[a] from Reference [23]

Table 4–2: d-spacing and Intensity data for EUO materials prepared

EU-1[b]		AEUO2		AEUO2C[a]		Est.
d (Å)	I/I_o	d (Å)	I/I_o	d (Å)	I/I_o	error (d)
11.16	vs	11.12	s	11.19	vs	0.07
10.10	s	10.10	s	10.11	s	0.06
9.72	sh	9.77	sh	9.72	sh	0.06
6.84	w	6.84	vw	6.86	m	0.05
5.86	vw	5.75	vw	5.79	w	0.05
4.66	vs	4.65	vs	4.64	vs	0.05
4.31	vs	4.32	vs	4.33	vs	0.04
4.00	vs	4.00	vs	4.00	vs	0.03
3.82	s	3.81	s	3.80	s	0.03
3.71	s	3.71	m	3.73	m	0.03
3.44	m	3.43	m	3.43	m	0.02
3.38	s	3.35	m	3.35	m	0.02
3.26	s	3.27	vs	3.27	vs	0.02
3.16	vw	3.17	vw	3.24	w	0.02
3.11	vw	3.08	vw	3.09	m	0.02
2.96	vw	2.96	vw	2.94	w	0.02
-	-	2.89	vw	2.89	vw	0.002
2.71	vw	2.70	vw	2.70	vw	0.01
2.55	w	2.54	vw	2.53	vw	0.01
2.48	vw	2.47	vw	2.47	vw	0.01
2.42	vw	2.41	vw	2.42	vw	0.01
2.33	vw	2.32	vw	2.33	vw	0.01
2.30	vw	2.29	vw	2.29	vw	0.01

[b] from Reference [49]

vs = very strong (100-55%), s = strong (54-30%), m = medium (29-20%), w = weak (19-10%), vw = very weak (<10%), sh = shoulder

[a] C = calcined

Table 4–3: d-spacing and Intensity data for as-made and calcined AEUO4

AEUO4		AEUO4C[a]		Est.
d (Å)	I/I_o	d (Å)	I/I_o	error (d)
11.19	s	11.12	vs	0.07
10.28	m	10.16	s	0.06
9.77	sh	9.72	sh	0.06
6.92	vw	6.85	vw	0.05
5.79	vw	5.83	w	0.05
5.72	vw	5.72	vw	0.05
5.52	vw	5.54	vw	0.05
4.84	vw	4.87	vw	0.05
4.70	s	4.62	s	0.05
4.35	vs	4.33	vs	0.04
4.03	vs	3.99	vs	0.03
3.85	s	3.81	s	0.03
3.72	s	3.72	s	0.03
3.62	vw	3.63	vw	0.02
3.43	m	3.42	m	0.02
3.36	m	3.35	s	0.02
3.27	vs	3.27	vs	0.02
3.07	vw	3.09	w	0.02
2.95	w	2.94	w	0.02
2.71	vw	2.70	vw	0.01
2.55	vw	-	-	0.01
2.49	vw	2.52	vw	0.01
2.41	vw	2.41	vw	0.01
2.32	vw	2.32	w	0.01
2.30	vw	2.29	vw	0.01

vs = very strong (100-55%), s = strong (54-30%), m = medium (29-20%), w = weak (19-10%), vw = very weak (<10%), sh = shoulder

[a] C = calcined

also the diffraction intensity is a function of the number of atoms per unit cell. Since there are now fewer atoms per unit cell after calcination, different intensity changes are observed from the various Miller indexed planes. The effect is not the same for all planes and so some diffraction peaks are affected more strongly than others. The d-spacings tabulated are typical of the materials prepared and are in good agreement with the literature values, which are also tabulated [151].

The EUO4 syntheses which contained more than 1.5 Ga_2O_3 or Al_2O_3 in the synthesis gel produced NU-85 from what was essentially an EUO preparation, as was expected from gel compositions [64, 216] with such high metal content. In the XRPD patterns of EUO materials the most important signals for unambiguous identification of structure type are those at 8.6° , 23.1° and 26.4° 2θ. If the diffracted intensity at 23.1° 2θ is greater than 60% of that of the next lower angle peak, then the sample has the EUO structure type. If, however, the intensity is less than this value the sample is deemed to be NU-85. Another indicator of the NU-85 structure is the suppression of the XRPD intensities of the other lines mentioned along with a slight displacement to lower angles. Thus the formation of NU-85 was readily determined from the XRPD patterns by the pronounced reduction in intensity of the peak at 23.1° 2θ to below the height of the peak at 24.0° 2θ. This analysis for the identification of the NU-85 structure type was arrived at by the patent authors [64] who noted these XRPD changes when carefully examining a range of EUO-type materials with increasing metal content in the composition. The authors also used electron diffraction to examine the phenomenon and since they also knew that NU-85 was an intergrowth phase of the EUO (EU-1) and NES (NU-87) structure types, they simulated the powder patterns for NU-85 by using various degrees of intergrowth of the EU-1 and NU-87 structure types and found this empirical correlation to hold for the the NU-85 structure [215].

XRPD patterns of the MFI samples closely resembled those expected for the MFI structure type. However, on increasing the metal content a small amount of analcime (ANA) impurity was obtained. This was indicated by the presence of peaks at 15.8° 2θ and 25.9° 2θ, the positions of the most intense analcime peaks. These peaks were used to obtain a semi-quantitative estimate for the amount of

Table 4–4: Structure identification of the D series of syntheses[a] by XRPD.

Sample	Time (days)	Assignment
D1	5	[Al]-EU-1, 30% α-quartz impurity
D2	7	[Ga]-EU-1, 15% α-quartz impurity
D4	5	[Ga]-EU-1
D6	5	[Ga]-NU-85
D7	4.5	[Ga]-EU-1, trace α-quartz impurity
D8	5	[Al]-EU-1
D9	6	[Ga]-NU-85

[a]Syntheses carried out at 453 K except D1 which was carried out at 477 K, all with constant stirring

analcime impurity present. The denser analcime phase is a favoured product from reaction mixtures at high pH levels and high aluminium or heteroatom concentrations, thus analcime can be regarded as an aluminium *sink* [13, 216]. It is therefore proposed that the MFI product obtained from these crystallisations has the maximum level of Al/Ga per unit cell (*i.e.* 8 metals per unit cell) and the extra metal detected by elemental analysis was incorporated into the metal rich analcime phase. This proposition will be further discussed in the analysis of the PPLP refinements of XRPD patterns (Chapter 5, Table 5–7).

The D series of reactions (carried out in the 1l stainless steel autoclave) also produced the expected EUO and NU-85 structures; however, the main impurity observed was α-quartz. This dense phase material suggested product *over-run* in some of these early syntheses. This was to be expected since these crystallisations were carried out in the 1l stainless steel autoclave which had no sampling mechanism and so reactions were stopped after an arbitrary time. By using the signal at 26.8° 2θ an estimate was made of the α-quartz impurity level (shown in Table 4–4). The products obtained from the crystallisations carried out in this study are summarised in Tables 4–4, 4–5 and 4–6

Table 4–5: Structure identification of EUO series of syntheses[a] by XRPD.

Sample	Time (days)	Assignment
AEUO1	3	[Al]-EU-1
AEUO2	3	[Al]-EU-1
AEUO3	3.5	[Al]-EU-1
AEUO4	4	[Al]-NU-85
CEUO1	4	[Ga]-EU-1
CEUO2	4	[Ga]-EU-1
CEUO3	4.5	[Ga]-EU-1
CEUO4	4	[Ga]-NU-85

[a]Syntheses carried out at 433 K, stirred at 300rpm

Table 4–6: Structure identification for the MFI series of syntheses[a] by XRPD.

Sample	Time (days)	Assignment
AMFI1	1	ZSM-5
AMFI2	1	ZSM-5
AMFI3	1.2	ZSM-5, trace analcime impurity
AMFI4	2	ZSM-5, ≈15% analcime impurity
CMFI1	2	[Ga]-ZSM-5
CMFI2	4	[Ga]-ZSM-5
CMFI3	3	[Ga]-ZSM-5, trace analcime impurity
CMFI4	3	[Ga]-ZSM-5, ≈15% analcime impurity

[a]Syntheses carried out at 433 K, stirred at 300rpm

4.2.2 Scanning Electron Microscopy (SEM)

The crystallites produced in this work were predominantly of a very poor morphology and of submicron dimensions. Hence, the average crystallite dimensions could not be readily determined by SEM. The poor morphology and the extremely small size of the crystallites prepared meant that SEM analysis was not very useful in providing images of the samples. Transmission electron microscopy (TEM) would have been more appropriate for the study of such small crystallites; however, this technique was unavailable to this work.

The EUO series produced cleaner agglomerates of laths in the typical ellipsoidal habit [49]. Figure 4–3 a) shows the typical SEM photomicrographs for these materials.

CMFI4 has a significant analcime impurity, as determined by XRPD, which was observable by SEM. Figure 4–3 b) shows the truncated polyhedra of the dense phase analcime impurity, clearly distinguished from the MFI crystallites. Since the analcime impurity phase has formed as discrete crystals this suggests that the contaminated samples are MFI crystallites with the maximum 8 metal atoms per unit cell and the analcime acting as a sink for the extra metal species.

4.2.3 Crystallite Size Determination From XRPD

If the average crystallite size in a powder is $\leq$2000Å broadening of diffracted X-ray beams occurs [152]. XRPD pattern peaks have a finite width since radiation is not absolutely monochromatic, *i.e.* K_α has an intrinsic width and the focusing geometry of any instrument is never perfect.

The Bragg angle corresponds to the situation where each plane diffracts exactly 1λ later than the previous one, *i.e.* all diffracted beams are in phase and constructively interfere as represented by Figure 4–4.

However, for an incident beam θ_1 there is a phase lag of slightly $> \lambda$ for X-rays diffracted from subsequent planes. Now, if the assumption is made that the cumulative phase lag is, $\sum \delta\lambda = \frac{\lambda}{2}$, as the X-ray reaches plane (j+1), then since

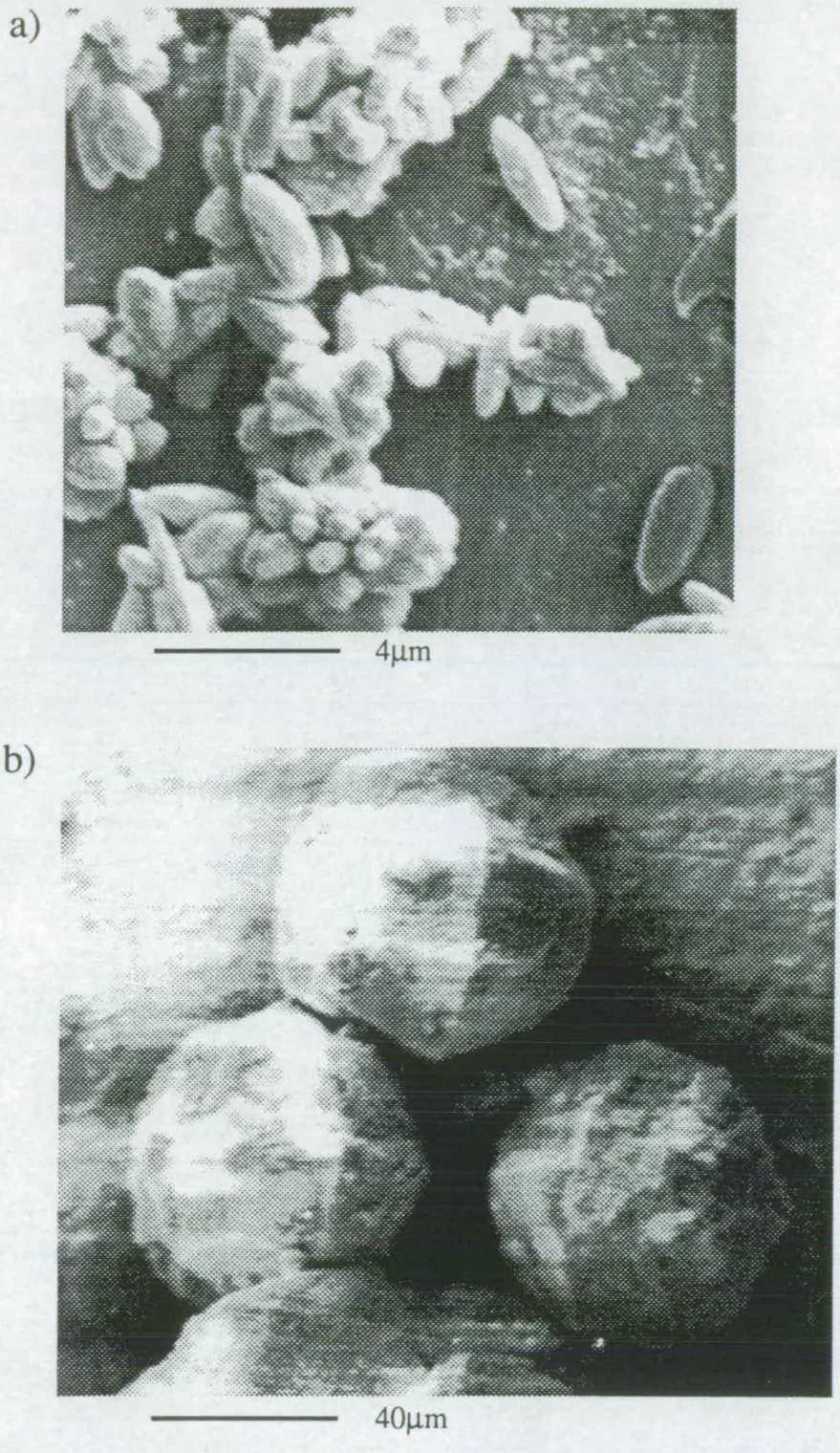

Figure 4–3: SEM photomicrographs of; a) elliptical agglomerates of EUO laths and b) the truncated polyhedra of the gallosilicate analcime impurity observed in CMFI4.

Figure 4–4: Diffraction model used to illustrate the Scherrer observation of peak broadening with reduction in crystallite size.

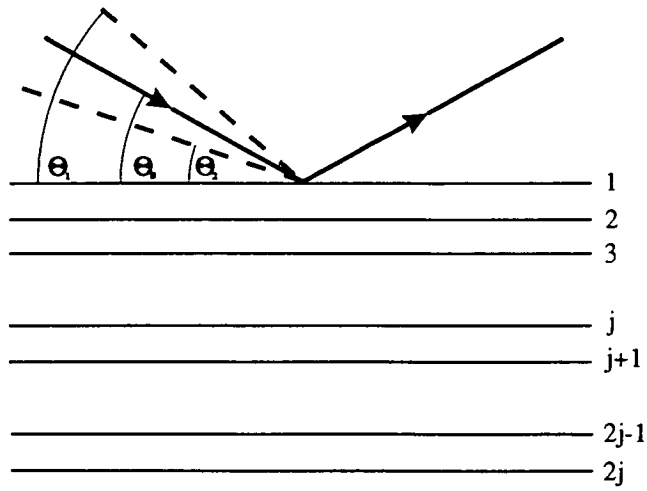

planes 1 and (j+1) are exactly λ out of phase these destructively interfere and cancel each other out. If there are 2j planes, then the diffraction intensity at $\theta_1 = 0$ as the rays diffracted from (j+1) to 2j cancel those from 1 to j. The angular range from θ_{Bragg} to θ_1 is the range for which intensity falls from the maximum value to 0. A similar lower angle exists, (θ_2), for X-rays diffracted from adjacent planes with a phase difference of ($\lambda - \delta\lambda$). The magnitude of the angular range (θ_1 - θ_2) *i.e.* breadth of the diffraction peak is governed by the number of planes (2j) *i.e.* the crystal thickness. If the number of planes is very large then no significant broadening is observed as $\delta\lambda$ *i.e.* (θ_1 - θ_2) is negligibly small. However, if there are only a smaller number of planes in the crystallites then broadening is observed as represented by the Scherrer equation 4.1,

$$t = \frac{K \prec \lambda}{B \times cos\ \theta_{Bragg}} \tag{4.1}$$

where t the thickness (Å) is determined from θ_{Bragg}, the Bragg angle obtained from XRPD (in radians), λ the wavelength of radiation, K is a constant determined to be 0.94 for spherical particles and B is the extra broadening in the peak relative to an intrinsic linewidth, as determined by an internal standard [161]. B is obtained from the Warren formula *i.e.* $B = \sqrt{B_M^2 - B_S^2}$ where B_M is the measured peak width at half maximum height and B_S the corresponding quantity for the standard

peak. Such a formula is required to determine the *extra* line broadening associated with the crystallite size. Each line has an intrinsic width and so measurement of linewidths includes this natural width. Consequently, this natural linewidth must be removed from the measured width. The Warren formula is a simple weighting procedure which allows the extra linewidth to be determined, relative to an internal standard, and so compensates for the natural linewidth of the apparatus.

Estimates of the average crystallite dimensions for the MFI series of materials were determined from the line broadening observed at two different diffraction signals in the XRPD traces *i.e.* the diffraction maxima at around 7.9° 2θ and 23.2° 2θ and these estimates are shown in Table 4–7. The EUO preparations in general, gave larger, cleaner agglomerates of laths (as observed by SEM) and the lath sizes are summarised in Table 4–8 where again two separate estimates are made for the average crystallite dimensions by examination of two separate diffraction maxima in the XRPD pattern at 7.9° and 20.9° 2θ. The two separate peaks examined to determine the average crystallite dimensions were from different parts of the XRPD pattern and each peak has its own inherent limitations. Signals at higher angles of 2θ are more likely to be compound signals composed of more than just one peak and so some of the broadening observed could be caused by the presence of multiple peaks overlapping rather than the intrinsic broadening associated with crystallite size. However, these peaks at higher angles of 2θ are measured more accurately and so a compromise must be struck between these features. It is apparent from Tables 4–7 and 4–8 that the broadening observed for the peaks at over 20° 2θ is greater than that observed for the lower angle signal, suggesting that there are overlapping peaks at these higher angles, increasing the broadening observed. It should also be noted that chemical heterogeneity and defects within the crystalline materials can also result in this line broadening and so would cause an underestimate in crystallite size.

These average crystallite dimensions determined by peak broadening are in excellent agreement with observations made by SEM studies which showed that the MFI materials prepared in this work all contained extremely small crystallites. This was true of both aluminosilicates and gallosilicate materials and the metal

Table 4–7: Average crystallite dimensions determined by the Scherrer equation for the MFI syntheses.

Sample	$B_{7.9}$ (° 2θ)	$t_{7.9}$ (thickness Å)	$B_{23.2}$ (° 2θ)	$t_{23.2}$ (thickness Å)
AMFI1	0.25±0.03	333±176	0.40±0.02	212±26
AMFI2	0.37±0.03	225±49	0.46±0.02	184±25
AMFI3	0.44±0.03	189±47	0.46±0.02	184±25
AMFI4	0.33±0.03	252±76	0.45±0.02	188±25
CMFI1	0.32±0.03	260±88	0.38±0.02	223±28
CMFI2	0.31±0.03	269±101	0.46±0.02	197±23
CMFI3	0.35±0.03	238±60	0.46±0.02	184±21
CMFI4	0.34±0.03	245±58	0.46±0.02	184±21

Table 4–8: Average crystallite dimensions determined by the Scherrer equation for the EUO syntheses.

Sample	$B_{7.9}$ (° 2θ)	$t_{7.9}$ (thickness Å)	$B_{20.9}$ (° 2θ)	$t_{20.9}$ (thickness Å)
AEUO1	0.12±0.03	693±352	0.27±0.02	313±152
AEUO2	0.17±0.03	490±286	0.41±0.02	206±54
AEUO3	0.33±0.03	490±286	0.47±0.02	180±45
AEUO4	0.40±0.03	252±76	0.56±0.02	151±21
CEUO1	0.30±0.03	416±216	0.23±0.02	367±187
CEUO2	0.35±0.03	462±252	0.26±0.02	211±27
CEUO3	0.32±0.03	416±216	0.37±0.02	228±28
CEUO4	0.42±0.03	245±68	0.36±0.02	235±29

Table 4–9: Micromeritic Analyses of The MFI materials prepared.

Sample Name	BET area m^2g^{-1}	External area m^2g^{-1}	Micropore vol. $cm^3/100g$
AMFI1	374	88	12.1
AMFI2	378	103	12.2
AMFI3	357	122	11.4
AMFI4	293	96	9.8
CMFI1	360	115	11.4
CMFI2	333	98	11.1
CMFI3	333	104	11.1
CMFI4	305	87	10.3

content of the samples appears not to have had a significant effect on the average crystallite size produced in any individual MFI synthesis. This conclusion is in good agreement with the general observation made during the MFI product recovery, that filtration was difficult and membrane filters were required. In general the estimates of EUO lath sizes are larger than the MFI crystallite sizes, however, these estimates have relatively large errors associated with them and it is therefore reasonable to suggest that all the materials prepared in the A and C series of EUO and MFI syntheses are of similar crystallite dimensions.

4.2.4 Micromeritics

Some typical isotherms produced by these samples are included in Figure 4–5 and these show the typical hysteresis loop for such molecular sieve materials.

The results of analyses carried out on the MFI series of materials is included in Table 4–9. Although BET surface area analyses are included for completeness these values are not considered as very useful, but rather the pore volume data is considered in relation to these materials.

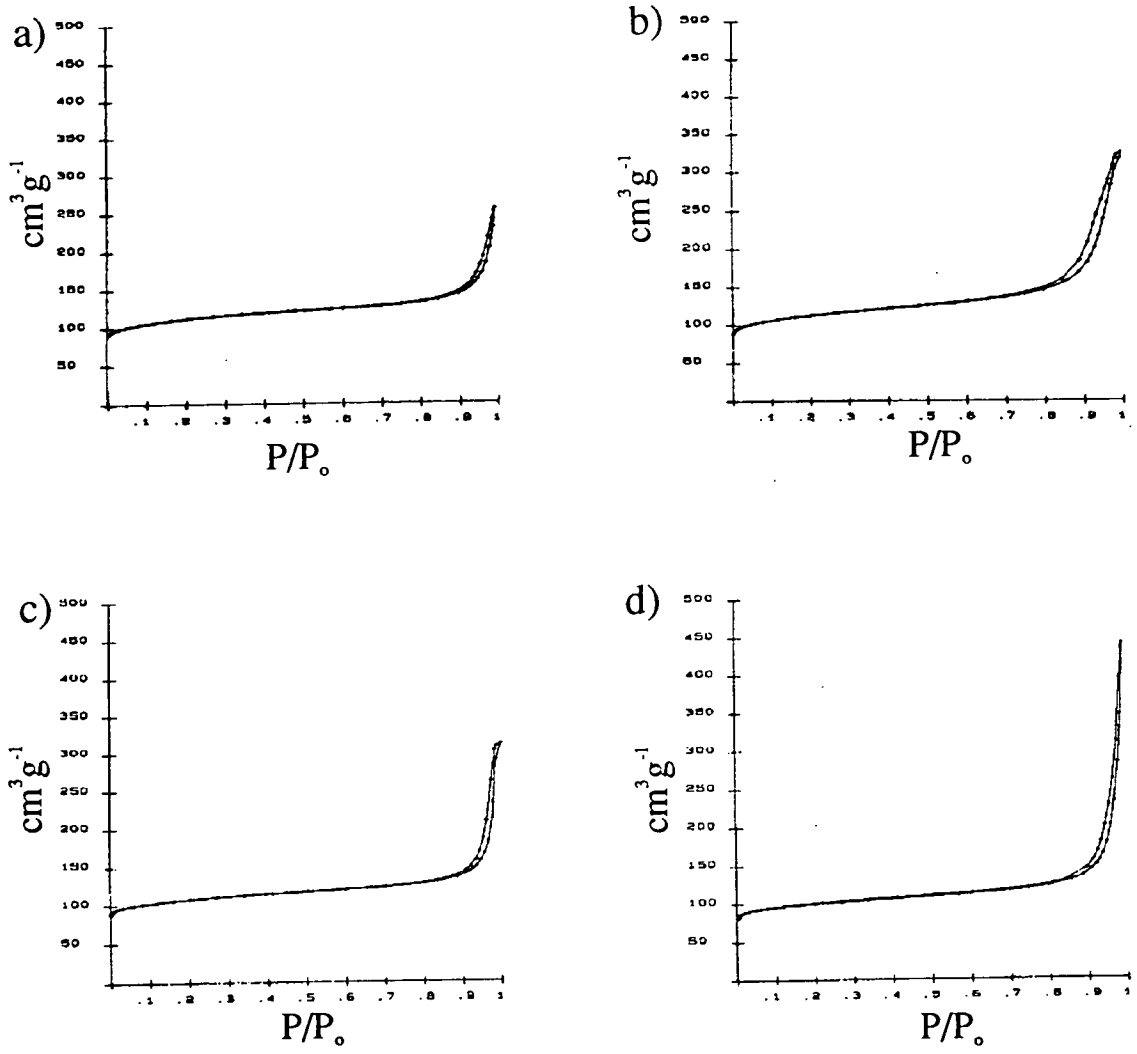

Figure 4–5: Nitrogen uptake for some of the MFI materials prepared[a], a) AMFI1, b)AMFI2, c) CMFI1 and d) CMFI2.

[a]Isotherms obtained courtesy of I.C.I.

It is clear that there is a reduction in micropore volume for AMFI3 and AMFI4 compared to the samples AMFI1 and AMFI2. This is as would be expected for materials which are known to be contaminated with the dense phase analcime. The CMFI series of materials all show lower than expected micropore volumes which suggests that there is a degree of pore blockage in these materials. This could be due to the occlusion of gallium species which had either been ejected from the framework during the calcination or had been occluded during the synthesis procedure. Thus it can be suggested that gallium is less readily incorporated into the MFI framework than aluminium. Although the bulk gallium content increases through the series CMFI1 to CMFI4, it is likely that not all of the gallium is incorporated into the framework, with much of it supported on the external surface of the crystallites or occluded in the channels of the molecular sieve. This would account for the reduction in micropore volume observed for the gallosilicate materials.

Nitrogen micromeritics analysis of some of the materials which were later examined in the flow microreactor at I.C.I., Wilton are included in Table 4–10. The range of ZP materials, prepared by I.C.I. C.& P. Ltd., all have micropore volumes in the range expected for EU-1 materials [49] however, ZP6-5% IW shows a significant deviation from this which may suggest a degree of pore blockage when larger dopant concentrations are loaded onto the material. The significant difference in crystallite size between the ZP2 and ZP6 materials was clearly observed in the nitrogen isotherms where a greater hysteresis was observed for the smaller ZP2 crystallites, as shown in Figure 4–6. This is as expected for smaller crystallites which would have a greater degree of capillary condensation in the mesoporous structure formed between the crystallites.

For the D range of materials the micropore volumes were again indicative of the EUO channel structure; however, there were significant deviations for D2 and D7 as was expected for materials with α-quartz contamination. D2 was more heavily contaminated and showed a larger deviation, as expected.

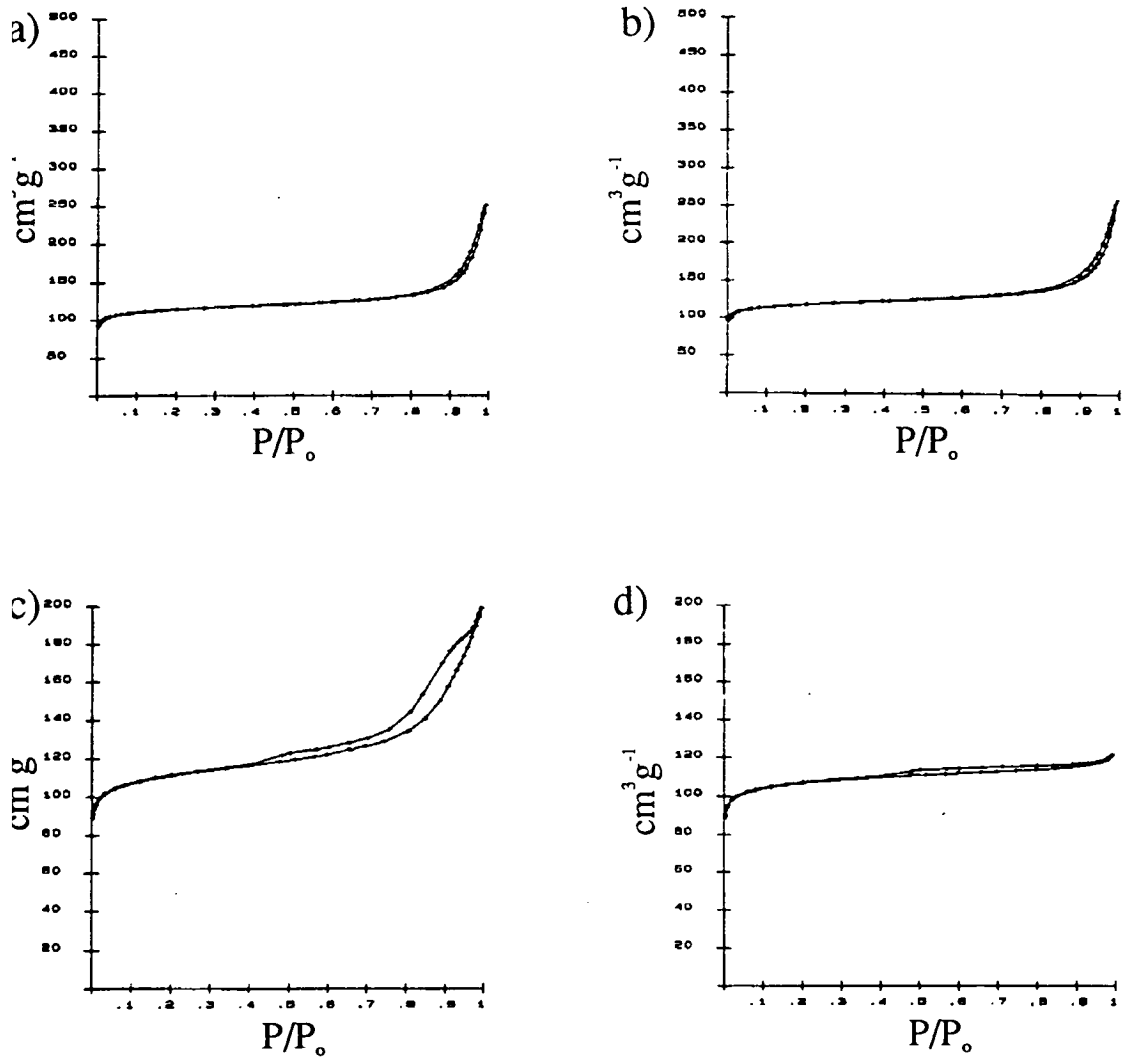

Figure 4–6: Nitrogen uptake for some of the D series of materials prepared and the EU-1 materials obtained from I.C.I., a) D6, b) D9, c) ZP2-3%IW and d) ZP6-3%IW.

Table 4–10: Micromeritic Analyses of some of the D series of materials and some of the doped EU-1 materials which were later examined in Propane conversion studies at I.C.I., Wilton.

Sample Name	BET area m^2g^{-1}	External area m^2g^{-1}	Micropore vol. $cm^3/100g$	Pore Diameters Å[a]
ZP6-5%-IW	347.9	6.2	11.3	35
ZP6-3%-IW	356.6	4.3	12.5	35
ZP6-1%-IE	347.5	5.6	12.1	35
ZP2-5%-IW	370.8	52.5	12.2	30, 150
ZP2-3%-IW	373.2	50.2	12.3	30, 150
ZP2-1%-IE	385.4	52.6	12.4	30, 150
D2	319.3	25.4	10.6	30, 500
D4	396.9	48.8	13.0	35, 250
D6	382.2	50.0	12.7	35, 400
D7	332.2	19.0	11.5	35, 400
D8	382.3	6.1	13.7	35, 500
D9	396.8	51.1	13.2	35, 500

[a]Average diameters of the mesopores and macropores (void space) created by the agglomeration of the crystallites.

4.3 Unit Cell Composition

The composition of all the materials prepared in this study have been determined by the use of a variety of elemental analysis techniques together with thermal gravimetric analyses to determine the template content of the unit cell. Further analysis of XRPD patterns have also been used to examine the metal content of the MFI materials prepared.

4.3.1 Elemental Analysis

As has been discussed in Chapter 3, a variety of elemental analysis procedures were examined before X-ray Fluorescence was adopted as the most appropriate method of elemental analysis for this study. It is interesting to note that XRF has also been recommended by other workers in the field [147]. The results of initial studies with Neutron Activation Analysis and Atomic Absorption Spectroscopy are included to allow comparison with the results generated by XRF.

The elemental analyses for silicon, aluminium, sodium and gallium obtained by ICPAAS/AES and XRF are included along with the gallium analysis given by NAA for some of the D series of gallosilicate materials in Table 4–11.

This shows that the techniques are in broad agreement, however, as stated previously, ICPAAS is notorious for giving low silicon values, so it was not surprising to find larger Si contents by XRF analysis. The NAA analysis was only attempted for Ga and so routine elemental analysis could not be obtained from this technique which had proven to be expensive and unwieldy.

X-ray Fluorescence Analysis (XRF)

A summary of the elemental analyses of the calcined A and C materials are included in Tables 4–12 and 4–13. From this data the unit cell composition for these materials was determined and are shown in Tables 4–14 and 4–15. It should

Table 4–11: Comparison of ICPAAS/AES, NAA and XRF analyses for the D series of materials.

Sample	ICPAAS/AES[a]				NAA[b]	XRF[c]			
Name	%Si	%Al	%Na	%Ga	%Ga	%Si	%Al	%Na	%Ga
D2	38.6	0.05	0.17	3.55	3.8	43.35	0.08	0.24	3.91
D4	37.4	0.05	0.12	4.38	4.8	42.33	0.09	0.23	4.92
D6	36.2	0.05	0.05	6.50	7.1	40.33	0.07	0.11	7.34
D7	39.4	0.05	0.34	1.94	2.1	44.38	0.07	0.31	2.25
D8	40.0	1.41	0.30	0.0	-	41.19	1.69	0.31	0.0
D9	36.4	0.05	0.22	7.75	8.1	41.19	1.69	0.31	8.70

[a] σ(Standard Deviation) = 0.05, [b] σ = 0.05, [c] σ = 0.114

be noted that the bulk elemental analyses shown in these tables does not add to 100%wt. This is due to the small amount of sample lost during the preparation procedure (heated to 1373 K). This loss contains contributions from not only framework atoms but species which were occluded in the microporous channels and retained after the calcination and drying procedures *eg.* water and residual carbonaceous species.

Table 4–14 shows that for materials with the highest metal content in the reaction gels, in both the aluminosilicate and gallosilicate syntheses, there are more than 8 metal atoms per unit cell which is the theoretical limit for the MFI structure. This maximum level of framework incorporation was determined from an examination of the number of charge balancing cations which can be occluded per unit cell of the MFI structure. This limit is examined further in the discussion of the thermal analyses. However, the sieves with the highest metal content were contaminated with the metal rich analcime phase and so bulk elemental analysis could be misleading with a significant proportion of the metal detected not being associated with the MFI structure but with the analcime impurity. If the MFI materials which show analcime impurity are formed with a maximum of 8 metal atoms per unit cell and the remaining metal was incorporated into the anal-

Table 4–12: Bulk elemental analysis by XRF[a] for MFI materials.

Sample	SiO_2 wt%	Al_2O_3 wt%	Ga_2O_3 wt%	Na_2O wt%
AMFI1	91.52	3.49	0.00	0.94
AMFI2	87.51	4.89	0.00	1.16
AMFI3	86.31	6.14	0.00	2.20
AMFI4	81.26	8.32	0.00	3.93
CMFI1	90.98	0.16	6.10	0.50
CMFI2	86.03	0.19	7.63	1.73
CMFI3	84.91	0.13	9.56	1.76
CMFI4	80.66	0.19	13.24	2.96

[a] $\sigma = 0.114$, this standard deviation is primarily associated with weighing errors in sample preparation rather than instrumental limitations.

Table 4–13: Bulk elemental analysis by XRF[a] for EUO materials.

Sample	SiO_2 wt%	Al_2O_3 wt%	Ga_2O_3 wt%	Na_2O wt%
AEUO1	93.54	1.88	0.05	0.53
AEUO2	92.22	3.67	0.00	0.49
AEUO3	90.18	5.28	0.00	0.47
AEUO4	88.04	6.14	0.01	0.39
CEUO1	93.18	0.15	3.37	0.49
CEUO2	89.92	0.25	6.32	0.58
CEUO3	88.16	0.15	8.53	0.43
CEUO4	86.34	0.23	11.17	0.28

[a] $\sigma = 0.114$, this standard deviation is primarily associated with weighing errors in sample preparation rather than instrumental limitations.

cime impurity then there should be ≈16% by weight analcime impurity in the sample, which is in excellent agreement with the ≈15% determined by XRPD. This calculated level of analcime impurity was based on unit cell compositions of $[Ga_{16}Si_{32}O_{96}]$ for analcime and $[Ga_8Si_{88}O_{192}]$ for the gallosilicate MFI4. This suggests that the proposition of analcime formation as a result of metal over-spill is correct. Consequently these elemental analyses have been corrected for this analcime impurity. This assumption of the formation a gallosilicate analcime is confirmed by unit cell volume calculations carried out on the XRPD analyses of the CMFI3 and CMFI4 samples, which contained the contaminant (Chapter 5, Table 5–7).

It should also be noted that each of the gallosilicate materials contains a very small amount of aluminium impurity. This metal content has been neglected when unit cell compositions have been determined since it is a very small and constant level of impurity (associated with the Ga_2O_3 used in the synthesis) when compared to the very large amounts of gallium incorporated into these materials.

Associated with the increase in metal contents observed is a dramatic increase in the sodium content of the MFI materials. This is in response to the need for an increase in cations to balance the framework charge as the metal content increases above the level able to be neutralised by the occluded TPA^+ species in the intracrystalline void space. This observation is discussed further in Section 4.3.3. The charge balancing required for the negative framework is obtained from either organic or inorganic cations, however, the organic species are very large compared to the inorganic cations and so fewer may be occluded ($\leq$4) per unit cell. Hence, as the requirement for charge neutralisation increases the number of smaller sodium ions increases at the expense of the larger TMA^+ species.

Table 4–15 shows that unlike the MFI system the sodium content of the EUO materials does not increase with increasing metal content. This too is a consequence of the charge balancing cations. In the EUO materials a doubly charged organic species (Hexamethonium, Hex^{2+}) was used as the void filler material with 4 such species able to be accommodated per unit cell of EUO. Hence, there are 8 organic cationic functions able to balance the 8 framework metal species and

Table 4–14: Unit Cell Compositions of the MFI Materials.

Sample	Na[a]	Al or Ga[a]	Si[a]	O
AMFI1	0.9	4.3	91.7	192
AMFI2	2.2	6.3	89.7	192
AMFI3	4.5	7.0	89.0	192
AMFI4	7.5	8.0[b]	88.0	192
CMFI1	0.5	4.1	91.9	192
CMFI2	3.8	5.5	90.5	192
CMFI3	3.9	7.0	89.0	192
CMFI4	6.7	8.0[b]	88.0	192

[a] standard deviation $\sigma = 0.2$ [b] assuming the maximum metal content of 8 per unit cell with residual metal incorporated into the analcime phase.

Table 4–15: Unit Cell Compositions of the EUO Materials.

Sample	Na[a]	Al or Ga[a]	Si[a]	O
AEUO1	0.5	2.7	109.3	224
AEUO2	0.5	5.3	106.7	224
AEUO3	0.5	7.7	104.3	224
AEUO4	0.4	9.2[b]	102.8	224
CEUO1	0.5	2.6	109.4	224
CEUO2	0.5	5.0	107.0	224
CEUO3	0.5	7.0	105.0	224
CEUO4	0.4	9.4[b]	102.6	224

[a] standard deviation $\sigma = 0.2$ [b] NU-85 material

so there is no need for sodium ions to counter the framework charge. This is an important feature to note; the stabilisation observed for framework metal species associated with organic cations rather than inorganic cations will be discussed further in the thermal gravimetric analyses (Section 4.3.2).

4.3.2 Thermal Analysis

As mentioned previously, two separate instruments were used for thermal analysis investigations. Firstly, results obtained from the Stanton Redcroft TG-770 thermal gravimetric analyser are presented, followed by those from the simultaneous thermal analyser (Stanton-Redcroft ST-780). The TG-770 apparatus was used initially because of the unavailability of the simultaneous thermal analysis (STA) instrument at that time. The initial TG-770 analyses were required to confirm the integrity of the materials prepared, before subsequent analyses and catalytic studies commenced.

The total weight losses observed on heating the samples from 298K to 1173K are tabulated. Table 4–16 contains the results from TGA of the D series of molecular sieves and Tables 4–17 and 4–18 summarise the results of the investigations of the A and C series of the MFI and EUO of molecular sieves respectively.

Weight losses from samples D1 and D2 were significantly lower than expected for pure EUO samples. However, each of these have significant α-quartz impurities with no associated organic void filler, so a reduced weight loss was expected. D1 had a larger amount of quartz impurity and consequently showed the largest deviation from the expected value of $\approx$ 14 %. Similarly D7 has a slight α-quartz impurity and so it too showed a slightly reduced weight loss on heating. This level of 14% weight loss is a very approximate estimate of the expected weight loss associated with 4 hexamethonium cations per unit cell (4 Hex^{2+}= 808 amu, typical unit cell of EUO with a composition of $Al_8Si_{104}O_{224}$= $\approx$5850 amu, thus a loss of 4 Hex^{2+} corresponds to a weight loss of $\approx$ 12.2 %) and a small contribution from the water of hydration associated with the molecular sieve (assumed to be

Table 4–16: Thermal Gravimetric Analysis data[a] for the D series of preparations.

Sample	Total Weight Loss (%) ±0.05%
D1	8.4
D2	10.4
D4	13.5
D6	13.0
D7	12.5
D8	13.6
D9	13.8

[a]Analysis by the Stanton-Redcroft TG 770 analyser, heated to 973 K.

Table 4–17: Thermal Gravimetric Analysis data[a] for the A and C series of MFI syntheses.

Sample	Total Weight Loss (%) ±0.05%
AMFI1	14.0
AMFI2	14.1
AMFI3	14.1
AMFI4	14.0
CMFI1	14.6
CMFI2	15.1
CMFI3	13.0
CMFI4	12.3

[a]Analysis by the Stanton-Redcroft TG 770 analyser, heated to 973 K.

Table 4–18: Thermal Gravimetric Analysis data[a] for the A and C series of EUO syntheses.

Sample	Total Weight Loss (%) ±0.05%
AEUO1	14.3
AEUO2	15.2
AEUO3	15.2
AEUO4	14.1
CEUO1	14.0
CEUO2	14.8
CEUO3	13.4
CEUO4	13.9

[a]Analysis by the Stanton-Redcroft TG 770 analyser, heated to 973 K.

≈1-2%) and so a total loss of around 14% by weight would be expected from an EUO material.

In the A and C series of EUO and MFI samples, weight losses from EUO materials remained relatively constant throughout the series, however, the MFI series showed a marked reduction in weight loss as the level of metal increased in the reaction gel. These observations were expected and are discussed below.

Simultaneous Thermal Analysis

The thermal analysis of both the aluminosilicate and gallosilicate EUO materials are shown in Figures 4–7 and 4–8 and those for the MFI materials in Figures 4–9 and 4–10. The simultaneous thermal analysis traces of the as-made A and C series of materials are similar to those reported by other workers [49, 77]. Table 4–19 summarises the quantitative breakdown of the weight loss processes.

At temperatures between 298 K to ≈522 K all materials showed endotherms in the DTA profiles and small weight losses of ≈2% associated with the removal

Figure 4–7: Simultaneous thermal analysis traces for, a) AEUO1, b) AEUO2, c) AEUO3 and d) AEUO4.

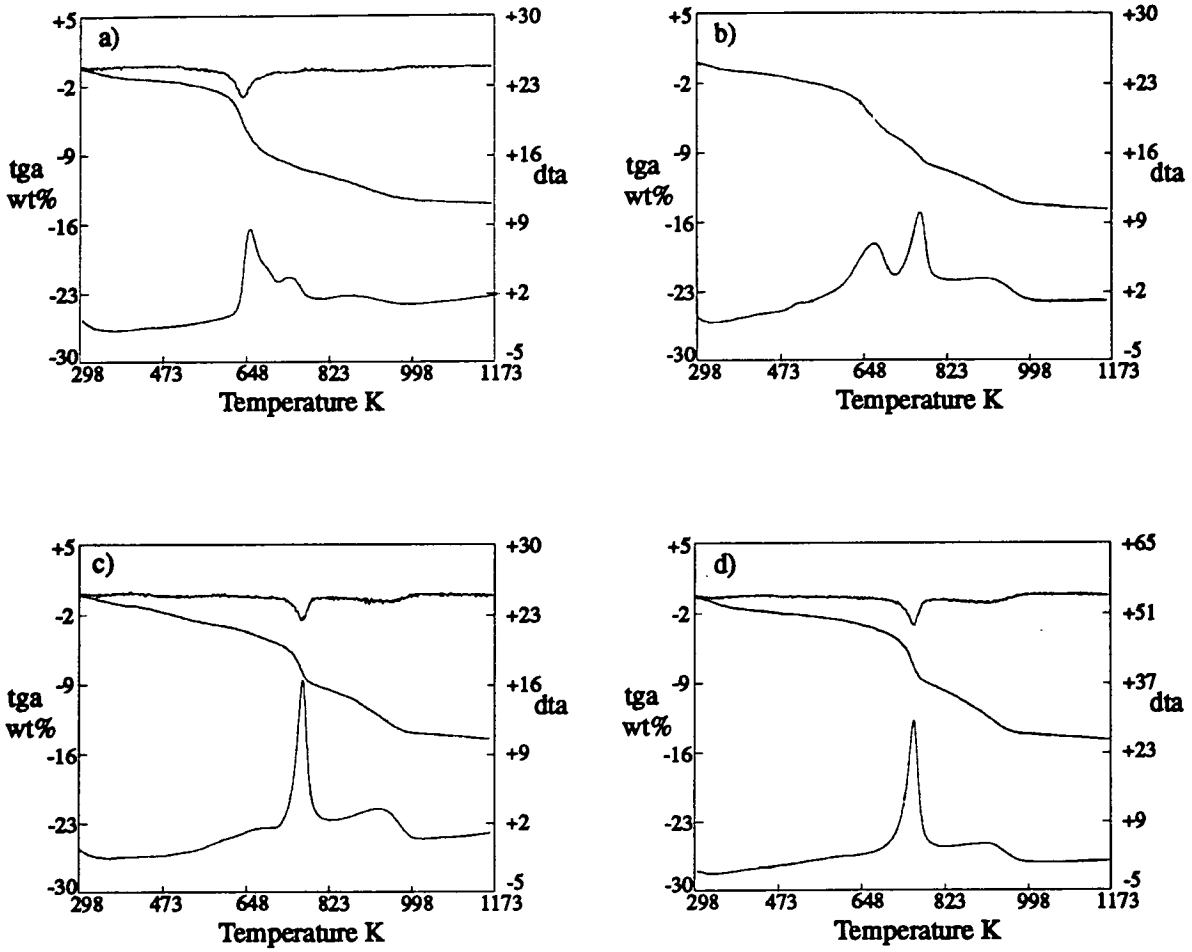

Figure 4–8: Simultaneous thermal analysis traces for, a) CEUO1, b) CEUO2, c) CEUO3 and d) CEUO4.

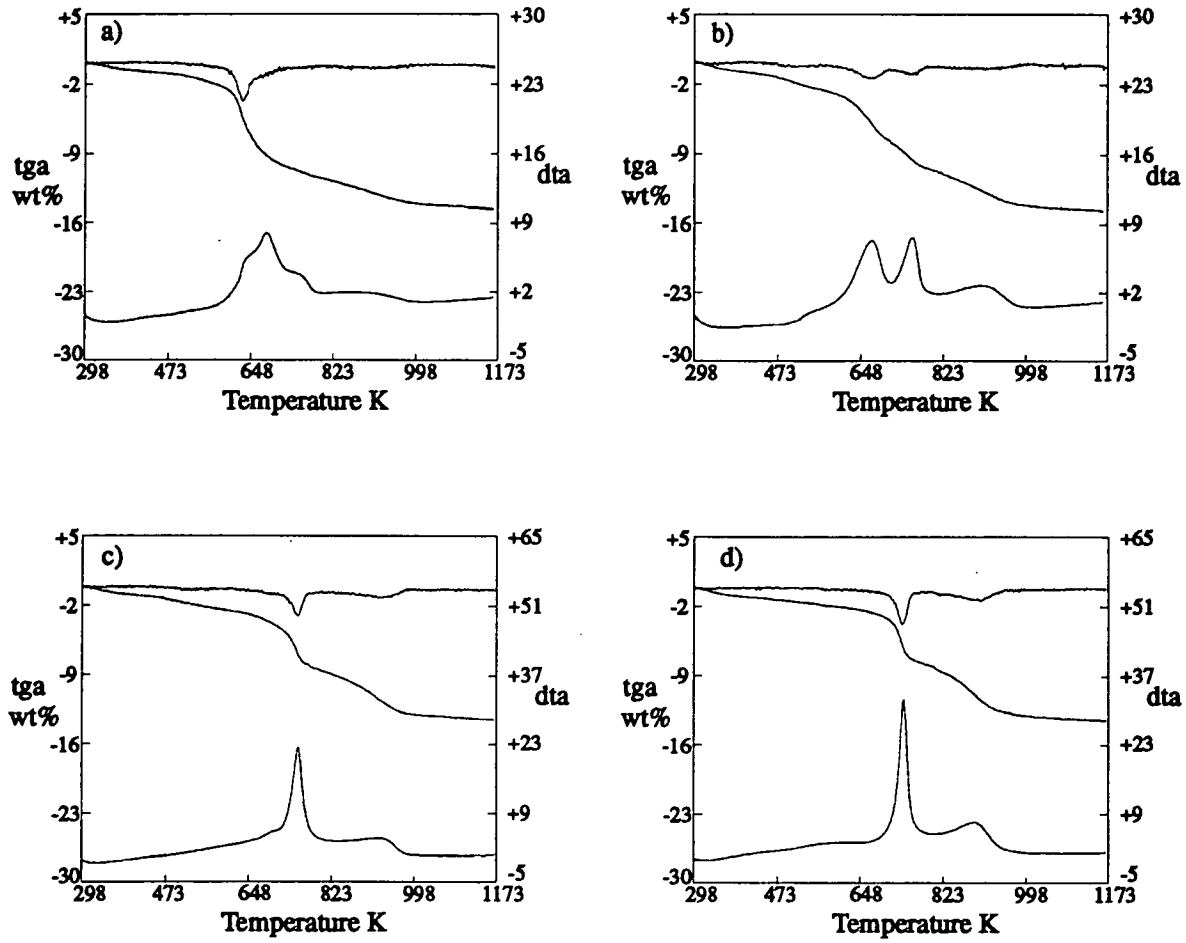

Figure 4–9: Simultaneous thermal analysis traces for, a) AMFI1, b) AMFI2, c) AMFI3 and d) AMFI4.

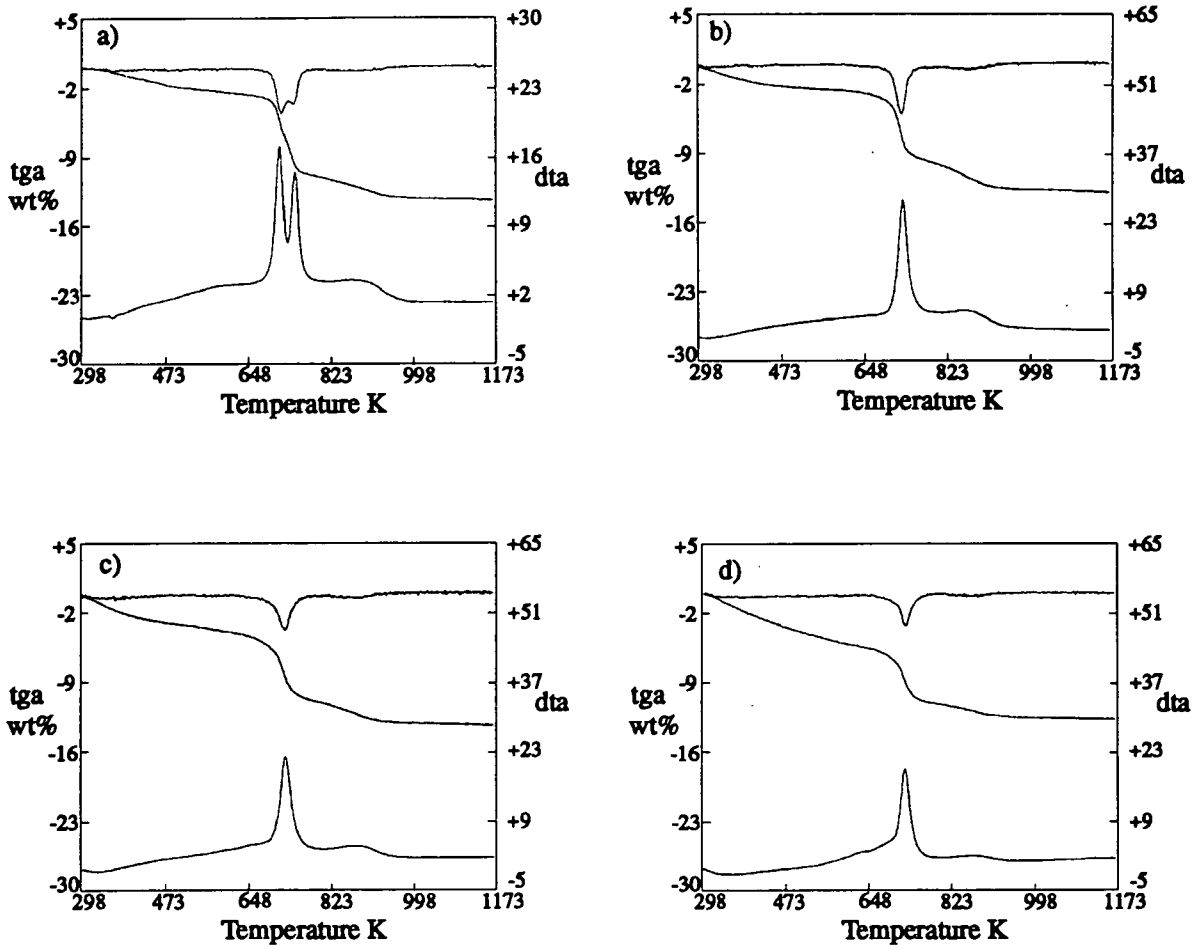

Figure 4–10: Simultaneous thermal analysis traces for, a) CMFI1, b) CMFI2, c) CMFI3 and d) CMFI4.

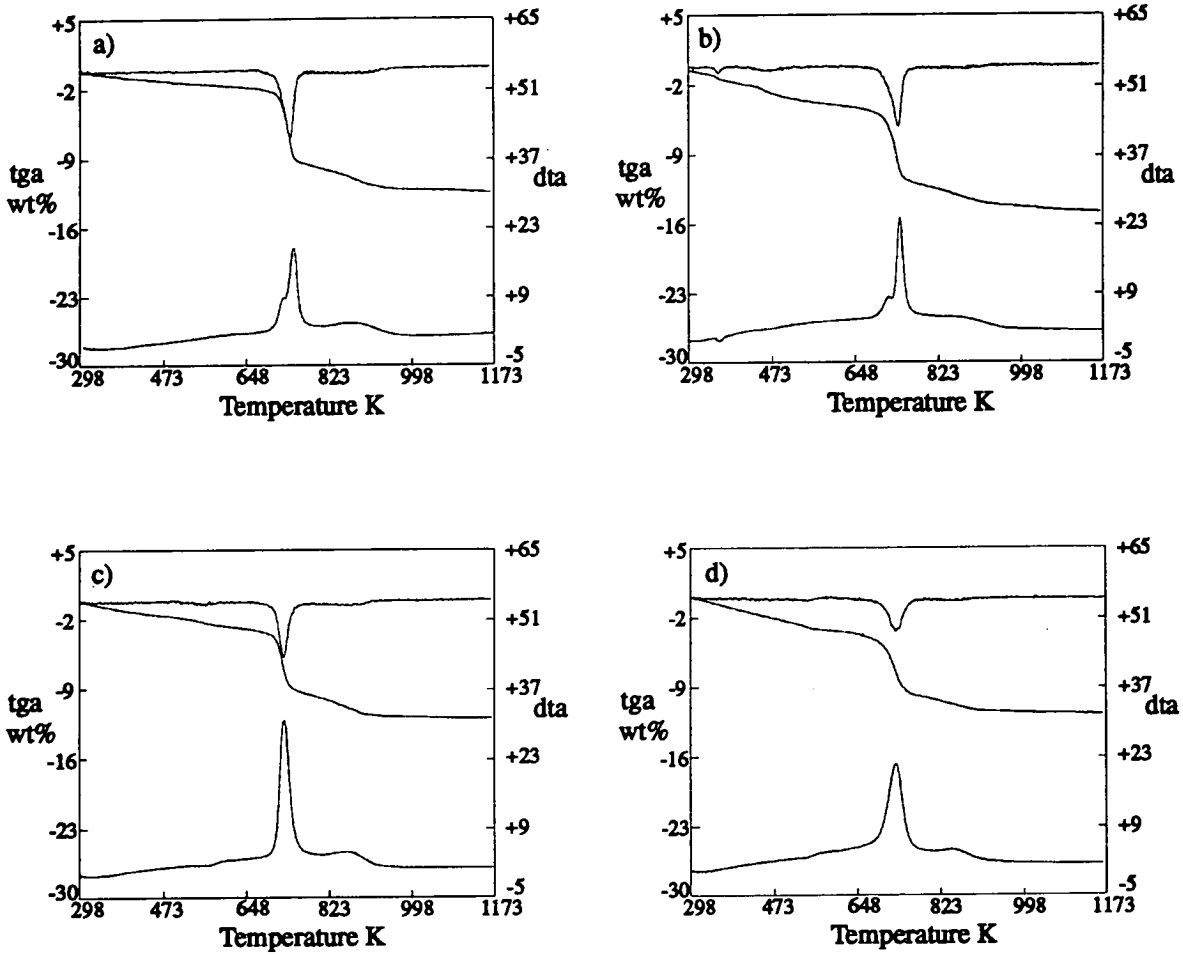

Table 4–19: STA Data for the EUO series of syntheses.

Sample	Total Wgt Loss (%)	Process Breakdown Temperature Ranges (K)			Theoretical Organic + OH^- Wgt Loss (%)
		298-522	523-973	974-1173	
AEUO1	14.0	1.22	11.85	0.93	11.87
AEUO2	14.3	1.89	11.36	1.05	11.36
AEUO3	14.2	2.43	10.87	0.90	10.89
AEUO4	14.2	1.86	10.81	1.53	10.73
CEUO1	14.5	1.36	11.79	1.35	11.72
CEUO2	14.5	2.19	11.12	0.85	11.11
CEUO3	13.0	1.77	10.56	0.78	10.61
CEUO4	13.3	1.55	10.65	1.10	10.50

of occluded water molecules. From 523 K to ≈973 K the main weight losses are observed and have been correlated with the removal of organic void filler material. The losses from materials 1 and 2 in the EUO series are significantly larger than materials 3 and 4. This observation is rationalised by consideration of the form of the organic void filler. As has been described previously the syntheses used the doubly charged Hexamethonium (Hex^{2+}) species as a void filler and so with 4 Hex^{2+} per unit cell there are 8 positive charges along with the positive charge associated with Na^+ present. Materials 1,2 and 3 have less than the maximum 8 Al or Ga per unit cell so there remains unbalanced positive charge which is neutralised by the presence of OH^- ions [215] and it is the removal of those species (as water) after a Hoffman elimination interaction with the organic Hex^{2+} (as represented schematically in Figure 4–11) that accounts for the extra weight loss. The Hoffman elimination simply involves a base catalysed β hydrogen abstraction, followed by the evolution of trimethylamine and the formation of a primary alkene. After the removal of the occluded organic species, any previously trapped water molecules are now free to leave the porous structure and so contribute to the observed weight loss.

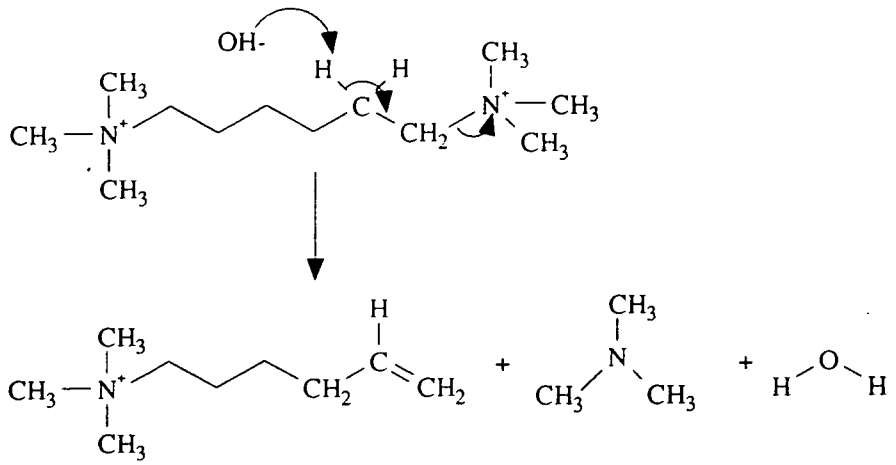

Figure 4–11: Schematic of the Hoffman elimination reaction which leads to Hexamethonium degradation.

At temperatures above 973 K dehydration of the framework structure is observed and accounts for the small weight loss above this temperature. Table 4–19 also shows a comparison of the actual weight loss in the 523 K to 973 K range to the theoretically predicted weight loss associated with the removal of the organic filler material and allowing for the presence of Hex^{2+}/OH^{-}, required for charge balancing in the materials. These show excellent agreement and suggest that this model describes the mode of interaction of the Hex^{2+} species in the EUO preparations very well.

4.3.3 Relationship Between Organic and Metal Content

The weight loss profiles for the EUO materials (Figures 4–7 and 4–8) show separate weight loss processes at different temperatures in the 523 K to 973 K range, as shown by TGA and DTG. However, the clearest indication of separate decomposition processes comes from the DTA profiles which show 2 distinct exothermic weight loss events for the samples with the lowest metal contents but these merge into one exotherm as the metal content *i.e.* framework negative charge increases.

The two most likely modes of decomposition of occluded organic species are; direct thermal decomposition (combustion) or base catalysed Hoffman elimination reactions leading to degradation of the quaternary amines if the organic species was associated with an OH^- rather than a negative charge on the framework. The different types of Hexamethonium cations whether associated with OH^- or framework charge serve different functions and are resolvable in the STA analyses. Positive charges on the Hexamethonium species could be associated with framework metal species and so be charge balancing whereas $Hex(OH)_2$ is a void filler which will be released at lower temperatures because of the different type of interaction with the framework and the facility for the Hoffman degradative process. The proposition that the occluded Hexamethonium cations are balanced by OH^- species when not associated with framework charge has been confirmed by other workers in the field [215] who have found no evidence of Br^- occlusion or any other simple salt species which could counter the quaternary amine's positive charge.

Thermal decomposition leads directly to the formation of CO_2, NO_2 and hydrocarbon fragments from the decomposition of quaternary amines. However, in the presence of base these quaternary amines are extremely prone to β-hydrogen abstraction to leave a primary alkene with the evolution of the volatile trimethylamine as described previously. Hexamethonium is a diquaternary and so this process could be repeated if both positive charges were associated with base rather than framework negative charge to produce a hydrocarbon diene which is likely to cyclise in the confines of the molecular sieve channel structure. Such a base induced decomposition is a more facile process than thermal decomposition and so would occur at a lower temperature than the combustion process. Ready study of these proposed processes could have been achieved by the use of thermal gravimetry in tandem with mass spectroscopy (tg/ms) or in tandem with infra-red techniques (tg/FTIR) where the composition of the evolved gases could be examined closely. However, such techniques were unavailable to this study. As has been discussed for EUO materials with less than 8 Al or Ga present per unit cell there are charge balancing OH^- species present. Hence the positive ends of the Hexamethonium

Table 4–20: Contributions to the exothermic signal from Hoffman and thermal degradative processes for the EUO series of sieves.

Sample	Metal atoms per uc	Exotherm Breakdown[a]		Theoretical Breakdown	
		Low Temp. peak	High Temp. peak	Low Temp. peak	High Temp. peak
AEUO1	2.7	70	30	66	34
AEUO2	5.3	40	60	34	66
AEUO3	7.7	5	95	4	96
CEUO1	2.6	70	30	67	33
CEUO2	5.0	60	40	33	67
CEUO3	7.0	5-10	90-95	12	88

[a] Estimate from relative peak areas in Figures 4–7 and 4–8.

void filler material can either be associated with this base and be subsequently degraded via a Hoffman interaction or be associated with a framework charge and thus be removed by thermal decomposition *i.e.* combustion. These two types of interaction are schematically represented for the EUO series of materials in Figure 4–12.

Table 4–20 shows the proportion of low temperature exotherm peaks to high temperature exotherm peaks (in %) in the temperature range 522 K to 973 K, for the EUO materials prepared. The low temperature peaks have been assigned as decomposition of the Hexamethonium by a Hoffman induced degradation and the high temperature peak as decomposition by thermally induced combustion. The theoretical values have been obtained by considering the ratio of interactions between framework charges and Hex^{2+} species and the number of free amine functions from Hexamethonium which decompose via the base induced Hoffman degradation. Clearly, although the estimates of high and low temperature exotherm peaks are crude, there is an excellent agreement between the theoretically predicted contributions and the experimental results. This suggests that the proposed model of two different degradation pathways depending on the counter charge to the amine

Figure 4–12: Interactions of the Hexamethonium void filler with the EUO framework structure, a) EUO1, b) EUO2, c) EUO3 and d) EUO4.

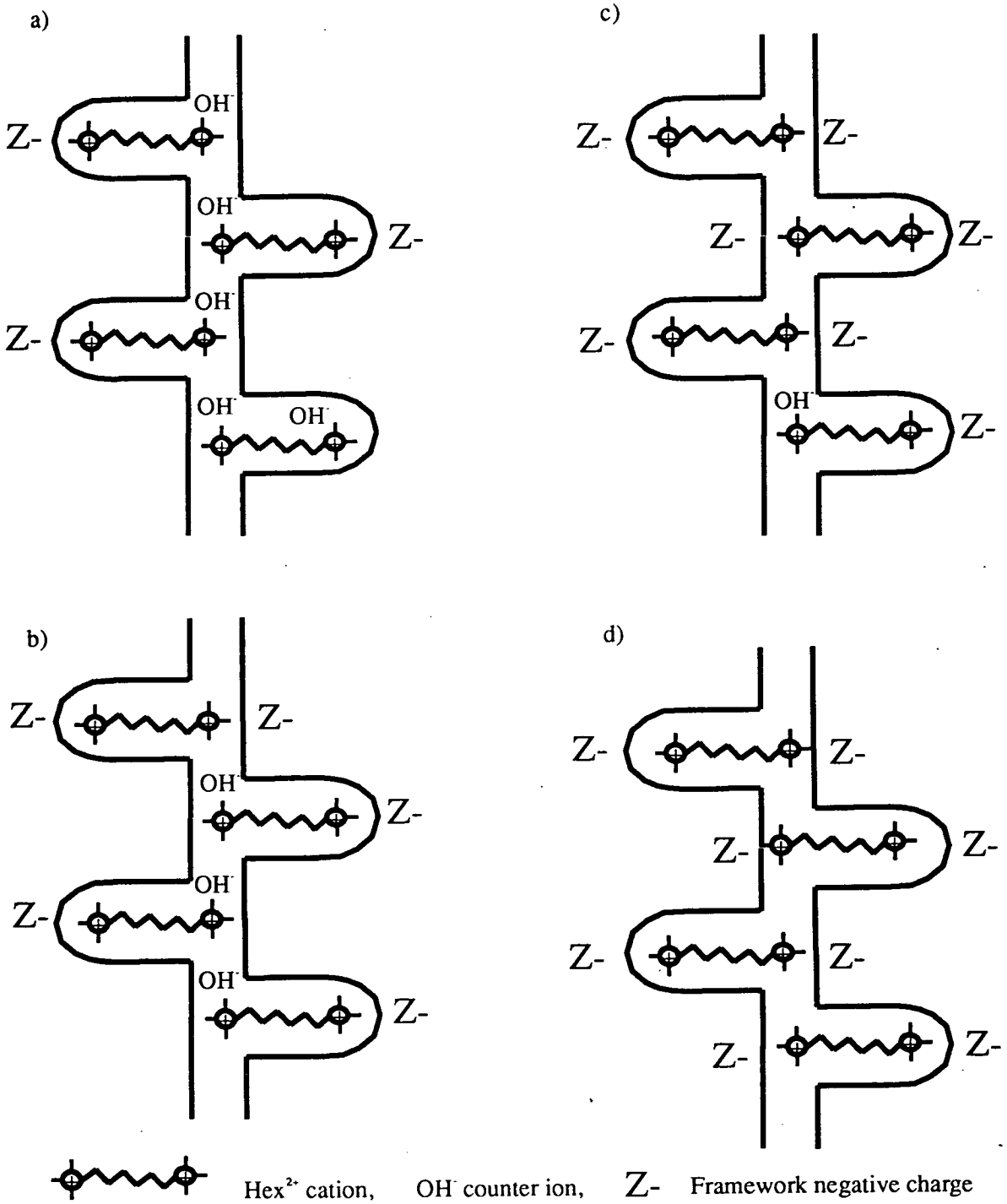

function (Hoffman for amines balanced by OH^- and thermal for amines associated with framework negative charge) is valid. Thus, this model for the association of Hex^{2+} with either framework charge or OH^- species can be used as a predictive tool for proposing the relative siting of the framework metal species.

Figures 4–9 and 4–10 show the STA traces for the MFI series of sieves where there are again two different types of organic weight loss. The weight losses are summarised in Table 4–21. These different weight loss processes have been observed by other workers and have been rationalised as the combustion of the occluded organic materials in different environments within the molecular sieve structure *i.e.* either in a siliceous environment with no interaction with hetero T-atoms or in an environment where there is significant interaction with these framework species [217, 218]. However, as the heteroatom concentration increased the exotherms merged and appeared as a single combustion process, indicative of a more homogeneous interaction of the occluded organics with the framework structure. Similar observations have also been rationalised as an oxygen starvation mechanism [219], where larger samples or faster temperature ramps increased the effect observed. However, in this work the experimental conditions were constant throughout.

The interaction of the TPA^+ and Na^+ counter ions for the MFI materials are represented schematically in Figure 4–13. This illustrates that there are more framework negative charges than can be countered by the 4 TPA^+ species and so the extra Na^+ ions are required to maintain charge neutrality. This increase in sodium content on increasing the metal content of the framework was expected and was clearly observed in the elemental analysis of the sieves prepared with the MFI structure type. This level of Na^+ and TPA^+ cation occlusion is in agreement with the model proposed by Cox [220] who used a Monte Carlo simulation approach allowing free relaxation of the cations in the MFI channels to generate the image reproduced in Figure 4–14.

Figures 4–15 a) and b) show plots of the number of organic and sodium cations present, per unit cell, against the number of Al or Ga present per unit cell for the A and C series of EUO and MFI preparations. Clearly as the number of Ga or Al

Figure 4–13: Interactions of the TPA^+ void filler and Na^+ cations with the MFI framework structure.

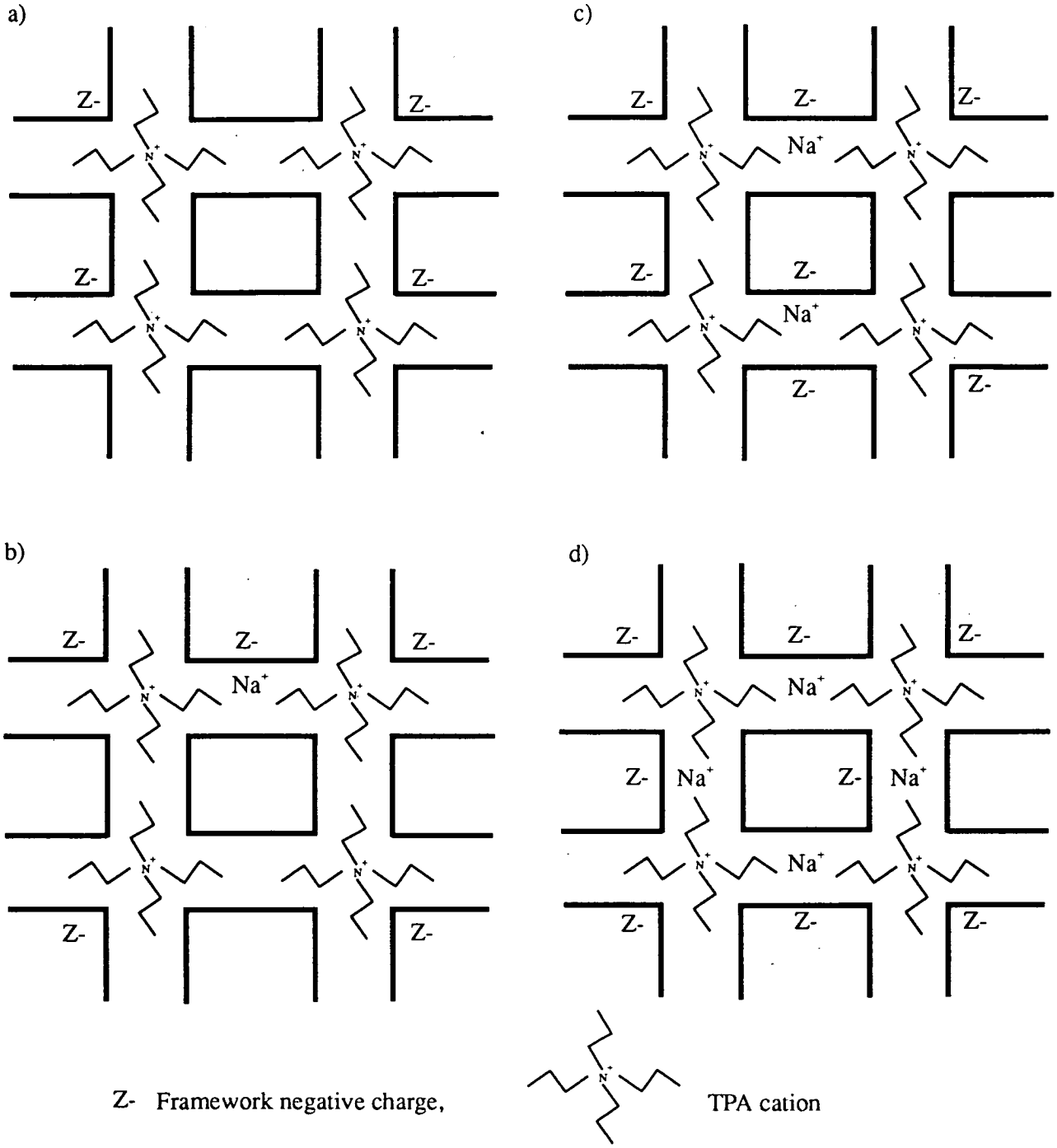

Figure 4–14: Image of TPA^+ and Na^+ cations in a unit cell of MFI, prepared from a Monte Carlo calculation by P. Cox.

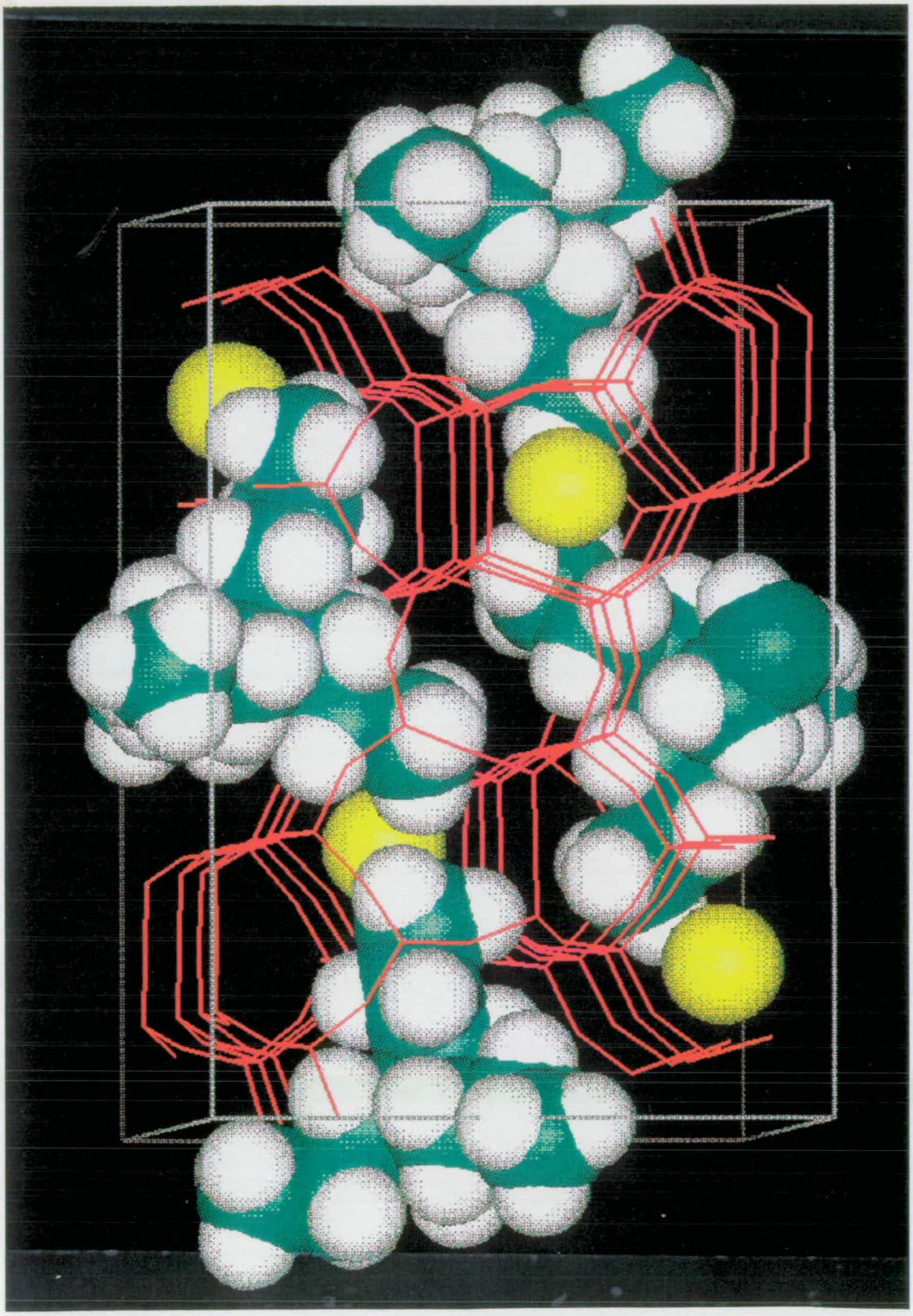

Table 4–21: Simultaneous Thermal Analysis Data for the MFI series of syntheses.

Sample	Total Wgt Loss (%)	Process Breakdown Temperature Ranges (K)		
		298-522	523-973	974-1173
AMFI1	13.53	1.96	10.50	0.9
AMFI2	12.13	2.39	9.33	0.41
AMFI3	12.83	3.02	8.87	0.94
AMFI4	12.37	4.15	7.20	1.02
CMFI1	12.37	1.11	10.73	0.53
CMFI2	14.23	3.25	10.03	0.95
CMFI3	11.67	1.90	8.40	1.37
CMFI4	11.43	2.70	7.7	1.03

atoms per unit cell increases the number of organic molecules occluded per unit cell is different for the two structure types. In the EUO syntheses, the organic used ($HexBr_2$) is doubly charged and so four Hex^{2+} are sufficient to balance the 8 gallium atoms which would be the maximum number accommodated in the EUO framework structure [215] and so there is no need to occlude large amounts of sodium ions to balance an excess in the framework charge. The MFI series shows a reduction in organic present with increasing metal content. This is readily rationalised by considering that the TPA^+ template used in these syntheses is singly charged and that only four TPA^+ cations can fit into a unit cell of MFI [221]. Consequently, as the number of aluminium or gallium atoms increases, above four, there is insufficient charge balancing by the organic cations. The additional framework charge is balanced by the smaller sodium ions. However, as the amount of Al or Ga is further increased, more sodium ions are required to balance the negative framework charge and consequently fewer TPA^+ ions are accommodated in the void space to allow for the increase in sodium ions. Thus, a reduction in the amount of occluded organic was observed.

Figure 4–15: Plots of a) number of Hexamethonium (Hex^{2+}, organic "template") and number of sodium ions occluded per unit cell of the EUO sieve against the number of metal atoms per unit cell and b) number of Tetrapropylammonium (TPA^{+}) ions and number of sodium ions per unit cell against the number of metal atoms per unit cell of MFI material.

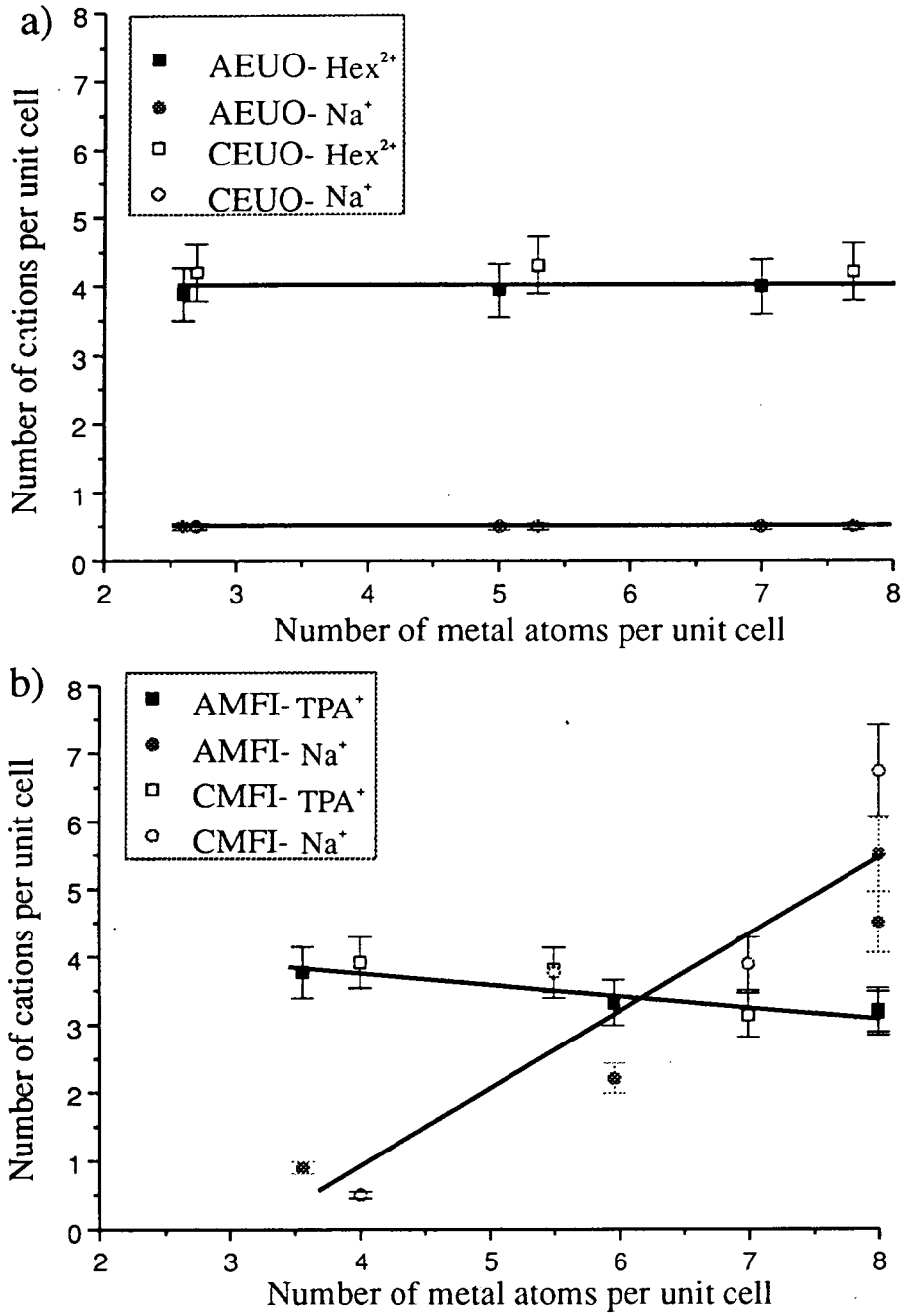

Figure 4–16: Comparison of the STA traces for the aluminosilicate and gallosilicate materials. a) Comparison of AEUO3 (trace 1) and CEUO3 (trace 2) and b) Comparison of AMFI3 (trace 1) and CMFI3 (trace 2).

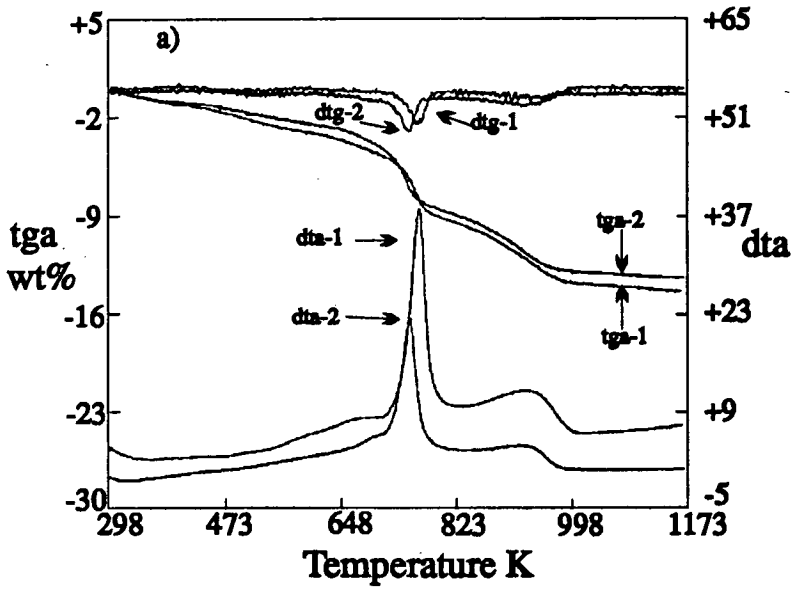

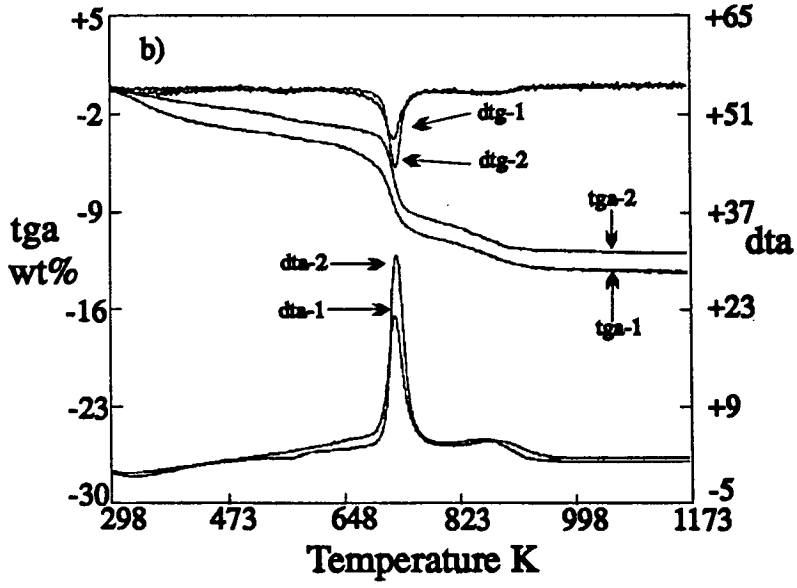

Comparison of the aluminosilicate materials with their gallium analogues highlights a marked difference in the temperature at which the exothermic processes occur which has also been observed by other workers [222]. Figure 4–16 shows that for the MFI structure type, the organic void filler is removed from the aluminous sieve at a lower temperature than the corresponding gallium analogue. However, this trend is reversed for the EUO materials where the gallosilicate EUO material releases the organic at a lower temperature than the aluminous material. These features were observed throughout the MFI and EUO series of materials. Quantitative data obtained from STA of the A and C series of MFI materials are shown in Table 4–21. For the EUO sieves this observation can be rationalised as a weaker interaction between the gallosilicate framework and the Hexamethonium than the interaction between the Hexamethonium and the analogous aluminosilicate framework. This could be expected from the lower electronegativity of the gallium species than the aluminium framework species. However, for the MFI sieves the temperature difference is not quite so significant and the observation can be explained by considering that not all the gallium present is in the framework and as such could be partially blocking the channel structure causing a delay in the release of the organic species. This partial channel blockage was observed in the micromeritic pore volume determination for these materials (Section 4.2.4, Table 4–9).

4.3.4 Metal Content of Sieves Determined From XRPD

A simple method for the determination of the metal content in ZSM-5 materials from XRPD patterns has been used by a number of workers [3, 223, 224]. The method was derived from the empirical observation that the splitting (δ) between the peaks at around 45.0 and 45.5° 2θ in the XRPD patterns of the calcined materials, can be related to the metal content by equation 4.2,

$$\% \, Al_2O_3 = 16.5 - 30.8 \, \delta \qquad (4.2)$$

It was suggested that such a procedure was also applicable to zeotypes with the MFI framework structure [225]; however, reservations were expressed that for gal-

losilicates extensive ejection of Ga from the framework during calcination would result in a lower estimate of the Ga content from such a graphical approach. This approach, initially proposed by Bibby [224] has its basis derived from a correlation of the splitting with framework metal species only.

The δs for the AMFI and CMFI series of materials are plotted against the Mole % M_2O_3 (as determined by XRF) in Figure 4–17 a). Similar to Bibby *et al.* [224] a linear correlation was obtained when data points for AMFI4 and CMFI4 were omitted from the least squares fit, Bibby *et al.* observed significant deviations for materials which had "non-homogeneous metal incorporation" *i.e.* contained impurities. The samples AMFI4 and CMFI4 have both been shown, by XRPD, to contain analcime impurity (≈15%) and so on this basis, their exclusion from the relationship is justified.

The least squares fits obtained for the AMFI and CMFI series are very similar to that of Bibby and are given by equations 4.3, 4.4.

$$Mole\ \%\ Al_2O_3 = 10.1 - 17.6\ \delta \tag{4.3}$$

$$Mole\ \%\ M_2O_3 = 8.1 - 11.6\ \delta \tag{4.4}$$

This correlation suggests that such an empirical relationship does hold for gallosilicate MFI materials provided the gallium species are associated with the MFI material and not present as any other impurity phase. The difference between the empirical relationships for the gallosilicate and aluminosilicates would be expected since it has been suggested [65] that this splitting between the peaks from the (10,0,0) and (0,10,0) Miller Indexed planes is associated with the distortions in the lattice of the crystallites caused by the metal isomorphously substituting into the MFI framework. The two planes should be equivalent but as the metal is incorporated into the framework they become inequivalent and this leads to their splitting. Consequently, since gallium (0.61 Å) is larger than aluminium (0.53 Å) then as the metal is incorporated into the framework structure, the larger gallium

Figure 4–17: Plots of δ against metal content for a) AMFI and CMFI materials and b) MFI materials, excluding MFI4 samples, and the linear correlation suggested by Bibby (dashed line).

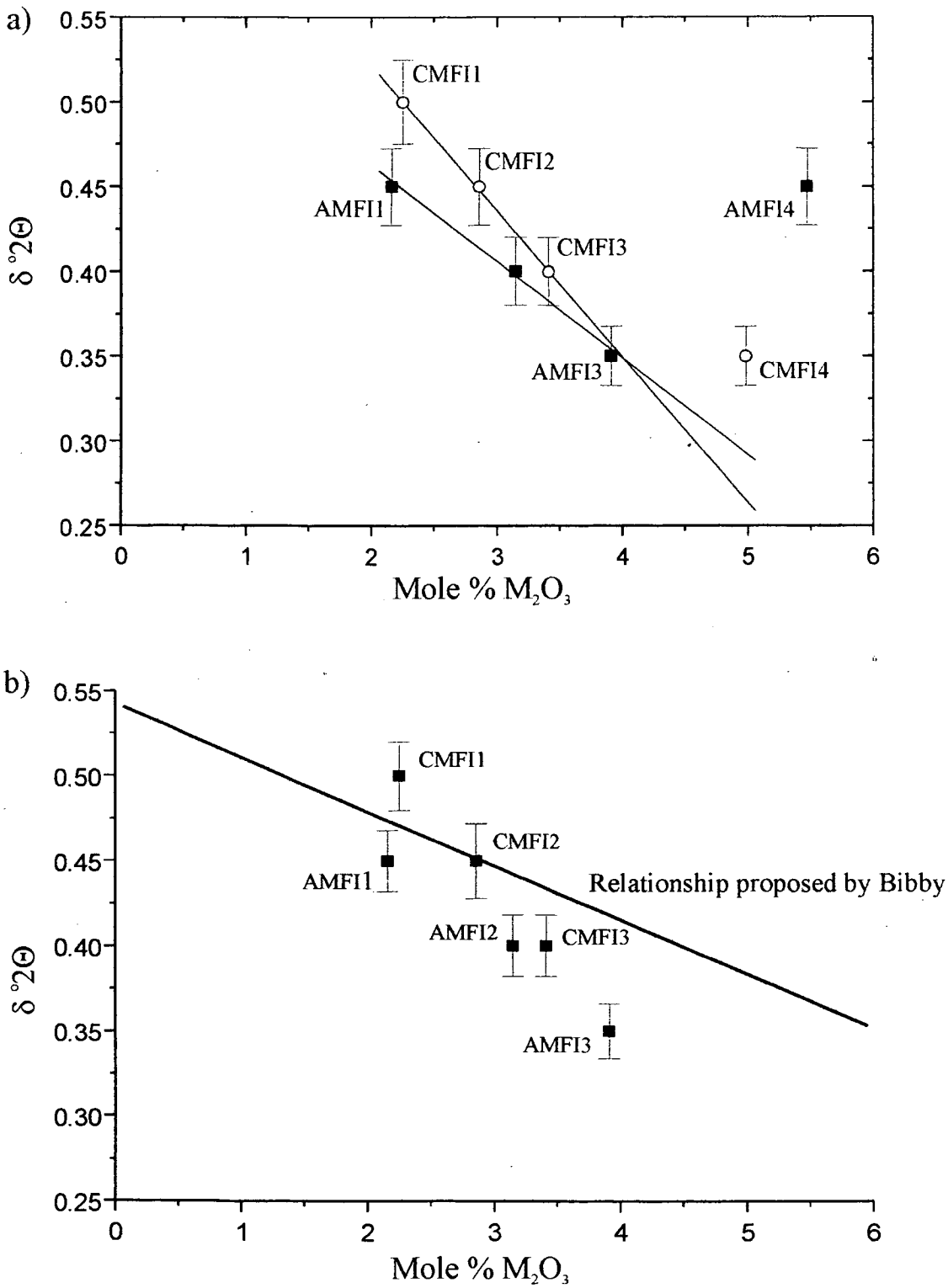

Table 4–22: Unit Cell Composition Summary Table for the EUO syntheses.

Sample	Structure	Unit Cell composition					
		Na	Al	Ga	Si	O	Hex^{2+}/OH^-
AEUO1	[Al]-EUO	0.5	2.7	0.0	109.3	224	3.98
AEUO2	[Al]-EUO	0.5	5.3	0.0	106.7	224	4.00
AEUO3	[Al]-EUO	0.5	7.7	0.0	104.3	224	4.01
AEUO4	[Al]-NU-85	0.4	9.2	0.0	102.8	224	3.97
CEUO1	[Ga]-EUO	0.5	0.0	2.6	109.4	224	3.88
CEUO2	[Ga]-EUO	0.5	0.0	5.0	107.0	224	3.93
CEUO3	[Ga]-EUO	0.5	0.0	7.0	105.0	224	3.98
CEUO4	[Ga]-NU-85	0.4	0.0	9.4	102.6	224	3.98

would be expected to cause a greater distortion of the lattice and so result in larger peak splitting (δ).This was observed and is clearly repesented in Figure 4–17 a) where the gallosilicate MFI materials consistantly shows greater splitting than the analogous aluminosilicate materials.

Summary of Unit Cell Compositions

The unit cell compositions of the A and C series of EUO and MFI materials prepared in this work are summarised in Tables 4–22 and 4–23.

Table 4–23: Unit Cell Composition Summary Table for the MFI syntheses.

Sample	Structure	Unit Cell composition					
		Na	Al	Ga	Si	O	TPA^+
AMFI1	[Al]-MFI	0.9	4.3	0.0	91.7	192	3.77
AMFI2	[Al]-MFI	2.2	6.3	0.0	89.7	192	3.32
AMFI3	[Al]-MFI, tr ANA	4.5	7.0	0.0	89.0	192	3.21
AMFI4	[Al]-MFI, ≈15%ANA	7.5	8.0	0.0	88.0	192	3.16
CMFI1	[Ga]-MFI	0.5	0.0	4.1	91.9	192	3.91
CMFI2	[Ga]-MFI	3.8	0.0	5.5	90.5	192	3.81
CMFI3	[Ga]-MFI, tr ANA	3.9	0.0	6.9	89.1	192	3.14
CMFI4	[Ga]-MFI, ≈15%ANA	6.7	0.0	8.0	88.0	192	3.06

ANA = analcime, tr = trace

4.4 Acidity of Materials Prepared

A test reaction and direct measurement using basic probe molecules have been used to determine the number, and relative strengths, of the acid sites associated with the molecular sieves examined in this work.

4.4.1 Cyclopropane Isomerisation

Acidity is often examined by means of a test reaction *eg.* n-hexane or n-decane cracking [171, 172]. The isomerisation of cyclopropane is also a useful test reaction which gives a direct indication of the amount of Brönsted acidity in a sample, as described previously. The results from this acidity test reaction are shown in Figure 4–18 which is a plot of % propene produced from the isomerisation of cyclopropane against reaction time. Visual interpretation shows the materials of lowest $\frac{SiO_2}{Al_2O_3}$ ratio to have the fastest rate of isomerisation. This is quantified in Figure 4–19 which is a plot of log ν (ν is the initial rate of isomerisation, determined from Figure 4–18) against $\frac{SiO_2}{Al_2O_3}$. Fitting a function to the behaviour of the ZP materials predicts an empirical relationship between the $\frac{SiO_2}{Al_2O_3}$ and log ν. This simple exponential best fit is rearranged to yield equation 4.5.

$$\frac{SiO_2}{Al_2O_3} = 29.42 - 18.33 \times ln \left\{ \frac{log\ \nu + 0.394}{1.774} \right\} \qquad (4.5)$$

This approach applied to materials D1 and D2 gave $\frac{SiO_2}{Al_2O_3}$ ratios of 56±6 and 59±6 compared to 51 and 53 as determined by XRF elemental analysis. This is in good agreement although it is observed that these values are equivalent within experimental error. However, they do offer the correct relative levels of acidity for these materials. It is suggested that this procedure offers a good method for the estimation of relative acidities for a range of molecular sieves. This cyclopropane isomerisation test reaction was not used to examine the acidic nature of the A and C series of materials prepared because the apparatus was required for catalytic investigations and the NH_3 TPD apparatus was available to offer direct acidity measurements.

Figure 4–18: % Propene in recirculating gas during the isomerisation of cyclopropane to propene over a range of molecular sieves.

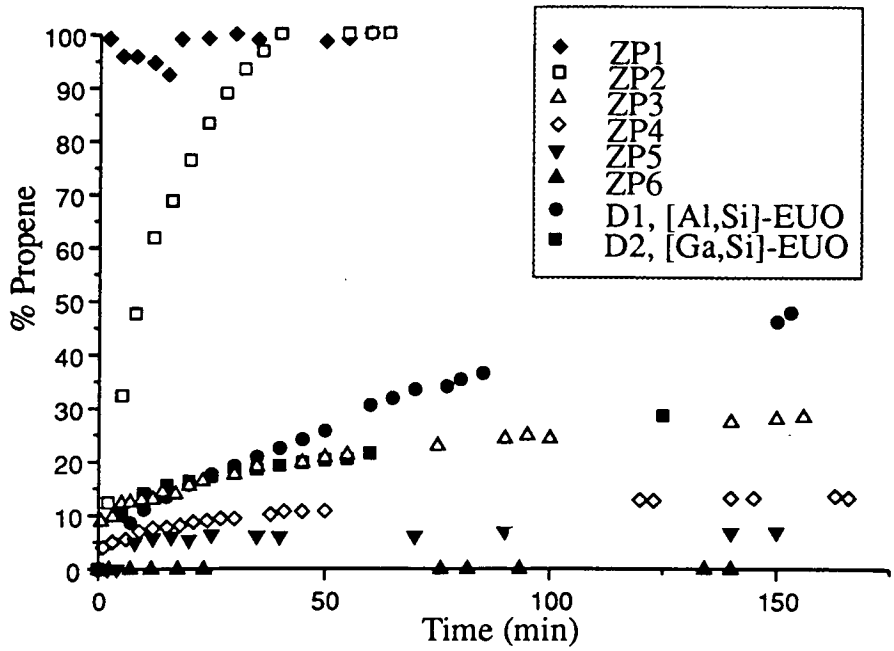

Figure 4–19: Plot of log ν (initial rate of isomerisation) against $\frac{SiO_2}{Al_2O_3}$ ratio.

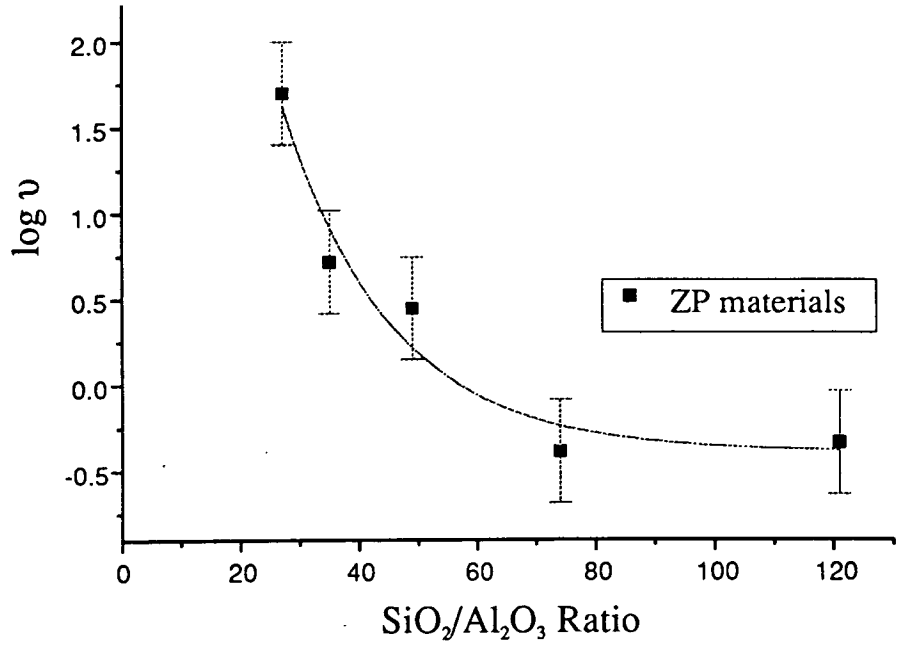

4.4.2 Temperature Programmed Desorption of Ammonia (NH_3 TPD)

Limitations of TPD Studies of Molecular Sieves

The problems associated with TPD procedures are well known for more traditional *flat* surfaces where the substrate under examination can be dramatically altered by the thermal treatments of the experimental procedure. This often results in the loss of some of the *sites* under scrutiny with the creation of other species, which may also be detected by the analysis and the creation of a range of sites can result in misleading analyses. The problem of readsorption of the probe molecules onto the newly created active sites has led to many workers avoiding the TPD approach *eg.* metal surface area determination, where many workers prefer to use hydrogen pulse chemisorption techniques [226]. The inherent problems of the TPD experiment are greatly exaggerated in the confines of a molecular sieve where readsorption of desorbed base probe molecules is common and rapid. Also the Brönsted acid sites are known to dehydrate under thermal treatments to create extra-framework Lewis acid species (as described in Chapter 1) which are also able to interact with the probe molecule. Consequently, the Redhead approach to the determination of the heats of desorption from these acid sites is not completely applicable. The T_{max} value measured cannot be directly attributed to desorption from specific sites, but rather as the temperature when the probe molecule has been able to evolve from the microporous structure and be detected. With a heating rate of 10 $Kmin^{-1}$, significant delay between desorption of the probe molecule and its detection would result in large errors in the observed T_{max} and consequently the calculated heat of desorption.

A further complication in the TPD approach, used in this work, is that the temperature measured is not the actual temperature of the material under investigation but that of the external surface of the vessel holding the material. There will be a temperature difference between an insulating sample, such as a molecular sieve, and the external surface of the the stainless steel reaction vessel. Also, since the sample is not homogeneously distributed in the sample vessel there will be

temperature gradients through the sample itself. Hence, the temperature measured is not the temperature of the entire sample and these temperature gradients would lead to a smearing of the desorption profile.

Inherent in the TPD approach is the assumption that all the probe molecules are desorbed at the end of the TPD experiment. In the NH_3 TPD studies, described in this work, the materials were maintained at 873 K until the baseline of the TCD output became steady and the experiment was deemed to be complete. However, there remains the possibility that some of the probe molecules remain associated with the acid sites of the molecular sieves when the experiment was stopped. This would result in an underestimate of the number of acid sites present. This underestimate is worse for materials which have a large number of strong acid sites, since these are the sites most likely to retain the probe molecules after the TPD experiment had been stopped. This is of particular concern when it is considered that there is a significant temperature difference between that measured on the surface of the vessel and the molecular sieves themselves. Hence, it is proposed that there is likely to be some undesorbed species in the samples after these TPD studies were completed and this difference between the total number of acid sites, determined by TPD, and the actual number of sites present is likely to be greatest for the materials with the highest level of framework metal incorporation.

The apparatus used in these NH_3 TPD studies was prone to a degree of variance with the sensitivity of the amplifier in the TCD unit changing quite dramatically through the temperature range investigated in these experiments. This resulted in sloping baselines which can be quite difficult to satisfactorily correct. Hence, it is difficult to determine suitable *end-points* for the desorption profiles. This uncertainty in the TCD value, which corresponds to completion of desorption, can cause a very large error in the area determined under the desorption peak *i.e.* the number of NH_3 molecules detected. This potential uncertainty is represented in Figure 4–20. This shows some raw experimental data and highlights the potential difficulty in assigning the point of completion of desorption. The shaded area shows the potentially huge differences in areas which could be determined from this

Figure 4–20: Schematic representation of the potential errors associated with the area determination under a TCD desorption profile. The raw experimental trace is shown with the shaded area representing the difference in areas that would be determined by choosing the end-point of the desorption profile to be either of the extremes indicated.

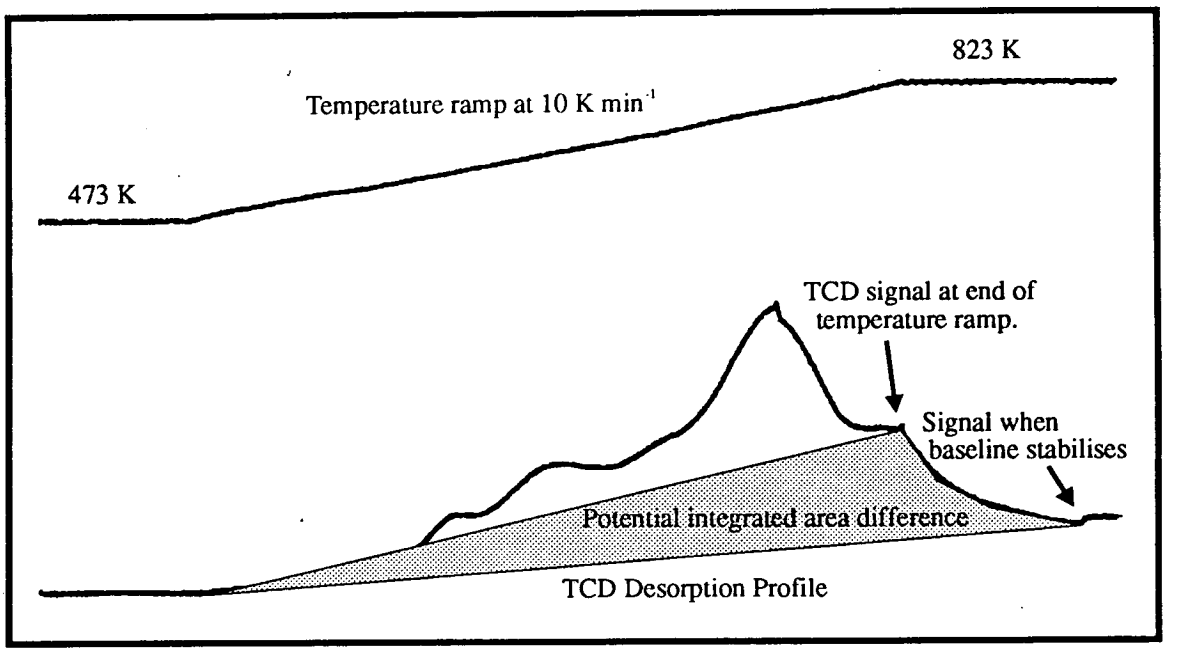

data. This is not a systematic error as some TCD desorption profiles are inherently simpler to analyse than others; however, provided a systematic approach to area determination is undertaken then good relative analyses can be obtained. Since an appreciation of the potential limitations of this approach was held then every effort was made to select the integration boundaries carefully and to compensate for the observed drift in the baseline of the desorption trace.

There is also the possibility that molecular sieves can be further dehydrated during the NH_3 TPD experimental procedure and these H_2O molecules would be indistinguishable from NH_3 by this analysis technique and so some of the desorption area could be due to H_2O rather than NH_3. This contribution is likely to be very small compared to the number of NH_3 molecules detected.

Determination of Heats of Desorption

A detailed breakdown of the strengths of the acid sites, in terms of the heats of desorption of the NH_3 probe molecule obtained for the ZP series of materials and the ZSM-5 Laposil sample are included in Table 4–24. This clearly indicates the increased strength of binding between the base probe molecule and the sites in the Laposil ZSM-5 material (used to prepare the gallium impregnated ZSM-5 benchmark catalyst) compared to those of the range of ZP (EU-1) materials obtained from I.C.I., C.&P. It has already been proposed that the determination of a precise heat of adsorption can not be accurately determined from this particular experimental procedure and that the grouping of the desorption profiles into broad bands of strong, medium and weak acid strengths, depending on the temperature of desorption is a more reasonable approach. These correspond to the components of the desorption profile which occur in the temperature ranges, 673 K to 823 K, 573 K to 672 K and 473 K to 572 K respectively. Consequently the detailed analyses, described by Redhead, of the heats of desorption of ammonia from the aluminosilicate and gallosilicate materials with the MFI and EUO structure type, prepared in this work, are not included.

Quantitative Acidity Determination

Inherent in the TPD approach is the assumption that all the probe molecules are desorbed at the end of the TPD experiment. This is not necessarily the case in these studies where it is accepted that it is unlikely that all the sample under investigation reached 823 K and it is likely that some of the NH_3 probe molecules remain in the sample. The NH_3 molecules which may be retained in the samples after completion of the TPD experiments would result in an underestimate of the number of acid sites present. This would be worse for materials which have a large number of strong acid sites, which are most likely to retain NH_3 molecules. The significant shortcomings of this TPD approach have been discussed (Section 4.4.2). Nevertheless, examination of this series of well characterised materials has shown this approach to be applicable to such ranges of molecular sieves. Hence,

Table 4–24: Heats of desorption of ammonia from a series of molecular sieves.

Sample	$T_{max}\pm10$ (K)	$E_d\pm10$ (kJmol^{-1})
Laposil	535	135
H-ZSM-5	628	160
$\frac{SiO_2}{Al_2O_3}$=35	695	175
	725	185
	760	195
	815	210
ZP-1	505	130
$\frac{SiO_2}{Al_2O_3}$=27	550	140
	665	170
	705	180
ZP-2	500	125
$\frac{SiO_2}{Al_2O_3}$=35	545	140
	680	175
ZP-3	510	130
$\frac{SiO_2}{Al_2O_3}$=49	550	140
	385	170
	435	180
ZP-4	510	125
$\frac{SiO_2}{Al_2O_3}$=121	640	165
	710	180
ZP-6	550	140
$\frac{SiO_2}{Al_2O_3}$=712	700	180

it is proposed that this approach is able to offer good relative analyses of series of materials and consequently has been used to examine the A and C series of sieves prepared in this work.

Table 4–25 summarises the acidity estimates obtained from the NH_3 tpd studies of the series of ZP samples of EU-1 along with the relative fractions of strong, medium and weak sites detected for each of the materials.

The experimentally determined acidity in terms of mmoles (1×10^{-3} moles) of NH_3 desorbed g^{-1} of dry sample, for the ZP series of materials are in extremely good agreement with those calculated by assuming a model where one NH_3 molecule is associated with each Brönsted acid site created by the charge associated with framework metal atoms. The errors associated with the tabulated acidity values contain contributions from; sample weighing errors, an inherent error associated with the assumption that 10% of the sample weight was associated with occluded water molecules which were desorbed on drying and also errors from both peak area integration and the error associated with the calibration of the peak areas to physical amounts of NH_3 desorbed from the samples.

Table 4–25 shows that the EU-1 framework of the ZP series of materials does not contain many of the strong acid sites with the majority of the sites being of weak or medium strength. The materials of lowest $\frac{SiO_2}{Al_2O_3}$ ratio (*i.e.* highest Al content) showed primarily acid sites of medium strength and only a very small number of the strongest type of acid sites. As the $\frac{SiO_2}{Al_2O_3}$ ratio increases the majority of the acid sites observed were only weakly acidic in strength. This increase in the proportion of weak sites was at the expense of the medium strength sites with only a small reduction in the number of the strong acid sites.

A and C Series of EUO and MFI Materials

The desorption profiles of some of the CEUO materials examined are included in Figure 4–21. These are representative of the desorption profiles obtained in this work and so the other profiles are not included, but all relevant quantitative data are included in Tables 4–25, 4–26 and 4–27.

Table 4–25: Number of mmoles of NH_3 desorbed from the ZP ([Al]-EU-1, obtained from I.C.I.) materials, compared to theoretical values.

Sample	Experimental Value mmoles×100 NH_3 (g^{-1} dry sample[a])	Theoretical Value mmoles×100 NH_3 (g^{-1} dry sample[a])	Fractions of different sites		
			weak	medium	strong
ZP1	106±9	120	0.3	0.6	0.1
ZP2	99±9	90	0.4	0.5	0.1
ZP3	72±6	66	0.9	0.05	0.05
ZP4	52±5	45	0.9	0.05	0.05
ZP5	29±3	30	0.95	0.0	0.05
ZP6	0.5±1	5	0.95	0.0	0.05

[a] assuming a 10 % weight loss after the removal of occluded water molecules

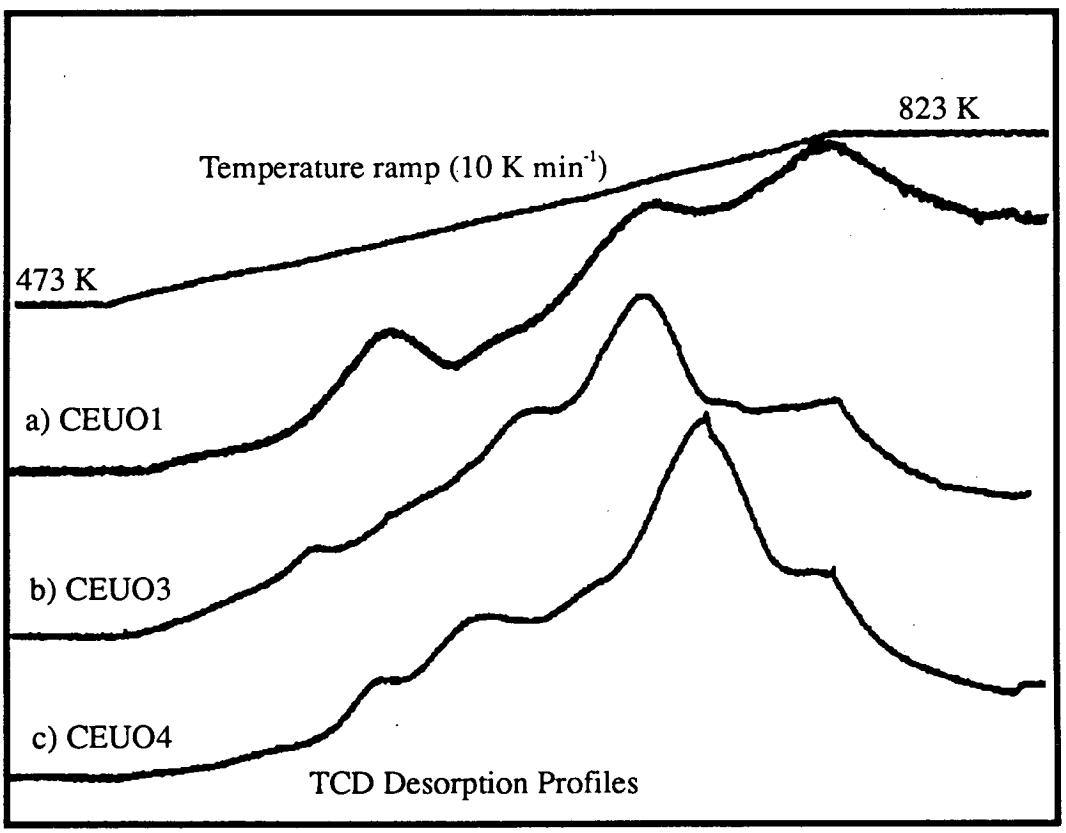

Figure 4–21: TPD profiles for; a) CEUO1, b) CEUO3 and c) CEUO4, ramped to 823 K and held isothermally.

Table 4–26 summarised the observed and theoretical levels of acidity for the A and C series of EUO materials. The EUO series of molecular sieves show relatively good agreement between theoretical and experimentally observed numbers of acid sites, as determined by NH_3 desorption, although there appears to be larger deviations at lower $\frac{SiO_2}{Al_2O_3}$ ratios *i.e.* materials with higher metal contents as determined by XRF. Underestimates in the number of acid sites observed in the EUO series of materials can be partially explained by the suggestion that any material occluded within the unidimensional channel structure can cause pore blockage and so would restrict access to the acid sites and hinder the initial adsorption and/or desorption of NH_3 species during the TPD experiment. It has been suggested that the EUO structure readily allows metal atom incorporation upto the maximum level of 8 metal atoms per unit cell. However, the acid ion-exchange procedure carried out before the NH_3 TPD may have resulted in significant leaching of the metal species from their framework sites. Formation of the acidic form of these molecular sieves could have been achieved by conversion of the material to its ammonium form (NH_4^+-zeolite) or by direct exchange with an acid solution. The ammonium form is obtained by exchange with a solution of an ammonium salt followed by a second calcination step to degrade the ammonium to NH_3 gas and leave the protonic form of the zeolite. It had been supposed that the direct acid exchange procedure was simpler to perform and would also result in less framework structure degradation. However, since the framework metal species were no longer stabilised by the organic cations, framework ejection could be much more facile than during the initial calcination, which appeared not to have caused significant ejection from the EUO framework. The reduction in observed acidity is more pronounced for the materials with the highest levels of metal incorporation, as would be expected since metal leaching by acid attack is more likely for molecular sieves with higher metal contents. The CEUO series showed a lower than expected level of acidity which suggests that removal of gallium from the molecular sieve framework is more readily achieved than removal of framework aluminium species, under the acidic conditions of the exchange procedure.

Table 4–26: Number of moles of NH_3 desorbed from EUO molecular sieve samples, compared to theoretical values.

Sample	Experimental Value mmoles×100 NH_3 (g^{-1} dry sample[a])	Theoretical Value mmoles×100 NH_3 (g^{-1} dry sample[a])	Fractions of different sites		
			weak	medium	strong
AEUO1	59±5	40	0.31	0.21	0.48
AEUO2	72±7	79	0.42	0.28	0.30
AEUO3	79±7	115	0.38	0.38	0.24
AEUO4	111±10	137	0.35	0.22	0.43
CEUO1	51±5	38	0.30	0.30	0.40
CEUO2	68±6	72	0.32	0.31	0.37
CEUO3	68±6	99	0.30	0.40	0.30
CEUO4	77±7	132	0.29	0.58	0.13

[a] assuming a 10 % weight loss after the removal of occluded water molecules

The observed and calculated NH_3 desorption profiles are shown in Table 4–27 for the A and C series of MFI molecular sieves.

For the AMFI series of molecular sieves there is relatively good agreement between predicted and experimentally determined acidity. The materials with the highest metal content showed fewer than expected acid sites, although these shortcomings have been proposed to be due to limitations of the experimental approach, with some NH_3 remaining undesorbed after completion of the experiment. It should be noted that the AMFI3 material which has the greatest deviation from the expected number of acid sites has a significantly reduced proportion of strong acid sites observed and so it could be proposed that this material has retained a large number of NH_3 molecules on its strongest acid sites. However, it was suggested (Section 4.3.3) that incorporation of metal species into the MFI framework structure above a level of 4 metal atoms per unit cell was not facile. This suggestion is further discussed in the following Chapter where XRPD analysis has been used to determine the unit cell volumes for these materials. It is assumed that the probe base molecules are associated with the framework metal species (Al/Ga T-atoms). Hence, if not all the metal has been retained in the framework it is not surprising that the observed levels of acidity, as determined by this technique, are below those predicted from theoretical calculations with the reduction in the number of Brönsted acid sites present caused by the partial removal of framework metal species during the calcination or ion-exchange procedures.

For the gallosilicate series of MFI materials (CMFI) there is almost a constant level of acidity observed in terms of mmoles of NH_3 desorbed g^{-1} of sample. This is in excellent agreement with the previous suggestion that incorporation of more than 4 Ga atoms per unit cell of MFI is not readily achieved and so the number of Brönsted acid sites created by tetrahedrally coordinated Ga species is approximately constant throughout this range of gallosilicate materials. The bulk gallium elemental analysis of these materials shows them to contain dramatically different amounts of gallium and so the theoretical number of acid sites increases through the series of materials; however, it is only framework species which are determined by this approach and so it can be suggested that these materials all have approx-

Table 4–27: Number of mmoles of NH_3 desorbed from MFI molecular sieve samples, compared to theoretical values.

Sample	Experimental Value mmoles×100 NH_3 (g^{-1} dry sample[a])	Theoretical Value mmoles×100 NH_3 (g^{-1} dry sample[a])	Fractions of different sites		
			weak	medium	strong
AMFI1	57±5	75	0.33	0.26	0.41
AMFI2	75±7	109	0.21	0.38	0.41
AMFI3	76±7	121	0.39	0.38	0.23
AMFI4	119±10	139	0.37	0.25	0.38
CMFI1	64±6	69	0.15	0.40	0.45
CMFI2	68±6	92	0.26	0.38	0.36
CMFI3	72±6	114	0.48	0.12	0.40
CMFI4	71±7	131	0.28	0.48	0.24

[a] assuming a 10 % weight loss after the removal of occluded water molecules

imately the same number of framework metal atoms per unit cell. The CMFI4 material, similar to the AMFI3 sample, shows significant deviation from the expected number of NH_3 molecules desorbed and again has an associated reduction in the number of strong acid sites observed, so again it is likely that this material could have retained large numbers of undesorbed NH_3 molecules. However, it is clear that all the CMFI materials show an approximately constant number of acid sites [72, 173, 180, 215].

Both A and C series of MFI materials show a range of acid sites, with significant levels of strong, medium and weak acid sites present in each of the materials. This is in accord with suggestions that the multidimensional MFI structure allows a wide range of metal sites in its framework and consequently a broad range of acid strengths are created [72, 173].

Comparison of the results for the EUO and MFI structure types indicates that the MFI framework contains slightly more strong acid sites than the EUO structure although the distribution of strong, medium and weak acid sites is similar for both

the MFI and EUO structure types of the materials prepared in this work. For the materials with the highest metal content there is an apparent reduction in the proportion of the strongest acid sites. However, this could be a consequence of incomplete desorption of the NH_3 probe molecules resulting in an underestimate of the number of acid sites present in the samples.

Laposil H-ZSM-5

The results of the acidity determination of the Laposil ZSM-5 material, used to prepare the gallium impregnated benchmark catalyst, are summarised in Table 4–28. The same sample was examined twice, without removal from the sample vessel in the NH_3 TPD apparatus. The first analysis gave a level of acidity which was in excellent agreement with theoretical values; however, upon reanalysis a significant reduction in the number of acid sites was observed. These TCD desorption traces are included in Figure 4–22 which clearly indicates the marked reduction in the number of the medium strength acid sites in the second analysis of the sample. This may be attributed to the ejection of framework Al from the Laposil sieve during the course of the first experimental run. This is analogous to the process of Lewis acid site formation by the dehydration of Brönsted acid sites (described in Chapter 1). This particular process can be partially reversed in the presence of water; however, since the sample was not exposed to such moisture before reanalysis such annealing was not achieved and so a net loss in Brönsted acidity was observed.

Ammonia temperature programmed desorption studies (NH_3 TPD) provide a good qualitative evaluation of the relative acidities of these ranges of molecular sieves and also a semi-quantitative estimate of the number of acid sites present. However, there are still significant deviations observed between experimental and theoretical values. These differences have been rationalised in terms of loss of Brönsted acidity caused by thermally induced framework metal ejection form the MFI frameworks and also the acid leaching of metal species from the EUO framework structure. The EUO samples also suffer the potential problem of channel blockage caused by this framework metal ejection. Hence the major differences in

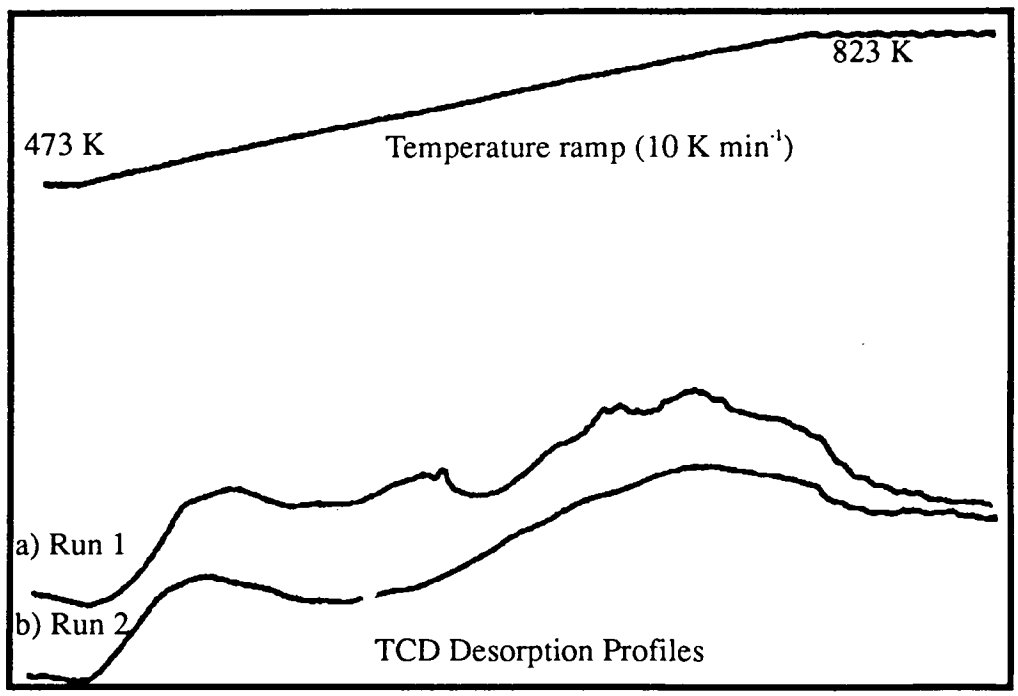

Figure 4–22: TPD profiles for; a) H-ZSM-5, first analysis and b) H-ZSM-5 sample retained in the reaction vessel and reanalysed. Samples ramped to 823 K and held isothermally.

Table 4–28: Number of moles of NH_3 desorbed from the Laposil H-ZSM-5 sample, compared to theoretical values.

Sample	Experimental Value mmoles×100 NH_3 (g^{-1} dry sample[a])	Theoretical Value mmoles×100 NH_3 (g^{-1} dry sample[a])	Fractions of different sites		
			weak	medium	strong
H-ZSM-5[b]	96±8	98	0.2	0.2	0.6
H-ZSM-5[c]	51±5	98	0.3	0.05	0.65

[a] assuming a 10 % weight loss after the removal of occluded water molecules, [b] initial analysis of Laposil sample, [c] repeat analysis without exposure of the sample to water vapour.

Sample	Structure	Unit Cell Composition				Acidity	Acid Sites
	(XRPD)	Na	Al/Ga	Si	O	mmoles×100 NH_3	w:m:s
AEUO1	[Al,Si]-EUO	0.5	2.7	109.3	224	59±5	0.31:0.21:0.48
AEUO2	[Al,Si]-EUO	0.5	5.3	106.7	224	72±7	0.42:0.28:0.30
AEUO3	[Al,Si]-EUO	0.5	7.7	104.3	224	79±7	0.38:0.38:0.24
AEUO4	[Al,Si]-NU-85	0.4	9.2	102.8	224	111±10	0.35:0.22:0.43
CEUO1	[Ga,Si]-EUO	0.7	2.6	109.4	224	51±5	0.30:0.30:0.40
CEUO2	[Ga,Si]-EUO	0.5	5.0	107.0	224	68±6	0.32:0.31:0.37
CEUO3	[Ga,Si]-EUO	0.5	7.0	105.0	224	68±6	0.30:0.40:0.30
CEUO4	[Ga,Si]-NU-85	0.4	9.4	102.6	224	77±7	0.29:0.58:0.13

Table 4–29: Summary of the characterisation of the EUO materials prepared.

the acidity of the materials prepared is associated with the number of framework metal species retained after thermal and ion-exchange activation procedures.

Comparison of the aluminosilicate and gallosilicate molecular sieves shows that the gallosilicates have less acidic character than the aluminosilicates. This effect is more marked in the MFI materials than in the EUO materials. It is known that in calcination and other thermal/hydrothermal treatments framework metal species can be ejected from the framework which results in a reduction in Brönsted acidity. Hence underestimates in the number of acid sites compared to theoretically calculated numbers of sites could be partially explained in terms of the loss of framework acidity by these thermal treatments.

4.4.3 Summary of Characterisation

The characterisation data derived in this Chapter is summarised in tabular form with the analyses of the EUO materials in Table 4–29 and the MFI materials contained in Table 4–30.

Sample	Structure	Unit Cell Composition				Pore Vol.	External area	Acidity	Acid sites
	(XRPD)	Na	Al/Ga	Si	O	$cm^3/100g$	m^2g^{-1}	mmoles×100 NH_3	w:m:s
AMFI1	ZSM-5	0.9	4.3	91.7	192	12.1	88	57±5	0.33:0.26:0.41
AMFI2	ZSM-5	2.2	6.3	89.7	192	12.2	103	75±7	0.21:0.38:0.41
AMFI3	ZSM-5[a]	4.5	8.0	88.0	192	11.4	122	76±7	0.39:0.38:0.23
AMFI4	ZSM-5[b]	7.0	8.0	88.0	192	9.8	96	119±10	0.37:0.25:0.38
CMFI1	[Ga,Si]-MFI	0.5	4.1	91.9	192	11.4	115	64±6	0.15:0.40:0.45
CMFI2	[Ga,Si]-MFI	3.8	5.5	90.5	192	11.1	98	68±6	0.26:0.38:0.36
CMFI3	[Ga,Si]-MFI[a]	3.9	6.9	89.1	192	11.1	104	72±6	0.48:0.12:0.40
CMFI4	[Ga,Si]-MFI[b]	6.7	8.0	88.0	192	10.3	87	71±7	0.28:0.48:0.24

Table 4–30: Summary of the characterisation of the MFI materials prepared.

[a] trace analcime, [b] ≈15% analcime.

Chapter 5

Nature and Location of the Gallium Species

5.1 Introduction

This Chapter presents the results obtained from a number of analytical techniques used to determine the location of the gallium species in the molecular sieve materials examined and also to determine the nature of these gallium species.

5.2 Effect of Crystallisation Time

Crystallisation is often associated with a significant increase in pH of the reaction mixture and so can be used to estimate the time taken for the onset of crystallisation and the rate of crystal growth, as described previously. Since this work is not primarily synthesis based this technique was not used to obtain detailed information on the crystallisation kinetics of the syntheses carried out. In the present work the plots of pH against reaction time merely serve to illustrate the differences in the times taken to obtain aluminosilicate and gallosilicate molecular sieves from similar gel compositions.

The pH of the samples taken from the autoclaves during the molecular sieve syntheses was measured after completion of the crystallisation. The physical appearance of these samples was used to estimate a suitable end-point for each synthesis. When crystals were observed to have settled in the sample, to leave a

clear supernatant liquid, the reaction was stopped. This, of course, was dependent upon the crystals being sufficiently large to rapidly settle from the mother liquor and it was noted that the samples taken during MFI crystallisations did not rapidly separate into two phases (white solid and clear liquid). This suggested that the product formed in the MFI syntheses were composed of extremely small crystallites, as was found to be the case from SEM analysis.

Figure 5–1 shows the pH versus reaction time plots for some of the EUO materials prepared in this work. These show the increase in pH associated with the crystallisation of high-silica molecular sieves. Figure 5–1 shows that at extended times of the EUO crystallisations, after the pH maximum, a decrease in pH was observed. This may be associated with consumption of free base in the reaction vessel as part of the Hoffman Elimination reaction which degrades some of the quaternary ammonium template present as organic void fillers in the reaction gels. This involves a β hydrogen abstraction followed by the formation and evolution of a primary alkene accompanied by the production of trimethylamine (TMA) which will be present in both the liquid and vapour phases. This Hoffman elimination was shown schematically in Figure 4–11. It is apparent from the plots included in Figure 5–1 that the AEUO3 and CEUO4 materials, which both contain large amounts of metal in the synthesis gel, show very similar times for crystallisation. For each of the materials prepared the samples taken from the reaction gels which are either side of the large pH increase were analysed by XRPD. In each case, the sample with the low pH value showed only the onset of crystallisation with $\leq$10% crystallinity observed. However, the samples examined after the pH rise were deemed to be 100% crystalline by XRPD. Hence these plots of pH against crystallisation time all show the low pH region were nucleation occurs and then the sharp increase in pH associated with the crystallisation process with the pH value then stabilising as the metastable solid phase is in a state of equilibrium with the mother liquor. The pH value remains high in the MFI syntheses; however, a decrease in pH is observed in the EUO syntheses associated with the consumption of free base in the organic degradation process already described.

Since AEUO3 and CEUO4 show such similar times for crystallisation, it can be proposed that Ga and Al can be readily incorporated into the EUO structure.

Comparison of the CEUO1 and CEUO4 pH plots shows that the CEUO1 material has crystallised after a much shorter time than the CEUO4 material. This was as expected as it is well known that increasing the metal content of a reaction gel increases the time required for crystallisation [3, 215, 96].

To obtain semi-quantitative information on the relative times required for crystallisation of the EUO aluminosilicate and EUO gallosilicate sieves, plots of the number of moles of metal oxide in the synthesis gel (x) against 1/(crystallisation time) were made. Figure 5–2 includes the plots for the AEUO series, CEUO series and a combined plot which includes both data sets. The extended symbols used represent the range of time during which crystallisation occurred. The solid symbol represents the point in the reaction where crystallisation was deemed to be complete, as determined by XRPD analysis of the solid sample withdrawn from the autoclave, and the top end of the *bar* is the point where crystallisation was deemed to begin (again as determined by XRPD of the solid sample). Since the sample which corresponds to the solid symbol was deemed to be 100% crystalline by XRPD and the sample which is represented by the top of the *bar* was $\leq$10% crystalline, it is reasonable to assume that the actual time that 100% crystallinity was achieved was nearer the solid symbol than the top of the *bar*. However, it is accepted that crystallisation could have been completed at any point during the time interval represented by these bars. Even from these rather qualitative plots it is clear that increasing the metal content of the reaction gel increases the crystallisation time. This is well known [3] and may be attributed to the disruptive effect of incorporating Al or Ga into the zeolite framework where the Al-O and Ga-O bonds are longer than the Si-O bonds. This effect can also be explained as a steric ordering effect where specific geometries of reactant species are required before the larger metals can be incorporated into the sieve framework [215]. Comparison of both these plots of 1/(crystallisation time) against metal oxide content of the gel (x) for the A and C series of EUO materials is shown in Figure 5–2 c). The EUO gallosilicates appeared to crystallise after a time similar to that of the analogous

Figure 5–1: Plot of pH versus reaction time (hr) for some of the EUO preparations, a) AEUO3, b) CEUO4 and c) CEUO1.

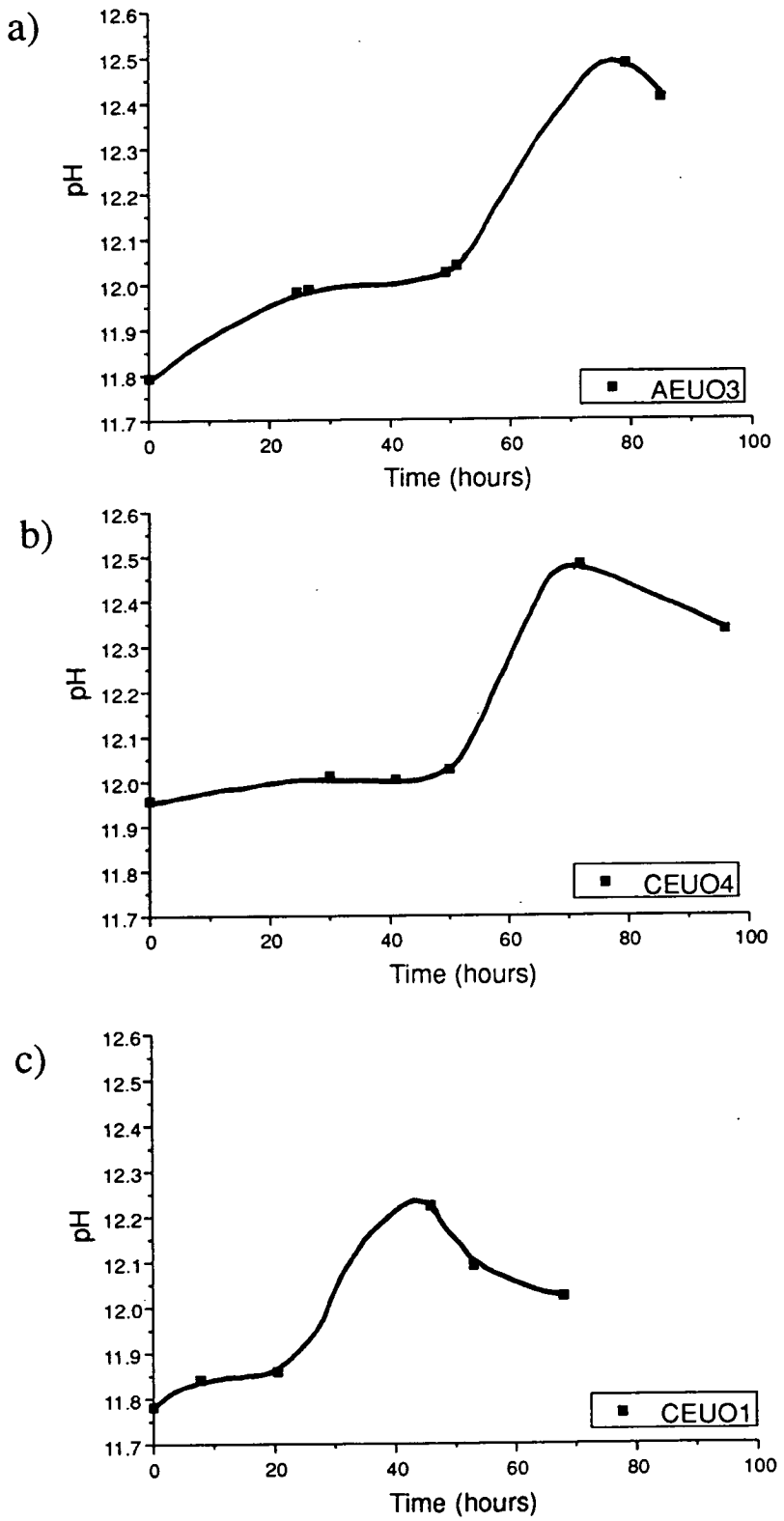

Figure 5–2: Plots of 1/crystallisation time (hr^{-1}) versus moles of metal oxide (x) in the gel (60 SiO_2 + xM_2O_3 + 10 $HexBr_2$ + 10Na_2O + 3000H_2O) for, a) AEUO materials, b) CEUO materials and c) both AEUO and CEUO materials.

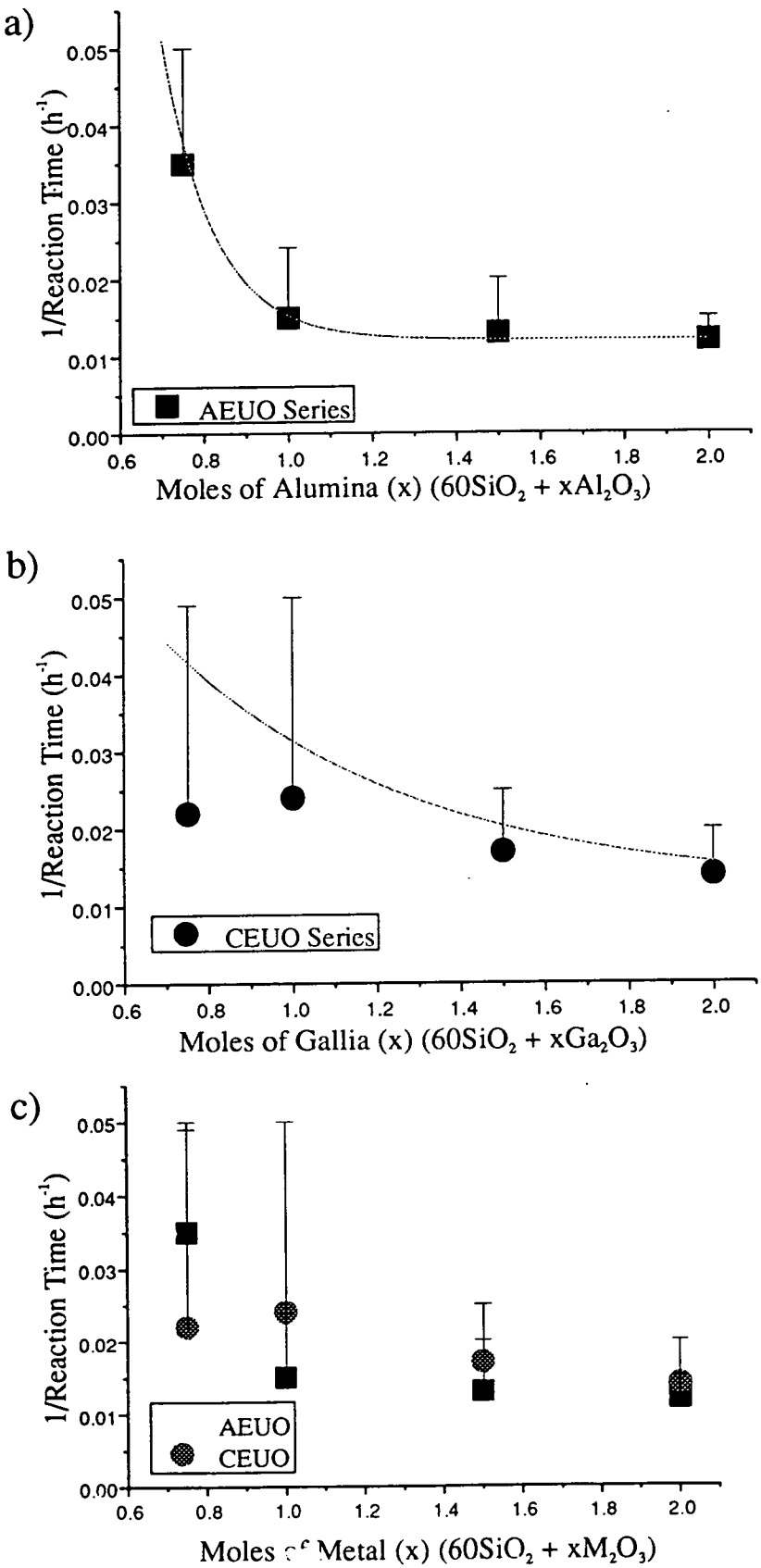

aluminosilicates.The first sample to be confirmed as 100% crystalline by XRPD was consistently after a shorter reaction time for the C series [Ga,Si]-EUO of materials than the analogous A series [Al,Si]-EUO. This is not completely obvious for the AEUO1 and CEUO1 materials because the samples taken for the CEUO1 preparation were after longer reaction times than desired. The sample which shows the CEUO1 crystallisation to be complete was withdrawn from the autoclave later then had been intended and so the end-point of crystallisation had been poorly determined for this particular sample. This range of crystallisation times for CEUO1 shown in Figure 5–2 c) extends below that for the AEUO1 material, however, it is reasonable to suggest that the trend for gallosilicate EUO materials to crystallise faster than the aluminosilicate EUO materials does hold. This suggests that the EUO structure form readily from a reaction gel which contains gallium.

Figure 5–3 shows typical pH against reaction time plots for some of the MFI materials prepared. These highlight the expected slowing of crystallisation with increasing metal content.

MFI gallosilicate materials are well known to take much longer to crystallise than there aluminosilicate analogues [96]. This was not readily detected during this series of MFI syntheses because the crystallisation conditions were such that all the MFI materials were formed during the first few hours of the preparation and since sampling was carried out after relatively large time intervals, accurate determination of the end-point of MFI crystallisations was not obtained. Hence, the reported slowing of gallosilicate MFI formation compared to the aluminosilicate MFI formation was not observed.

5.3 ^{71}Ga NMR

The ^{71}Ga NMR presented in this work was carried out on the SERC service instrument at UMIST, with only a limited time available to this work. This has resulted in an incomplete study of the gallosilicate materials prepared in this work. Samples have been submitted for analysis over a three year period and so a coherent

Figure 5–3: Plot of pH versus reaction time (hr) for some MFI preparations, a) CMFI1 and b) CMFI3

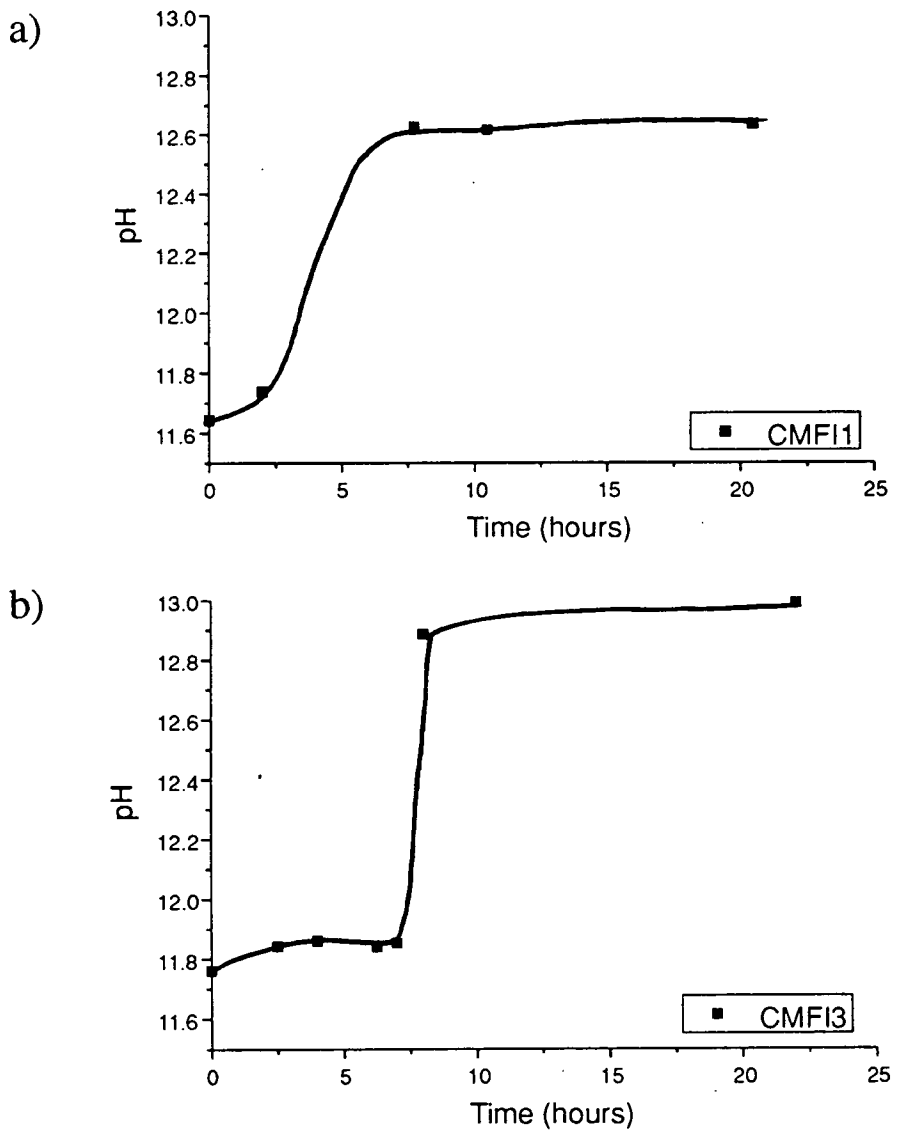

examination of a range of materials has not been achieved. This was partially due to the difficult nature of the ^{71}Ga NMR experiment and consistency in experimental parameters was not possible. Nevertheless, some interesting and valuable results did emerge. No quantitative information was extracted from the spectra obtained since the relative peak heights of the tetrahedral and octahedral gallium species are not necessarily indicative of the relative amounts of these species present. Consequently, ^{71}Ga NMR has been used purely on a qualitative basis in this work.

Material D2 ([Ga,Si]-EUO) was examined in its as-made form, calcined form and also after extreme thermal treatments which included calcination at 873 K for 16 hours followed by a further 16 hour treatment under flowing H_2 at 823 K. The spectra obtained for the as-made and extensively treated samples are shown in Figure 5–4. This clearly shows that there is a degree of gallium ejection from the EUO framework. However, this was only observed after extended calcination and reduction treatments under extremely severe conditions. Simple calcination did not result in significant levels of gallium ejection from the EUO framework.

The C series of EUO and MFI materials could not be extensively investigated because of the time restrictions described, however, some materials were examined and are included in Figures 5–5 and 5–6.

These studies clearly indicate that the as-made gallosilicate materials contain only tetrahedrally coordinated gallium species, with a signal at ≈150 ppm. The lack of signal at ≈0 ppm suggests that no octahedral gallium species are present in the as-made samples. Hence, the ^{71}Ga NMR studies of the gallosilicate EUO and MFI materials confirm that the gallium is incorporated into the molecular sieve framework. The as-made EUO and MFI materials which were examined all show only tetrahedral gallium to be present, however, as described previously, octahedral gallium species are notoriously difficult to observe because of the severe peak broadening associated with the quadrapolar interactions. Octahedral gallium species have only been observed after the gallosilicate EUO sample was exposed to extended and severe thermal treatments (D2, Figure 5–4).

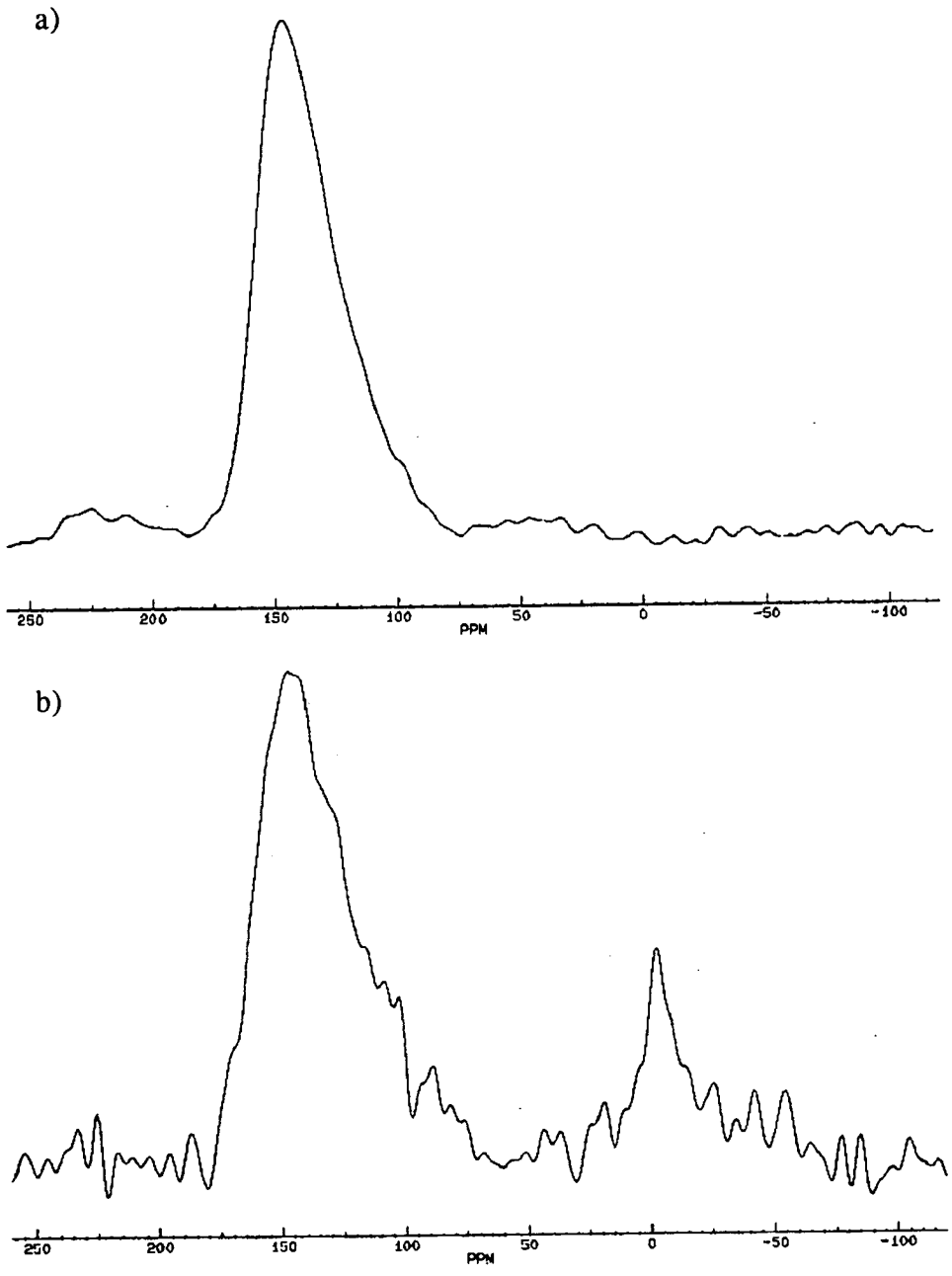

Figure 5–4: ^{71}Ga NMR of a) as-made D2 [Ga,Si]-EUO and b) extensively treated D2.

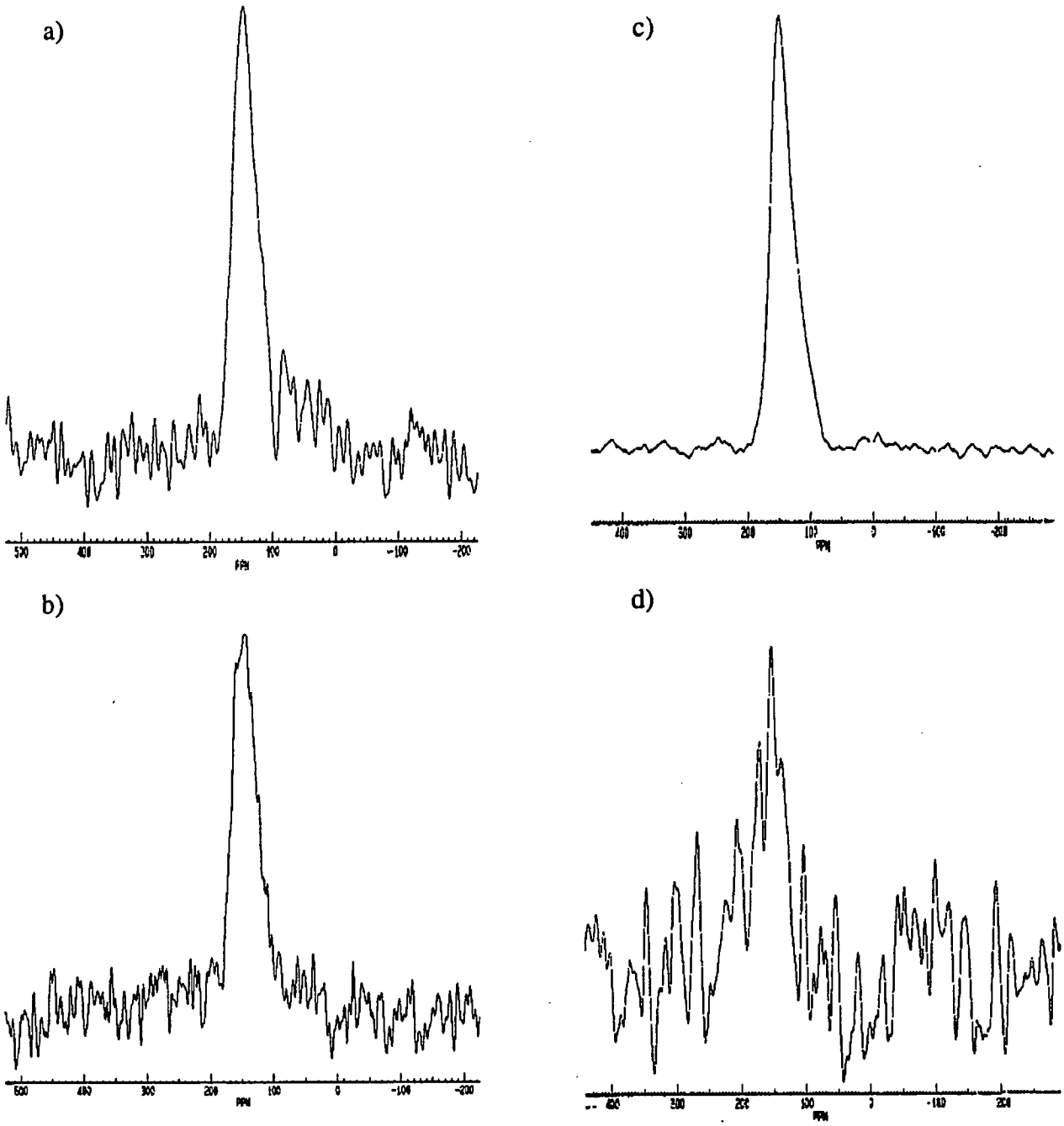

Figure 5–5: ^{71}Ga NMR of a) as-made CEUO1, b) as-made CEUO2, c) as-made CEUO3 and d) calcined CEUO3.

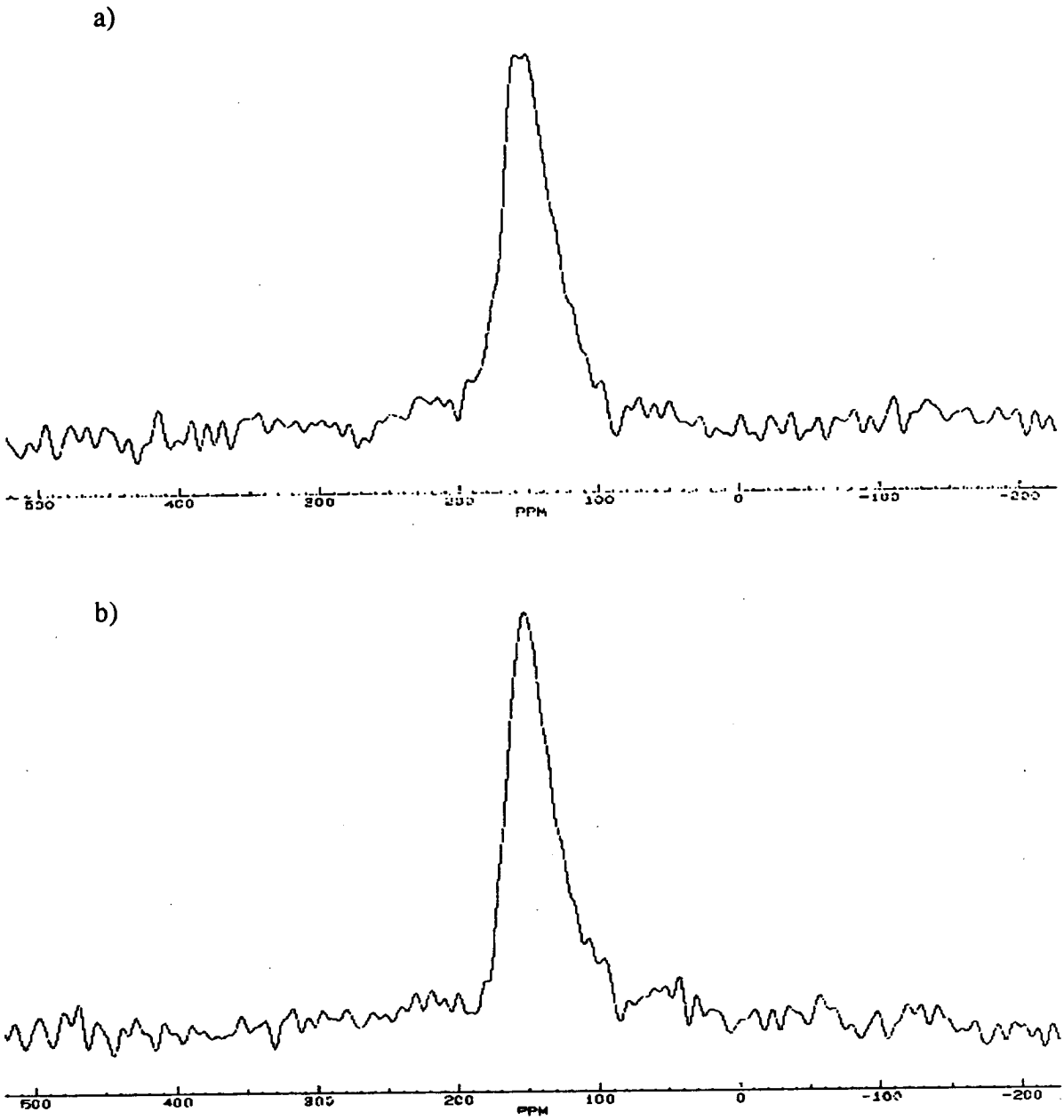

Figure 5–6: ^{71}Ga NMR of a) as-made CMFI1 and b) as-made CMFI3.

5.4 Unit Cell Volumes

The NCRVAX Crystal Structure System PPLP (Powder Pattern Lattice Parameters) software was used to refine the lattice parameters for the A and C series of molecular sieves from their XRPD patterns. The package allowed indexing of observed patterns and used a least squares routine to derive improved lattice parameters from a suitable starting data set. The initial lattice parameters and the peak indexing were obtained from the collection of molecular sieve XRPD patterns [151].

PPLP required the wavelength of radiation used (Cu K_α = 1.5418 Å), Laue group of the crystallites (3 for both the MFI and EUO crystallites in the orthorhombic habit) and the starting cell parameters (a, b, c, α, β, γ). Any systematic absences expected in the pattern from these materials were also required (2 for the Pnma of MFI and 3 for the Cmma of EUO) [65].

The refinements were carried out on XRPD patterns of both as-made and calcined samples, which had been internally referenced to the Si peaks at 28.47 ° 2θ and 47.3 ° 2θ. The unit cell parameters obtained for the MFI materials in their as-made and calcined forms are tabulated along with literature values in Tables 5–3 and 5–4. Similar unit cell analyses for the as-made and calcined EUO series of molecular sieves are included in Tables 5–5 and 5–6.

Extremely simplified theoretical unit cell volumes can be calculated for the framework structures relative to an all-silica analogue *i.e.*

$$\frac{\text{Number of Si + Number of Metal (Al/Ga)atoms}}{\text{Number of T} - \text{atoms per unit cell}}$$

By using the number of metal atoms per unit cell determined by bulk XRF analysis, 96 T-atoms in a unit cell of MFI and 112 for EUO and assuming ionic radii of 0.40Å for Si^{4+}, 0.53Å for Al^{3+} and 0.61Å for Ga^{3+}, theoretical unit cell volumes relative to all-silica frameworks were calculated and are shown in Tables 5–1 and 5–2. The theoretical expansion is greater for the MFI sieves than the EUO sieves

Table 5–1: Theoretical Unit Cell Volumes for the MFI materials.

Sample	Unit Cell Vol. Expansion
All-silica	1.000
AMFI1	1.015
AMFI2	1.021
AMFI3	1.027
AMFI4	1.027
CMFI1	1.022
CMFI2	1.030
CMFI3	1.038
CMFI4	1.044

as would be expected since there are a maximum of 8 metal atoms in a total of 96 T-atoms in MFI compared with 8 metal atoms out of 112 T-atoms in EUO and so their presence has a proportionally larger effect on the unit cell volumes of the MFI materials than the EUO materials. The potential unit cell volume expansions are small, maximum expansions of ≈2.7% for AMFI4 and ≈4.4% in the CMFI4 material compared to ≈2.3% for AEUO3 and ≈3.8% for CEUO3. Hence the substitution of Ga/Al into the molecular sieve framework is expected to cause a small but observable unit cell expansion. However, these assumptions would only hold true if the metal species were incorporated into the framework structure and not simply occluded extra-framework species.

The tabulated theoretical unit cell volume expansions are much larger than the observed expansions; however, this was not unexpected as the model used to obtain the theoretical expansions was extremely simplified and took no account of the metal atom sites and packing. In the framework structure the T-atoms are offset from each other and so the increase in size of the Ga/Al species compared to the Si atoms is not directly translated into a unit cell expansion.

Figure 5–7 a) shows that there is an approximately linear unit cell expansion for the aluminosilicate series of MFI materials in both their as-made and calcined

Table 5–2: Theoretical Unit Cell Volumes for the EUO materials.

Sample	Unit Cell Vol. Expansion
All-silica	1.000
AEUO1	1.008
AEUO2	1.015
AEUO3	1.022
AEUO4	1.023
CEUO1	1.012
CEUO2	1.023
CEUO3	1.033
CEUO4	1.038

Table 5–3: Unit Cell parameters refined for the XRPD data of the as-made MFI materials by, PPLP software.

Sample	a (Å)	b (Å)	c (Å)	unit cell vol. (Å^3)
ZSM-5[a]	20.1	19.9	13.4	5360
AMFI1	20.050±0.007	19.940±0.007	13.420±0.005	5365±5
AMFI2	20.015±0.009	19.968±0.009	13.424±0.006	5365±6
AMFI3	20.128±0.006	19.968±0.006	13.454±0.004	5407±5
AMFI4	20.168±0.010	20.036±0.010	13.485±0.007	5440±6
CMFI1	20.080±0.006	19.967±0.006	13.456±0.004	5395±4
CMFI2	20.049±0.009	19.997±0.009	13.440±0.006	5402±6
CMFI3	20.051±0.007	19.957±0.007	13.450±0.005	5382±4
CMFI4	20.052±0.009	19.980±0.009	13.441±0.006	5385±4

[a] data taken from [23]

Table 5–4: Unit Cell parameters refined for the XRPD data of the calcined MFI materials by, PPLP software.

Sample	a (Å)	b (Å)	c (Å)	unit cell vol. (Å^3)
ZSM-5[a]	20.1	19.9	13.4	5360
AMFI1	20.090±0.006	19.943±0.006	13.416±0.004	5375±5
AMFI2	20.056±0.010	20.056±0.010	13.418±0.007	5398±8
AMFI3	20.164±0.006	20.005±0.006	13.482±0.004	5439±5
AMFI4	20.214±0.007	20.010±0.007	13.465±0.005	5446±6
CMFI1	20.138±0.005	19.961±0.005	13.436±0.003	5401±5
CMFI2	20.155±0.010	20.018±0.010	13.436±0.007	5420±8
CMFI3	20.112±0.005	19.981±0.005	13.374±0.003	5375±5
CMFI4	20.163±0.005	20.022±0.005	13.420±0.003	5418±5

[a] data taken from [23]

Table 5–5: Unit Cell parameters refined for the XRPD data of the as-made EUO materials by, PPLP software.

Sample	a (Å)	b (Å)	c (Å)	unit cell vol. (Å^3)
EU-1[a]	13.7	22.3	20.2	6171
AEUO1	13.657±0.006	22.278±0.009	20.167±0.008	6113±7
AEUO2	13.700±0.005	22.278±0.009	20.284±0.008	6191±7
AEUO3	13.718±0.006	22.228±0.010	20.336±0.009	6201±7
AEUO4	13.744±0.007	22.341±0.012	20.430±0.011	6273±8
CEUO1	13.719±0.007	22.299±0.011	20.295±0.010	6209±8
CEUO2	13.720±0.005	22.322±0.008	20.369±0.007	6238±8
CEUO3	13.760±0.005	22.347±0.008	20.416±0.007	6278±8
CEUO4	13.761±0.005	22.359±0.008	20.430±0.007	6286±9

[a] data taken from [23]

Figure 5–7: Plot of unit cell volumes for a) as-made and calcined AMFI materials and b) as-made and calcined CMFI materials.

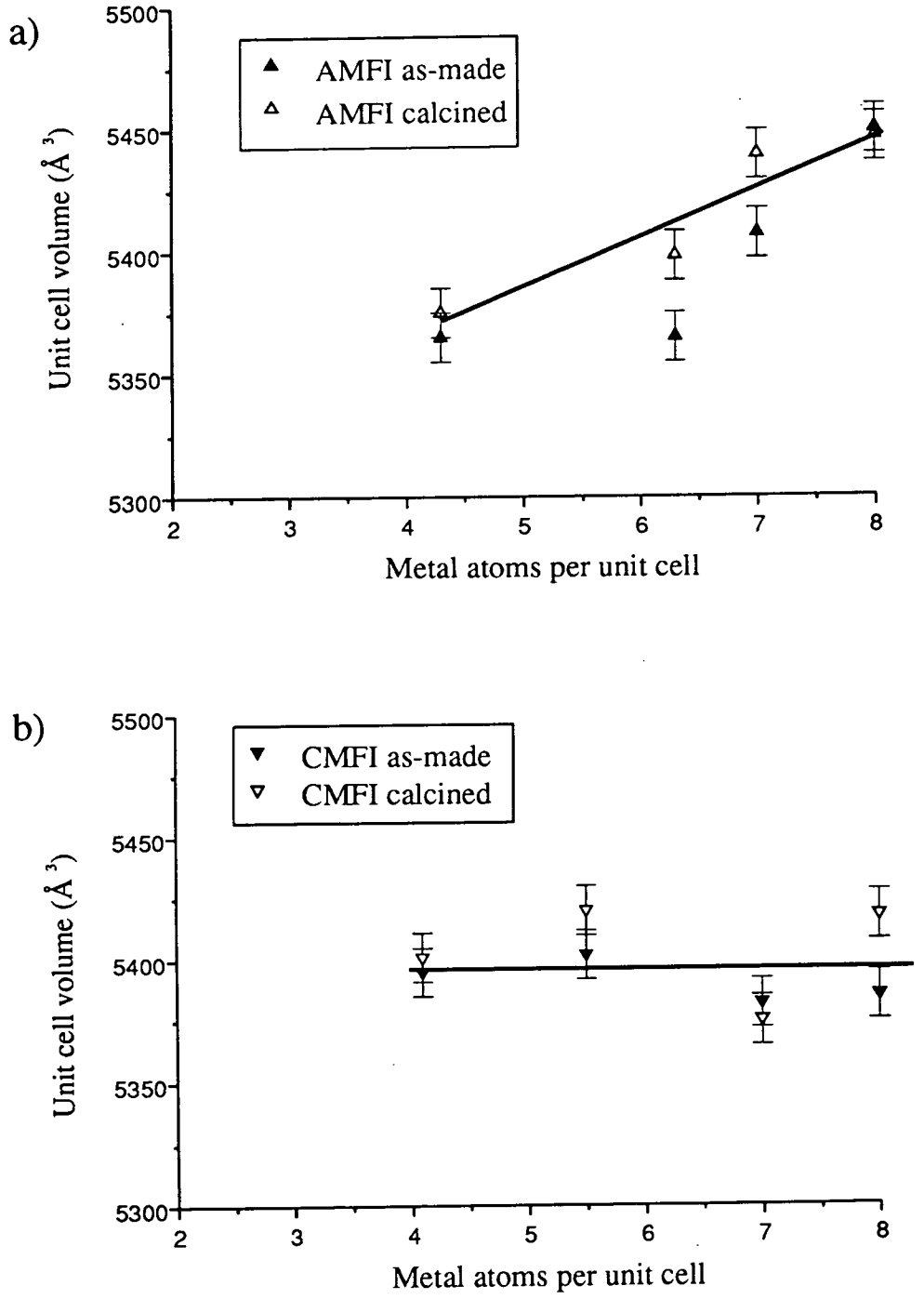

Table 5–6: Unit Cell parameters refined for the XRPD data of the calcined EUO materials by, PPLP software.

Sample	a (Å)	b (Å)	c (Å)	unit cell vol. (Å^3)
EU-1[a]	13.7	21.5	20.1	6171
AEUO1	13.705±0.005	22.241±0.007	20.067±0.007	6117±5
AEUO2	13.698±0.005	22.272±0.008	20.124±0.007	6140±5
AEUO3	13.679±0.005	22.310±0.008	20.141±0.008	6147±5
AEUO4	13.697±0.005	22.328±0.008	20.189±0.007	6174±7
CEUO1	13.691±0.005	22.280±0.006	20.134±0.007	6142±5
CEUO2	13.706±0.004	22.304±0.006	20.170±0.005	6166±7
CEUO3	13.730±0.008	22.321±0.012	20.163±0.011	6179±9
CEUO4	13.712±0.010	22.419±0.017	20.215±0.015	6215±9

[a] data taken from [23]

forms. This suggest that the ZSM-5 materials prepared did allow ready incorporation of Al into tetrahedral framework sites and that the Al remained in the framework after the calcination of the AMFI materials. However, Figure 5–7 b) shows the gallosilicate (C series) of MFI materials to all show an approximately constant unit cell volume, regardless of the metal content of the sample. This suggests that the gallium was less readily incorporated into the MFI framework. The residual gallium species are not incorporated into the framework but occluded in the channels and cavities or deposited on the external surface of the crystallites. This observation can be rationalised in terms of the metal being less readily incorporated into the framework after the the 4 TPA^+ species are already associated with framework charges. This suggests that Ga can be readily incorporated into the MFI framework while it is associated with the organic charge balancing species; however, when the framework charge would be countered by a sodium ion, the gallium is less stabilised in the framework and so is not readily incorporated. These observations are more clearly represented in Figure 5–8 where the comparison of the as-made A and C series of sieves is represented in Figure 5–8 a) and the calcined A and C series in b). These plots show that for both the as-made

and calcined materials the aluminosilicate (A series) unit cell volumes increase with increasing metal content whereas the gallosilicate MFI sieves (C series) remain around a constant unit cell volume which indicates that some of the gallium incorporated does not occupy framework sites but is present as extra-framework species occluded in the void space or supported on the external surface of the crystallite agglomerates. This is in excellent agreement with the suggestion that gallium can be incorporated into the MFI structure but is readily ejected from these framework positions by thermal treatments [3].

Figure 5–9 shows the plots of unit cell volume for the A and C series of EUO preparations with the materials in their as-made form plotted in Figure 5–9 a) and in their calcined form in 5–9 b). These both show a clear linear relationship between unit cell volume and metal content with an increase in unit cell volume observed with increasing metal content. The as-made materials (both aluminosilicates and gallosilicates) have larger unit cell volumes than their analogous calcined materials. This was expected since the as-made EUO materials have occluded organic species which force the framework structure to expand slightly. After calcination, with the decomposition and removal of the organic species, this strain is removed and allows the unit cell to relax and contract slightly. Upon calcination both the AEUO and CEUO series show the expected contractions in the unit cell volumes associated with this removal of the occluded organic species from the intracrystalline void space.

Figure 5–10 a) compares the as-made A and C series of EUO preparations and 5–10 b) shows the analogous calcined materials. The direct relationship between unit cell volume and metal content is clearly represented with the gallosilicate materials (C series) having consistently larger unit cell volumes than the aluminosilicate materials (A series). This was expected since the Ga^{3+} species (0.61Å) is significantly larger than the Al^{3+} species (0.55Å) and confirms the suggestion that these metal species are incorporated into tetrahedrally coordinated framework sites.

Figure 5–10 b) indicates that after calcination the gallosilicate materials still have larger unit cell volumes than the analogous aluminosilicate materials. This

Figure 5–8: Plot of unit cell volumes for a) as-made AMFI and CMFI materials and b) calcined AMFI and CMFI materials.

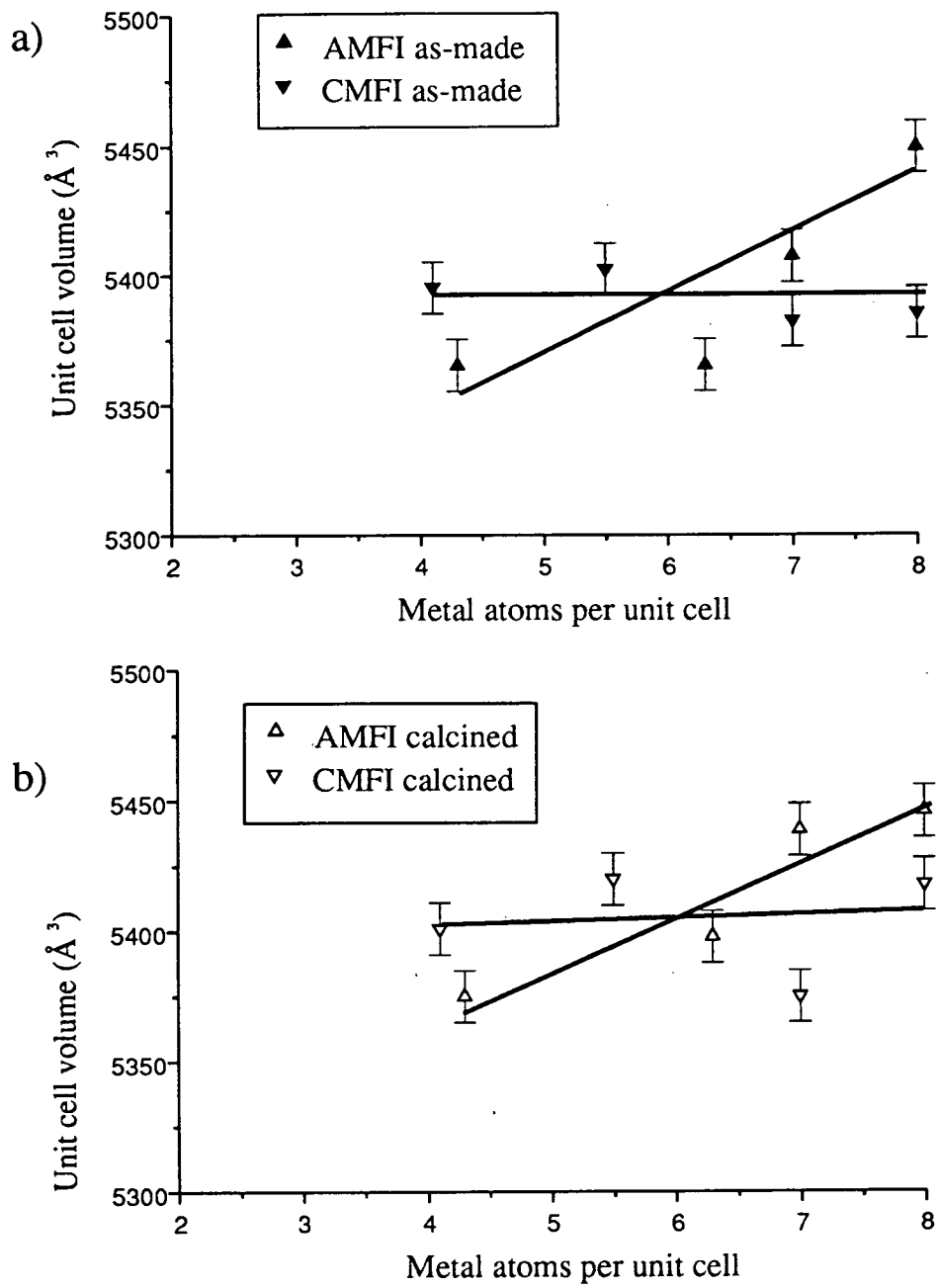

Figure 5–9: Plot of unit cell volumes for a) as-made and calcined AEUO materials and b) as-made and calcined CEUO materials.

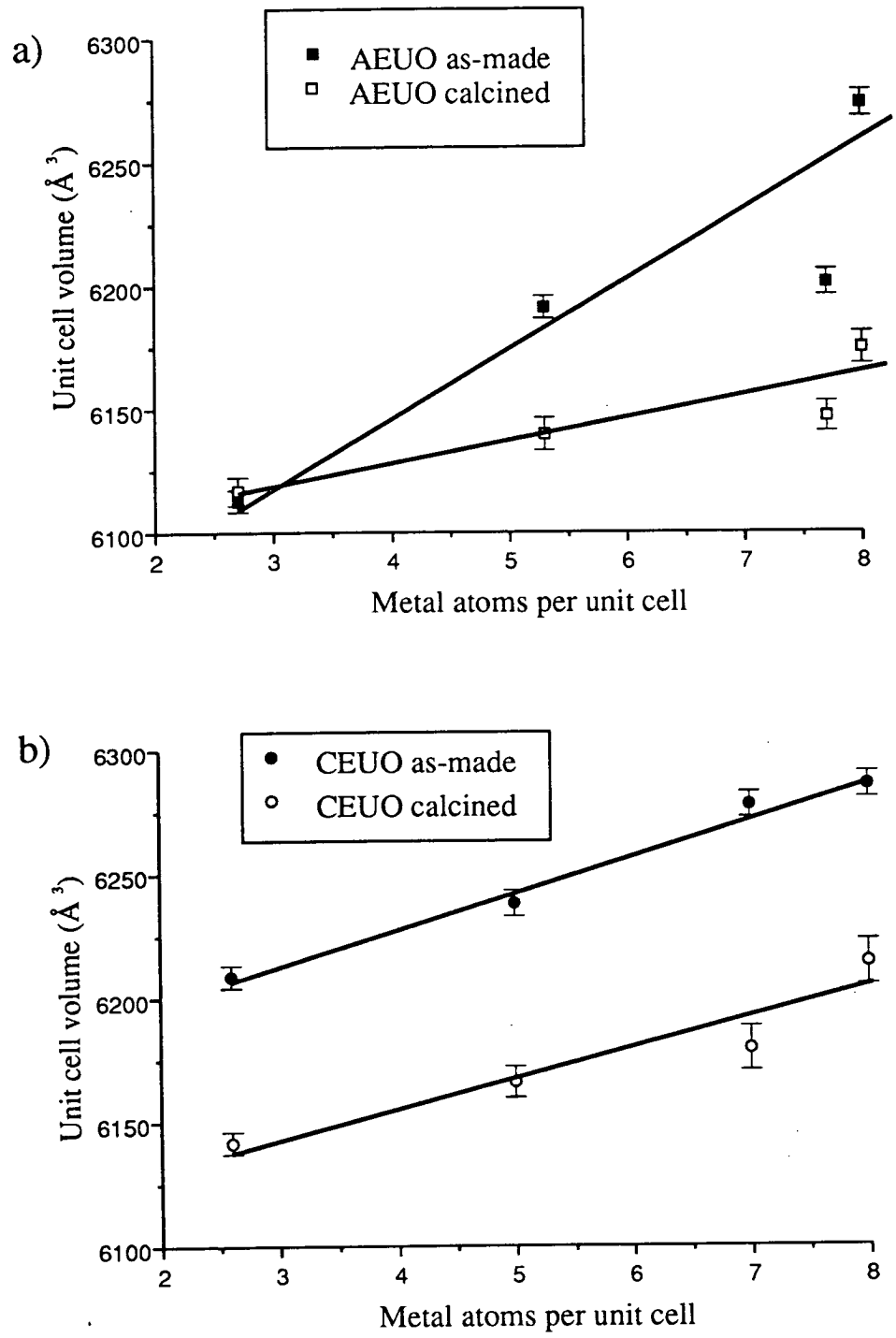

suggests that there is very little or no metal ejection from the EUO framework structure, unlike the MFI framework where the framework metal species appear to be less readily retained.

This approach to determining the fate of the metal species in the molecular sieves prepared has suggested that the qualitative analyses from ^{71}Ga NMR may not be completely conclusive. These unit cell volume analyses have suggested that there is likely to be extra-framework metal species in the molecular sieves which have more than 4 metal atoms per unit cell. This effect is particularly apparent for the CMFI materials which showed poor framework incorporation of Ga^{3+} above a level proposed to be, 4 metal atoms per unit cell. However, the EUO materials readily supported up to 8 metal atoms per unit cell. This suggests a correlation between the stabilised substitution into tetrahedral framework sites and the amount of occluded organic material. Since it is possible for all 8 metal atoms per unit cell in EUO to be associated with positive charges associated with the diquaternary amine (Hex^{2+}), this appears to offer increased stability and more ready incorporation of metals into the EUO framework structure. This is apparent from the analysis of calcined EUO materials which show very little ejection of gallium from the framework sites. This is in agreement with the ^{71}Ga NMR analyses which suggested that it was relatively difficult to obtain extra-framework gallium species from gallosilicate EUO materials by simple calcination. However, for the MFI materials the maximum number of framework metals which can be associated with charge on an organic amine (TPA^{+}) is 4 and at gallium levels greater than this there appears to be less facile framework substitution and more ready ejection of gallium from the framework upon calcination.

Gallosilicate Analcime

The analcime impurity detected in the MFI molecular sieves with higher metal concentrations in the synthesis gels were also examined using the PPLP package to investigate the analcime unit cell in the aluminosilicate and gallosilicate preparations. The cell parameters for the cubic ANA structure are shown in Table 5–7.

Figure 5–10: Plot of unit cell volumes for a) as-made AEUO and CEUO materials and b) calcined AEUO and CEUO materials.

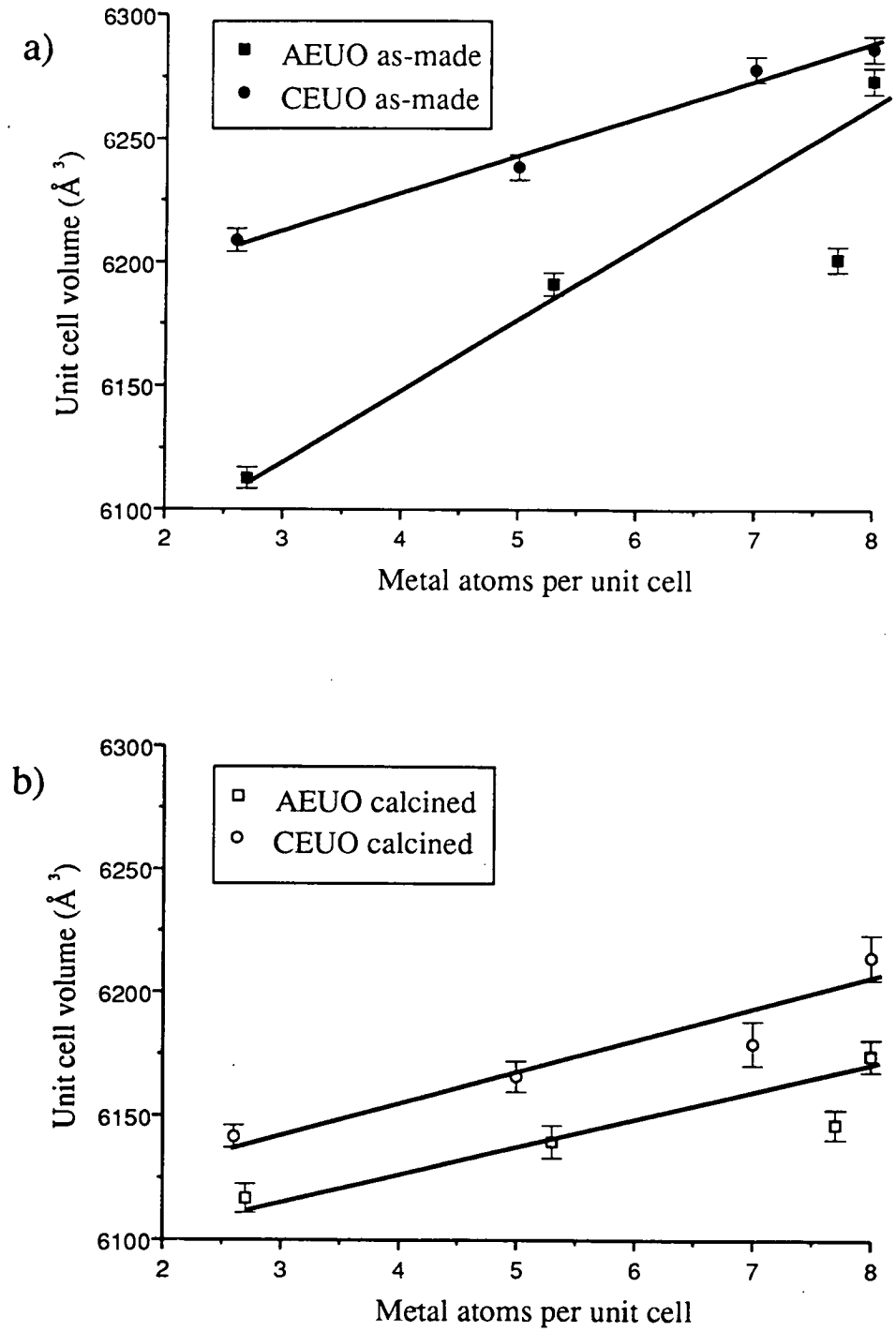

Table 5–7: Unit Cell parameters refined from the XRPD data of analcime (ANA) impurities found in the MFI syntheses with the highest metal contents in the synthesis gels, by PPLP software.

Sample	a = b = c ($\AA$)	unit cell vol.($\AA^3$)
ANA[a]	13.73	2588
AMFI4	13.748±0.004	2598 ± 3
CMFI3	13.824±0.004	2642 ± 3
CMFI4	13.877±0.007	2672 ± 3

[a] data taken from [23]

It is apparent from this that the analcime impurity phase obtained in the CMFI preparations has a significantly larger unit cell volume than that observed for the analcime (ANA) observed in the AMFI preparations. This is direct evidence for the formation of a gallosilicate form of analcime and so adds weight to the proposition that this impurity phase is a metal atom sink in the crystallisation process. It is believed that this is the first report of the preparation of a gallosilicate analcime phase.

5.5 X-ray Photoelectron Spectroscopy (XPS)

A representative set of scan envelopes for the regions of interest from sample CMFI4, after calcination, are included in Figure 5–11. These scan envelopes are typical of those observed for the gallosilicate materials examined and so similar envelopes are not included for the other gallosilicate materials. However, all the analysis details for the gallosilicate (C) series of EUO and MFI materials are included at the end of this section in Tables 5–12 to 5–25. The scan region included in Figure 5–11 show the Shirley fitting procedure used to determine the peak areas for quantitative analyses and also the potential gallium contamination of the silicon analyses, highlighted in the Figures 5–11 d) and e). To aid the subtraction of these contaminant signals, the areas of these gallium signals were predicted using the

relative Schofield sensitivity factors and the area of the Ga $2p_{3/2}$ signal at around 1118eV.

It is the close proximity of the Ga 3d and O 2s signals which makes their use in compositional analysis through different depths applicable to this work. A typical *scan envelope* is included in Figure 5–12 a). This shows the Ga 3d region for the as-made and calcined CMFI1 samples. The apparent appearance of a small contribution from the Na 2p signal at ≈31eV was noted and could be rationalised as the migration of occluded sodium species, originally present as charge balancing species, to the external surface of the crystallites to form a Na_2O type species. However, this appearance of the Na 2p signal was not observed for all the materials examined upon calcination and was observed for some as-made materials. Consequently this feature has been proposed to be associated with sample surface contamination from handling rather than a feature of the materials themselves.

Figure 5–12 b) shows the O 1s *scan envelope* and it is clear that upon calcination there is an O 1s contribution at a slightly higher binding energy of ≈534 eV which can be assigned to an OH type species [117, 210]. These would be formed by the ejection of gallium from the framework on calcination to leave a hydroxyl nest. Such a feature has been observed for all the CMFI materials and can be correlated with the appearance of a second feature at a lower binding energy (≈ 1118 eV) in the Ga $2p_{3/2}$ scan which can be suggested as a contribution from an extra-framework gallium species. As gallium is ejected from the framework it would leave an *hydroxyl nest* which contains 4 OH groups and so the emergence of such a signal was expected.

The ratios of Ga $2p_{3/2}$: O 1s and Ga $2p_{3/2}$: Si 2s represent quantitative evaluation of the *surface* composition of the crystallites. The Ga 3d : O 2s ratio represents a quantitative estimate of the *near-surface* Ga : O ratio averaged through a slightly greater volume of the crystallites. This difference in analysis depths is a direct consequence of the extremely large differences in the E_k of the photoelectrons from the Ga $2p_{3/2}$ and 3d levels. These have been proposed to represent analysis depths of ≈10nm and ≈25nm respectively, described in more detail in

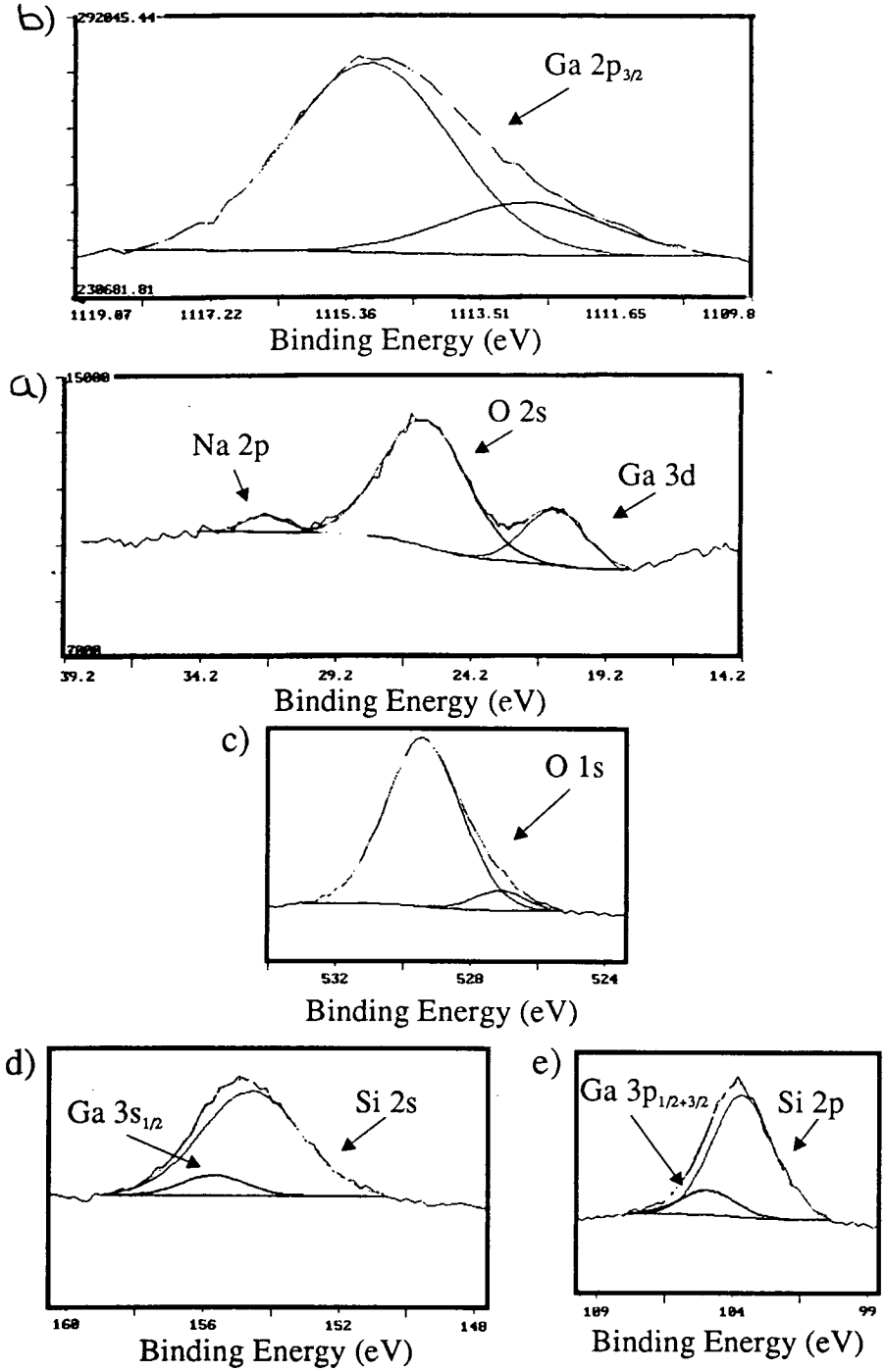

Figure 5–11: Representative scan envelopes for the regions of interest for the calcined sample CMFI4; a) low B.E., *i.e.* high E_k signals used to determine *near-surface* compositions, b) main gallium region, c) main oxygen region, d) and e) main silicon regions.

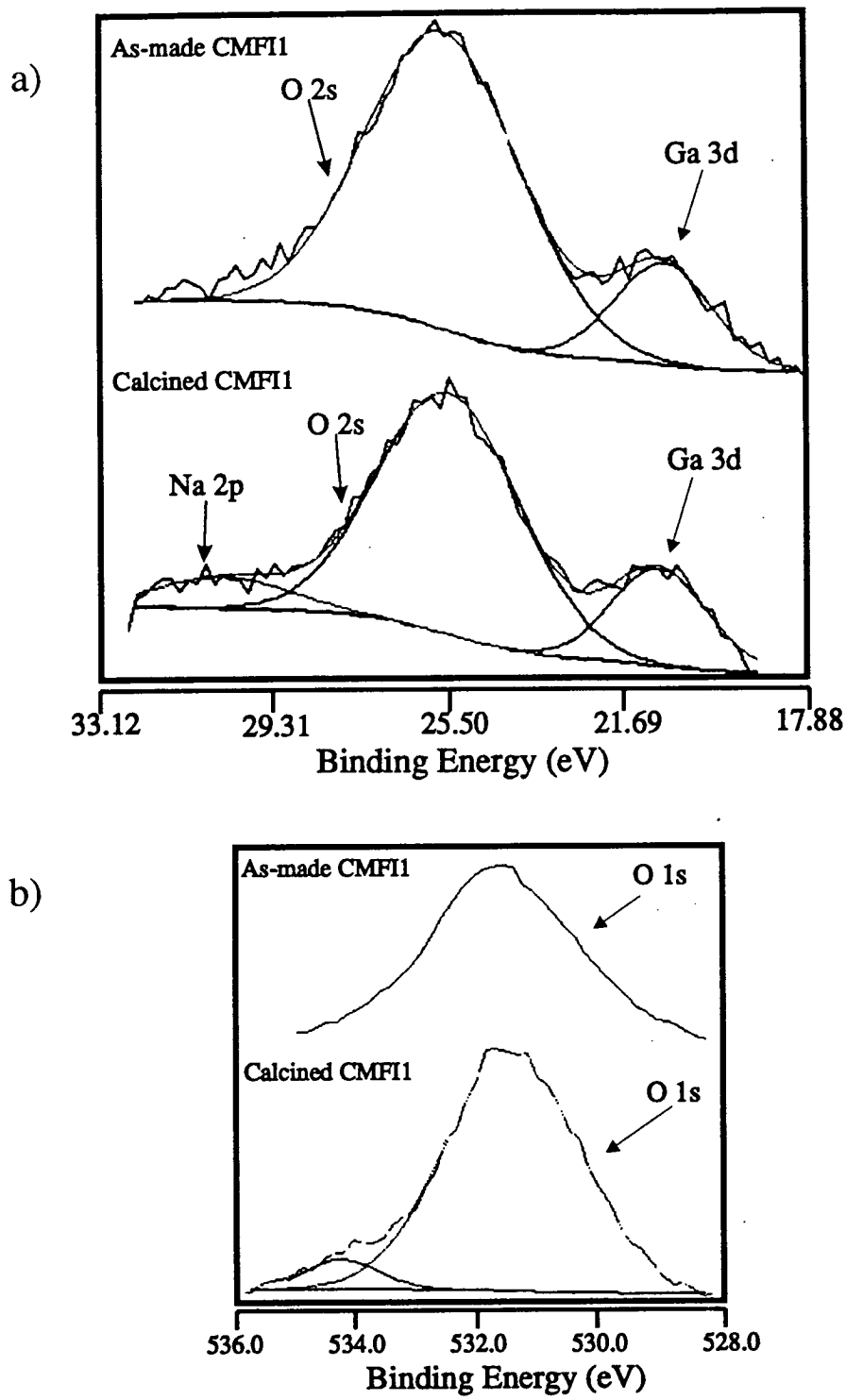

Figure 5–12: *Scan envelopes* for the a) Ga 3d, O 2s regions and b) the O 1s regions for the as-made and calcined CMFI1 samples.

Chapter 3. The Ga 3d and O 2s signals are very close in energy and are analysed in the same *scan envelope*. Hence it is reasonable to assume that these signals are well matched and provide a realistic determination of the Ga : O ratio of the *near-surface* composition of the materials. Tables 5–12 to 5–25 also include quantitative estimates of Si 2p : O 2s and Ga 3d : Si 2p. However, it is obvious from the Si 2p : O 2s ratios obtained for all the materials that this approach is ineffective since a ratio of $\approx$ 0.33 Si : 0.67 O, which represents SiO_2 (the empirical formula for zeotype materials) was not observed. All the materials appeared to have a Si 2p : O 2s ratio of $\approx$ 0.5 : 0.5 which correlates with an SiO empirical formula, which is not the case for these materials. This suggests that such a depth profile, using the Si 2p signal intensity as a measure of Si content below the external surface of the crystallites was not possible for gallosilicate molecular sieves. This is as would be expected since the two Si signals which were examined were the 2p (BE$\approx$104eV) and the 2s (BE$\approx$150eV) which can be considered to have come from the same part of the sample. This has been observed to be the case with the relative areas of these two signals being equal. It is proposed that the inadequacy of this approach for the analysis of Si composition at the *near-surface* is a consequence of the nature of the Si 2p signal and its subsequent comparison to the much weaker Ga 3d and O 2s signals, rather than an intrinsic flaw in the approach. The Si 2p does not represent the same analysis volume as the Ga 3d or the O 2s photoelectrons.

Tables 5–8 and 5–9 summarise the ratios between the Si/Ga/O components of the CMFI and CEUO sieves examined, in their as-made and calcined forms respectively. The Si 2s : O 1s ratios for all the materials in their as-made and calcined forms show an empirical formula SiO_2 which is consistent with the expected analyses for such gallosilicate molecular sieves. The *surface* concentrations, determined as Ga $2p_{3/2}$: Si 2s ratios are represented in Figures 5–13 a) and b) for the CMFI and CEUO series of materials respectively.

Figure 5–13 a) shows the Ga : Si ratio of the external surface of the crystallites in their as-made and calcined forms. Also plotted are the bulk Ga : Si ratios as determined by XRF. These bulk Ga : Si ratios (determined by XRF elemental

Table 5–8: XPS analysis of as-made CEUO and CMFI materials.

Sample	Si 2s : O 1s	Ga $2p_{\frac{3}{2}}$: Si 2s	Ga $2p_{\frac{3}{2}}$: O 1s	Ga 3d: O 2s	Bulk Ga:Si
CEUO1	0.329 : 0.671	0.041 : 0.959	0.021 : 0.979	0.001 : 0.999	0.025
CEUO2	0.333 : 0.667	0.076 : 0.924	0.039 : 0.961	0.023 : 0.977	0.047
CEUO3	0.299 : 0.701	0.088 : 0.912	0.039 : 0.961	0.033 : 0.967	0.067
CMFI1	0.300 : 0.700	0.114 : 0.886	0.052 : 0.948	0.030 : 0.970	0.045
CMFI2	0.294 : 0.706	0.107 : 0.893	0.048 : 0.952	0.028 : 0.972	0.061
CMFI3	0.325 : 0.675	0.107 : 0.893	0.054 : 0.946	0.035 : 0.965	0.077
CMFI4	0.324 : 0.676	0.114 : 0.886	0.054 : 0.946	0.048 : 0.952	0.091

Table 5–9: XPS analysis of calcined CEUO and CMFI materials.

Sample	Si 2s : O 1s	Ga $2p_{\frac{3}{2}}$: Si 2s	Ga $2p_{\frac{3}{2}}$: O 1s	Ga 3d : O 2s	Bulk Ga:Si
CEUO1	0.310 : 0.690	0.065 : 0.935	0.031 : 0.969	0.033 : 0.967	0.025
CEUO2	0.309 : 0.691	0.059 : 0.941	0.028 : 0.972	0.018 : 0.982	0.047
CEUO3	0.322 : 0.678	0.074 : 0.926	0.036 : 0.964	0.036 : 0.964	0.067
CMFI1	0.328 : 0.672	0.092 : 0.908	0.047 : 0.953	0.020 : 0.980	0.045
CMFI2	0.333 : 0.667	0.048 : 0.952	0.025 : 0.975	0.020 : 0.980	0.061
CMFI3	0.296 : 0.704	0.099 : 0.901	0.044 : 0.966	0.046 : 0.954	0.077
CMFI4	0.352 : 0.648	0.074 : 0.916	0.042 : 0.958	0.043 : 0.957	0.091

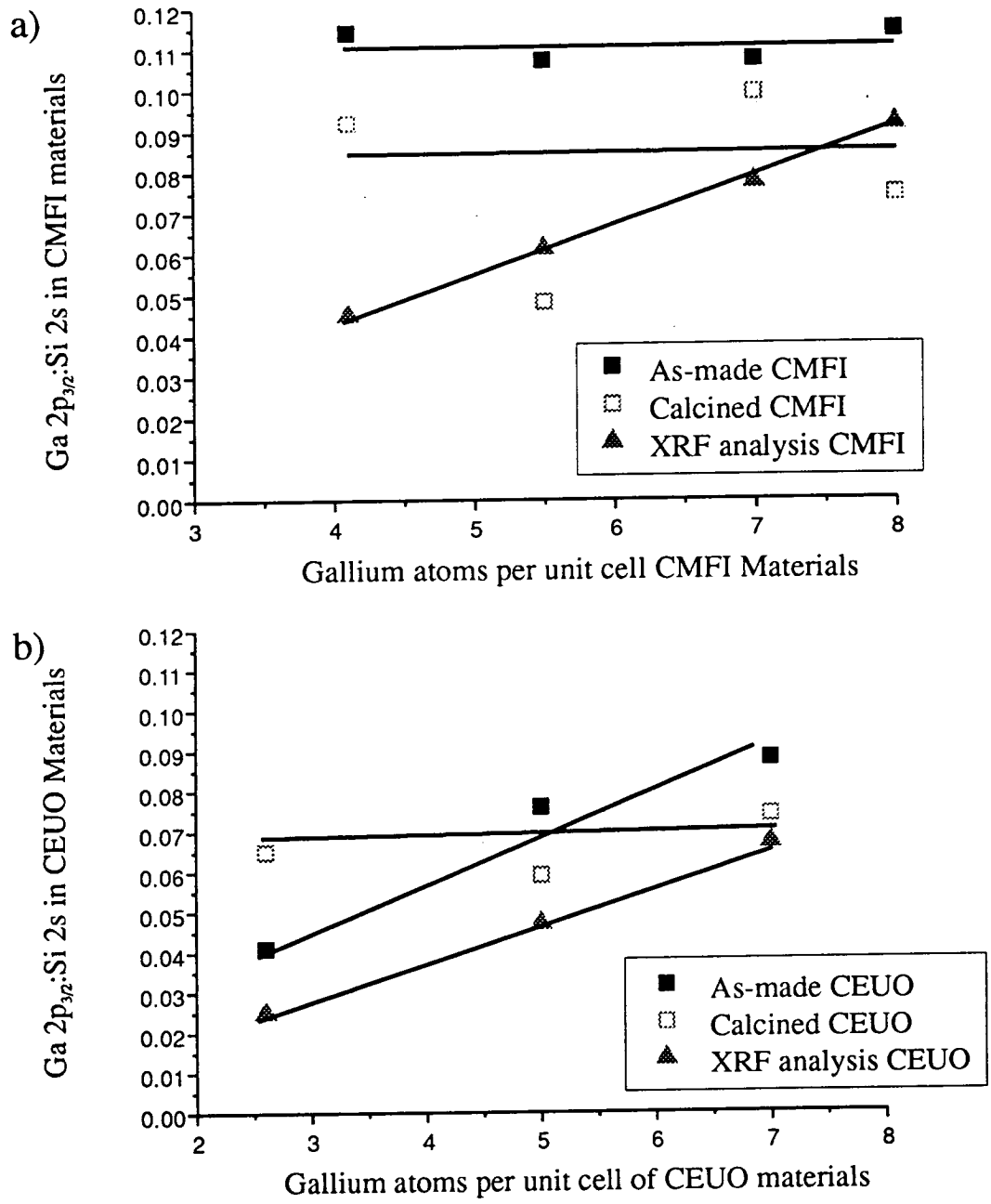

Figure 5–13: a) Ga : Si for as-made and calcined CMFI materials and bulk Ga : Si ratio (determined by XRF), b) Ga : Si for as-made and calcined CEUO materials and bulk Ga : Si ratio (determined by XRF).

analysis) increase linearly for the materials CMFI1 to CMFI4. The gallium level for the as-made materials is almost constant on the *surface* and is greater than the bulk gallium content. This suggests that each of the CMFI materials has a gallium rich crust, each with a similar composition. Since there is more gallium on the external surface than the average per unit volume of the bulk, then it can be assumed that there is a gallium concentration gradient through the samples from the gallium rich crust to a siliceous core. The calcined materials do not show such a coherent trend with a range of Ga : Si ratios observed. The largest deviation from the expected Ga : Si ratio is exhibited by the calcined CMFI2 sample. This spread of apparent gallium contents is in agreement with the suggestion that the gallium incorporated into the MFI framework structure is not very stable and can be readily ejected upon calcination. Each of the analyses for the calcined materials is lower than for the analogous as-made materials. This is rationalised in terms of the relative analysis volumes of the as-made and calcined materials. It has already been described in Chapter 3 that the analysis depth of the XPS technique is directly related to the sample matrix. The analysis volume of calcined materials would be expected to be greater than that of the as-made molecular sieves since the contribution to photoelectron attenuation by the occluded organic species would be removed. The signals detected from the as-made samples are attenuated by the occluded organic void filler material; however, for the calcined materials, this attenuation has been removed and consequently there is a greater volume analysed. It has been suggested that there is a gallium concentration gradient through the CMFI materials with the gallium level decreasing further into the crystallites and so this larger sample volume will result in less gallium per unit of volume analysed for the calcined materials. The proposition of a gallium rich crust being formed in these materials is in agreement with observations made during the original material syntheses. It was noted that there was no significant increase in the time required for crystallisation of the gallosilicate MFI materials compared to the aluminosilicate sieves. This was surprising; however, it could be proposed that the C series of MFI molecular sieves initially crystallised as a silica rich phase (similar to silicalite) with gallium incorporation achieved later in the crystallisation process when the composition of the reaction gel had altered, such

that the solid sieve was *forced* to accept gallium into the framework to continue crystal growth.

Figure 5–13 a) also highlights the feature that all the as-made materials have an external Ga : Si ratio which is greater than the maximum level that the MFI framework can accommodate (8 Ga per unit cell, equivalent to a Ga : Si ratio of 0.091). Thus it is concluded that there are extra-framework gallium species deposited on the external surface of the CMFI series of molecular sieves. This contradicts the ^{71}Ga NMR analysis which suggested that these materials contained no extra-framework (octahedral) gallium species. Figures 5–14 a) and b) confirm the proposition that the as-made CMFI materials have a gallium rich crust. The Ga $2p_{3/2}$: O 1s ratio is an analysis of only the *surface* of the crystallites and as mentioned previously shows a constant gallium level (this time with respect to the Ga : O ratio). The Ga 3d : O 2s ratio probes further into the crystallites and shows the gallium level of the *near-surface* to increase through the series CMFI1 to CMFI4. This is in agreement with the model of a gallium gradient through the crystallites. Since CMFI4 has the highest gallium content it must retain higher levels of gallium deeper into the crystallite since all the samples have a similar gallium level on the external surface of the crystallites. A similar model is observed for the calcined CMFI materials, also represented in Figures 5–14 a) and b). The same features are noted for the calcined materials with the exception of the calcined CMFI2 sample which, as has already been stated, appears to be somewhat anomalous in this study. The XPS analysis of this material was interrupted by a technical problem and although the analysis was restarted and apparently completed, it is possible that this *trip* could have led to this surprising result.

Figures 5–13 a) and b) allow comparison of the Ga:Si ratios of the *surfaces* of the CMFI and CEUO materials. Unlike the CMFI series of sieves the Ga : Si ratio of the as-made CEUO materials increases with the bulk Ga : Si ratio which suggests that the gallium is more homogeneously incorporated into the EUO framework structure than the MFI framework type. The level of gallium on the *surface* of the crystallites is again higher than the bulk Ga : Si ratio which

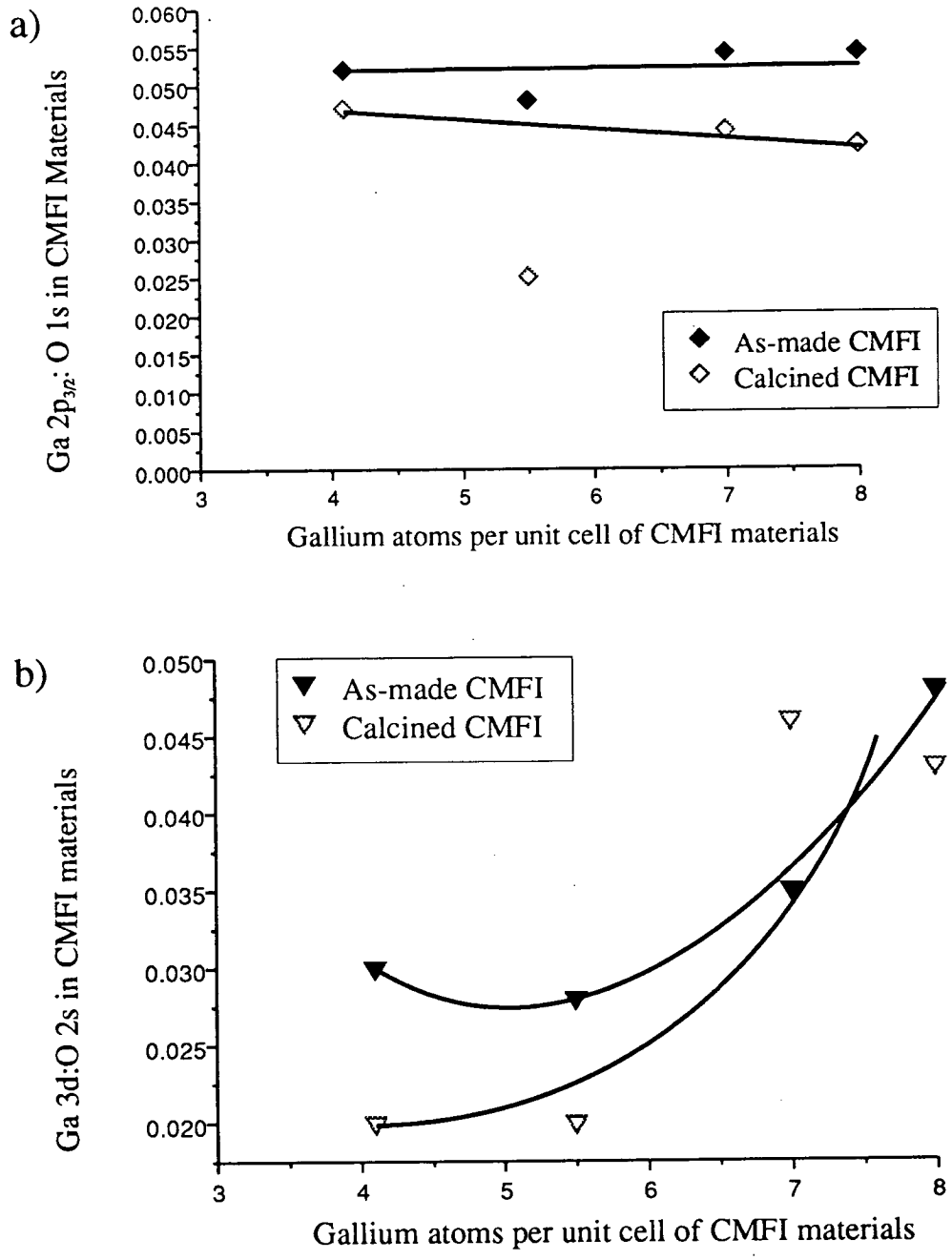

Figure 5–14: a) Ga $2p_{3/2}$:O 1s for as-made and calcined CMFI materials (analysis of *surface* of samples) and b) Ga 3d:O 2s for as-made and calcined CMFI materials (analysis of *near-surface* of samples).

again suggests the formation of a gallium rich crust with a more siliceous core. This is a model thought to be appropriate for crystallisation from such reaction gels [215]. CEUO3 apparently has more gallium at the external surface than can be incorporated into the EUO framework structure and so it is concluded that there must be some extra-framework gallium species in this sample. This disagrees with the earlier observation from ^{71} Ga NMR which suggested that there were only tetrahedrally coordinated gallium species present in these samples. The Ga : Si ratios for the calcined samples are generally less than those of the as-made samples which is in accord with the model of a gallium rich crust and a gallium gradient through the crystallites. As described previously, the occluded organic species attenuate the signal detected and so upon calcination the analysis volume is greater and the reduction in gallium concentration through the crystallites causes the detected Ga : Si ratio to be reduced for the calcined materials.

A compositional analysis through different depths of the CEUO samples, in terms of the Ga : O ratios of the as-made and calcined materials, are shown in Figures 5–15 a) and b). Here there is much closer agreement between the gallium levels on the *surface* of the crystallites and at a slightly greater depth in the *near-surface* of the crystallites. This suggests a much more homogeneous distribution of gallium species in the calcined EUO materials.

I.C.I. Prepared Catalysts

The gallium impregnated ZSM-5 material obtained from I.C.I. was examined prior to catalytic study and the sample had not experienced any thermal activation treatments. The sample of [Ga,Si]-NU-87 obtained from I.C.I. was also examined prior to any catalytic studies and the quantitative data derived from their study is included at the end of this Chapter in Tables 5–26 and 5–27. A summary of the *surface* and *near-surface* analyses for these materials is shown in Table 5–10.

The external gallium levels detected, as determined from Ga $2p_{3/2}$: O 1s and Ga $2p_{3/2}$: Si 2s, are consistent with a ZSM-5 sample with $\approx$ 2% wt Ga_2O_3 . However, there was no detectable Ga 3d signal which suggests that there was no

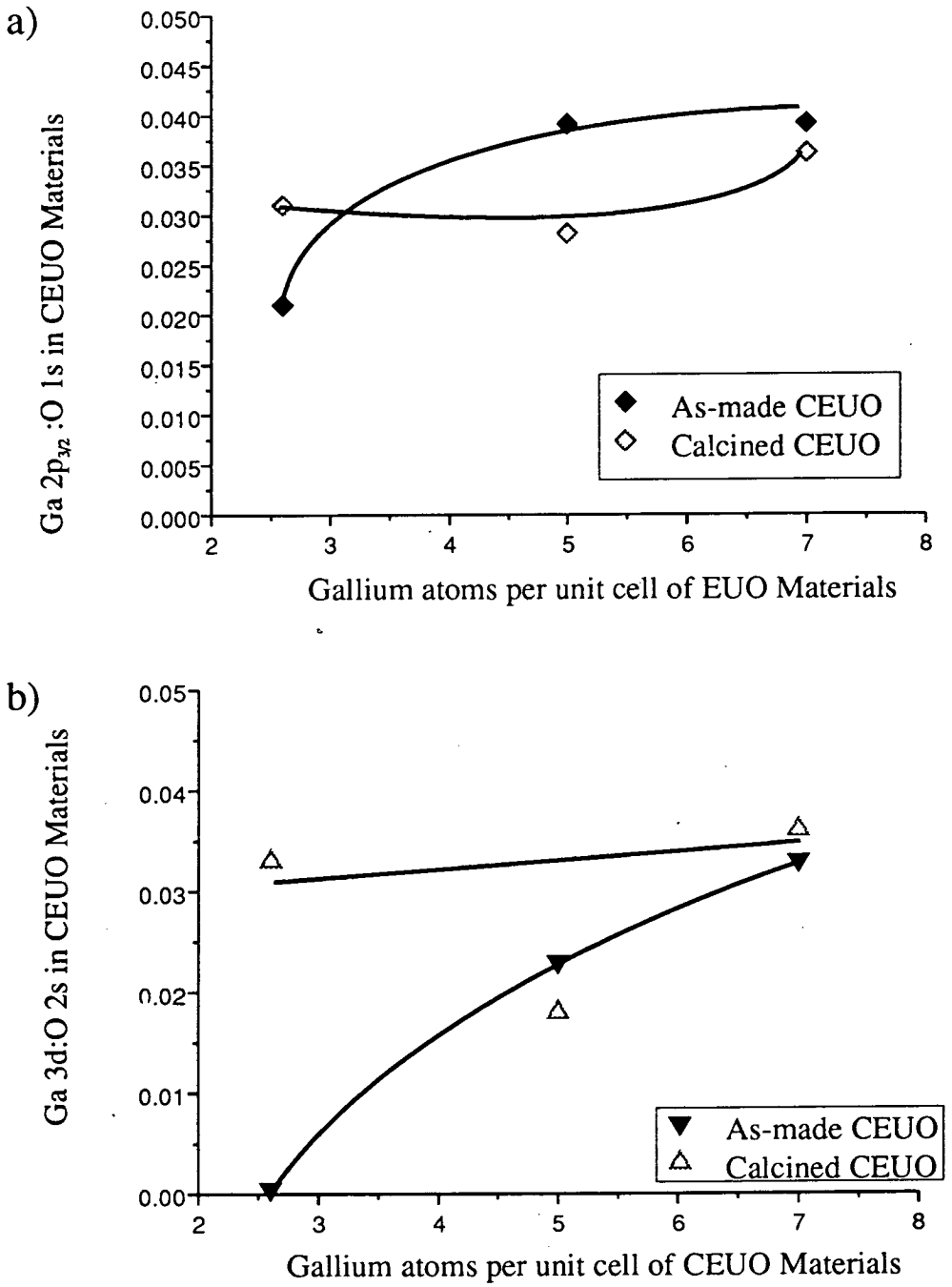

Figure 5–15: a) Ga $2p_{3/2}$:O 1s for as-made and calcined CEUO materials (analysis of *surface* of samples) and b) Ga 3d:O 2s for as-made and calcined CEUO materials (analysis of *near-surface* of samples).

Table 5–10: XPS analysis of I.C.I. prepared materials.

Sample	Si 2s : O 1s	Ga $2p_{\frac{3}{2}}$: Si 2s	Ga $2p_{\frac{3}{2}}$: O 1s	Ga 3d : O 2s
[Ga]-ZSM-5[a]	0.330 : 0.670	0.076 : 0.924	0.027 : 0.973	Not detected
[Ga,Si]-NU-87	0.306 : 0.694	0.107 : 0.893	0.046 : 0.954	0.026 : 0.974

[a] Laposil Ga impregnated ZSM-5, obtained from I.C.I.

gallium deeper into the crystallites. This Ga 3d feature is a very weak transition and it is conceivable that since all the gallium is concentrated on the external surface of the material and that the analysis volume is relatively large for this particular peak that only a very small signal area would be expected. The Schofield sensitivity factor for the Ga $2p_{3/2}$ signal is 21.4 *cf.* only 1.08 for the Ga 3d signal and so it is likely that such a weak feature could be lost in the background noise of that scan envelope.

As expected, the gallosilicate [Ga,Si]-NU-87 material shows a gallium concentration profile similar to those of the gallosilicate materials which have high levels of metal incorporation. This material is examined in much more detail in Chapter 6 where it is compared to a sample which has been examined in the propane conversion reaction and differences in the nature of the materials, caused by exposure to such reducing conditions, are discussed (Section 6.5.2).

Hence, in summary, XPS has shown the gallosilicate materials with the EUO and MFI structure types to form with a gallium rich external crust and a strong gallium concentration gradient, through the crystallites, to a siliceous core. This concentration gradient is stronger for the MFI framework structure than the EUO framework structure. Hence, the framework gallium species are more homogeneously distributed throughout the EUO framework structure than the MFI structure. The CMFI materials have an almost constant gallium level on the external surface of the crystallites. This level is above the maximum level which can be incorporated into the framework structure so there must be extra-framework gallium species supported in the external surface of these crystallites, which contradicts

Table 5–11: Nature of the gallium species in the gallosilicate materials prepared.

Sample	Cryst. Time	XRPD (PPLP)	^{71}Ga NMR	XPS
D2	-	f	Td	-
D2(calc.)	-	f	Td, tr Oh	-
D2(extreme cal.[a])	-	f	Td, Oh	-
CMFI1	f+nf	nf+f	Td	f+nf
CMFI2	f+nf	nf+f	-	f+nf
CMFI3	f+nf	nf+f	Td	f+nf
CMFI4	f+nf	nf+f	-	f+nf
CEUO1	f+nf	f	Td	f
CEUO2	f+nf	f	Td	f
CEUO3	f+nf	f	Td	f, tr nf
CEUO4	f+nf	f	-	-

[a]Sample exposed to extreme calcination and reduction treatments. f = framework, nf = non-framework, Td = tetrahedral, Oh = octahedral, tr = trace.

the ^{71}Ga NMR analyses which suggested only tetrahedral gallium were present in these materials.

Calcination of these gallosilicate materials results in the ejection of some framework gallium atoms which subsequently migrate to the external surface of the crystallites where sintering can more readily occur. The nature of the gallium species, as determined by the techniques described in this Chapter, are summarised in Table 5–11.

Table 5–12: XPS analysis of as-made CEUO1.

Sample Name CEUO1		Maximum Framework Ga : Si 0.077		Bulk Ga : Si by XRF 0.025	
Peak	Total area	S_f used	B.E.	Surface	Depth profile
Ga $2p_{\frac{3}{2}}$	1946	21.4	1119.3-1116.6	Ga $2p_{\frac{3}{2}}$: O 1s	Ga 3d : O 2s
O 1s	24302	2.93	530.4-527.6	0.021 : 0.979	0.005 : 0.995
Si 2s	4106	0.955	152.4-150.0	Si 2s : O 1s	Si 2p : O 2s
Ga 3d	25	1.08	21.4	0.329 : 0.671	0.515 : 0.485
O 2s	741	0.14	26.0	Ga $2_{\frac{3}{2}}$: Si 2s	Ga 3d : Si 2p
Si 2p	3758	0.817	104.6	0.041 : 0.959	0.042 : 0.958

Table 5–13: XPS analysis of calcined CEUO1.

Sample Name CEUO1 calc.		Maximum Framework Ga : Si 0.077		Bulk Ga : Si by XRF 0.025	
Peak	Total area	S_f used	B.E.	Surface	Depth profile
Ga $2p_{\frac{3}{2}}$	2037	21.4	1119.7-1116.0	Ga $2p_{\frac{3}{2}}$: O 1s	Ga 3d : O 2s
O 1s	16892	2.93	533.1-534.8	0.031 : 0.969	0.033 : 0.967
Si 2s	2601	0.955	156.8-154.6	Si 2s : O 1s	Si 2p : O 2s
Ga 3d	85	1.08	18.1	0.310 : 0.690	0.592 : 0.408
O 2s	352	0.14	27.7	Ga $2_{\frac{3}{2}}$: Si 2s	Ga 3d : Si 2p
Si 2p	2426	0.817	105.4-103.1	0.065 : 0.935	0.024 : 0.976

Table 5–14: XPS analysis of as-made CEUO2.

Sample Name CEUO2		Maximum Framework Ga : Si 0.077		Bulk Ga : Si by XRF 0.047	
Peak	Total area	S_f used	B.E.	Surface	Depth profile
Ga $2p_{\frac{3}{2}}$	3046	21.4	1119.3-1116.8	Ga $2p_{\frac{3}{2}}$: O 1s	Ga 3d : O 2s
O 1s	19618	2.93	533.8-532.1	0.039 : 0.961	0.023 : 0.977
Si 2s	3387	0.955	155.4-151.4	Si 2s : O 1s	Si 2p : O 2s
Ga 3d	88	1.08	21.3	0.333 : 0.667	0.558 : 0.442
O 2s	533	0.14	26:6	Ga $2p_{\frac{3}{2}}$: Si 2s	Ga 3d : Si 2p
Si 2p	3204	0.817	104.4	0.076 : 0.924	0.018 : 0.982

Table 5–15: XPS analysis of calcined CEUO2.

Sample Name CEUO2 calc.		Maximum Framework Ga : Si 0.077		Bulk Ga : Si by XRF 0.047	
Peak	Total area	S_f used	B.E.	Surface	Depth profile
Ga $2p_{\frac{3}{2}}$	2489	21.4	1119.7-1117.4	Ga $2p_{\frac{3}{2}}$: O 1s	Ga 3d : O 2s
O 1s	23490	2.93	533.8-532.1	0.028 : 0.972	0.018 : 0.982
Si 2s	3615	0.955	158.8-154.0	Si 2s : O 1s	Si 2p : O 2s
Ga 3d	101	1.08	21.5	0.309 : 0.691	0.485 : 0.515
O 2s	793	0.14	26.5	Ga $2p_{\frac{3}{2}}$: Si 2s	Ga 3d : Si 2p
Si 2p	3545	0.817	104.4-101.4	0.059 : 0.941	0.019 : 0.981

Table 5–16: XPS analysis of as-made CEUO3.

Sample Name CEUO3		Maximum Framework Ga : Si 0.077		Bulk Ga : Si by XRF 0.067	
Peak	Total area	S_f used	B.E.	Surface	Depth profile
Ga $2p_{\frac{3}{2}}$	3537	21.4	1119.3-1116.7	Ga $2p_{\frac{3}{2}}$: O 1s	Ga 3d : O 2s
O 1s	22843	2.93	533.8-531.3	0.039 : 0.961	0.033 : 0.967
Si 2s	3350	0.955	155.9-153.8	Si 2s : O 1s	Si 2p : O 2s
Ga 3d	153	1.08	21.6	0.299 : 0.701	0.520 : 0.480
O 2s	646	0.14	26.7	Ga $2p_{\frac{3}{2}}$: Si 2s	Ga 3d : Si 2p
Si 2p	3385	0.817	104.7-102.8	0.088 : 0.912	0.031 : 0.969

Table 5–17: XPS analysis of calcined CEUO3.

Sample Name CEUO3 calc.		Maximum Framework Ga : Si 0.077		Bulk Ga : Si by XRF 0.067	
Peak	Total area	S_f used	B.E.	Surface	Depth profile
Ga $2p_{\frac{3}{2}}$	4920	21.4	1120-1117.7	Ga $2p_{\frac{3}{2}}$: O 1s	Ga 3d : O 2s
O 1s	34304	2.93	534-532.4	0.036 : 0.964	0.036 : 0.964
Si 2s	5627	0.955	155.8-153	Si 2s : O 1s	Si 2p : O 2s
Ga 3d	285	1.08	21.2	0.322 : 0.678	0.512 : 0.488
O 2s	1097	0.14	26.6	Ga $2p_{\frac{3}{2}}$: Si 2s	Ga 3d : Si 2p
Si 2p	5510	0.817	104.6-101.5	0.074 : 0.926	0.034 : 0.966

Table 5–18: XPS analysis of as-made CMFI1.

Sample Name CMFI1		Maximum Framework Ga : Si 0.091		Bulk Ga : Si by XRF 0.045	
Peak	Total area	S_f used	B.E.	Surface	Depth profile
Ga $2p_{\frac{3}{2}}$	5684	21.4	1119.1-1118.1	Ga $2p_{\frac{3}{2}}$: O 1s	Ga 3d : O 2s
O 1s	27229	2.93	533.9-531.9	0.052 : 0.948	0.030 : 0.970
Si 2s	4027	0.955	155.7-153.4	Si 2s : O 1s	Si 2p : O 2s
Ga 3d	180	1.08	20.5	0.300 : 0.700	0.495 : 0.505
O 2s	836	0.14	26.5	Ga $2p_{\frac{3}{2}}$: Si 2s	Ga 3d : Si 2p
Si 2p	3908	0.817	104.8-103	0.114 : 0.886	0.031 : 0.969

Table 5–19: XPS analysis of calcined CMFI1.

Sample Name CMFI1 calc.		Maximum Framework Ga : Si 0.091		Bulk Ga : Si by XRF 0.045	
Peak	Total area	S_f used	B.E.	Surface	Depth profile
Ga $2p_{\frac{3}{2}}$	3572	21.4	1119.4	Ga $2p_{\frac{3}{2}}$: O 1s	Ga 3d : O 2s
O 1s	19199	2.93	534	0.047 : 0.953	0.020 : 0.980
Si 2s	3232	0.955	155.4	Si 2s : O 1s	Si 2p : O 2s
Ga 3d	174	1.08	21.7	0.328 : 0.672	0.523 : 0.477
O 2s	597	0.14	26.5	Ga $2p_{\frac{3}{2}}$: Si 2s	Ga 3d : Si 2p
Si 2p	3134	0.817	104.8	0.092 : 0.908	0.037 : 0.963

Table 5–20: XPS analysis of as-made CMFI2.

Sample Name CMFI2		Maximum Framework Ga : Si 0.091		Bulk Ga : Si by XRF 0.061	
Peak	Total area	S_f used	B.E.	Surface	Depth profile
Ga $2p_{\frac{3}{2}}$	4104	21.4	1118.5-1115.7	Ga $2p_{\frac{3}{2}}$: O 1s	Ga 3d : O 2s
O 1s	21642	2.93	533.2-531.0	0.048 : 0.952	0.028 : 0.972
Si 2s	3113	0.955	154.9-152	Si 2s : O 1s	Si 2p : O 2s
Ga 3d	134	1.08	21.0	0.294 : 0.706	0.482 : 0.518
O 2s	667	0.14	26.0	Ga $2p_{\frac{3}{2}}$: Si 2s	Ga 3d : Si 2p
Si 2p	2982	0.817	104.1	0.107 : 0.893	0.030 : 0.970

Table 5–21: XPS analysis of calcined CMFI2.

Sample Name CMFI2 calc.		Maximum Framework Ga : Si 0.091		Bulk Ga : Si by XRF 0.061	
Peak	Total area	S_f used	B.E.	Surface	Depth profile
Ga $2p_{\frac{3}{2}}$	2221	21.4	1119.1	Ga $2p_{\frac{3}{2}}$: O 1s	Ga 3d : O 2s
O 1s	23520	2.93	533.8	0.025 : 0.975	0.020 : 0.980
Si 2s	4054	0.955	155.6	Si 2s : O 1s	Si 2p : O 2s
Ga 3d	107	1.08	201.8	0.333 : 0.667	0.521 : 0.479
O 2s	732	0.14	26.6	Ga $2p_{\frac{3}{2}}$: Si 2s	Ga 3d : Si 2p
Si 2p	3862	0.817	104.8	0.048 : 0.952	0.019 : 0.981

Table 5–22: XPS analysis of as-made CMFI3.

Sample Name CMFI3		Maximum Framework Ga : Si 0.091		Bulk Ga : Si by XRF 0.077	
Peak	Total area	S_f used	B.E.	Surface	Depth profile
Ga $2p_{\frac{3}{2}}$	5461	21.4	1119.0	Ga $2p_{\frac{3}{2}}$: O 1s	Ga 3d : O 2s
O 1s	25042	2.93	533.4	0.054 : 0.946	0.035 : 0.965
Si 2s	4157	0.955	155.0	Si 2s : O 1s	Si 2p : O 2s
Ga 3d	204	1.08	21.5	0.325 : 0.675	0.505 : 0.495
O 2s	812	0.14	26.5	Ga $2p_{\frac{3}{2}}$: Si 2s	Ga 3d : Si 2p
Si 2p	3957	0.817	104.4	0.107 : 0.893	0.034 : 0.966

Table 5–23: XPS analysis of calcined CMFI3.

Sample Name CMFI3 calc.		Maximum Framework Ga : Si 0.091		Bulk Ga : Si by XRF 0.077	
Peak	Total area	S_f used	B.E.	Surface	Depth profile
Ga $2p_{\frac{3}{2}}$	3343	21.4	1120	Ga $2p_{\frac{3}{2}}$: O 1s	Ga 3d : O 2s
O 1s	19198	2.93	534.0	0.044 : 0.956	0.046 : 0.954
Si 2s	2779	0.955	155.8	Si 2s : O 1s	Si 2p : O 2s
Ga 3d	155	1.08	22.0	0.296 : 0.704	0.505 : 0.495
O 2s	465	0.14	26.8	Ga $2p_{\frac{3}{2}}$: Si 2s	Ga 3d : Si 2p
Si 2p	2838	0.817	104.8	0.099 : 0.901	0.036 : 0.964

Table 5–24: XPS analysis of as-made CMFI4.

Sample Name CMFI4		Maximum Framework Ga: Si 0.091		Bulk Ga : Si by XRF 0.091	
Peak	Total area	S_f used	B.E.	Surface	Depth profile
Ga $2p_{\frac{3}{2}}$	8048	21.4	1118.9	Ga $2p_{\frac{3}{2}}$: O 1s	Ga 3d : O 2s
O 1s	34559	2.93	533.4	0.058 : 0.942	0.048 : 0.952
Si 2s	5724	0.955	155.6	Si 2s : O 1s	Si 2p : O 2s
Ga 3d	422	1.08	21.5	0.324 : 0.676	0.475 : 0.525
O 2s	1213	0.14	26.3	Ga $2p_{\frac{3}{2}}$: Si 2s	Ga 3d : Si 2p
Si 2p	5189	0.817	104.2	0.114 : 0.886	0.053 : 0.947

Table 5–25: XPS analysis of calcined CMFI4.

Sample Name CMFI4 calc.		Maximum Framework Ga : Si 0.091		Bulk Ga : Si by XRF 0.091	
Peak	Total area	S_f used	B.E.	Surface	Depth profile
Ga $2p_{\frac{3}{2}}$	3540	21.4	1119.9	Ga $2p_{\frac{3}{2}}$: O 1s	Ga 3d : O 2s
O 1s	21516	2.93	534.2	0.042 : 0.958	0.043 : 0.957
Si 2s	4044	0.955	156.2	Si 2s : O 1s	Si 2p : O 2s
Ga 3d	218	1.08	22.2	0.352 : 0.648	0.538 : 0.462
O 2s	691	0.14	27.0	Ga $2p_{\frac{3}{2}}$: Si 2s	Ga 3d : Si 2p
Si 2p	3852	0.817	105.0	0.074 : 0.916	0.037 : 0.963

Table 5–26: XPS analysis of unreacted Ga impregnated H-ZSM-5.

Sample Ga-ZSM-5, 2% Ga_2O_3 by weight					
Peak	Total area	S_f used	B.E.	Surface	Depth profile
Ga $2p_{\frac{3}{2}}$	3772	21.4	1119.1-1116.2	Ga $2p_{\frac{3}{2}}$: O 1s	Ga 3d : O 2s
O 1s	35585	2.93	536.1-533.9	0.027 : 0.973	-
Si 2s	5045	0.955	154.5	Si 2s : O 1s	Si 2p : O 2s
Ga 3d	-	1.08	22	0.330 : 0.670	0.474 : 0.526
O 2s	880	0.14	25.8	Ga $2p_{\frac{3}{2}}$: Si 2s	Ga 3d : Si 2p
Si 2p	4789	0.817	103.8	0.076 : 0.924	-

Table 5–27: XPS analysis of unreacted [Ga,Si]-NU-87.

Sample [Ga,Si]-NU-87, gallosilicate NU-87 from I.C.I.					
Peak	Total area	S_f used	B.E.	Surface	Depth profile
Ga $2p_{\frac{3}{2}}$	2350	21.4	1120.3-1117.0	Ga $2p_{\frac{3}{2}}$: O 1s	Ga 3d : O 2s
O 1s	12958	2.93	533.9-536.0	0.046 : 0.954	0.026 : 0.974
Si 2s	1916	0.955	155.7	Si 2s : O 1s	Si 2p : O 2s
Ga 3d	66	1.08	22.5	0.306 : 0.694	0.484 : 0.516
O 2s	273	0.14	27.2	Ga $2p_{\frac{3}{2}}$: Si 2s	Ga 3d : Si 2p
Si 2p	1581	0.817	104.6	0.107 : 0.893	0.027 : 0.973

Chapter 6

Catalytic Examinations

6.1 Introduction

This Chapter describes the procedures and results from the catalytic examination of a range of the molecular sieves. The majority of the experiments were carried out in a batch recirculating reactor, however, a flow microreactor was also used to investigate some of the catalysts prepared. These flow studies were designed to directly mimic the complex and sophisticated processes which occur in the propane aromatisation reaction, in an attempt to further elucidate the mechanisms involved. These flow studies were carried out at I.C.I. C.&P. Ltd., Wilton. The experimental procedures are described and followed by the results and a discussion of the features noted from them. The raw experimental data for the flow and recirculating batch studies are summarised in tabular form and are included at the end of each catalysis section.

Flow and recirculating reactor systems provide different types of information about the process under examination. However, in deciding what type of catalytic studies to undertake, other more practical aspects of the studies must be considered. Flow studies effectively represent a first derivative, with respect to time, of the data generated in a recirculating system. In a flow experiment, over an ideal catalyst, conversion would be constant with time. However, such ideal catalytic systems rarely exist since some degree of poisoning or deactivation usually occurs. This causes the conversion, with time on stream, to appear as a decaying curve rather than a constant level of conversion. In a recirculating study, the composition of the feed gas is constantly changing, containing less of the initial reactant

and more of the products generated, and so rates of conversion are not as readily determined as they are in a flow system where the rate of conversion of reactants is directly measured. The decay in reactants in a batch system is usually assumed to follow a predefined order of reaction (most often first order) and so a plot of *eg.* $\ln$ [Concentration] against time should yield a straight line of gradient $-k$, where k is the rate constant for the reaction (assuming first order kinetics, units of s^{-1}). However, non-linearity is introduced to this data analysis by the inherent reduction in activity by poisoning and/or deactivation of the catalyst by coking. Hence, it is usual to obtain kinetic data from such studies by consideration of only the initial conversion ($\leq$15%) before significant catalyst deactivation occurs. This has also been shown statistically to represent the time after which it is likely that reactant molecules will start to visit the catalyst surface for the second time [227]. Determination of these initial rates can only be applied to relatively simple reactions where further conversion of the primary products does not interfere with the activity observed.

The raw data derived from a flow study is more useful than that derived from a batch recirculating system since data obtained from recirculating studies requires further manipulation to obtain quantitative rate of reaction information. The experimentalist must undertake studies which best suit the available resources and so the practical needs of the two techniques must be considered. Flow systems tend to be sophisticated and complex and consequently are more expensive to build and operate. Flow systems also require far stricter safety measures compared to a recirculating apparatus. The recirculating system is extremely convenient and versatile and since lower gas pressures are involved, these systems are inherently safer, requiring less stringent laboratory safety specifications.

A flow reactor was not readily available in Edinburgh and so the flow studies undertaken were carried out in the laboratories of I.C.I. C.& P. Ltd., Wilton. This system was decommissioned immediately after the series of experiments described in this Chapter and so further studies could not be carried out. A recirculating apparatus was available in Edinburgh and so the majority of the catalysis studies were carried out using this apparatus.

6.2 Flow Reactor Studies

6.2.1 Materials Examined

The calcined gallosilicate materials D6 ([Ga,Si]-NU-85), D7 ([Ga,Si]-EUO) and D9 ([Ga,Si]-NU-85) were converted to their *active* H-form, by repeated ion exchange with 1M HCl at 313 K. These gallosilicate materials have either the 1-D channel structure of EUO or the partially 2-D, NU-85 channel structure. The NU-87 framework structure creates a truly 2-D network of channels and a sample of the gallosilicate [Ga,Si]-NU-87 material was obtained in an activated H-form from I.C.I., C.&P. Ltd., Wilton.

The acid exchange procedure was also carried out on batches of the I.C.I. supplied zeolites ZP2 and ZP6, prior to their doping with gallium nitrate. This doping, either by IW or IE, has been described previously (Chapter 2) and was used to prepare samples with a range of loadings (typically $\leq$ 5% by weight of Ga_2O_3).

A sample of gallium doped ZSM-5 (Ga-ZSM-5), in its activated H-form, was also obtained from I.C.I., C.&P., Wilton. This material closely resembles the proposed industrial catalyst for propane aromatisation. All catalyst samples were pelletised, crushed and sieved as described previously. Details of the samples examined are summarised in Table 6–1.

Sample	Structure (XRPD)	$\frac{SiO_2}{M_2O_3}$ ratio	Ga_2O_3 %wt	Pore Vol. $cm^3/100g$	Ext. area m^2g^{-1}	Acidity NH_3^a	Acid site strengths w:m:s	Ga[b]
Ga-ZSM-5[c]	MFI	36	2.0	-	-	96±8	0.2:0.2:0.6	nf,X
[Ga,Si]-NU-87[d]	NES	-	11.8	-	-	-	-	f,I
D6	NU-85	-	9.8	12.7	50.0	-	-	f,I
D7	EUO[e]	-	3.0	11.5	19.0	-	-	f,I
D9	NU-85	-	11.6	13.2	51.1	-	-	f,I/X
ZP2-5%IE	EUO	35	4.98	12.2	52.5	99±9	0.4:0.5:0.1	nf,I/X
ZP2-3%IW	EUO	35	2.51	12.3	50.2	99±9	0.4:0.5:0.1	nf,X
ZP6-5%IW	EUO	712	4.61	11.3	4.3	0.5±1	0.95:0:0.05	nf,X
ZP6-3%IW	EUO	712	2.26	12.5	5.6	0.5±1	0.95:0:0.05	nf,X
ZP6-3%IE	EUO	712	2.03	12.4	5.6	0.5±1	0.95:0:0.05	nf,X
ZP6-1%IE	EUO	712	0.92	11.3	6.2	0.5±1	0.95:0:0.05	nf,X

Table 6–1: Summary of the materials examined.

[a]Acid sites determined as mmoles of $NH_3 \times 100\ g^{-1}$ sample, [b]gallium position summarised as; f=framework, nf=non-framework, I=inside the channel system and X=supported on the external surface of the crystallites, [d]material and characterisation obtained from I.C.I. C.&P., [e]trace of α-quartz.

Chapter 5 presented the results from a number of techniques used to determine the nature and location of the gallium species in the gallosilicate materials examined in this work. These analyses using XPS, unit cell volumes and ^{71}Ga NMR have been used to propose the position of the majority of the gallium in the catalysts. These assignments are summarised in Table 6–1, as either inside the channel structure or supported on the external surface of the crystallites and as framework or non-framework species. It should be noted that these are general observations and it is likely that not all the gallium species are of the form nominally ascribed to that sample. The gallosilicate materials have the majority of their gallium species sited in the framework structures prior to reaction (as shown by ^{71}Ga NMR and unit cell volumes), however, the extreme conditions of the catalysis test reaction can cause ejection of these framework species which can subsequently migrate to the external surface of the crystallites where sintering can occur (as observed by XPS). Such an observation is in accord with the findings of others [95, 134]. The Ga-ZSM-5 material has only extra-framework gallium species which, as a result of the XPS investigation, described in Section 5.5 (Table 5–26), have been proposed to be in a very thin layer on the external surface of the Laposil ZSM-5 crystallites. The IE and IW doping techniques used to load gallium species onto the EU-1 (ZP2 and ZP6) catalysts are not dramatically different for these large gallium loadings because the ZP2 and ZP6 materials cannot ion exchange such a large number of Ga^{3+} species and consequently a large proportion of the gallium remains outside the channel structure, supported on the external surface of the crystallites. ZP2 has a $\frac{SiO_2}{Al_2O_3}$ ratio of 35 which corresponds to $6AlO_2$ species to $106SiO_2$ species per unit cell of the EUO framework. Hence a maximum of $2Ga^{3+}$ species could be ion-exchanged per unit cell of this material. This maximum loading would be equivalent to $\approx$3.4% by wt. Ga_2O_3 in the ZP2, EU-1 catalyst. The ZP6 material has a $\frac{SiO_2}{Al_2O_3}$ ratio of 712 and so only $0.3AlO_2$ to 111.7 SiO_2 are found in the framework, so a single Ga^{3+} species would require the negative charge available in $\approx$ 9 unit cells to be ion-exchanged. The poor ion exchange capability of EU-1 for ions which are multivalent has been examined by Rees *et al.* [228, 229]. It has been proposed that the Ga^{3+} species when fully hydrated may be too large to enter the 10-ring windows of EUO and may be forced to reside on the external surface

of the EUO crystallites. Hence, it is proposed that only a very small proportion of the bulk gallium content is located inside the porous structure. There is the possibility of small amounts of gallium occlusion associated with defects inside the crystallites and also the possibility of framework substitution of Si/Al by Ga which would apparently increase the potential ion-exchange capacity of these materials; however, this would only account for an extremely small proportion of these high gallium dopant levels.

6.2.2 Flow Reactor Experimental Procedure

The flow reactor apparatus is shown schematically in Figure 6–1. The unit had twin reactors, with reactant gases only passing through one reactor at a time, while the other reactor was being purged with flowing air. The stainless steel reactor vessel was charged with the sieved catalyst granules as represented in Figure 6–2.

Catalyst weight was a critical parameter and so the charge was measured accurately, typically $\approx$ 0.7g. This represented $\approx$ 1.5ml in volume and so the catalyst bed was $\approx$ 9cm deep when loaded into the $\frac{1}{4}''$ o.d. stainless steel reactor vessel (as represented in Figure 6–2). The loaded reactor vessel was fastened into a cylindrical heating block. The block was then locked into an insulated reactor housing and was leak tested prior to commencing the experimental run.

The analysis of the product stream was fully automated and controlled from a Multichrom software package (VG Instruments) which required Control, Run Sequence, Method and Calibration files. The Analysis files were entered by the operator and were named in the Run Sequence file which created the subsequent gas chromatograph analysis files.

The cartridge heaters in the reactor blocks were controlled by Eurotherm temperature controllers which were sequentially incremented to attain the desired reaction temperature (803 K), measured by two thermocouples and displayed by a Comark digital thermometer.

Samples were routinely pretreated with a calcination procedure *i.e.* maintained at 803 K for 16h under a flow of air (the reactor regeneration mode). Whilst the

Figure 6–1: Schematic of the Flow Microreactor Apparatus.

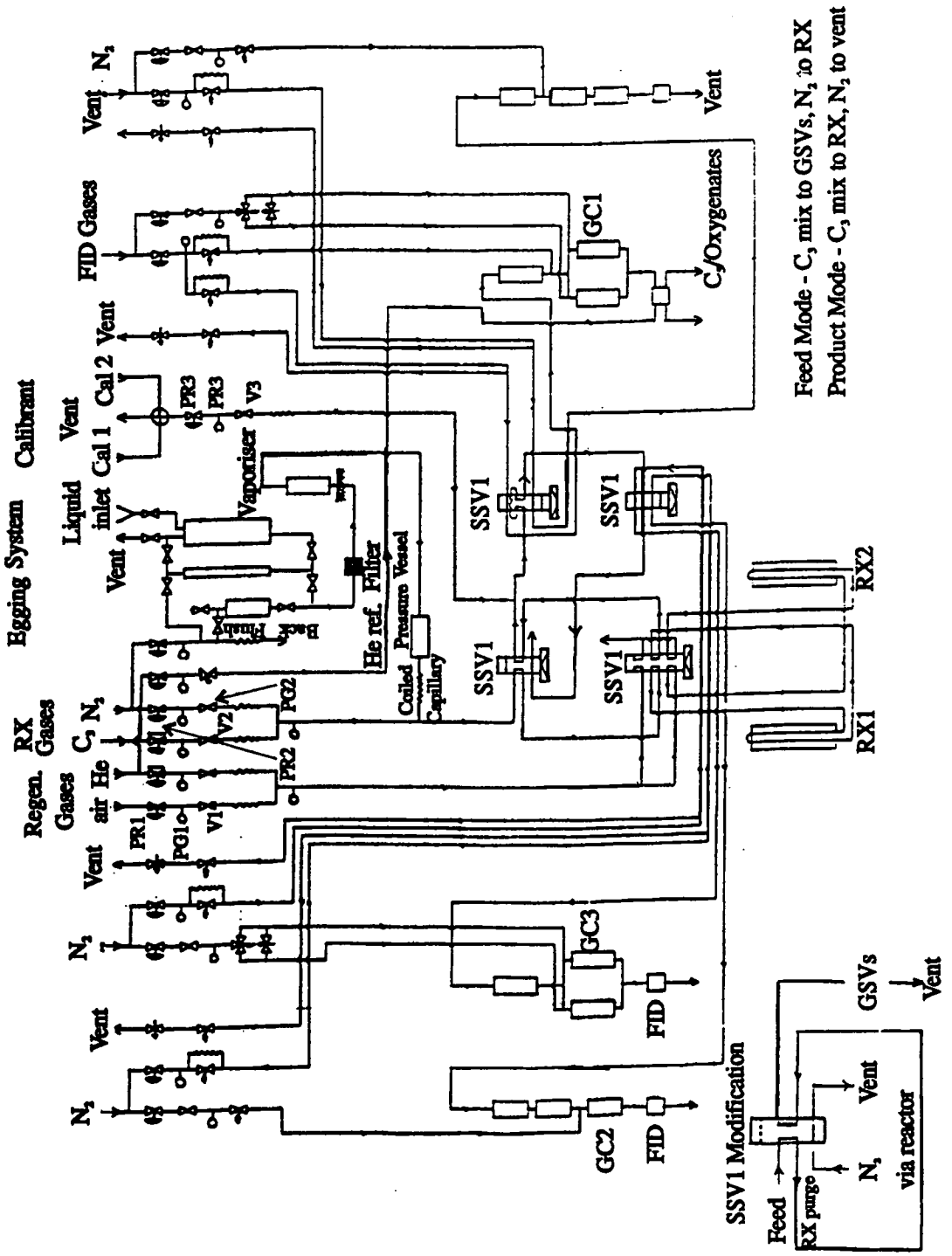

Figure 6–2: Schematic of the stainless steel reaction vessel.

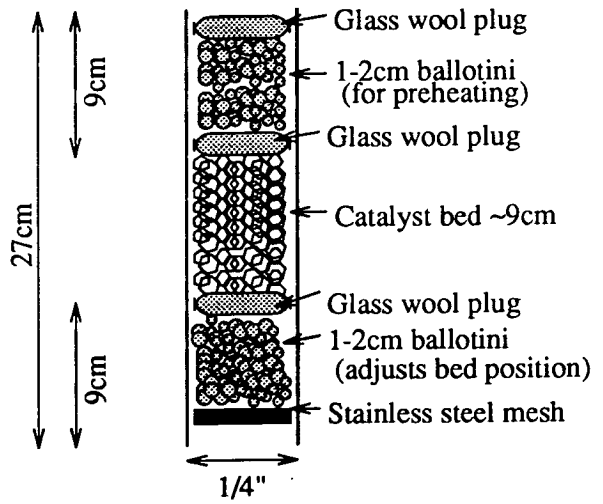

reactor was in this regeneration mode the gas blending was undertaken. The propane feed pressure was altered to deliver the required weight hourly space velocity (g of reactant per g of catalyst per hour *i.e.* units of h^{-1}). The actual flowrate was the critical measurement and was verified using a soap bubble flow meter. The propane feed stream initially by-passed the reactor and went to vent while the diluent gas, nitrogen, was introduced to give a suitable total reactant gas flow.

Aliquots of the feed stream were taken prior to reaction, to obtain accurate feed analysis. Reaction commenced when the feed/product stream selector was switched to product mode which allowed the process gas stream to flow through the catalyst bed.

Analysis acquisition was initiated by manually entered commands to the Multichrom system with analysis cycles taking $\approx$ 45 minutes. After experimental runs the catalysts were retrieved and retained. However, the reactor configuration was such that the catalyst was cooled with the reactor in regeneration mode *i.e.* under flowing air, and so the catalyst discharges were exposed to severe oxidative conditions prior to retrieval. Thus the catalyst discharges are more correctly described as *partially regenerated* rather than *reacted.*

Table 6–2: Possible propane conversions used to determine the dilution effect in samples analysed.

$1C_3H_8$	$\longrightarrow$	$C + 2\ CH_4$
$1C_3H_8$	$\longrightarrow$	$3\ CH_4 - 2\ H_2$
$2C_3H_8$	$\longrightarrow$	$3\ C_2H_4 + 2\ H_2$
$1C_3H_8$	$\longrightarrow$	$C_2H_6 + CH_4 - 1\ H_2$
$1C_3H_8$	$\longrightarrow$	$1\ C_3H_6 + 1\ H_2$
$4C_3H_8$	$\longrightarrow$	$3\ C_4H_8 + 4\ H_2$
$4C_3H_8$	$\longrightarrow$	$3\ C_4H_{10} + 1\ H_2$
$5C_3H_8$	$\longrightarrow$	$3\ C_5H_{12} + 2\ H_2$
$2C_3H_8$	$\longrightarrow$	$1\ C_6H_{14} + 1\ H_2$
$2C_3H_8$	$\longrightarrow$	$1\ C_6H_6 + 5\ H_2$
$7C_3H_8$	$\longrightarrow$	$3\ C_7H_8 + 16\ H_2$
$8C_3H_8$	$\longrightarrow$	$3\ C_8H_{10} + 17\ H_2$

6.2.3 Flow Reactor Results

The gas chromatograph analysis of the product stream was in % by volume. This was potentially misleading since some reactions can produce large amounts of hydrogen as a by-product. This has a dilution effect on the sample analysis with proportionally less hydrocarbons measured in each sample aliquot. This effect was greatest for runs with large aromatic (benzene, toluene and xylene, abbreviated to BTX) production as these involve the largest H_2 evolution. The recalculation of product concentrations from this diluted stream is an extremely laborious one and so a computer program was used to manipulate the data generated. The calculation involved the determination of the H_2 production which would have been associated with the organic product distribution observed. A range of the possible equations for the various conversions were considered, as summarised in Table 6–2.

These possible reactions are by no means exhaustive and many other possible schemes could be envisaged, however, they are extremely useful in offering a real-

istic manipulation of the raw data and allow compensation for the dilution of the product gas stream. This approach allowed the amount of propane required to produce a particular product to be calculated. The equation for each individual product generated was then considered and the H_2 evolution/consumption calculated and consequently the actual composition of the product stream was derived. It should be considered that propane which is lost to the catalyst surface, as carbonaceous deposits (coke), could produce a substantial dilution effect if there was significant H_2 production *eg.*

$$C_3H_8 \longrightarrow 3C \text{ (Coke deposits)} + 4\ H_2$$

This is particularly apparent in the early stages of a reaction where the rate of coking would be greatest. However, complete correction for this coking cannot be readily achieved. Thermal gravimetric analysis (TGA) of the catalyst discharges would give the total carbon laydown during the reaction; however, samples could not be removed during the catalysis experiment to determine this level of coking. Analysis of samples after completion of the experimental run would offer the cumulative carbon laydown, but this cannot give information about the time during the reaction when this coking occurred *i.e.* its rate of formation. As stated previously the reaction shutdown procedure in the flow apparatus was such that the reactor was automatically set to regeneration mode *i.e.* purged with flowing air while cooling from 803 K and so resulted in a partial regeneration of the catalysts. Hence, determination of the carbon content of the catalyst discharges would be irrelevant.

The experiments used $\approx$ 25% propane and balance N_2, so this *expansion effect* was itself buffered by the nitrogen diluent. A *Dilution Factor* was then calculated for each of the analyses from equation 6.1.

$$Dilution = \frac{100 - Feed\ C_3H_8\ +\ Total\ Products}{100} \tag{6.1}$$

This *Dilution Factor* was then used to adjust all the product concentrations observed to compensate for the expansion effect. Such dilutions could be determined directly by using a small amount of an inert gas in the analysed flow *eg.* 5% He,

and comparison of this to the undiluted gas composition giving the *expansion factor.* Such calibrations had been previously carried out by I.C.I. staff at Wilton and the approach described for compensating for the dilution of the hydrocarbon flow detected had been deemed to be adequate for such catalytic studies. The conversions were then calculated from equation 6.2.

$$\text{Conversion} = \frac{\text{Total } C_3 \text{ Feed} - \text{Adjusted Products}}{\text{Total } C_3 \text{ Feed (Propane + Propene)}} \times 100\% \qquad (6.2)$$

The main products detected were readily divided into three groups; (i) propene, (ii) BTX and (iii) fuel gases methane, ethane and ethene (denoted as C1/C2s). The propene formed was removed from the product analysis and considered as part of the reactant gas feed to determine the conversion of the total C_3 feed. Propane aromatisation requires propene formation before subsequent oligomerisation, cyclisation and aromatisation, as described in Chapter 1, and so it is reasonable to consider the propene component of the gas stream as a feedstock in the aromatisation reaction. Such a consideration is analogous to the data interpretation procedures employed in the study of methanol to gasoline (MTG) catalysts where initial creation of dimethylether is required before the goal conversion can proceed [230-234]. The raw data for the catalysts examined are included in tabular form at the end of this section. Table 6–5 summarises the analysis for the Ga-ZSM-5 catalyst, Tables 6–6 to 6–9 for the gallosilicate catalysts, Tables 6–10 to 6–13 for the ZP6 based catalysts and the analyses of the ZP2 based materials are presented in Tables 6–14 and 6–15. The tables show the corrected product stream analyses in terms of % volume of; unreacted propane, the fuel gas component (C_1/C_2s), propene, oligomerised fraction (C_4/C_5s) and the aromatics (BTX). The tables also include the levels of conversion of the total C_3 (propane and propene) feed, per g of catalyst. The product distributions from the conversion of the C_3 feed (C_3H_8 and C_3H_6) are tabulated in terms of selectivity to the C_1/C_2, C_4/C_5 and BTX fractions. Also tabulated is the amount of propene detected in the product stream analysis described as % propene yield from the propane feed.

The conversion levels observed from the first feed analyses and those obtained after a short time on stream, over the catalysts examined, are shown in Table

Table 6–3: Summary of conversions observed over the catalysts examined in the flow reactor studies.

Sample Name	Total C_3 Con. (g^{-1}) after 0.25 h on line	Total C_3 Con. (g^{-1}) after 2.5h on line
Ga-ZSM-5	96	99
[Ga,Si]-NU-87	39	12
D6	13	10
D7	2	8
D9	12	10
ZP2+5%IW	55[a]	20[b]
ZP2+3%IW	33	20
ZP6+5%IW	11	4
ZP6+3%IW	37	17
ZP6+3%IE	13	12
ZP6+1%IE	9	4

[a] after 0.06 hours and [b] after 2.31 hours

6–3. This shows the low conversions observed for the molecular sieve materials examined, compared to the industrially employed Ga impregnated ZSM-5 material (Ga-ZSM-5). Analysis of these low levels of conversions leads to significantly larger errors in product distribution and conversion determination, since any fluctuations in the feed composition or analysis errors have a greater effect on the quantities determined.

6.2.4 Discussion of Propane Aromatisation Studies

Ga-ZSM-5

The remarkable activity and selectivity of the Ga-ZSM-5 material is represented in Figure 6–3 which uses a stacked plot to show the variation in product stream composition with conversion over the Ga-ZSM-5 catalyst. The composition of the product stream was extremely diverse with hydrocarbons up to C_6 detected along with the aromatic products as represented by the large number of component blocks in each analysis stack.

Table 6–5 shows that the selectivity to BTX ($\approx$ 40%), exhibited by Ga-ZSM-5, was maintained for extended times ($\geq$ 16 h). The extremely high activity observed over the Ga-ZSM-5 material is shown in Figure 6–4. This activity can be partially rationalised by consideration of the remarkable resistance to coking exhibited by the MFI structure. There is apparently a short induction period before the material achieves its highest level of conversion. This has been suggested to be associated with the time required to achieve a partial reduction in the oxidation state of the active gallium species, under the reducing atmosphere of the propane aromatisation reaction [115, 117, 207, 235, 236]. This reduction in oxidation state of the gallium, in catalysts which have been exposed to this type of reaction has been clearly observed in XPS studies, described in Section 6.5.2. The precise nature of these gallium species cannot be elucidated, however, it is proposed to be a suboxide form of gallium.

Gallosilicate Molecular Sieves

Conversion with time on stream, observed over the gallosilicate materials D6 ([Ga,Si]-NU-85), D7 ([Ga,Si]-EUO) and [Ga,Si]-NU-87, is summarised in Figure 6–5. The [Ga,Si]-NU-87 material was initially significantly more active than the D series of materials, however, this conversion ($\approx$ 39%) was very short lived and in less than 2 hours the [Ga,Si]-NU-87 showed conversion which was similar to that of the other gallosilicate catalysts. The conversion of the total C_3 feed ($C_3 + C_3^=$)

Figure 6–3: Product stream composition over Ga-ZSM-5 with time on stream.

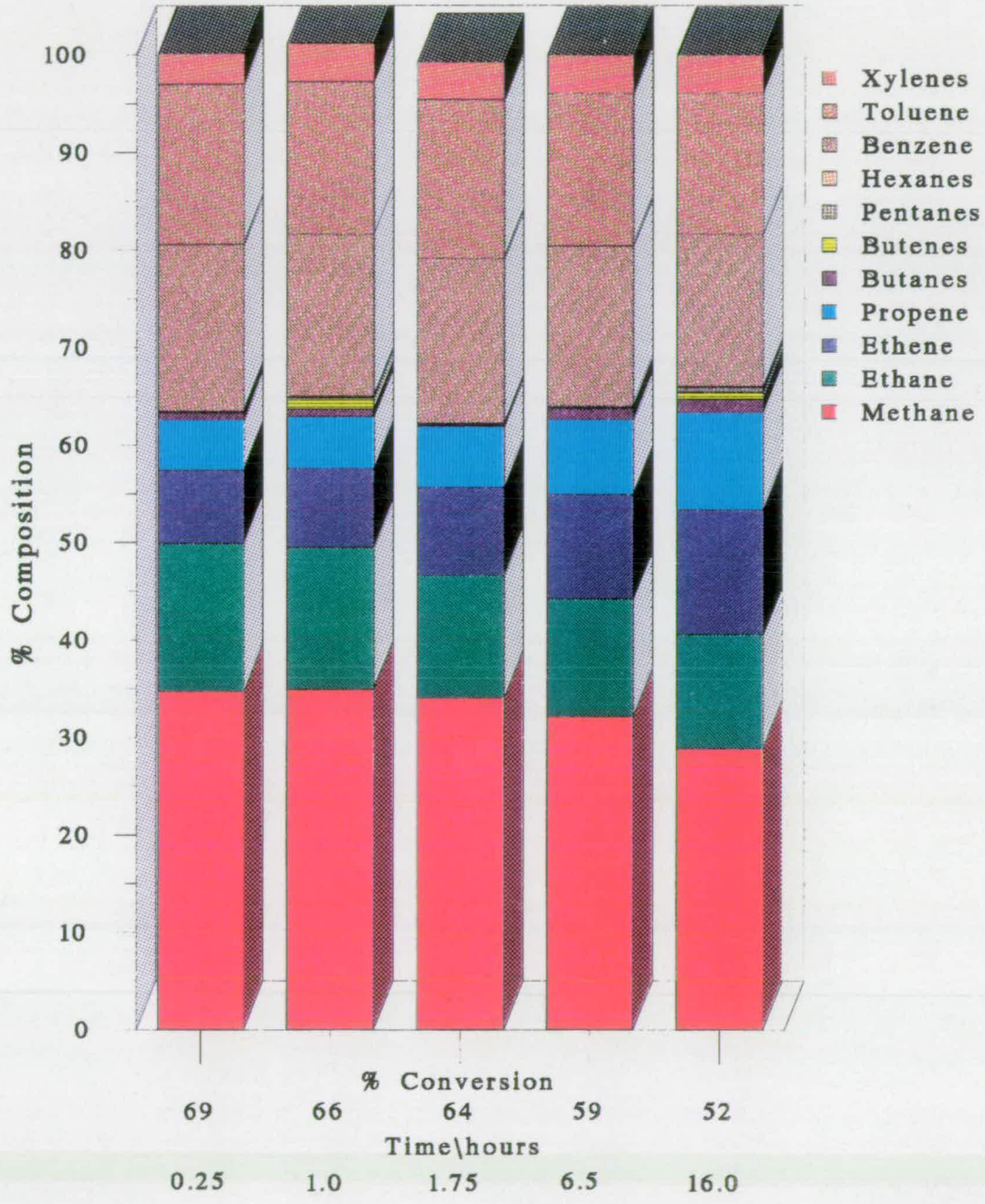

Figure 6–4: Conversion with time on stream over the Ga-ZSM-5 material.

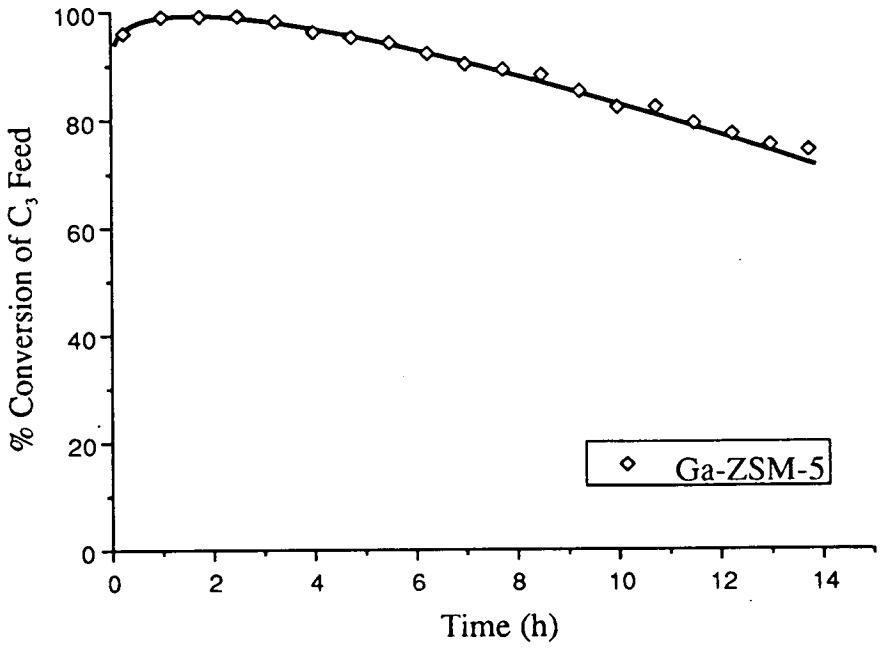

over the D series of samples was low, but constant, at around 5-10 %. Reliable analysis is difficult at these lower conversion levels; however, these materials are clearly less active than the [Ga,Si]-NU-87 catalyst, at the time the first feed analysis was obtained. This observation can be rationalised from the theoretical lifetimes of the materials. D7 has a unidimensional EUO channel structure and so would be most easily blocked by carbonaceous deposits. D6 ([Ga,Si]-NU-85) is partially multidimensional, since it has some NU-87 (2-D) character intergrown with the EUO channels, and so would be expected to retain activity for longer than the pure EUO material. The [Ga,Si]-NU-87 catalyst has a completely 2-D channel structure and so would be expected to retain activity for longer than either of the other gallosilicate materials examined. This order is reflected in the C_3 conversion observed, shown in Figure 6–5, with the three levels of conversion all falling to around the same level once the materials had been deactivated. The EUO and NES structure types exhibit an extremely high propensity to deactivation by coke formation and there were relatively long periods between sample analyses, a consequence of the reactor configuration, and so it is proposed that the activity of these materials for very short periods of time could be as impressive

Figure 6–5: Conversion with time on stream over the gallosilicate catalysts.

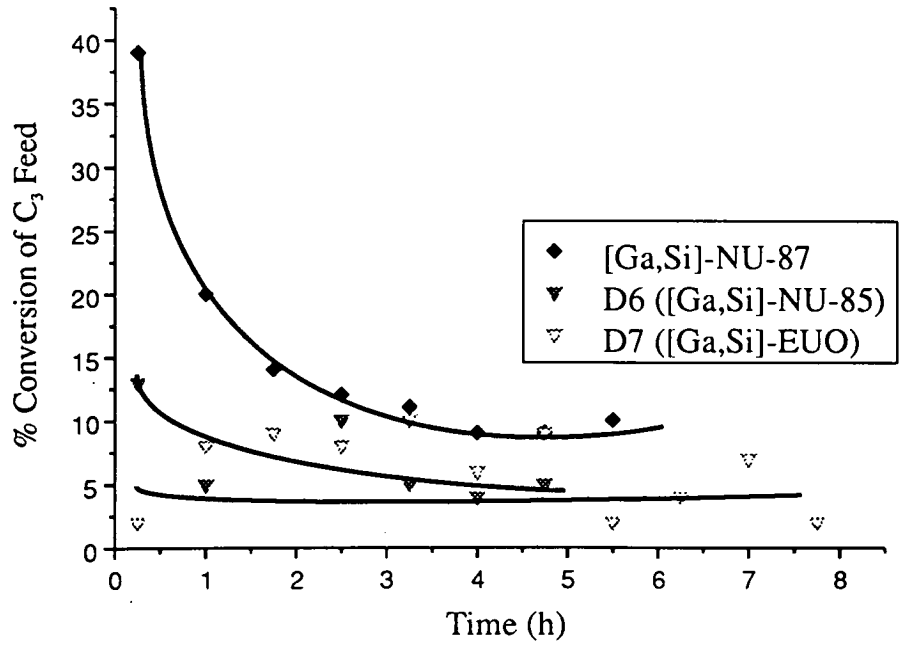

as the Ga-ZSM-5. However, the channel structures of these particular molecular sieves are such that deactivation by coke formation is fatal for successful propane aromatisation activity.

The propene yield from the propane feed passed over these gallosilicate materials is shown in Figure 6–6. D7 shows very low but constant levels of dehydrogenation activity. This suggests that the gallium in the [Ga,Si]-EUO material was not active towards dehydrogenation. This could be because either the gallium is retained in the framework, after the thermal treatments to which it has been exposed, or the gallium has been ejected from the framework, but has remained primarily inside the microporous structure. If the gallium has remained in the channels then it may not have been exposed to the propane feed, since it is proposed that the micropores have become blocked by coke. The suggestion that the framework gallium species are primarily retained in the tetrahedrally coordinated sites in the EUO structure is supported by the XRPD derived unit cell volume studies carried out for the A and C series of EUO and MFI materials in Chapter 5. These studies and the ^{71}Ga NMR studies have suggested that gallium is readily incorporated into the EUO structure type and although a small amount of ejection was observed upon calcination the majority of the gallium species remained in the

Figure 6–6: Propene formation over the gallosilicate catalysts.

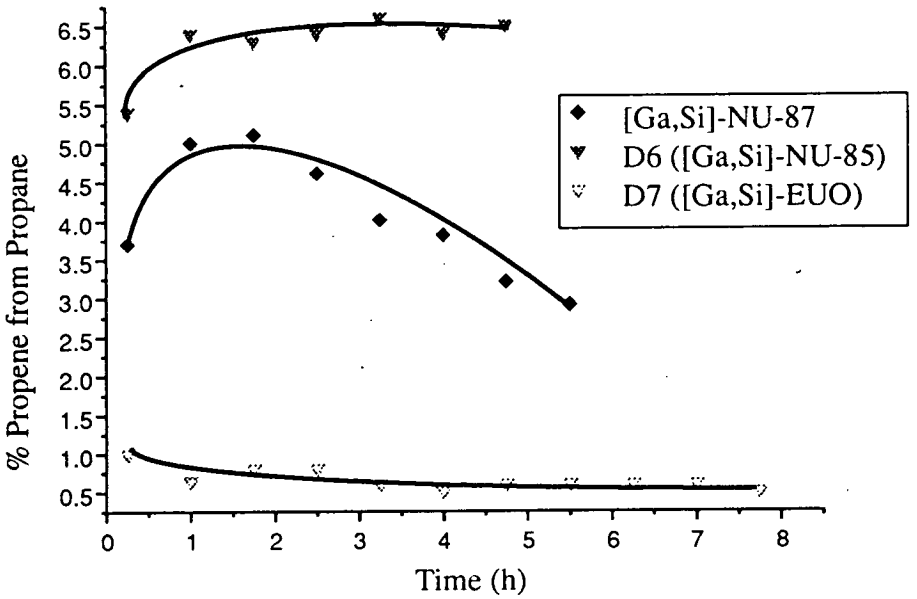

framework structure. It was noted in the study of D7 that there was a significant amount of carbon lost in the first sample analysis. This would be caused by carbon laydown on the catalyst, thus it is suggested that the material coked almost immediately. The low level of dehydrogenation observed could also be accounted for by a loss of gallium from the catalyst. Gallium oxide and suboxide species are known to be very mobile and relatively volatile and so could be lost from the catalyst [101, 102, 104, 110, 148].

The other gallosilicate materials show higher levels of dehydrogenation activity which suggest that there are more extra-framework gallium species present in the materials which do not have an exclusively EUO structure type and that these extra-framework gallium species are still accessible after pore blockage by coke. Both the D6 ([Ga,Si]-NU-85) and [Ga,Si]-NU-87 materials show increases in dehydrogenation activity after a short time on stream ($\approx$ 2h) which could be due to the creation of a larger number of active species under the conditions of the aromatisation reaction. These active dehydrogenation species could be created by either the ejection of gallium atoms from the framework and/or by the partial reduction of extra-framework gallium species. The increase in the amount of propene detected is in direct response to the reduction in aromatisation activity.

It has been proposed that propene formation is the rate determining step in this aromatisation reaction and so in the initial stages of the reaction, before deactivation of the catalysts, some of the propene produced was converted to BTX products. Hence, as this aromatisation activity was lost the apparent level of propene production increased. The [Ga,Si]-NU-87 material then loses its dehydrogenation activity much more rapidly than the D6 ([Ga,Si]-NU-85) material which suggest that the [Ga,Si]-NU-87 material initially had a much more homogeneous distribution of gallium in the framework which once ejected remained in the microporous channel structure and was subsequently lost from the dehydrogenation process by pore blockage from coking, whereas the [Ga,Si]-NU-85 material had a greater degree of externally supported gallium species which remained active in dehydrogenation for extended times.

Another important feature to consider is the external surface area of the crystallites [103]. D6 formed as smaller laths than the D7 material (D6 has an external surface area of $50m^2g^{-1}$ compared to $19m^2g^{-1}$ for D7) and so if the active gallium species were supported on the external surface of the crystallites then the smaller D6 crystallites offered a larger reaction area and consequently more active sites.

ZP2 Based Catalysts

The conversions of the total C_3 feed, over the ZP2 derived catalysts, are shown in Figure 6–7. It is apparent that the ZP2 derived catalysts were active in the short term but deactivated rapidly. Initially, the ZP2-5%IW material shows the highest level of conversion of all the samples prepared. This analysis was after a shorter time on stream (4 min) and so it could be suggested that this level of activity may also have been achieved by the other impregnated ZP2 catalyst before its rapid deactivation by coking. Clearly, the data sets for conversion over both ZP2-5IW and ZP2-3IW (Figure 6–7) could be represented by a single curve-fit. This would be expected if this conversion was related to the acidity of the materials and that conversion is insensitive to the difference between these Ga_2O_3 loadings. The conversion quoted is that of the total C_3 feed (propane and propene) and since the gallium is present to add a dehydrogenation function to create the propene,

Figure 6–7: Conversion of total C_3 feed, with time on stream, over the ZP2 based catalysts.

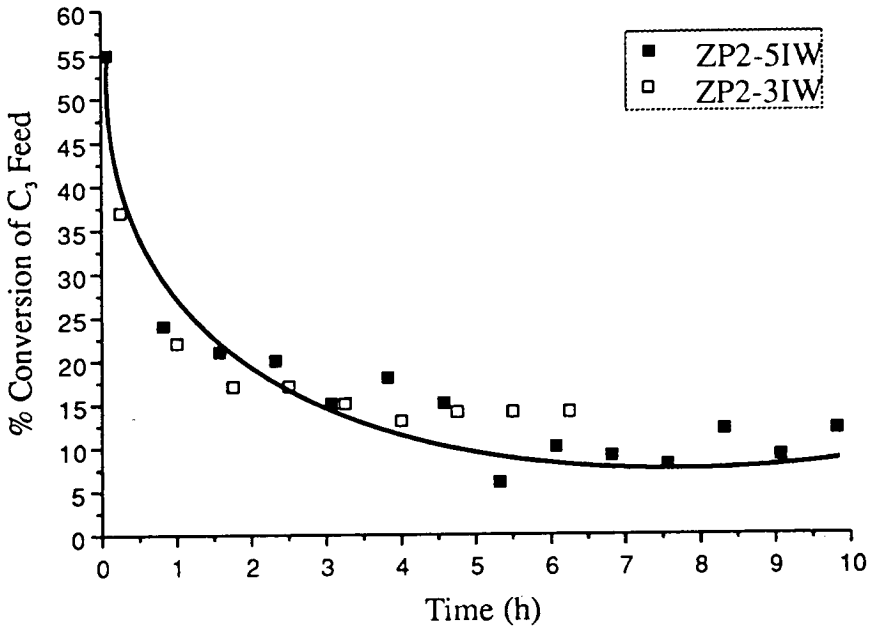

then these samples would be expected to show the same conversion since they have similar acidities. Hence, these materials cannot be discriminated by this reaction. This may be because of their similar acidity or that their Ga_2O_3 levels are essentially equivalent.

The dehydrogenation activity of these ZP2 based materials is represented in Figure 6–8. This shows that both of the impregnated materials are active towards dehydrogenation of the propane feed which suggests that the active gallium species for dehydrogenation are extra-framework and that these active species are still accessible even after deactivation of the BTX production of the catalyst. This suggests that the active gallium species are deposited on the external surface of the catalyst. It has already been stated that the IE and IW doping approaches adopted in this work would result in externally supported gallium species. There is an apparent induction period before the maximum level of dehydrogenation activity was observed. This correlates with the loss in aromatisation activity of the ZP2 based catalysts, as described previously. Some of the propene initially formed over these materials was rapidly converted to the BTX products while these acidic samples remained free from coke. However, as these materials deactivated,

Figure 6–8: Propene formation over the ZP2 based catalysts.

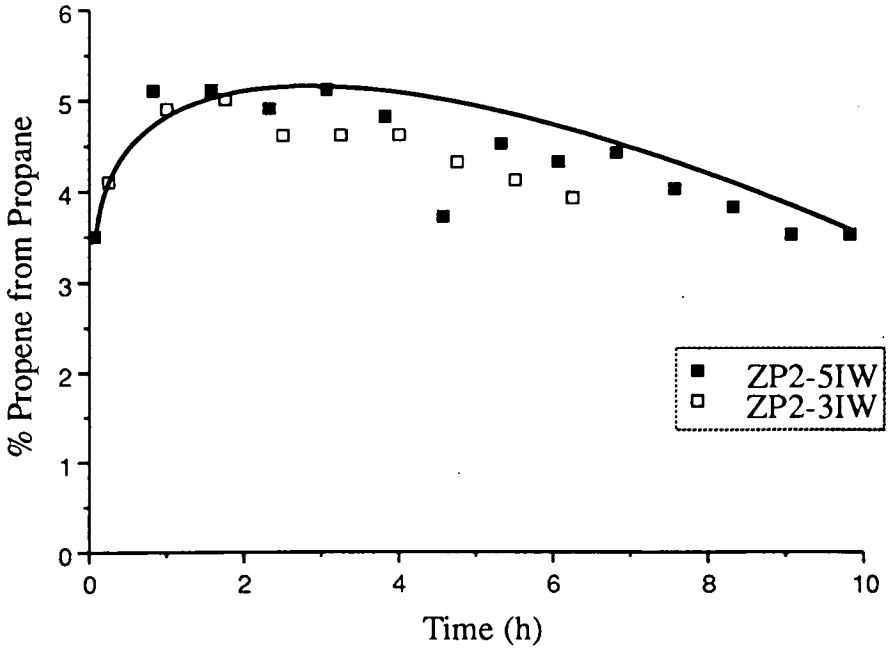

by coking, the acidic sites essential for the aromatisation reaction, were lost and consequently the propene in the product stream increased. This dehydrogenation activity decreased with time on stream due to further deactivation of the catalysts by coking of the external surface of the material and loss of active metal area by sintering of the active extra-framework species under the reaction conditions and loss of volatile gallium species from the catalyst [115, 148]. Since both ZP2-5IW and ZP2-3IW show almost identical dehydrogenation activity, it can be proposed that although the bulk gallium content varies between these catalysts the number of active sites is the same for both. This suggests that these gallium levels are possibly too high and that a saturation level has been reached, beyond the optimum gallium loading, with much of the gallium deposited on these zeolites inactive in this reaction.

ZP6 Based Catalysts

The conversions over the ZP6 derived catalysts are shown in Figure 6–9. It has already been stated that aromatisation activity is associated with the acidity of the catalyst. The ZP6 zeolite has an $\frac{SiO_2}{Al_2O_3}$ ratio of 712, so there are only a very small

number of acid sites in these materials and ZP6 based catalysts can effectively be considered as non-acidic. A small level of activity was observed over these catalysts with ZP6-3IW showing the highest level of conversion for the ZP6 based catalysts. The low conversions observed have relatively large errors associated with them, caused by both fluctuations in the feed composition and analysis errors and so these materials should be considered as showing equivalent levels of activity. This would be expected for materials based on the same non-acidic EU-1 zeolite. The ZP6 material has a negligible ion exchange capacity and so the IW and IE doping techniques can be considered as equivalent with the gallium species deposited on the external surface of the crystallites. The ZP6 crystallites are larger than the those of the ZP2 material (external surface area of $5m^2g^{-1}$ *cf.* $50m^2g^{-1}$) and so the high levels of gallium supported on the external surfaces are more likely to block the windows which lead to the microporous channel structure. Micromeritic pore volume analysis of these materials did not show significant loss of void volume after the doping procedures (Table 4–10); however, these pore volume analyses were carried out on samples which had not been fully activated so the gallium species were still in their nitrate form. Thermal activation of these freshly doped zeolites would result in sintering of the gallium, with the larger gallium oxide type species more likely to block the pore entrances and so reduce the activity of these materials. It should also be noted that these micropore volume measurements are based on uptake of N_2 which has a much smaller kinetic diameter than the hydrocarbon reactants. Hence, the N_2 micropore volume may underestimate the extent of pore blockage for the hydrocarbon reactants.

Figure 6–10 shows the level of propane dehydrogenation to propene observed over the ZP6 based catalysts. The ZP6 materials show levels of dehydrogenation activity which is directly proportional to the amount of Ga_2O_3 present. The ZP6-5IW sample shows a very high level of dehydrogenation activity which decreases at a constant rate. This loss of dehydrogenation activity is associated with deactivation of the sample by coking and also a loss in reactive metal surface area as the gallium species sinter to form larger clusters. As has already been stated it is also likely that a loss of dehydrogenation activity could be caused by the

Figure 6–9: Conversion of the total C_3 feed, with time on stream, over the ZP6 derived catalysts.

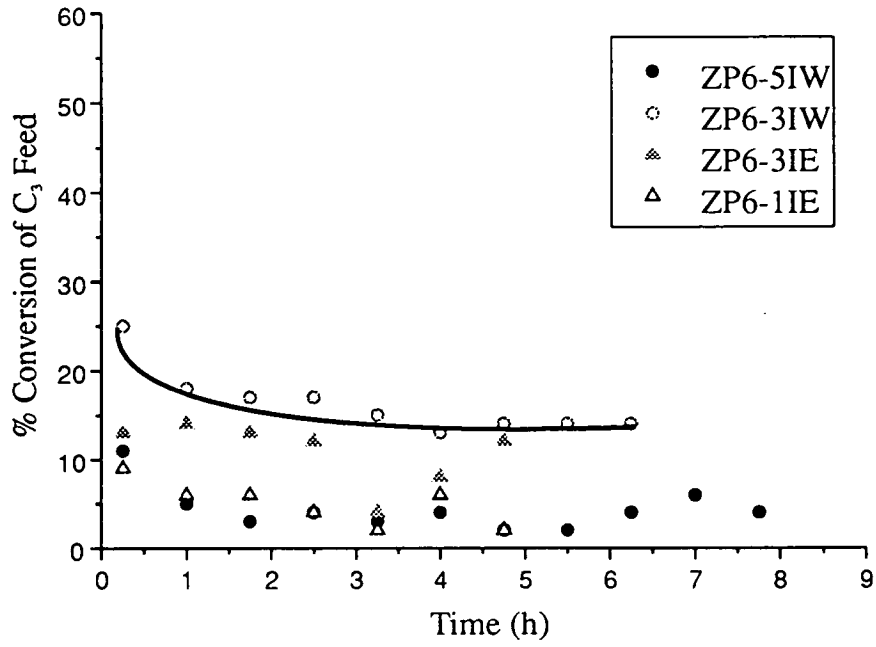

Figure 6–10: Propene formation over the ZP6 based catalysts.

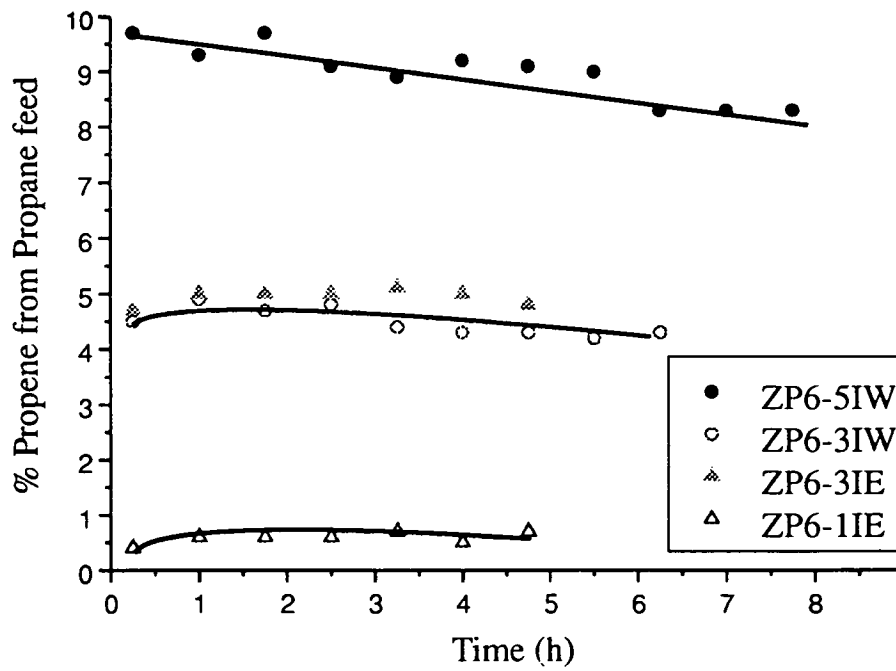

loss of volatile gallium species from the catalysts [148]. The ZP6-3IW shows a very slight initial increase in dehydrogenation activity which is associated with the reduction in conversion of the total C_3 feed. This is similar to the ZP2 series of materials where some of the propene initially produced was rapidly converted to the BTX products; however, as the catalyst deactivated, this conversion no longer occurred and the propene formed was left unreacted and so detected in the product gas stream. The ZP6-3IE showed dehydrogenation activity comparable to that of the ZP6-3IW material as expected since the doping procedures for these catalysts can be considered equivalent. The ZP6-1IE catalyst showed very low levels of dehydrogenation activity which suggests that this level of gallium doping was below the optimum level for significant propene production. It should also be considered that this surface deposition of gallium is highly irreproducible, as described in Chapter 1, and it is possible that the sample of ZP6-1IE examined had less than the average Ga_2O_3 loading of that batch of catalyst (0.8% Ga_2O_3) and consequently showed very low levels of dehydrogenation activity. Similarly, at such low gallium levels the deactivation by coking is likely to cause a more severe reduction in the number of available active gallium species and so result in the reduced dehydrogenation observed.

Comparison of EUO and NES Based Catalysts

Figure 6–11 compares the conversion of the total C_3 feed over the ZP2 and ZP6 based IW gallium doped catalysts. It is clear that all the EU-1 based catalysts show very rapid rates of deactivation caused by pore blockage of the unidimensional EUO channel structure. The ZP2 materials show higher levels of activity than the ZP6 based catalysts. This was expected since the ZP2 materials are very much more acidic than the ZP6 catalysts and it is known that these acid sites are essential for C_3 conversion. After around 6 hours on stream all the materials show a similar level of conversion which suggests that all these catalysts were essentially deactivated at that time.

Figure 6–12 compares the conversions over the EUO and NES materials. It is clear that the NES and ZP2 materials show extremely similar activities. It

Figure 6–11: Comparison of the conversion levels, with time on stream, over the ZP2 and ZP6 derived catalysts.

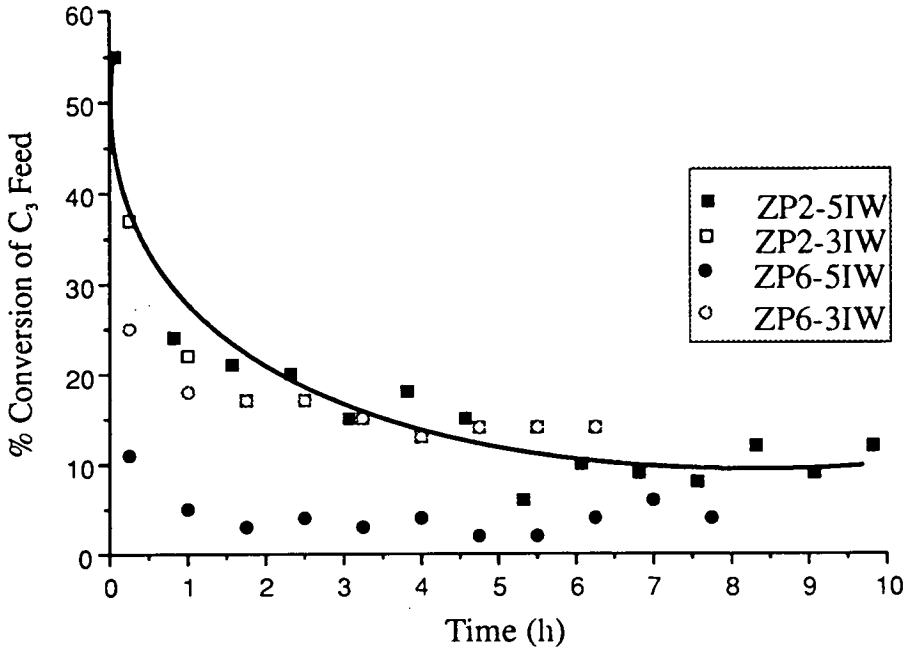

is proposed that this loss of total C_3 conversion over these catalysts (which do not have the benefit of the 3-D interconnecting channel structure of the MFI framework) is a consequence of the extremely rapid rates of deactivation by coking. It was suggested that materials with EUO and NES framework types deactivate rapidly, which is a reasonable proposition, for low dimensional materials. The ZP6 based material shows similar levels of conversion after deactivation but does not display the initial activity of the acidic materials. This was also expected since it was known that conversion of the C_3 feed required acid sites.

6.2.5 Modeling Selectivity

It has already been stated that the dehydrogenation and acidic functions may be treated as separate components in this process. A theoretical model for the product distributions expected from the materials examined is proposed from consideration of the range of possible reactions which could be responsible for the production of BTX products. The primary feed for the production of BTX has been proposed to be propene and so a list of possible reactions which could lead to Benzene,

Figure 6–12: Comparison of the conversion levels, with time on stream over, ZP2-5IW, ZP6-5IW and [Ga,Si]-NU-87.

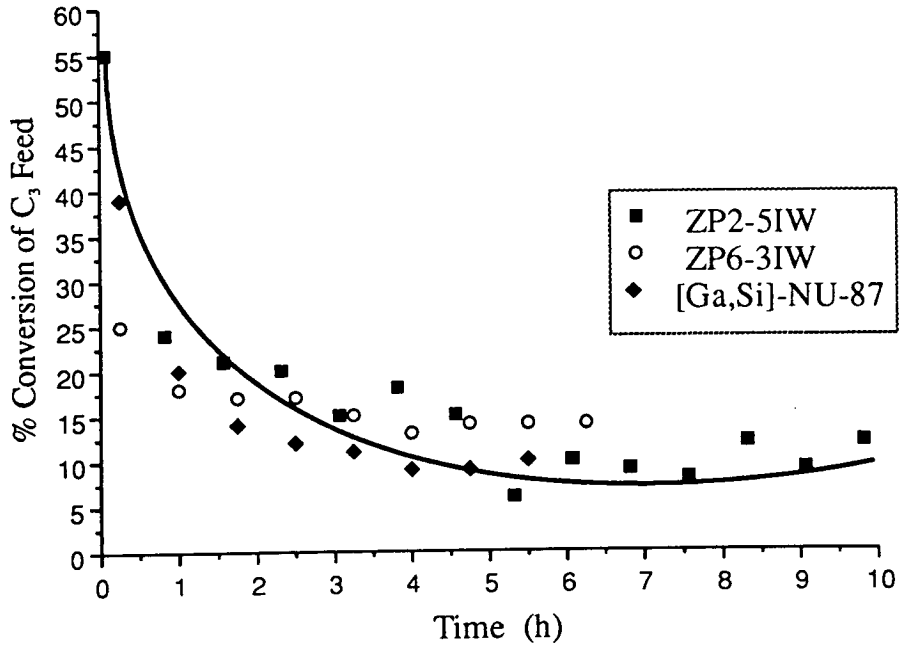

Toluene and Xylenes production is shown in Table 6–4. Reactions which result in carbon laydown (coking) are designated by the letter C and those which result in dilution of the gas stream by hydrogen evolution by the letter H.

From this table it is apparent that there are three possible reaction models to consider. Firstly, there is BTX production without significant coking. Secondly, there are processes which result purely in coking and thirdly there is the case where both BTX production and catalyst deactivation by coking are present. Each of these processes has a distinct BTX:C_1/C_2 selectivity ratio. Hence, it is proposed that examination of the selectivities to BTX and to cracked products, with conversion over these catalysts, could confirm the existence of such a model. The plots of selectivities against conversion for the Ga-ZSM-5 material and some of the catalysts prepared in this work are included in Figures 6–13, 6–14 and 6–15.

Figure 6–13 a) clearly show that the Ga-ZSM-5 catalyst fits the model perfectly for BTX production without significant coking. This was expected to be the case for the MFI derived material which exhibits a remarkable resistance to deactivation by coking. This model is extremely simplistic and is by no means completely

Table 6–4: Possible conversions leading to BTX and Coke formation.

Benzene formation from propene feed			
$2C_3H_6$	$\longrightarrow$	$C_6H_6 + 3H_2$	H
$3C_3H_6$	$\longrightarrow$	$C_6H_6 + 3C + 6H_2$	C,H
$3C_3H_6$	$\longrightarrow$	$C_6H_6 + 3CH_4$	-
$3C_3H_6$	$\longrightarrow$	$C_6H_6 + C + 2CH_4 + 2H_2$	C,H
$3C_3H_6$	$\longrightarrow$	$C_6H_6 + 2C + CH_4 + 4H_2$	C,H
$3C_3H_6$	$\longrightarrow$	$C_6H_6 + C_2H_6 + CH_4 + H_2$	H
$3C_3H_6$	$\longrightarrow$	$C_6H_6 + C_2H_4 + CH_4 + 2H_2$	H
Toluene formation from propene feed			
$3C_3H_6$	$\longrightarrow$	$C_7H_8 + 2C + 5H_2$	C,H
$3C_3H_6$	$\longrightarrow$	$C_7H_8 + C + CH_4 + 3H_2$	C,H
$3C_3H_6$	$\longrightarrow$	$C_7H_8 + CH_4 + H_2$	H
$3C_3H_6$	$\longrightarrow$	$C_7H_8 + C_2H_6 + H_2$	H
$3C_3H_6$	$\longrightarrow$	$C_7H_8 + C_2H_4 + 2H_2$	H
Xylenes formation from propene feed			
$3C_3H_6$	$\longrightarrow$	$C_8H_{10} + C + 4H_2$	C,H
$3C_3H_6$	$\longrightarrow$	$C_8H_{10} + CH_4 + 2H_2$	H
Total composition for non-coking reactions			
$23\ C_3H_6$	$\longrightarrow$	$8BTX + 12C_1/C_2$	H
		Selectivities; BTX 40 : C_1/C_2 60	
Total composition for only coking reactions			
$18\ C_3H_6$	$\longrightarrow$	$6BTX + 4C_1/C_2$	C
		Selectivities; BTX 60 : C_1/C_2 40	
This coking model neglects coke from other hydrocarbons. An estimate of this contribution can be obtained from the following			
$1C_3H_8$	$\longrightarrow$	$C + 2CH_4$	C
$2C_3H_8$	$\longrightarrow$	$3C_2H_4 + 2H_2$	H
$2C_3H_8$	$\longrightarrow$	$2C_2H_6 + 2CH_4 - 2H_2$	-H
$1C_2H_6$	$\longrightarrow$	$2CH_4 - 2H_2$	-H
$1C_2H_4$	$\longrightarrow$	$2CH_4 - H_2$	-H
Total composition for coking and non-coking reactions			
$41\ C_3H_6$	$\longrightarrow$	$14BTX + 28C_1/C_2$	C,H
		Selectivities; BTX 33 : C_1/C_2 67	

Figure 6–13: Plots of selectivity to BTX and C_1/C_2 fractions with conversion for, a) Ga-ZSM-5 and b) [Ga,Si]-NU-87.

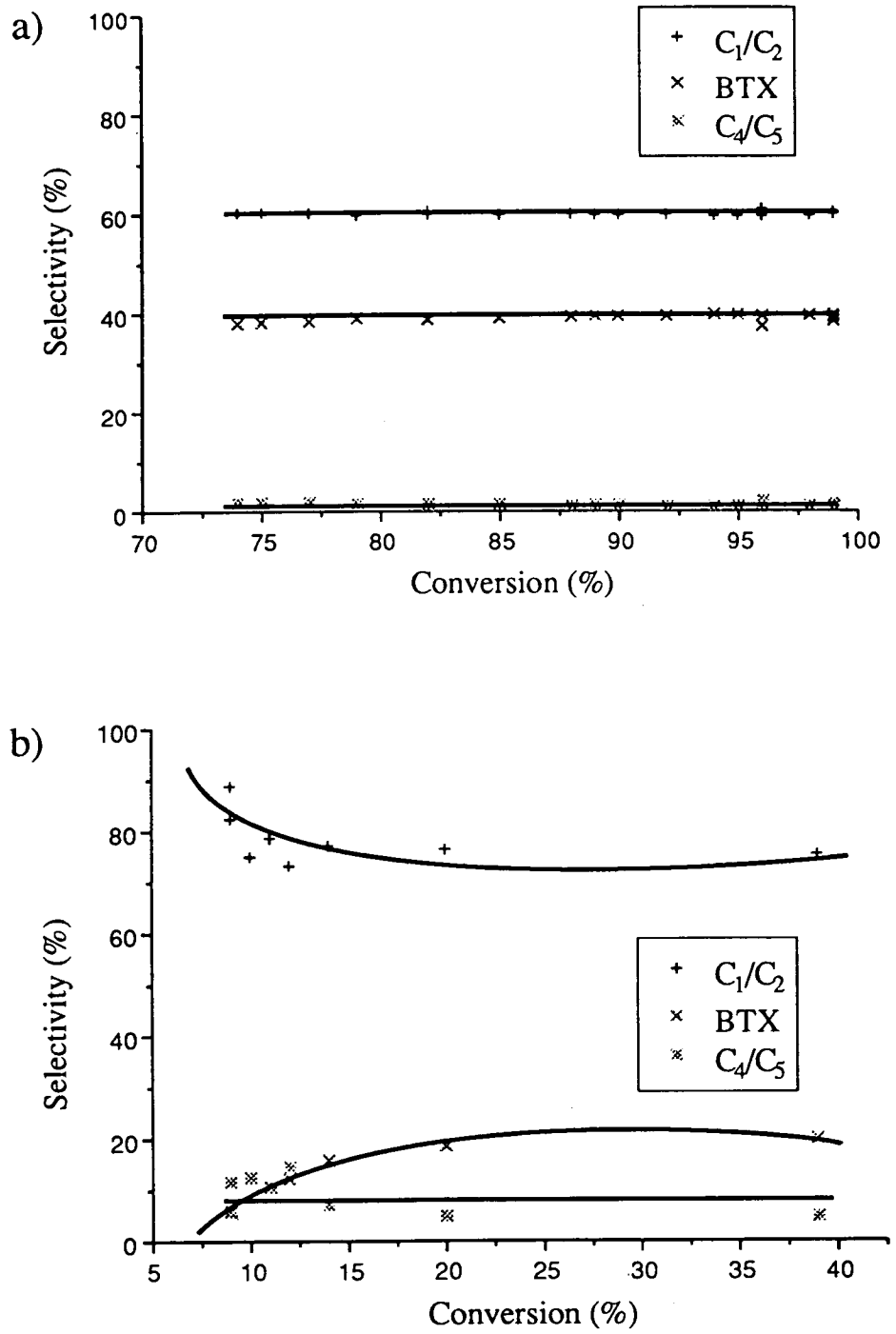

Figure 6–14: Plots of selectivity to BTX and C_1/C_2 fractions with conversion for, a) D6 and b) ZP2-5IW

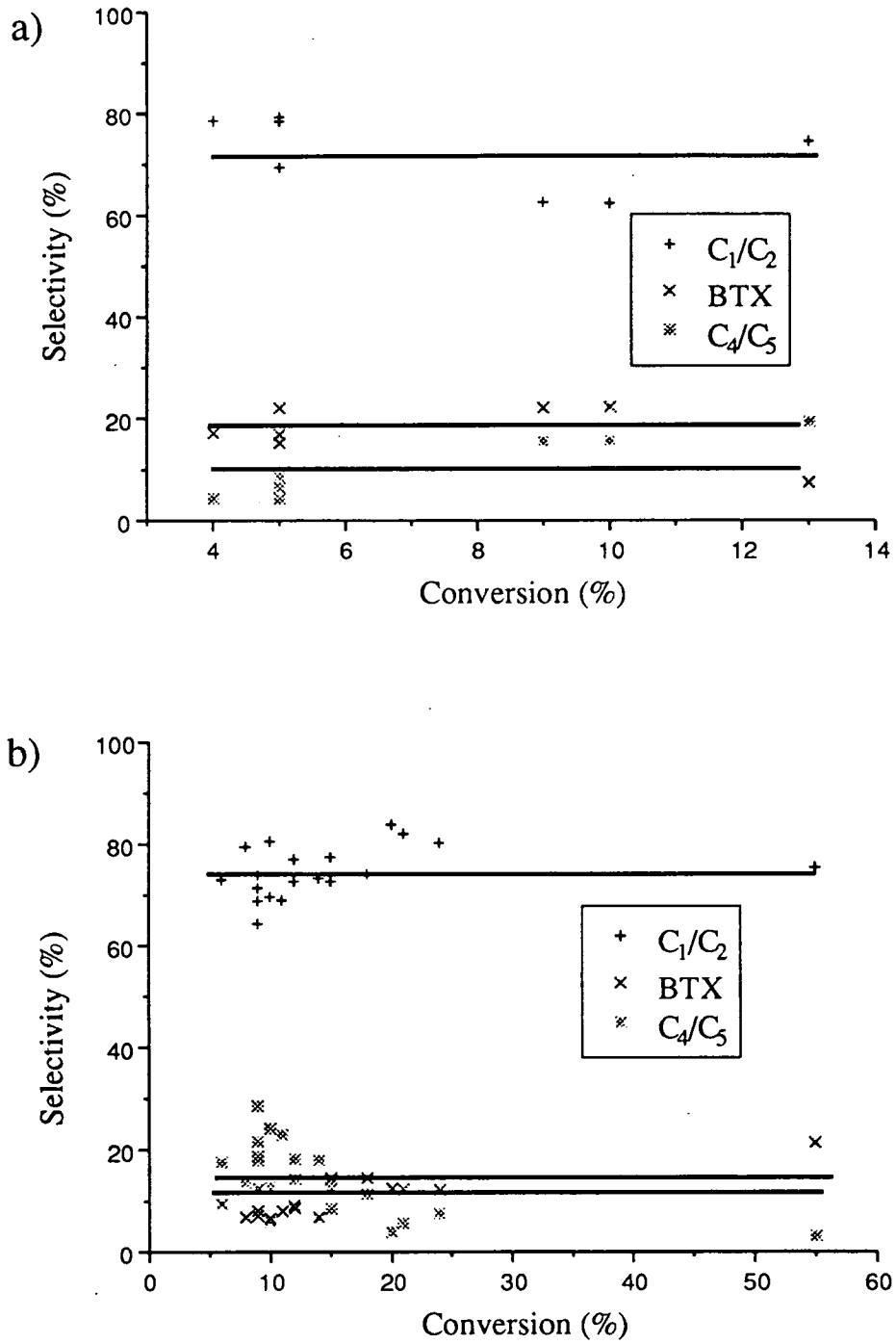

Figure 6–15: Plots of selectivity to BTX and C_1/C_2 fractions with conversion for, a) ZP6-3IE and b) Data from EUO, NU-85 and NES based catalysts.

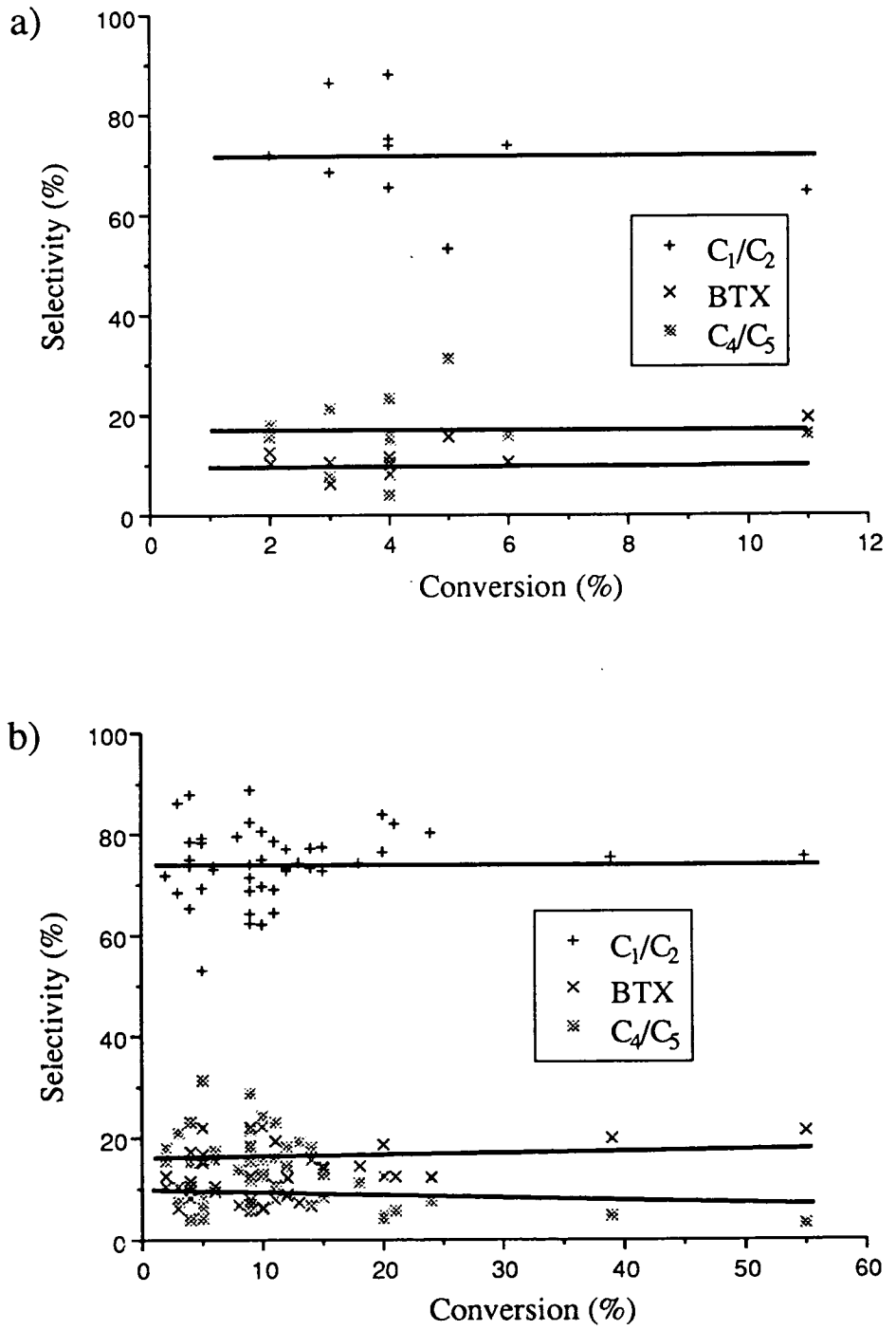

rigorous, however, it is proposed that successful BTX production, without significant deactivation by coking, would result in a BTX:C_1/C_2 ratio of 40:60. The Ga-ZSM-5 material shows precisely this and so is modeled remarkably well by this simple approach.

The [Ga,Si]-NU-87 material shown alongside the Ga-ZSM-5 material in Figure 6–13 b) shows a selectivity trend very close to that expected for the model which simulates BTX production which is severely hampered by coking. Significant coking would be associated with a significant evolution of hydrogen rich fragments (*eg.* CH_4) which are released as a consequence of the formation of the hydrogen deficient carbonaceous deposits (coke). As a result of this a BTX:C_1/C_2 ratio of 33:67 would be expected. It is known that as coke is formed it is also likely to partially degrade by releasing small hydrocarbon fragments [108] which would cause the observed ratio of BTX:C_1/C_2 to increase in favour of the C_1/C_2 fraction. This has not been quantified but it is proposed that a ratio of <33:>67 would be expected. The increase in C_1/C_2 selectivity at very low conversions (longer times on stream) over this material can be explained by this gradual degradation of the carbonaceous deposits on the [Ga,Si]-NU-87 material, as described previously, so increasing the selectivity to these small products.

Figures 6–14 a) and b) and Figure 6–15 a) show the EUO and NU-85 materials to closely mimic the model which accounts for coking of the active catalysts. This is in excellent agreement with the earlier propositions that the catalysts prepared were potentially active in the propane conversion reactions; however, they were rapidly deactivated by coking. The higher than expected selectivities to C_1/C_2 fragments can be assigned to the decomposition of some of the carbonaceous deposits which have deactivated the catalysts, as described previously. Small carbon containing fragments can readily break away from the carbonaceous layer and be detected as small hydrocarbons from these materials which have such a high propensity to form coke. Although this approach is extremely simplistic it models the selectivities observed over these catalysts remarkably well. The data for several of the EU-1, NU-85 and NU-87 catalysts are shown as a single plot in

Figure 6–15 b), which shows that this model excellently predicts the selectivities of these materials over a large range of conversions.

Hence, to summarise, the Ga-ZSM-5 material showed remarkable activity in the conversion of propane feed. This high level of activity was retained for extended times (>16 h) with an excellent selectivity to the desired BTX fraction. This selectivity was predicted by the simple model for BTX production without significant deactivation by coking. The gallosilicate and gallium loaded ZP2 (acidic EU-1) materials initially showed high levels of activity in the conversion of the total C_3 feed. This was short lived as the lower dimensional channel structures of the EUO, NES and NU-85 materials all deactivated rapidly by coking. The selectivities of these catalysts was also predicted by the model for activity with rapid deactivation by coking. This suggests that these materials were active in such a conversion; however, the low dimensional EUO and NES channel structures were more prone to coking than the ZSM-5 based material and so they were not as effective in catalysing this reaction. The aim of this study was to elucidate the components required for successful aromatisation of the propane feed. This has clearly been achieved since it can be concluded that the main requisites for aromatisation are extra-framework gallium species which are in close proximity to the strong acid sites of the zeolite framework and these must be maintained in a coke free environment. The theoretical model for product distribution excellently mimics the observed distributions for the materials examined and so comparison of experimental results with this model allows qualitative estimates to be made of the reaction pathway which was followed over the catalyst in question.

Table 6–5: Summary of product distributions over Ga-ZSM-5.

Time	C_3H_8	C_1/C_2	C_3H_6	C_4/C_5	BTX	Con.[a]	Selectivity[b]			
hours	%v/v	%v/v	%v/v	%v/v	%v/v	% g^{-1}	C_3H_6[c]	C_1/C_2	$C_{4/5}$	BTX
0.25	7.38	6.31	0.58	0.21	3.86	96	2.7	60.7	2.1	37.2
1.0	6.72	6.30	0.57	0.17	4.02	99	2.7	60.1	1.6	38.3
1.75	6.78	6.22	0.60	0.12	4.08	99	2.8	59.7	1.2	39.1
2.5	6.82	6.09	0.62	0.10	4.05	99	2.8	59.5	0.9	39.6
3.25	7.03	6.04	0.63	0.12	4.01	98	2.9	59.4	1.2	39.4
4.0	7.30	5.95	0.69	0.14	3.94	96	3.2	59.3	1.4	39.3
4.75	7.36	5.82	0.66	0.11	3.88	95	3.1	59.3	1.1	39.6
5.5	7.56	5.68	0.68	0.11	3.79	94	3.1	59.3	1.1	39.6
6.25	7.79	5.63	0.69	0.11	3.71	92	3.2	59.6	1.1	39.3
7.0	8.02	5.52	0.72	0.11	3.64	90	3.4	59.5	1.2	39.3
7.75	8.20	5.37	0.71	0.11	3.55	89	3.3	59.5	1.2	39.3
8.5	8.40	5.28	0.71	0.11	3.46	88	3.3	59.7	1.2	39.1
9.25	8.72	5.22	0.73	0.13	3.41	85	3.4	59.6	1.5	38.9
10.0	9.08	5.12	0.75	0.14	3.31	82	3.5	59.7	1.7	38.6
10.75	9.14	5.03	0.77	0.13	3.21	82	3.6	60.3	1.2	38.5
12.0	9.34	4.87	0.73	0.13	3.19	79	3.4	59.5	1.6	38.9
13.5	9.81	4.66	0.79	0.14	2.98	77	3.7	59.9	1.8	38.3
14.25	10.02	4.54	0.80	0.14	2.88	75	3.7	60.1	1.8	38.1
15.0	10.23	4.46	0.84	0.14	2.82	74	3.9	60.1	1.9	38.0

[a]Conversion from total C_3 feed (C_3H_8 + C_3H_6), [b] Selectivity from total C_3 feed (Propane and Propene). [c] % C_3H_6 produced from C_3H_8 feed.

Table 6–6: Summary of product distributions over [Ga,Si]-NU-87.

Time	C_3H_8	C_1/C_2	C_3H_6	C_4/C_5	BTX	Con.[a]	Selectivity[b]			
hours	%v/v	%v/v	%v/v	%v/v	%v/v	% g^{-1}	$C_3H_6^c$	C_1/C_2	$C_{4/5}$	BTX
0.25	17.39	1.78	0.92	0.11	0.47	39	3.7	75.4	4.7	19.9
1.0	20.11	0.78	1.22	0.05	0.19	20	5.0	76.5	4.9	18.6
1.75	21.13	0.44	1.25	0.04	0.09	14	5.1	77.2	7.0	15.8
2.5	21.58	0.30	1.13	0.06	0.05	12	4.6	73.2	14.6	12.2
3.25	21.84	0.22	0.99	0.03	0.03	11	4.0	78.6	10.5	10.7
4.0	22.24	0.24	0.93	0.02	0.01	9	3.8	88.8	5.5	5.7
4.75	22.29	0.14	0.80	0.02	0.01	9	3.2	82.4	11.7	5.9
5.5	22.26	0.12	0.72	0.02	0.02	10	2.9	75.0	12.5	12.5

[a]Conversion from total C_3 feed (C_3H_8 + C_3H_6), [b] Selectivity from total C_3 feed (Propane and Propene). [c] % C_3H_6 produced from C_3H_8 feed.

Table 6–7: Summary of product distributions over D6.

Time	C_3H_8	C_1/C_2	C_3H_6	C_4/C_5	BTX	Con.[a]	Selectivity[b]			
hours	%v/v	%v/v	%v/v	%v/v	%v/v	% g^{-1}	$C_3H_6^c$	C_1/C_2	$C_{4/5}$	BTX
0.25	22.23	1.01	1.44	0.10	0.25	13	5.4	74.3	19.3	7.4
1.0	23.77	0.72	1.68	0.09	0.23	5	6.4	69.3	8.6	22.1
1.75	22.95	0.58	1.66	0.15	0.20	9	6.3	62.4	15.5	22.1
2.5	22.71	0.56	1.68	0.14	0.20	10	6.4	62.2	15.6	22.2
3.25	23.69	0.76	1.75	0.04	0.16	5	6.6	79.2	4.1	16.7
4.0	24.0	0.73	1.70	0.04	0.16	4	6.4	78.5	4.3	17.2
4.75	23.67	0.72	1.71	0.06	0.14	5	6.3	78.3	6.5	15.2

[a]Conversion from total C_3 feed (C_3H_8 + C_3H_6), [b] Selectivity from total C_3 feed (Propane and Propene). [c] % C_3H_6 produced from C_3H_8 feed.

Table 6–8: Summary of product distributions over D7.

Time	C_3H_8	C_1/C_2	C_3H_6	C_4/C_5	BTX	Con.[a]	Selectivity[b]			
hours	%v/v	%v/v	%v/v	%v/v	%v/v	% g^{-1}	$C_3H_6^c$	C_1/C_2	$C_{4/5}$	BTX
0.25	23.01	0.11	0.22	0.10	0	2	1.0	52.4	47.6	0
1.0	22.05	0.06	0.15	0.10	0	8	0.64	37.5	62.5	0
1.75	21.83	0.05	0.19	0.13	0	9	0.8	27.8	72.2	0
2.5	22.04	0.03	0.19	0.13	0	8	0.8	18.75	81.25	0
3.25	21.74	0.06	0.13	0.01	0	10	0.6	86.8	13.2	0
4.0	22.42	0.11	0.10	0.001	0	6	0.5	92.6	7.4	0
4.75	21.93	0.03	0.13	0.01	0	9	0.6	42.9	47.1	0
5.5	23.28	0.12	0.14	0.01	0	2	0.6	92.3	7.7	0
6.25	22.70	0.12	0.14	0.01	0	4	0.6	92.3	7.7	0
7.0	22.15	0.11	0.13	0.01	0	7	0.6	91.7	8.3	0
7.75	23.58	0.11	0.12	0.01	0	2	0.5	91.7	8.3	0

[a]Conversion from total C_3 feed (C_3H_8 + C_3H_6), [b] Selectivity from total C_3 feed (Propane and Propene). [c] % C_3H_6 produced from C_3H_8 feed.

Table 6–9: Summary of product distributions over D9.

Time	C_3H_8	C_1/C_2	C_3H_6	C_4/C_5	BTX	Con.[a]	Selectivity[b]			
hours	%v/v	%v/v	%v/v	%v/v	%v/v	% g^{-1}	$C_3H_6^c$	C_1/C_2	$C_{4/5}$	BTX
0.25	26.44	0.13	0.21	0.12	0	12	0.7	52.0	48.0	0
1.0	27.37	0.12	0.27	0.12	0	6	0.9	50.0	50.0	0
1.75	27.57	0.17	0.18	0.11	0	5	0.6	60.7	39.3	0
2.5	26.81	0.11	0.14	0.14	0	10	0.5	44.0	56.0	0
8.5	26.71	0.15	0.11	0.06	0	11	0.5	71.4	28.6	0

[a]Conversion from total C_3 feed (C_3H_8 + C_3H_6), [b] Selectivity from total C_3 feed (Propane and Propene). [c] % C_3H_6 produced from C_3H_8 feed.

Table 6–10: Summary of product distributions over ZP6-5% IW.

Time	C_3H_8	C_1/C_2	C_3H_6	C_4/C_5	BTX	Con.[a]	Selectivity[b]			
hours	%v/v	%v/v	%v/v	%v/v	%v/v	% g^{-1}	$C_3H_6^c$	C_1/C_2	$C_{4/5}$	BTX
0.25	22.25	0.2	2.59	0.05	0.06	11	9.7	64.5	16.1	19.4
1.0	22.41	0.17	2.47	0.10	0.05	5	9.3	53.1	31.3	15.6
1.75	22.65	0.56	2.58	0.05	0.04	3	9.7	86.2	7.6	6.2
2.5	22.50	0.43	2.43	0.02	0.04	4	9.1	87.8	4.0	8.2
3.25	22.85	0.26	2.38	0.08	0.04	3	8.9	68.4	21.1	10.5
4.0	23.53	0.3	2.44	0.06	0.04	4	9.2	75.0	15.0	10.0
4.75	24.18	0.28	2.41	0.07	0.04	2	9.1	71.8	17.9	10.3
5.5	23.89	0.23	2.39	0.05	0.04	2	9.0	71.9	15.6	12.5
6.25	23.82	0.28	2.21	0.06	0.04	4	8.3	73.7	15.8	10.5
7.0	23.46	0.28	2.21	0.06	0.04	6	8.3	73.7	15.8	10.5
7.75	23.68	0.17	2.22	0.06	0.03	4	8.3	65.4	23.1	11.5

[a]Conversion from total C_3 feed (C_3H_8 + C_3H_6), [b] Selectivity from total C_3 feed (Propane and Propene). [c] % C_3H_6 produced from C_3H_8 feed.

Table 6–11: Summary of product distributions over ZP6-3% IW.

Time	C_3H_8	C_1/C_2	C_3H_6	C_4/C_5	BTX	Con.[a]	Selectivity[b]			
hours	%v/v	%v/v	%v/v	%v/v	%v/v	% g^{-1}	$C_3H_6^c$	C_1/C_2	$C_{4/5}$	BTX
0.25	20.43	1.47	1.16	0.20	0.66	25	4.5	63.1	8.6	28.3
1.0	20.77	0.43	1.28	0.07	0.31	18	4.9	53.1	8.6	38.3
1.75	21.31	0.10	1.21	0.12	0.15	17	4.7	27.0	23.0	40.0
2.5	21.46	0.09	1.24	0.06	0.15	15	4.8	30.0	20.0	50.0
3.25	21.79	0.09	1.15	0.05	0.12	17	4.4	34.6	19.2	46.2
4.0	21.59	0.10	1.13	0.07	0.09	15	4.3	38.5	26.9	34.6
4.75	21.51	0.09	1.14	0.04	0.08	14	4.3	42.9	19.0	38.1
5.5	21.66	0.08	1.09	0.04	0.04	16	4.2	50.0	25.0	25.0
6.25	21.54	0.08	1.11	0.06	0.01	14	4.3	53.3	40.0	6.7

[a]Conversion from total C_3 feed (C_3H_8 + C_3H_6), [b] Selectivity from total C_3 feed (Propane and Propene). [c] % C_3H_6 produced from C_3H_8 feed.

Table 6–12: Summary of product distributions over ZP6-3% IE.

Time	C_3H_8	C_1/C_2	C_3H_6	C_4/C_5	BTX	Con.[a]	Selectivity[b]			
hours	%v/v	%v/v	%v/v	%v/v	%v/v	% g^{-1}	$C_3H_6^c$	C_1/C_2	$C_{4/5}$	BTX
0.25	20.98	0.08	1.10	0.10	0	13	4.7	44.4	55.6	0
1.0	20.78	0.09	1.15	0.09	0	14	5.0	50.0	50.0	0
1.75	20.82	0.11	1.16	0.11	0	13	5.0	50.0	50.0	0
2.5	21.10	0.08	1.17	0.09	0	12	5.0	47.1	52.9	0
3.25	22.30	0.1	1.17	0.09	0	4	5.1	52.6	47.4	0
4.0	21.59	0.08	1.15	0.10	0	8	5.0	44.4	55.6	0
4.75	21.04	0.08	1.11	0.08	0	12	4.8	50.0	50.0	0

[a]Conversion from total C_3 feed (C_3H_8 + C_3H_6), [b] Selectivity from total C_3 feed (Propane and Propene). [c] % C_3H_6 produced from C_3H_8 feed.

Table 6–13: Summary of product distributions over ZP6-1% IE.

Time	C_3H_8	C_1/C_2	C_3H_6	C_4/C_5	BTX	Con.[a]	Selectivity[b]			
hours	%v/v	%v/v	%v/v	%v/v	%v/v	% g^{-1}	$C_3H_6^c$	C_1/C_2	$C_{4/5}$	BTX
0.25	22.52	0.08	0.10	0.09	0	9	0.4	47.1	52.9	0
1.0	22.88	0.12	0.15	0.10	0	6	0.6	54.5	45.5	0
1.75	22.90	0.02	0.15	0.09	0	6	0.6	18.8	81.2	0
2.5	23.18	0.08	0.16	0.01	0	4	0.6	88.8	11.2	0
3.25	23.48	0.14	0.20	0.02	0	2	0.7	81.5	18.5	0
4.0	22.91	0.01	0.12	0.07	0	6	0.5	12.5	87.5	0
4.75	23.72	0.13	0.19	0.01	0	2	0.7	92.9	7.1	0

[a]Conversion from total C_3 feed (C_3H_8 + C_3H_6), [b] Selectivity from total C_3 feed (Propane and Propene). [c] % C_3H_6 produced from C_3H_8 feed.

Table 6–14: Summary of product distributions over ZP2-5% IW.

Time	C_3H_8	C_1/C_2	C_3H_6	C_4/C_5	BTX	Con.[a]	Selectivity[b]			
hours	%v/v	%v/v	%v/v	%v/v	%v/v	% g^{-1}	$C_3H_6^c$	C_1/C_2	$C_{4/5}$	BTX
0.25	16.30	4.37	0.96	0.18	1.24	55	3.5	75.5	3.1	21.4
1.0	21.46	1.84	1.38	0.17	0.28	24	5.1	80.3	7.5	12.2
1.75	21.97	1.33	1.37	0.09	0.2	21	5.1	82.1	5.6	12.3
2.5	22.16	1.15	1.32	0.07	0.15	20	4.9	83.9	4.0	12.1
3.25	23.08	0.55	1.37	0.06	0.1	15	5.1	77.5	8.4	14.1
4.0	22.53	0.46	1.30	0.07	0.09	18	4.8	74.2	11.3	14.5
4.75	23.15	0.4	1.22	0.08	0.07	15	3.7	72.7	12.8	14.5
5.5	24.78	0.46	1.23	0.11	0.06	6	4.5	73.0	17.5	9.5
6.25	24.21	0.5	1.16	0.08	0.04	10	4.3	80.6	12.9	6.5
7.0	25.34	0.37	1.18	0.09	0.04	9	4.4	74.0	18.0	8.0
7.75	24.58	0.35	1.09	0.06	0.03	8	4.0	79.5	13.7	6.8
8.5	23.98	0.24	1.03	0.06	0.03	12	3.8	72.7	18.2	9.1
9.25	24.59	0.22	0.96	0.06	0.04	9	3.5	68.8	18.7	12.5
10.0	24.10	0.27	0.96	0.05	0.03	12	3.5	77.1	14.3	8.6
10.75	23.67	0.22	0.94	0.06	0.02	14	3.5	73.3	18.1	8.6
11.5	23.79	0.2	0.86	0.06	0.02	9	3.2	71.4	21.5	7.1
12.25	24.69	0.18	0.87	0.08	0.02	9	3.3	64.3	28.6	7.1
13.0	24.59	0.23	0.82	0.08	0.02	10	3.0	69.7	24.2	6.1
13.75	24.28	0.18	0.79	0.06	0.02	11	2.9	69.0	23.0	8.0

[a]Conversion from total C_3 feed (C_3H_8 + C_3H_6), [b] Selectivity from total C_3 feed (Propane and Propene). [c] % C_3H_6 produced from C_3H_8 feed.

Table 6–15: Summary of product distributions over ZP2-3% IW.

Time	C_3H_8	C_1/C_2	C_3H_6	C_4/C_5	BTX	Con.[a]	Selectivity[b]			
hours	%v/v	%v/v	%v/v	%v/v	%v/v	% g^{-1}	$C_3H_6^c$	C_1/C_2	$C_{4/5}$	BTX
0.25	18.14	2.53	1.03	0.12	0.78	37	4.1	73.8	3.5	22.7
1.0	20.26	1.23	1.22	0.10	0.37	22	4.9	72.4	5.8	21.8
1.75	20.92	0.89	1.24	0.11	0.21	17	5.0	73.6	9.0	17.4
2.5	21.24	0.67	1.14	0.06	0.16	17	4.6	75.3	6.7	18.0
3.25	21.46	0.53	1.14	0.06	0.11	15	4.6	75.7	9.6	15.7
4.0	21.78	0.44	1.08	0.06	0.08	13	4.3	75.9	10.3	13.8
4.75	21.63	0.39	1.03	0.06	0.06	14	4.1	76.5	11.7	11.8
5.5	21.65	0.33	0.96	0.04	0.06	14	3.9	76.7	9.3	14.0
6.25	21.72	0.29	0.92	0.03	0.03	14	3.7	82.9	8.5	8.6

[a]Conversion from total C_3 feed (C_3H_8 + C_3H_6), [b] Selectivity from total C_3 feed (Propane and Propene). [c] % C_3H_6 produced from C_3H_8 feed.

6.3 Recirculating Catalytic Studies

6.3.1 Introduction

This section details the catalytic investigations carried out in Edinburgh using a continuously recirculating gas apparatus to examine a range of materials in the propane aromatisation reaction.

6.3.2 Experimental Procedure

The recirculating apparatus is shown schematically in Figure 6–16 and may be considered as three separate components; the glass line where gas handling was carried out, the recirculating loop where the reactant gases were passed over the catalyst and the product identification section composed of a FID gas chromatograph, Integrator and chart recorder. The gas handling line was made from Pyrex glass partitioned by Springham ground glass vacuum taps sealed with Apiezon L grease. The glass line of the recycling loop also utilised Springham taps, however, the by-pass taps, located above the furnace, were greaseless Young's taps used to prevent any lubricant melting at the elevated temperatures observed in that region.

Two mercury diffusion pumps, backed by Edwards rotary pumps, with cold traps maintained before the diffusion pumps, were used to evacuate the apparatus. Sample gas pressure in the line was measured by a manometer and pressure in the line was measured by a McLeod gauge.

The catalyst was held in a U-shaped stainless-steel vessel ($\frac{1}{8}''$ with the catalyst pellets housed in a section of $\frac{1}{4}''$ stainless-steel) connected to the line by swagelok fittings to glass/metal joints. A furnace [237] was placed around the vessel and was controlled by a Eurotherm temperature controller with temperature displayed by a Comark 5000 digital thermometer. Thermocouples for both devices were held in intimate contact with the reaction vessel.

Gas pumping around the reaction system was achieved by a MB21E circulating pump (Metal Bellows Company) and samples were withdrawn from this circulated system from a Carle minivolume sampling valve. These were then analysed by a Sigma 3B FID gas chromatograph (Perkin Elmer). The best separations were achieved with a 3m column of $\frac{1}{8}''$ o.d. stainless steel loaded with 3% squalane on alumina. Nitrogen was used as the carrier gas (20psi) with hydrogen (18psi) and air (25psi) used as the flame feed and the column maintained at 353 K. These gases were obtained from B.O.C. and propane gas, the main reactant gas used in this work, was obtained from Matheson Gases (C.P. Grade, 99.5%).

Signals were amplified and sent to a Laboratory Data Control 308/9 integrator and displayed on a Servoscribe RE11.20 recorder. Calibration standards were used to determine retention times for the hydrocarbons expected from these reactions. Sensitivity factors for hydrocarbons were obtained from the tables prepared by Dietz [238]. These factors were all ≈ 1 for the hydrocarbons in these studies and so little difference in sensitivity between the components of the gas phase were expected. Once the peaks on the output trace of the GC analyser were identified by comparison of their retention time to the standard data the peak areas recorded by the integrator were corrected for carbon content of the hydrocarbons (equ. 6.3).

$$Corrected\ Area(x) = \frac{Peak\ Area\ Recorded(x)}{Carbon\ Fraction(x)\ \times\ Sensitivity\ Factor(x)} \qquad (6.3)$$

The percentage composition of the recirculating gas was then calculated (equ. 6.4).

$$\%Carbon(x) = \left\{ \frac{Corrected\ Area(x)}{\sum Corrected\ Areas} \right\} \times 100\% \qquad (6.4)$$

The product distributions obtained for the recirculating reactions are presented as Carbon %.

In recirculating reactors, initial rates of reactions can be obtained if conversion levels are low ($\leq$15%) and also given that the sampling procedure does not distort the composition of the recirculating gas significantly. The rate of reactant consumption is readily determined, however, estimation of the rate of product generation is complicated if there is more than one route to any particular product. In this work the production of C_1/C_2 fractions can be directly attributed to acid

Figure 6–16: Schematic of the glass line cycling reactor used for catalytic studies.

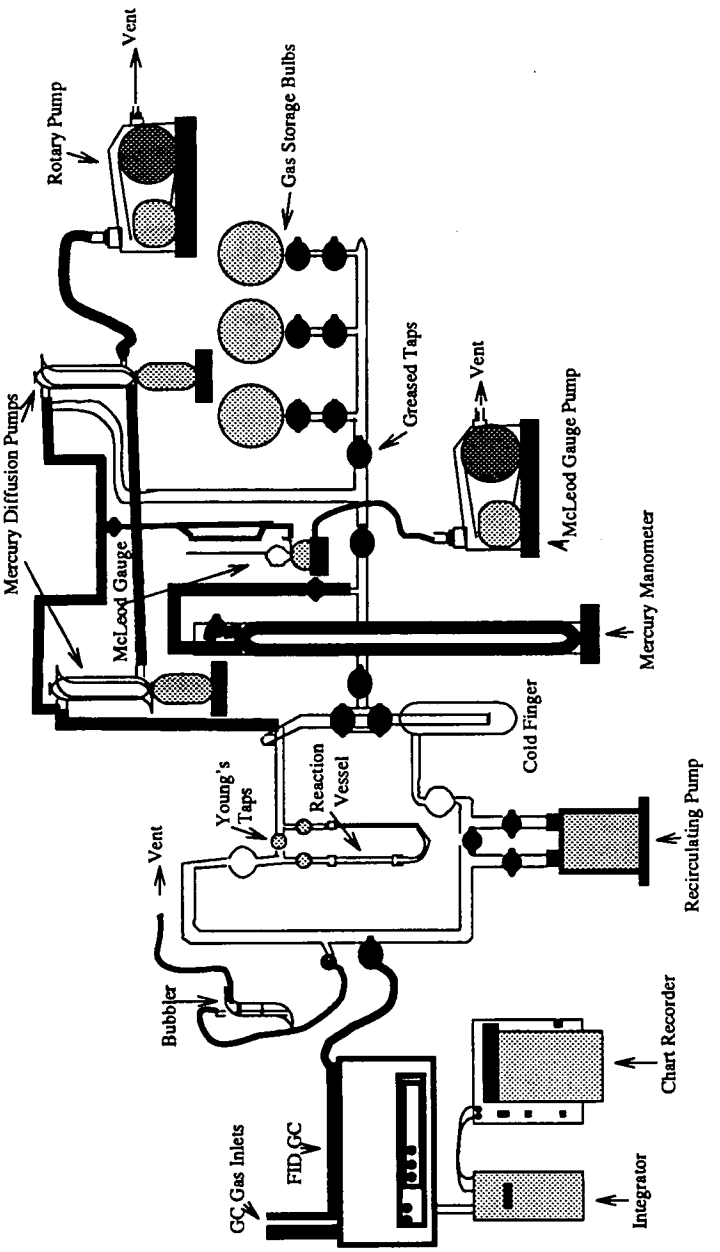

catalysed cracking. However, the propene production could be by a number of mechanisms and this propene is also liable to react further. Consequently, evaluation of rates of propene production are potentially misleading. Hence, in this work, the parameters examined are the rates of consumption of propane and production of the cracked fraction C_1/C_2. Rates of reaction were obtained from the gradient of the initial part of the concentration versus reaction time plots. These decaying concentration plots were fitted to a second order polynomial of the form $ax^2 + bx + c$. The first derivative of this expression $(2ax + b)$ represents the rate of change of the concentration and so the value for this initial rate of change of concentration *i.e.* when x=0, is the quantity b. Hence, the value b in these polynomial fits represents the initial rate of reaction, in $\%Cg^{-1}s^{-1}$.

6.3.3 Reaction Over H-ZSM-5 Based Catalysts

Reaction Over H-ZSM-5

The H-ZSM-5 (100mg) examined came from the same batch of Laposil zeolite used to prepare the Ga-ZSM-5 catalyst, described previously. The sample initially underwent an oxidative pretreatment *i.e.* calcined under flowing air ($\approx$ 30 $mlmin^{-1}$) at 837 K for 16 hours. The sample was then evacuated and a reaction gas mixture of 25% propane in diluent nitrogen was prepared. This gas mixture was then recirculated through the H-ZSM-5 catalyst bed and samples were withdrawn from the gas and its composition analysed by the FID GC as described. The product distribution is summarised by the stacked plot of Graph 6–17 a). Each stack represents a sample (aliquot) removed from the recirculating gas and analysed by GC. The composition of the aliquot is represented by the small blocks within each stack. This plot clearly shows that there is very little activity displayed by the acidic form of the ZSM-5 zeolite, which is similar to the findings of other workers [100].

Figure 6–17: Stacked plot showing the gas composition with time on stream over a) H-ZSM-5 and b) Ga-ZSM-5.

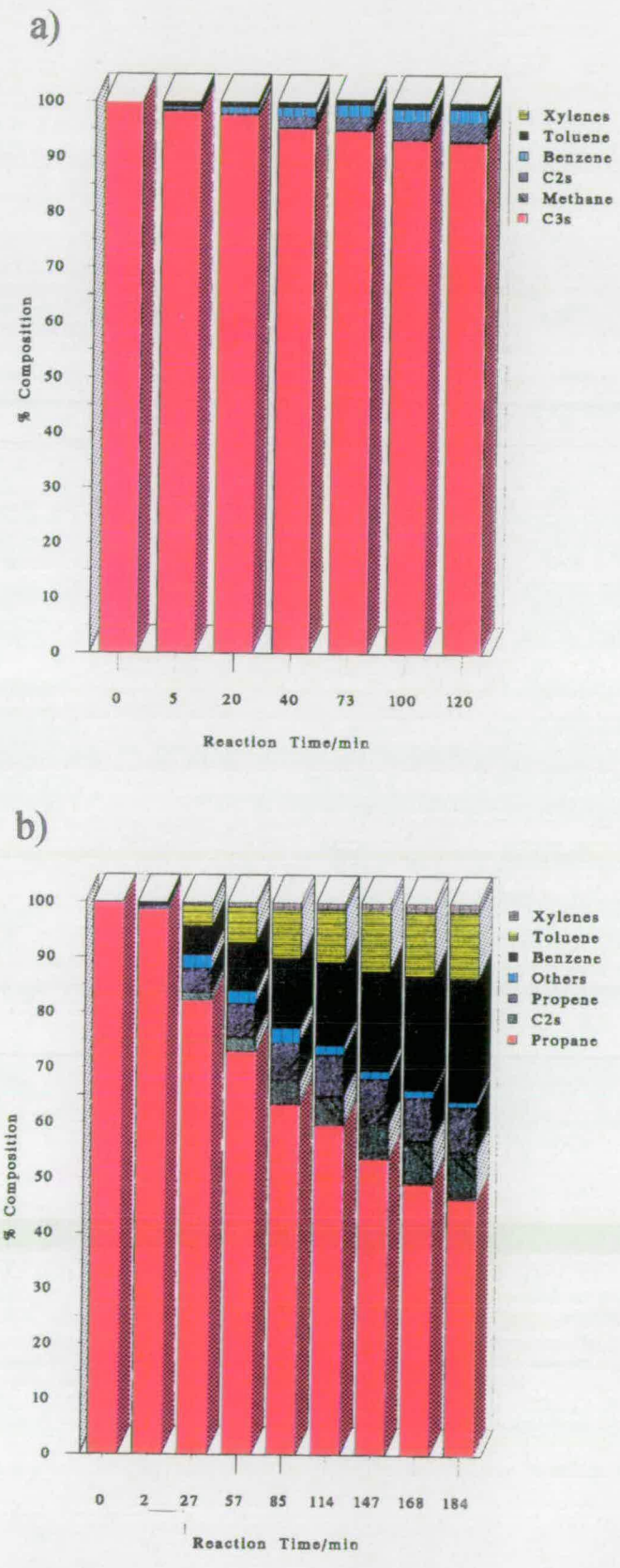

Examination of Ga-ZSM-5 with a Range of Activation and Regeneration Treatments

A sample of the Ga-ZSM-5 catalyst (98mg) examined in Section 6.2.1 was loaded into the stainless steel reaction vessel and fixed into the recirculating apparatus described previously. This catalyst was retained in the apparatus for 4 successive experimental reactions (Reactions 1 to 4) and was regenerated *in situ* to examine the effect of these high temperature treatments on catalyst performance.

Reaction 1 - Oxidative pretreatment The sample initially underwent an oxidative pretreatment *i.e.* calcined under flowing air ($\approx$ 30 mlmin^{-1}) at 837 K for 16 hours. The sample was then evacuated and a reaction gas mixture of 25% propane in diluent nitrogen was prepared. This gas mixture was then recirculated through the Ga-ZSM-5 catalyst bed and samples were withdrawn from the gas and its composition analysed by the FID GC as described.

Comparison of this product distribution to that of the H-ZSM-5 material is shown by the stacked plots in Figure 6–17 a) and b).

Reaction 2 - Oxidative regeneration, H_2 diluent. The Ga-ZSM-5 was regenerated *in situ* by a repeat of the oxidative pretreatment step *i.e.* calcination under flowing air at 837 K for 16h. As the catalyst was being evacuated a gas blend of 25% propane in diluent hydrogen was prepared. The hydrogen had been purified by diffusion through a hot Pd thimble. This reaction gas mixture was then circulated through the catalyst bed and the composition of the gas phase was analysed by the on-line GC analyser.

Reaction 3 - Oxidative then Reductive regenerations, N_2 diluent The Ga-ZSM-5 was once again regenerated *in situ* by the calcination procedure, described previously, before being evacuated and then exposed to a reductive treatment (flowing hydrogen at 837 K for 16h). The catalyst was again evacuated while the reaction gas mixture of 25% propane in nitrogen diluent was prepared and this was then circulated through the catalyst bed.

Reaction 4 - Oxidative regeneration The sample was treated as described in Reaction 1, *i.e.* regenerated in flowing air, then exposed to a reaction gas mixture of 25% propane in nitrogen.

The product distributions for all four of these reactions are shown in Figures 6–18 a) to d).

6.3.4 Results for H-ZSM-5 Based Catalysts

Comparison of the activity observed over the H-ZSM-5 and Ga-ZSM-5 catalysts is shown in Figures 6–17 a) and b), which clearly shows the extremely low levels of conversion observed over H-ZSM-5. The gallium doped material (Ga-ZSM-5) showed extremely high levels of activity with a remarkable selectivity to the desired BTX fraction. Hence, the extra-framework gallium component of this bifunctional system is essential if effective propane aromatisation is to be achieved. This was expected since it has been proposed that it is propene which is oligomerised and aromatised by the acidic functions of the zeolite and the addition of the gallium dehydrogenation function creates a suitable catalyst for this conversion.

The initial rates of reaction, derived from the initial conversion of the propane feed, in the 4 reactions are shown in Table 6–16. Comparison of Reactions 1 to 4 (Figures 6–18 a) to d)) shows that far from reducing the catalyst's performance, the successive thermal treatments enhance activity. This is in line with the findings of other workers [134]. Also the selectivity to the desired BTX product was significantly increased after the various reaction/regeneration cycles. Hence, these reaction/regeneration cycles must facilitate the formation of active gallium species in the catalyst [100]. The 3-D nature of the interconnecting MFI structure makes the migration of occluded species very simple and so allows a redistribution of the extra-framework gallium species from the external surface of the crystallites to a more homogeneous dispersion throughout the ZSM-5 channel system. This migration of gallium species through the MFI channel system has also been observed by a number of workers in this field [101, 104, 134].

Figure 6–18: Stacked plot showing the gas composition with time on stream over Ga-ZSM-5 in; a) Reaction 1, b) Reaction 2, c) Reaction 3 and d) Reaction 4.

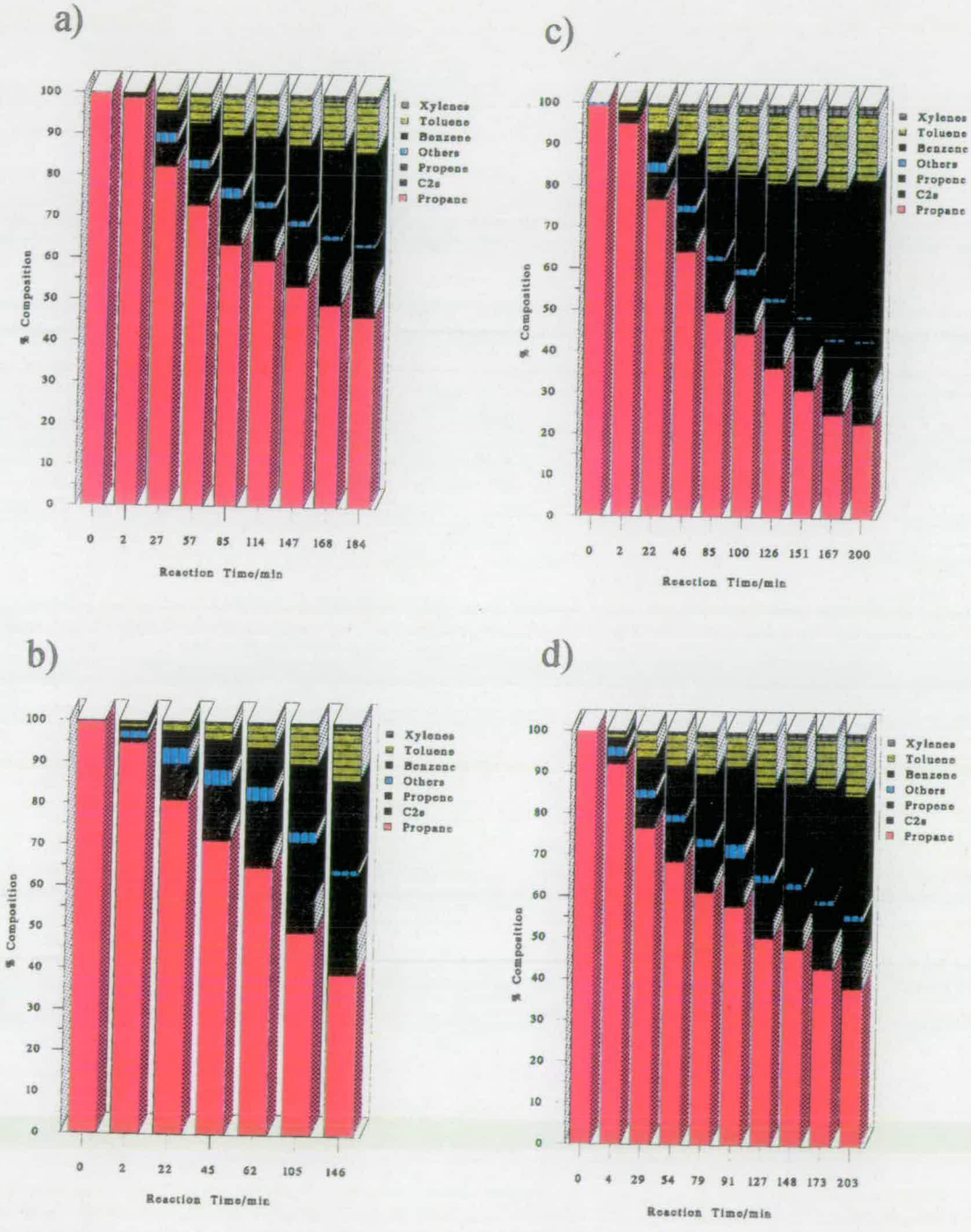

Table 6–16: Initial Rates for Reactions 1 to 4.

Reaction	Initial Rates$\times 10^3$(%C$g^{-1}s^{-1}$)
1	12.0±0.5
2	12.8±0.5
3	14.2±0.5
4	12.3±0.5

The highest level of activity and BTX selectivity was observed in Reaction 3 after the reductive treatment. It has also been proposed that the propane feed offers a reductive atmosphere to the catalyst. This is in accord with the flow reactor studies carried out on the same material where an induction time was noted before the maximum level of activity was observed (Figure 6–4). This was proposed to be due to the necessity for a partial reduction of the oxidation state of the gallium before effective conversions could be obtained [104, 110, 137]. Consequently, it can be proposed that this reductive pretreatment facilitated the required reduction in oxidation state of the active gallium species. It has been reported that the reduction of Ga_2O_3 is made more facile by the presence of an acidic zeolite like H-ZSM-5 [137]. XPS analysis of catalyst discharges highlights the existence of partially reduced gallium species. This suggests that this reduction procedure is beneficial for the production of an active and selective propane aromatisation catalyst. The precise nature of these active species remains unclear, however, a non-stoichiometric suboxide phase is most likely to form a major component in a successful aromatisation catalyst [104, 137]. This reduction in oxidation state of the gallium species will be discussed more fully in Section 6.5.2.

6.4 Catalysis of A and C Series of Materials

The recirculating glass apparatus described in Section 6.3.2 was again used to examine the catalytic capabilities of the molecular sieve materials prepared in the propane aromatisation reaction.

The experimental procedure adopted was as described for Reaction 1 (Section 6.3.3) *i.e.* calcination at 837 K for 16h under flowing air, followed by evacuation prior to exposure to the reaction gas mixture of 25% propane in diluent nitrogen.

A summary of the characteristics of the aluminosilicate and gallosilicate EUO and MFI materials examined are summarised in Tables 6–17 and 6–18.

Sample	Structure	Unit Cell Composition				Pore Vol.	Ext. Area	Acidity	Acid sites strengths	Gallium[a] Position
	(XRPD)	Na	Al/Ga	Si	O		m^2g^{-1}	mmoles×100g^{-1} g^{-1}sample	w:m:s	
AMFI1	ZSM-5	0.9	4.3	91.7	192	12.1	88	57±5	0.33:0.26:0.41	-
AMFI2	ZSM-5	2.2	6.3	89.7	192	12.2	103	75±7	0.21:0.38:0.41	-
AMFI3	ZSM-5[b]	4.5	7.0	89.0	192	11.4	122	76±7	0.39:0.38:0.23	-
AMFI4	ZSM-5[c]	7.0	8.0	88.0	192	9.8	96	119±10	0.37:0.25:0.38	-
CMFI1	[Ga,Si]-MFI	0.5	4.1	91.9	192	11.4	115	64±6	0.15:0.40:0.45	f,nf
CMFI2	[Ga,Si]-MFI	3.8	5.5	90.5	192	11.1	98	68±6	0.26:0.38:0.36	f,nf
CMFI3	[Ga,Si]-MFI[b]	3.9	6.9	89.1	192	11.1	104	72±6	0.48:0.12:0.40	f,nf
CMFI4	[Ga,Si]-MFI[c]	6.7	8.0	88.0	192	10.3	87	71±7	0.28:0.48:0.24	f,nf

Table 6–17: Summary of the A and C series of materials examined.

[a]Ga ascribed as; f=framework, nf=non-framework, [b]trace ANA, [c] ≈15% ANA.

Sample	Structure (XRPD)	Unit Cell Composition				Acidity NH_3^a	Acid site w:m:s	Ga^b
		Na	Al/Ga	Si	O			
AEUO1	[Al,Si]-EUO	0.5	2.7	109.3	224	59±5	0.31:0.21:0.48	-
AEUO2	[Al,Si]-EUO	0.5	5.3	106.7	224	72±7	0.42:0.28:0.30	-
AEUO3	[Al,Si]-EUO	0.5	7.7	104.3	224	79±7	0.38:0.38:0.24	-
AEUO4	[Al,Si]-NU-85	0.4	9.2	102.8	224	111±10	0.35:0.22:0.43	-
CEUO1	[Ga,Si]-EUO	0.7	2.6	109.4	224	51±5	0.30:0.30:0.40	f
CEUO2	[Ga,Si]-EUO	0.5	5.0	107.0	224	68±6	0.32:0.31:0.37	f
CEUO3	[Ga,Si]-EUO	0.5	7.0	105.0	224	68±6	0.30:0.40:0.30	f,nf
CEUO4	[Ga,Si]-NU-85	0.4	9.4	102.6	224	77±7	0.29:0.58:0.13	f,nf

Table 6–18: Summary of the A and C series of materials examined.

[a]Acidity as mmoles×100 NH_3 per g of dry zeolite, [b]gallium position summarised as; f=framework and nf=non-framework, determined by ^{71}Ga NMR, XPS and unit cell volumes..

Table 6–19: Initial rates of consumption of propane and production of propene and C_1/C_2, over the A and C series of MFI molecular sieves.

Sample	Mass Catalyst (mg)	Initial Rates$\times 10^3$ (%Cg^{-1}s^{-1})		
		Consumption	Production	
		Propane	Propene	C_1/C_2
AMFI1	189	48.3	43.0	5.0
AMFI2	192	138.7	53.0	14.0
AMFI3	202	90.7	63.7	27.0
AMFI4	204	99.8	73.7	4.7
CMFI1	150	45.2	29.3	16.3
CMFI2	182	3.0	0.7	2.0
CMFI3	190	2.0	0.3	1.7
CMFI4	197	5.7	1.7	4.0

6.4.1 Propane Aromatisation Over A and C Series of EUO and MFI Materials

The initial rates for the consumption of propane and the rate of production of propene and C_1/C_2 fractions are shown in Table 6–19 for the A and C series of MFI materials. The corresponding rates for the A and C series of EUO materials are included in Table 6–20.

The complete sample analyses for the A and C series of EUO and MFI materials are included at the end of this section in Tables 6–21 to 6–36. Table 6–19 shows that the most active materials in terms of propane conversion are the aluminosilicate MFI materials. The majority of the propane was converted to C_1/C_2s, primarily CH_4. This rate of cracking was much reduced for the gallosilicate MFI materials (CMFI) which is as would be expected since gallosilicate materials are known to be less acidic than their aluminous analogues [94, 100, 147]. Table 6–20 shows that all the EUO materials show much lower levels of activity in terms of propane conversion.

Table 6–20: Initial rates of consumption of propane and production of propene and C_1/C_2, over the A and C series of EUO molecular sieves.

Sample	Mass Catalyst (mg)	Initial Rates$\times 10^3$ (%Cg^{-1}s^{-1})		
		Consumption	Production	
		Propane	Propene	C_1/C_2
AEUO1	205	4.3	1.7	2.7
AEUO2	200	5.3	3.0	2.3
AEUO3	195	24.3	19.3	5.0
AEUO4	193	26.3	20.7	5.7
CEUO1	203	6.7	1.3	5.3
CEUO2	175	2.7	0.2	2.7
CEUO3	200	1.3	0.7	0.7
CEUO4	200	2.0	1.3	0.7

Figure 6–19 shows a) the amount of propane remaining in the recirculating gas and b) the amount of C_1/C_2 hydrocarbons in the gas phase, with time over the AMFI series of materials. It is apparent from Figure 6–19 a) that all these materials show extremely high levels of activity. They show similar rates of propane consumption and C_1/C_2 production (Table 6–19). This level of activity can be directly correlated with the number of available active sites [100]. Figure 6–21 shows that all the AMFI materials have very high levels of Al incorporation in the framework and it is proposed that a saturation level for this reaction has been achieved. This model for the positioning of the framework metal sites was described in Chapter 4 and was derived from information obtained from a combination of elemental and thermal analyses. It is reasonable to suggests that only a finite number of propane molecules can react per unit cell, per unit time and that this saturation level has been reached for all the AMFI materials prepared. This saturation level can be considered as a diffusion limit. With hindsight, these catalysts may have been prepared with an excessive active site density, which is in line with observations made by other workers [110]. Since all the AMFI ma-

terials have such high active site densities, they all show very similar levels of propane conversion. This constant level of activity could also be accounted for by the proposition that it is the external surface of the crystallites which is primarily responsible for the activity observed. XPS studies of the CMFI materials in Chapter 5 indicated that the CMFI series of materials had an almost constant Ga:Si ratio on the external surface of the crystallites and so it could be proposed that a similar situation would exist for the analogous aluminosilicate materials. Thus if all the materials have external surfaces which are effectively equivalent then constant levels of activity through this series of materials would be expected. This is similar to observations made by others [103].

Similar plots of % propane and % C_1/C_2 detected in the gas, with reaction time, over the gallosilicate (CMFI) materials are shown in Figures 6–20 a) and b). Here material CMFI1 shows high levels of activity, which is almost comparable to that exhibited by the AMFI series of zeolites. However, the other CMFI materials, which have higher metal contents, show very low levels of activity. This observation can be explained by a model similar to that of the AMFI materials where the same unit cells represented by Figure 6–21 can be considered to represent these gallosilicate materials. This Figure 6–21 indicates the very high active site density in these materials. The gallium containing catalysts are likely to cause a large amount of dehydrogenation of the propane feed to propene by either an acid catalysed hydride abstraction followed by Brönsted site reformation and propene evolution or by the more facile extra-framework gallium catalysed dehydrogenation [102], as described in Chapter 1. Unit cell volume studies and XPS measurements have already suggested that these gallosilicate MFI materials have large amounts of extra-framework gallium species and so the level of dehydrogenation over these catalysts could be expected to be very high. However, propene is known to oligomerise and cyclise extremely rapidly under the acidic conditions experienced in the channels of a molecular sieve and so it can be proposed that with the very high site density of these materials, the propene produced reacts immediately and blocks the pores of the CMFI materials with the higher levels of metal incorporation, similar to the observations of Kanai and Kawata [110]. It

Figure 6–19: a) % Propane and b)% C_1/C_2 in the recirculating gas stream with reaction time over the AMFI series of materials[a].

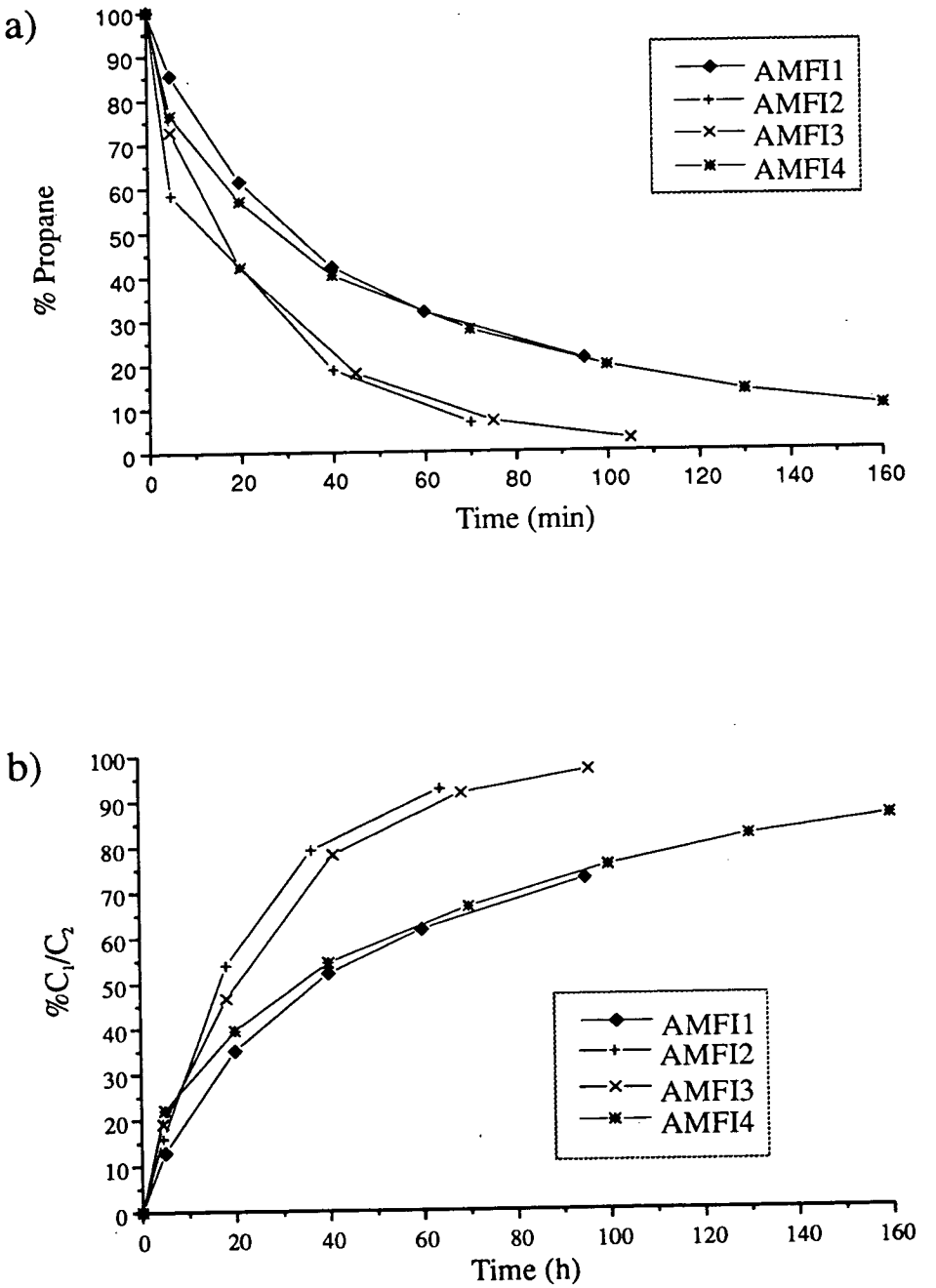

[a]This data is included in Tables 6–29 to 6–32.

must also be considered that the framework gallium species in MFI materials are not completely stable and it is likely that some ejection of gallium species into the channels would occur under reaction conditions. This would account for the reduction in pore volume measured for the gallosilicate materials by micromeritic analysis (Table 4–9). These extra-framework gallium species could add to the deactivation by blocking the pores, hindering reactant and product flow. The MFI structure type is known to be remarkably resistant to deactivation by pore blockage, however, the gallosilicate analogues appear not to behave as the aluminous materials [100, 110, 134]. Their very high rates of dehydrogenation (as exhibited by CMFI1, Table 6–19) results in high propene concentrations in the confines of the channel system which could lead to immediate and excessive oligomerisation. These reactions could cause rapid pore blockage and so deactivate these materials [110].

Plots of the % propane and % C_1/C_2 contents of the recirculating gas stream against reaction time over the A series of EUO materials are shown in Figures 6–22 a) and b). Plot a) shows the % propane, of the recirculating gas phase, to disappear more quickly for the materials with higher levels of metal incorporation. This is as would be expected with the degree of cracking observed over the catalysts being proportional to the number of acid sites present. Figure 6–22 shows the production of the cracked products C_1/C_2 to follow directly from the consumption of the propane feed, as was expected. The AEUO3 and AEUO4 samples are very similar in metal content with the EUO4 having the NU-85 structure type and consequently it is reasonable that they should show such similar levels of activity. The initial rates of propane consumption are included in Table 6–20 which shows the rates of propane consumption and C_1/C_2 production to increase through the series of aluminosilicate EUO materials, as would be expected for such an acid catalysed reaction.

Figures 6–23 a) and b) highlight the marked reduction in activity observed over the gallosilicate CEUO materials. Table 6–25 shows that the CEUO1 material, which is active in propane conversion, has a very different mode of conversion with propene forming the other major component of the recirculating gas stream. The

Figure 6–20: a) % Propane and b)% C_1/C_2 in the recirculating gas stream with reaction time over the CMFI series of materials[a].

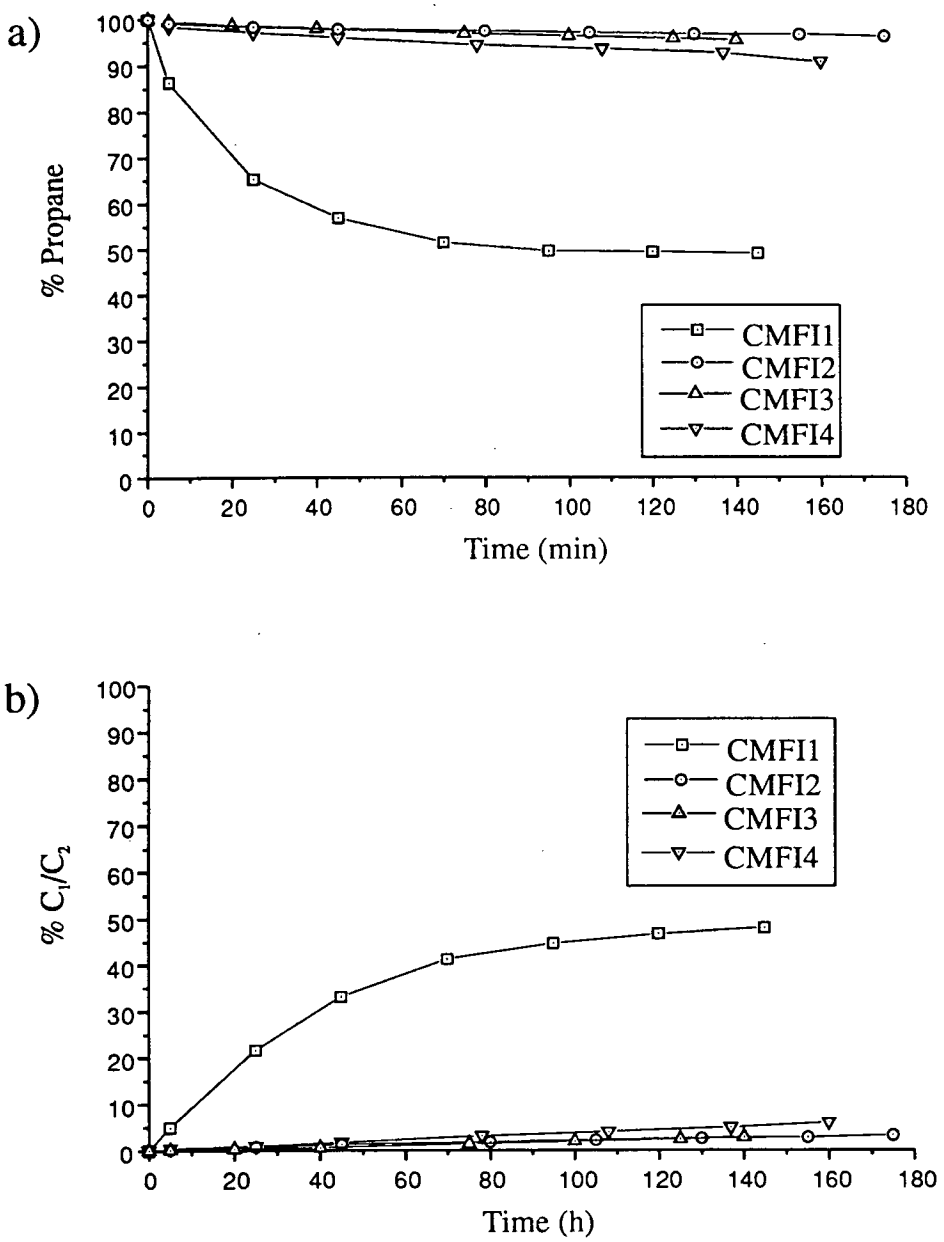

[a]This data is included in Tables 6–33 to 6–36.

Figure 6–21: Distribution of the framework metal sites in the MFI materials[a]: a) MFI1, b) MFI2, c) MFI3 and d) MFI4.

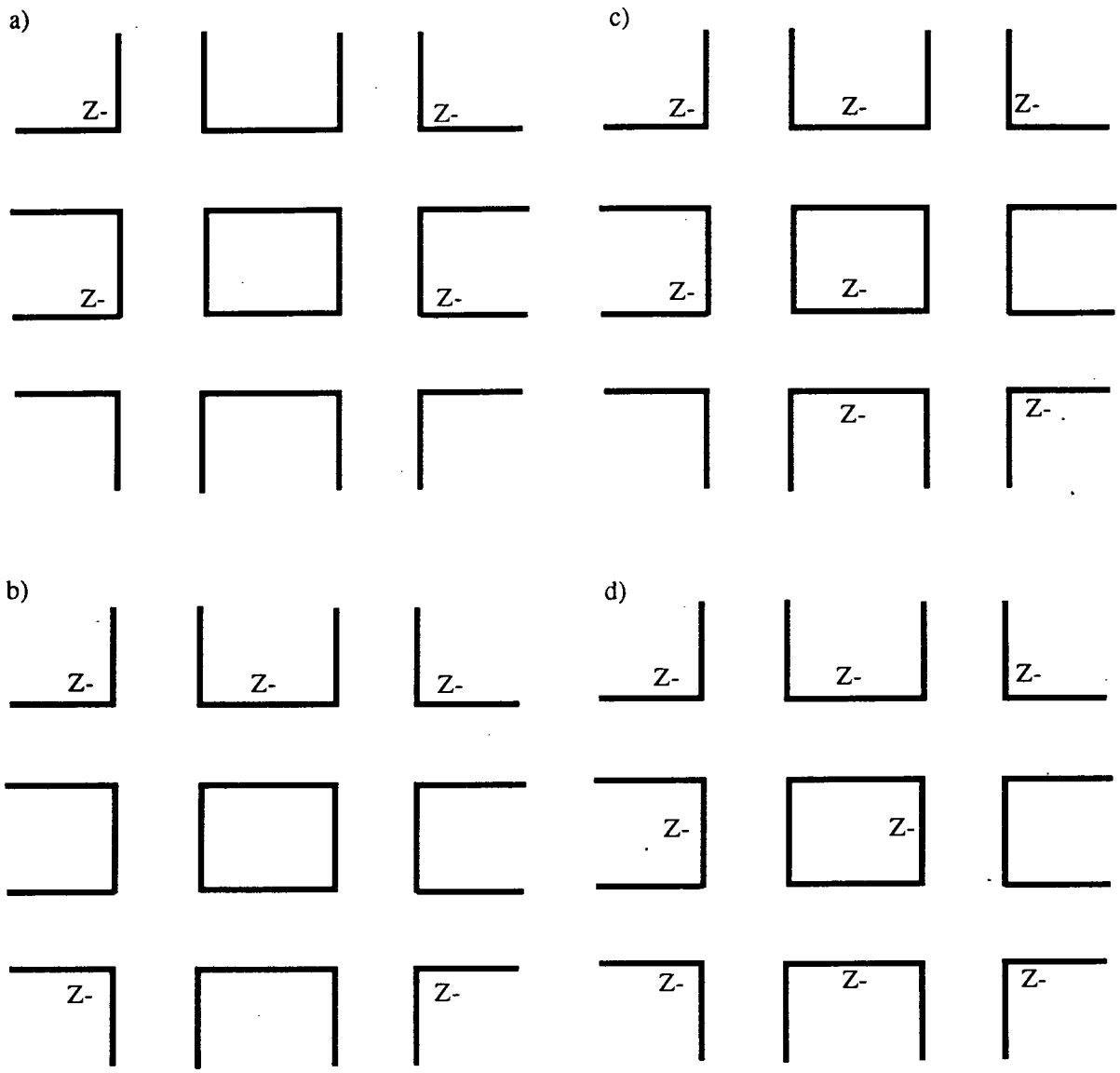

Z- Framework negative charge associated with active sites.

[a]This model was derived in Chapter 4 using elemental and thermal analyses.

Figure 6–22: a) % Propane and b) % C_1/C_2 in the recirculating gas stream with reaction time over the AEUO series of materials[a].

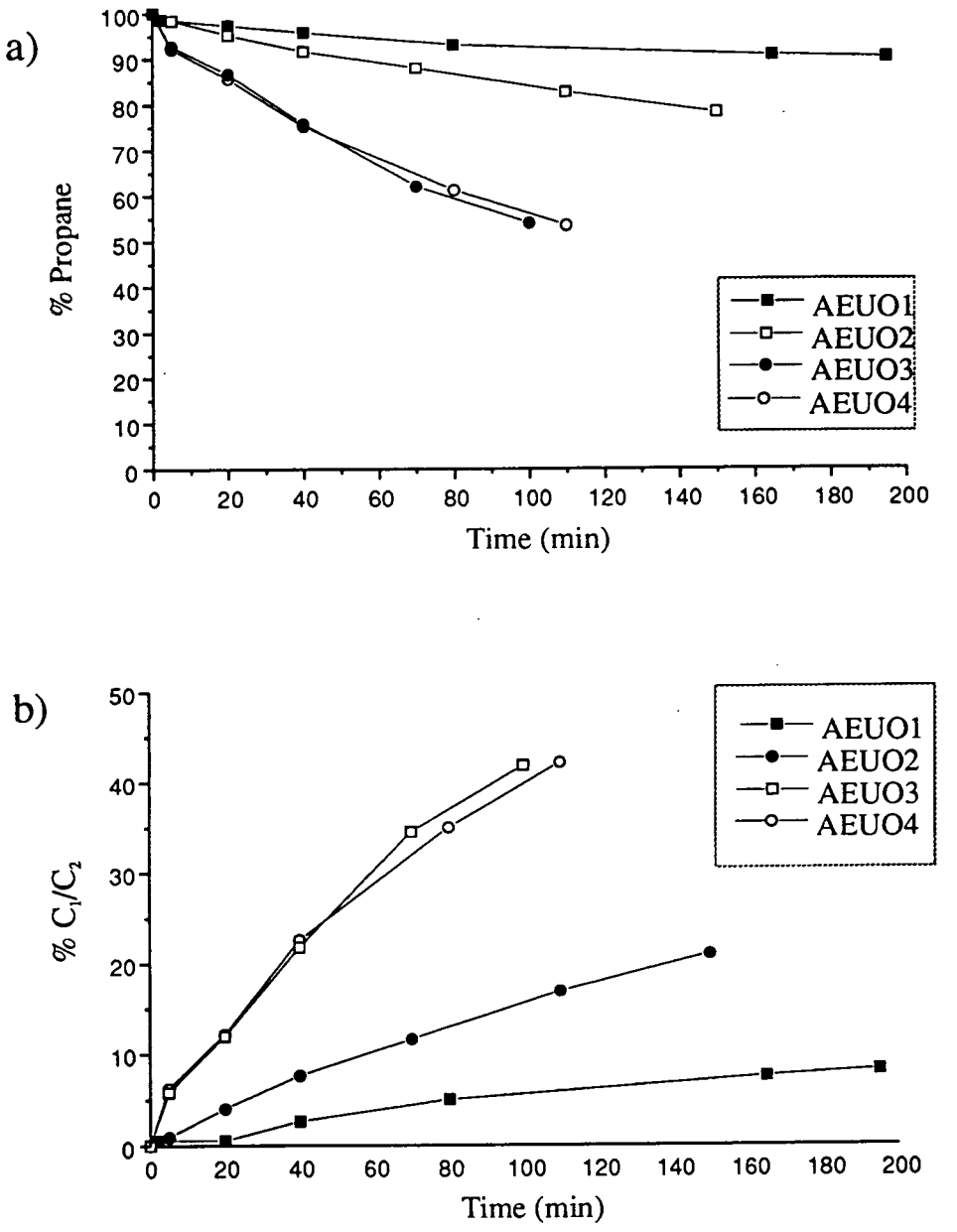

[a]This data is included in Tables 6–21 to 6–24.

CEUO1 sample shows much greater activity than the other CEUO materials yet this catalyst has the lowest gallium content. It is proposed that it is this lower gallium content which is responsible for the apparent improvement in activity, relative to the other CEUO samples. It has already been stated that the nature of the Hexamethonium template used in the synthesis of these EUO materials has a marked effect on the relative siting of these framework metal species. Figure 6–24 shows the likely positions of the framework metal sites for the EUO materials prepared. This model was derived using a combination of elemental analysis and thermal gravimetric analysis of the materials in Chapter 4. It is clear from Figure 6–24 that as the gallium level increases above that of CEUO1 the density of the framework sites increases dramatically such that any reaction occurring at a site *eg.* in a side-pocket, leads to primary products being formed in very close proximity to other framework sites *eg.* opposite the mouth of the side-pockets. It is well known that propene is extremely reactive in such acidic materials and so it could be proposed that it reacts vigorously at the mouths of the pockets, where it oligomerises and causes rapid pore blockage of the unidimensional channel structure of the EUO materials. The number of metal atoms per unit cell of CEUO1 is less than 4 and so it is likely that the active framework metal sites are sufficiently far apart to prevent this immediate pore blockage and so propane conversion is observed. The conversion of propane in the AEUO materials is primarily associated with the formation of smaller hydrocarbon fragments created by acid catalysed cracking of the propane feed. These fragments do not readily oligomerise and cyclise inside the EUO channels as the propene formed over the gallosilicate materials is likely to do. Consequently the AEUO materials show much higher levels of propane conversion than the gallosilicate EUO materials.

Hence, in summary, aluminosilicate MFI and EUO materials show high levels of propane cracking to the C_1/C_2 fraction. This was also observed over the gallosilicate molecular sieves to a much lesser extent. The primary conversion of these materials was the dehydrogenation of the propane feed to propene. It is proposed that the active site density and relative distribution of framework metal species is crucial for effective conversion and extended catalyst lifetimes. Extra-

Figure 6–23: a) % Propane and b) % C_1/C_2 in the recirculating gas stream with reaction time over the CEUO series of materials[a].

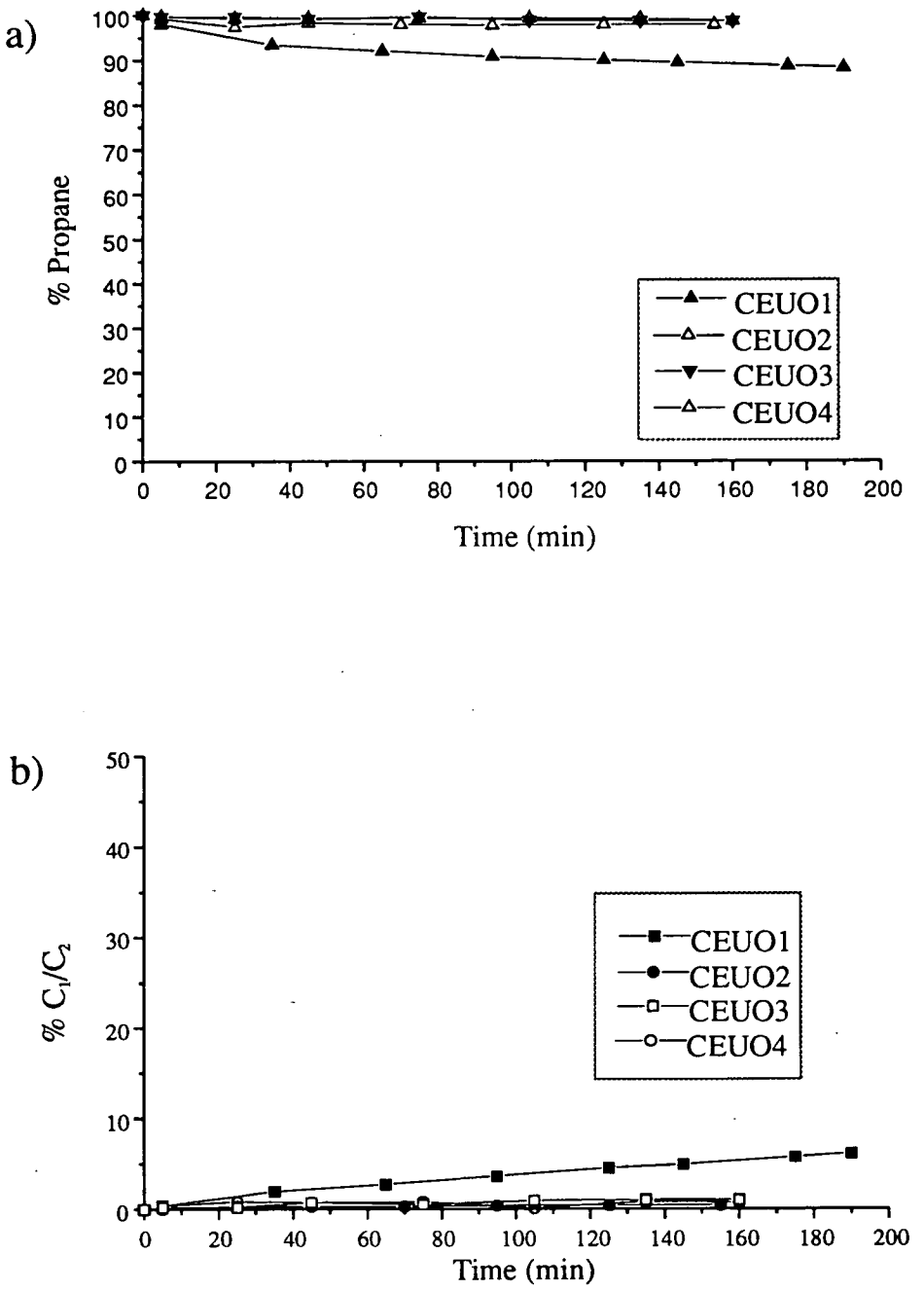

[a]This data is included in Tables 6–25 to 6–28.

Figure 6–24: Distribution of the framework metal sites in the EUO materials[a]: a) EUO1, b) EUO2, c) EUO3 and d) EUO4.

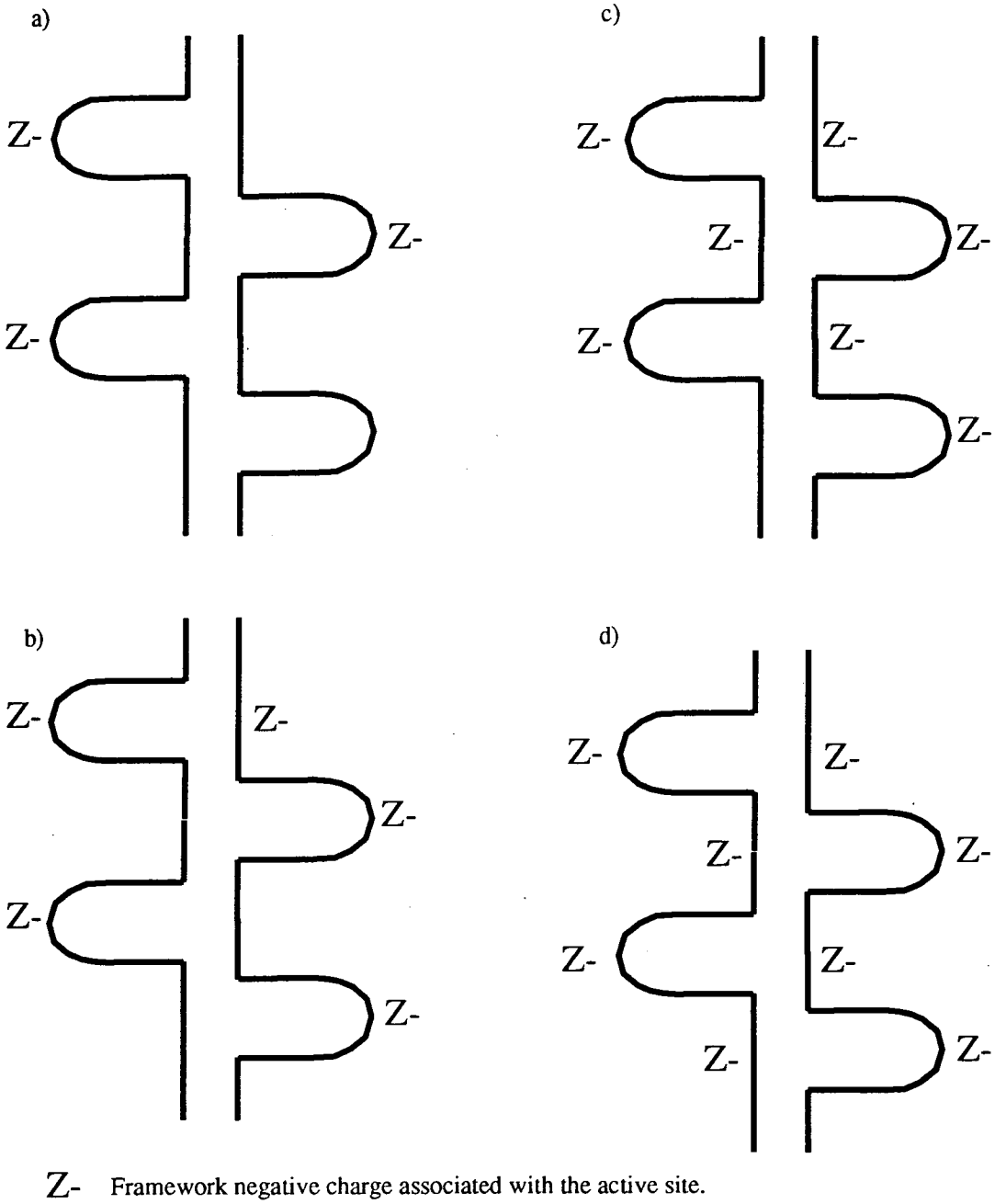

[a]This model was derived in Chapter 4 using elemental and thermal analyses.

framework gallium species are necessary for significant levels of dehydrogenation and the propene produced then rapidly oligomerises in an acidic environment. The EUO framework structure is prone to deactivation by pore blockage, whereas the MFI structure appears much more resistant to such deactivation. It appears that the MFI materials prepared in this work have formed as crystallites with effectively equivalent external surfaces. Hence, it can be proposed that the components required for a successful aromatisation catalyst can be ranked in an order of importance. Primarily, the catalyst must be resistant to deactivation by coking. The successful catalyst must contain both well dispersed, extra-framework gallium species and strong acid sites created by an aluminosilicate framework. These framework sites should be strongly acidic, however, it is their density and relative positioning which is more important than their absolute strengths. It is proposed that a framework concentration of ≤ 4 Al per unit cell of MFI could form the most effective aromatisation catalyst. It has been shown the 3% and 5% Ga_2O_3 doping levels are effectively equivalent and so it is proposed that a gallium level of less than this would offer good dehydrogenation activity. A good way of producing a well dispersed gallium loaded catalyst could be the preparation of a galloaluminosilicate MFI material, with controlled activation which could result in the creation of extra-framework gallium species, in close proximity to the strong acid sites of the 3-D, coke resistant, MFI framework.

Table 6–21: Product distributions over AEUO1.

Time (min)	Methane %C	Ethane %C	Ethene %C	Propane %C	Propene %C
5	0.2	0.3	0	98.7	0.8
20	0.4	1.0	0	97.2	1.4
40	0.8	1.8	0	95.7	1.7
80	1.6	3.4	0	92.8	2.2
165	2.7	4.8	0	90.4	2.1
195	3.0	5.2	0	89.8	2.0

Table 6–22: Product distributions over AEUO2.

Time (min)	Methane %C	Ethane %C	Ethene %C	Propane %C	Propene %C
5	0.4	0.5	0	98.4	0.7
20	1.6	2.4	0	95.2	0.8
40	3.0	4.6	0	91.5	0.9
70	5.1	6.5	0	87.7	0.7
110	7.6	9.3	0	82.4	0.8
150	9.8	11.2	0	78.0	1.0

Table 6–23: Product distributions over AEUO3.

Time (min)	Methane %C	Ethane %C	Ethene %C	Propane %C	Propene %C
5	3.4	2.4	0	92.7	1.5
20	5.4	6.5	0	86.6	1.5
40	10.4	11.4	0	75.7	2.4
70	16.5	18.0	0	61.8	3.6
100	21.3	20.6	0	53.8	4.3

Table 6–24: Product distributions over AEUO4.

Time (min)	Methane %C	Ethane %C	Ethene %C	Propane %C	Propene %C
5	3.6	2.6	0	92.1	1.7
20	5.3	6.8	0	85.6	1.9
40	10.6	11.6	0	75.1	2.6
80	16.7	18.3	0	61.0	3.9
110	21.5	20.7	0	53.3	4.5

Table 6–25: Product distributions over CEUO1.

Time (min)	Methane %C	Ethane %C	Ethene %C	Propane %C	Propene %C
5	0.0	0.4	0	98.0	1.6
35	0.8	1.1	0	93.2	4.9
65	0.6	2.1	0	91.7	5.6
95	0.8	2.8	0	90.4	6.0
125	1.0	3.5	0	89.5	6.0
145	1.1	3.8	0	89.0	6.0
175	1.3	4.4	0	88.2	6.1
190	1.4	4.7	0	87.8	6.1

Table 6–26: Product distributions over CEUO2.

Time (min)	Methane %C	Ethane %C	Ethene %C	Propane %C	Propene %C
5	0	0	0	99.2	0.8
25	0.2	0.1	0	97.9	1.8
45	0.2	0.1	0	98.1	1.6
70	0.2	0.1	0	97.7	2.0
95	0.2	0.2	0	97.4	2.2
125	0.2	0.2	0	97.5	2.1
155	0.2	0.2	0	97.4	2.2

Table 6–27: Product distributions over CEUO3.

Time (min)	Methane %C	Ethane %C	Ethene %C	Propane %C	Propene %C
5	0.1	0.1	0	99.6	0.2
25	0.1	0.1	0	99.5	0.2
45	0.2	0.5	0	98.9	0.4
75	0.1	0.4	0	99.3	0.3
105	0.2	0.7	0	98.5	0.6
135	0.2	0.8	0	98.3	0.7
160	0.2	0.8	0	98.2	0.8

Table 6–28: Product distributions over CEUO4.

Time (min)	Methane %C	Ethane %C	Ethene %C	Propane %C	Propene %C
5	0.3	0.1	0	99.4	0.2
25	0.3	0.1	0	99.1	0.5
45	0.3	0.2	0	99.1	0.4
75	0.3	0.2	0	99.0	0.5
105	0.2	0.2	0	98.8	0.8
135	0.4	0.4	0	98.2	1.0
160	0.4	0.3	0	98.2	1.1

Table 6–29: Product distributions over AMFI1.

Time (min)	Methane %C	Ethane %C	Ethene %C	Propane %C	Propene %C
5	5.8	0.2	6.9	85.5	1.5
20	16.1	1.2	17.7	61.4	3.6
40	25.7	3.3	23.0	42.0	6.0
60	33.1	5.0	23.5	31.7	6.7
95	42.1	7.6	23.0	20.9	6.4

Table 6–30: Product distributions over AMFI2.

Time (min)	Methane %C	Ethane %C	Ethene %C	Propane %C	Propene %C
5	6.3	0.9	8.7	58.4	4.2
20	36.7	5.8	11.4	42.2	3.7
40	61.6	9.6	8.0	18.6	2.1
70	76.3	11.6	4.6	6.6	0.9

Table 6–31: Product distributions over AMFI3.

Time (min)	Methane %C	Ethane %C	Ethene %C	Propane %C	Propene %C
5	6.1	0.6	12.4	72.8	8.1
20	30.1	4.1	17.6	42.1	6.0
45	58.0	8.4	11.8	17.9	3.9
75	75.8	11.3	4.5	6.9	1.6
105	83.5	12.1	1.0	2.7	0.7

Table 6–32: Product distributions over AMFI4.

Time (min)	Methane %C	Ethane %C	Ethene %C	Propane %C	Propene %C
5	15.1	0.6	6.4	76.5	1.4
20	20.2	1.5	17.7	57.0	3.6
40	29.4	4.0	21.0	40.1	5.5
70	38.5	7.6	20.5	27.6	5.8
100	46.6	10.4	18.6	19.3	5.1
130	52.9	12.4	16.8	13.5	4.4
160	57.3	13.6	15.3	9.9	3.9

Table 6–33: Product distributions over CMFI1.

Time (min)	Methane %C	Ethane %C	Ethene %C	Propane %C	Propene %C
5	1.8	0.9	2.2	86.3	8.8
25	6.9	0.6	14.1	65.2	13.3
45	12.0	1.6	19.5	56.7	10.2
70	16.9	3.5	20.8	51.3	7.7
95	20.3	4.6	19.7	48.4	6.0
120	23.2	6.0	17.5	49.2	4.1
145	25.4	7.1	15.5	48.9	3.1

Table 6–34: Product distributions over CMFI2.

Time (min)	Methane %C	Ethane %C	Ethene %C	Propane %C	Propene %C
5	0.1	0	0.1	99.1	0.6
25	0.2	0.1	0.5	98.2	1.0
45	0.4	0.1	0.8	97.6	1.2
80	0.6	0.1	1.1	97.1	1.1
105	0.8	0.1	1.3	96.7	1.1
130	1.0	0.1	1.5	96.3	1.1
155	1.1	0.1	1.6	96.2	1.0
175	1.2	0.2	1.8	95.8	1.0

Table 6–35: Product distributions over CMFI3.

Time (min)	Methane %C	Ethane %C	Ethene %C	Propane %C	Propene %C
5	0	0	0.1	99.4	0.5
20	0.1	0	0.2	98.6	1.1
40	0.1	0	0.5	97.8	1.6
75	0.3	0.1	1.0	96.6	2.0
100	0.4	0.1	1.4	96.0	2.1
125	0.5	0.1	1.8	95.4	2.2
140	0.6	0.2	2.0	95.0	2.2

Table 6–36: Product distributions over CMFI4.

Time (min)	Methane %C	Ethane %C	Ethene %C	Propane %C	Propene %C
5	0.2	0	0.3	98.3	1.2
25	0.2	0	0.7	97.0	2.1
45	0.4	0	1.3	95.8	2.5
78	0.8	0.1	2.2	94.1	2.8
108	1.1	0.1	2.8	93.2	2.8
137	1.4	0.2	3.3	92.3	2.8
160	1.7	0.3	3.9	90.3	2.8

6.5 Study of Catalyst Discharges

Some of the catalysts discharged from the flow and recirculating reactors have been examined to determine the fate of the catalytically active gallium species.

6.5.1 ^{71}Ga NMR

As has been described previously, an extensive ^{71}Ga NMR investigation was not possible, however, some interesting features were noted from the limited studies of some of the catalyst discharges from the flow reactor experiments carried out at I.C.I., Wilton.

The ^{71}Ga NMR spectrum of the Ga-ZSM-5 catalyst discharge (16h, 25% propane in N_2, 1.5lh^{-1}, 803 K) is shown in Figure 6–25 a), and this clearly shows the majority of the gallium species to be in octahedral environments, as was expected for a gallium doped zeolite. However, there is the appearance of some tetrahedral gallium species also ($\approx$ 150ppm). This could be caused by either some gallium substituting into the molecular sieve framework or simply gallium which is tetrahedrally coordinated in an extra-framework environment.

The ^{71}Ga NMR analysis of the [Ga,Si]-NU-87 catalyst discharge (7h, 25% propane in N_2, 1.5lh^{-1}, 803 K) is included in Figure 6–25 b). This indicates that the majority of the gallium species are retained in the tetrahedral framework sites, however, there is the appearance of some octahedral gallium species (0ppm) created by the ejection of some gallium from the NES framework structure. This supports the proposition that the dehydrogenation activity observed for the [Ga,Si]-NU-87 materials was associated with the formation of extra-framework gallium species.

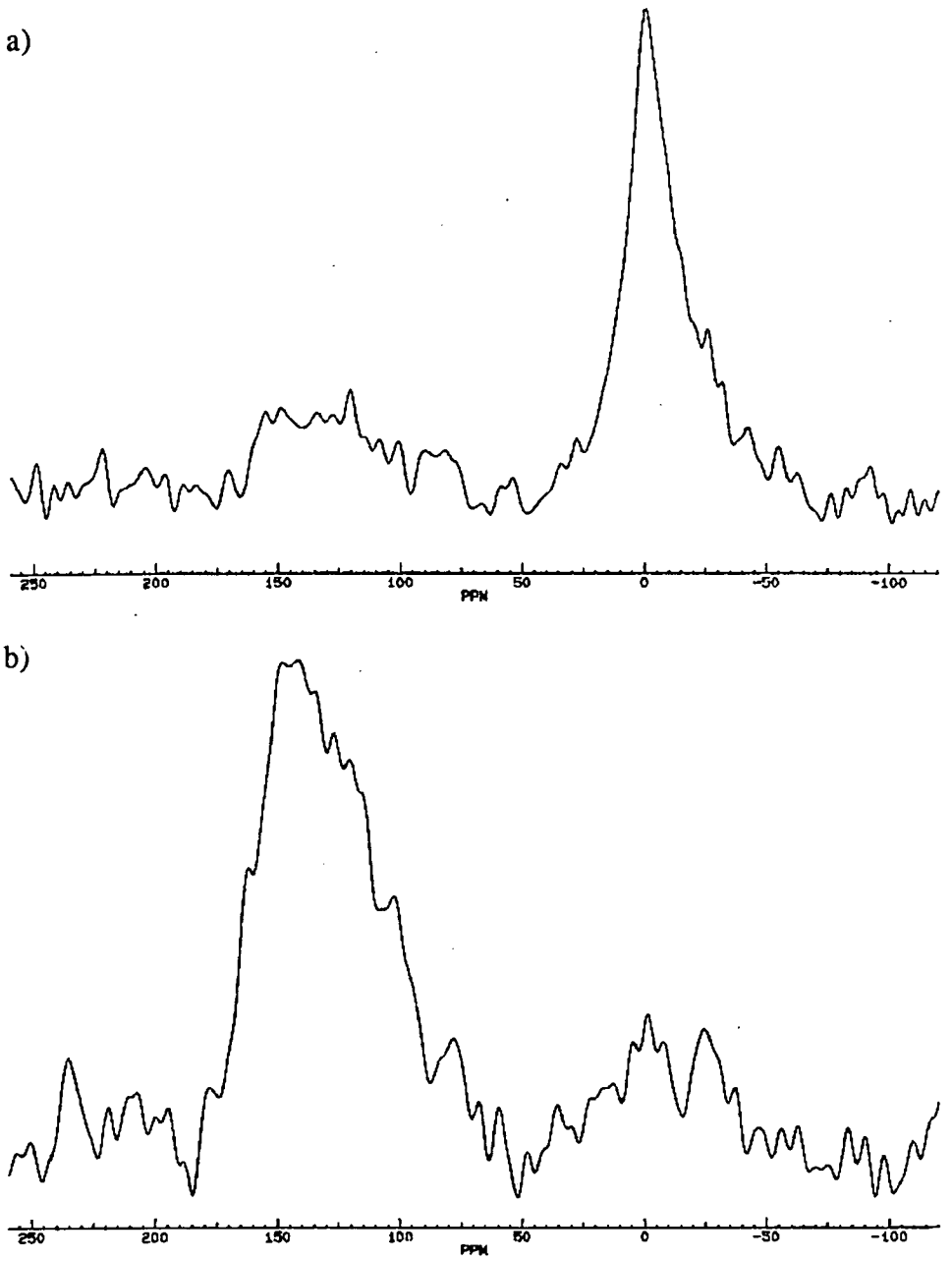

Figure 6–25: a) ^{71}Ga NMR of Ga-ZSM-5 discharge and b) ^{71}Ga NMR of [Ga,Si]-NU-87 discharge.

6.5.2 XPS Study of Catalyst Discharges

Some of the catalysts examined in this Chapter were examined by XPS after discharge from the reactor. From the Flow reactor studies carried out at I.C.I. Wilton the discharged [Ga,Si]-NU-87 material was examined (Section 6–1, Figure 6–5), and this sample is compared to a sample of fresh [Ga,Si]-NU-87 which had not been exposed to catalytic study. CEUO1, CEUO2, CEUO3 and CMFI1, catalyst discharges from the recirculating studies (described in Section 6.4, Figures 6–23 a) and b)) were also examined by XPS. The material names have been suffixed R, to denote that they are *reacted* catalyst discharges. The scan envelopes for the three CEUO catalyst discharges from the recirculating reactor studies are included in Figures 6–27 and 6–26. The analysis of the CMFI1 catalyst discharge resulted in very similar scan envelopes to these and consequently are not included.

For the CEUO1R to 3R series of reacted materials and the CMFI1R sample, it is proposed that gallium has been ejected from the framework sites during the high temperature reactions, however, the extensive external coking has made quantitative analysis difficult and irreproducible.

Figure 6–26 shows the scan envelopes for the Ga $2p_{3/2}$ signals, which show a marked shift to lower binding energy. This has been proposed to be due to the formation of some partially reduced gallium species [115, 117, 209, 210]. This is likely to be of the form Ga_2O which can be formed readily from the GaO^+ extra-framework species [115, 148]. The Si 2p and 2s envelopes at ≈105eV and 155eV are included in Figures 6–26 a) and b) and these show displacements to lower binding energy, which suggests that the EUO framework also degrades under these extreme conditions and gallium is ejected from the framework sites to leave hydroxyl nests with more free Si-OH groups [195, 209, 210].

The O 1s signals at ≈ 533eV are included in Figure 6–27 b) and are very broad, for all these reacted materials, which suggests that there is likely to be a range of oxygen species masked by the broadness of the signal. The framework oxygen signal is expected to be centred around 533eV [117, 195, 204, 210] with lower binding energy species at ≈ 531eV assigned as metal oxide type species.

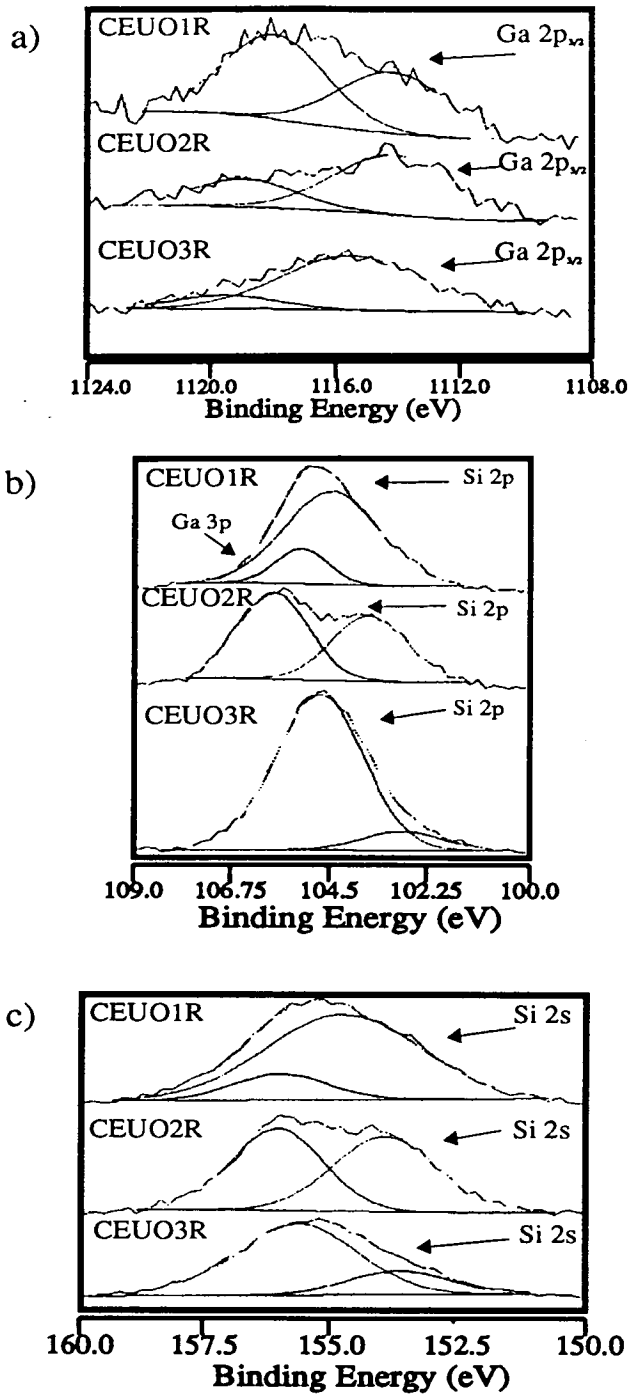

Figure 6–26: *Scan envelopes* for the a) Ga $2p_{3/2}$, b) Si 2p and c) Si 2s regions for the CEUO1-3R catalyst discharge materials.

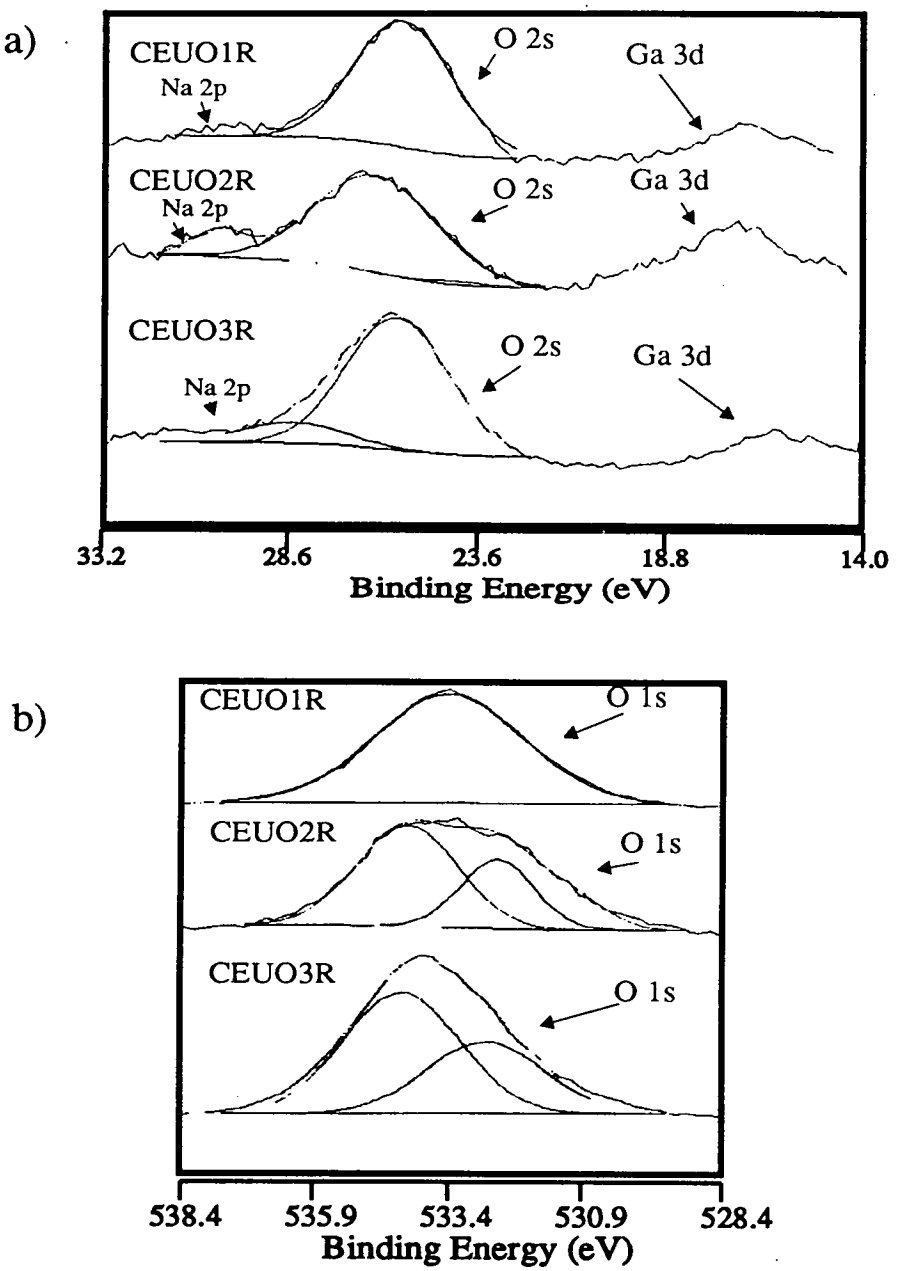

Figure 6–27: *Scan envelopes* for the a) O 2s and Ga 3d signals and b) O 1s envelope for the CEUO1-3R catalyst discharge materials.

Reference to tabulated binding energy values suggested that the higher binding energy contributions could be assigned to OH type species [195, 209, 210].

The scan envelope around 30eV, shown in Figure 6–27 a), clearly shows the significant shift to lower binding energy for the Ga 3d signal in all the reacted samples. This suggests that the gallium is in a partially reduced state in the catalyst discharges [117, 195, 207, 210, 239]. This is to be expected for a metal species which has been exposed to such a reducing atmosphere and as already stated there is a significant propensity for gallia species to reduce to Ga_2O under the conditions experienced in the present study [101, 104, 148].

The gallosilicate [Ga,Si]-NU-87 material, also obtained from I.C.I., was examined before and after exposure to a feed of 25 % propane in diluent nitrogen (7h, 1.5lh^{-1}, 803 K). These samples are referred to as [Ga,Si]-NU-87F (fresh) and [Ga,Si]-NU-87R (reacted).

The scan envelopes for the *fresh* and *reacted* [Ga,Si]-NU-87 samples are shown in Figures 6–28 and 6–29. Figures 6–28 a)-c) show the *scan envelopes* for the Ga and Si signals which represent analysis of the *surface* of the crystallites. Figure 6–28 a) clearly shows an apparent increase in the amount of gallium with a lower binding energy contribution to the overall Ga $2p_{3/2}$ signal. This is proposed to be associated with an extra-framework gallium species. It has also been suggested that this shift to lower binding energy is associated with a reduction in the oxidation state of the gallium species concerned [195, 209], as expected after such reaction conditions [101, 104, 137]. Figures 6–28 b) and c) both show the Si signals observed and the fitting procedure used to remove the contributions from the weaker gallium signals which interfere with the Si signals being examined. The fitting procedure used to remove these *contaminant* contributions was refined by using the gallium signal detected in the 1120 eV range (Ga $2p_{3/2}$) to estimate the area expected for the Ga $3p_{(1/2\ +\ 3/2)}$ and Ga $3s_{1/2}$ signals, given their relative Schofield sensitivity factors (S_f). Both of the Si features show apparent shifts to lower binding energy after reaction which has been proposed to be associated with an increase in the number of free Si-OH species which would be created after the

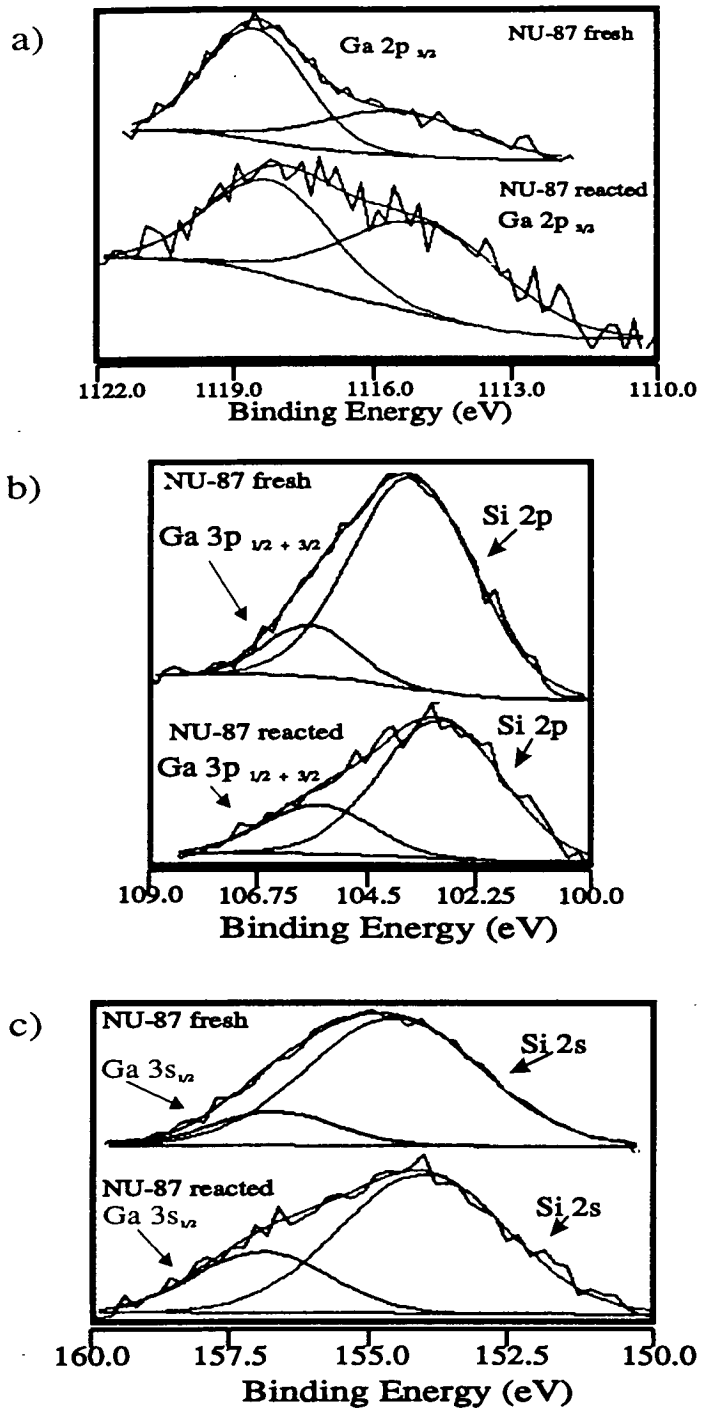

Figure 6–28: *Scan envelopes* for the a) Ga $2p_{3/2}$, b) Si 2p (contaminated with Ga 3p) and c) Si 2s (contaminated with Ga $3s_{1/2}$ regions in the fresh and reacted forms of [Ga,Si]-NU-87.

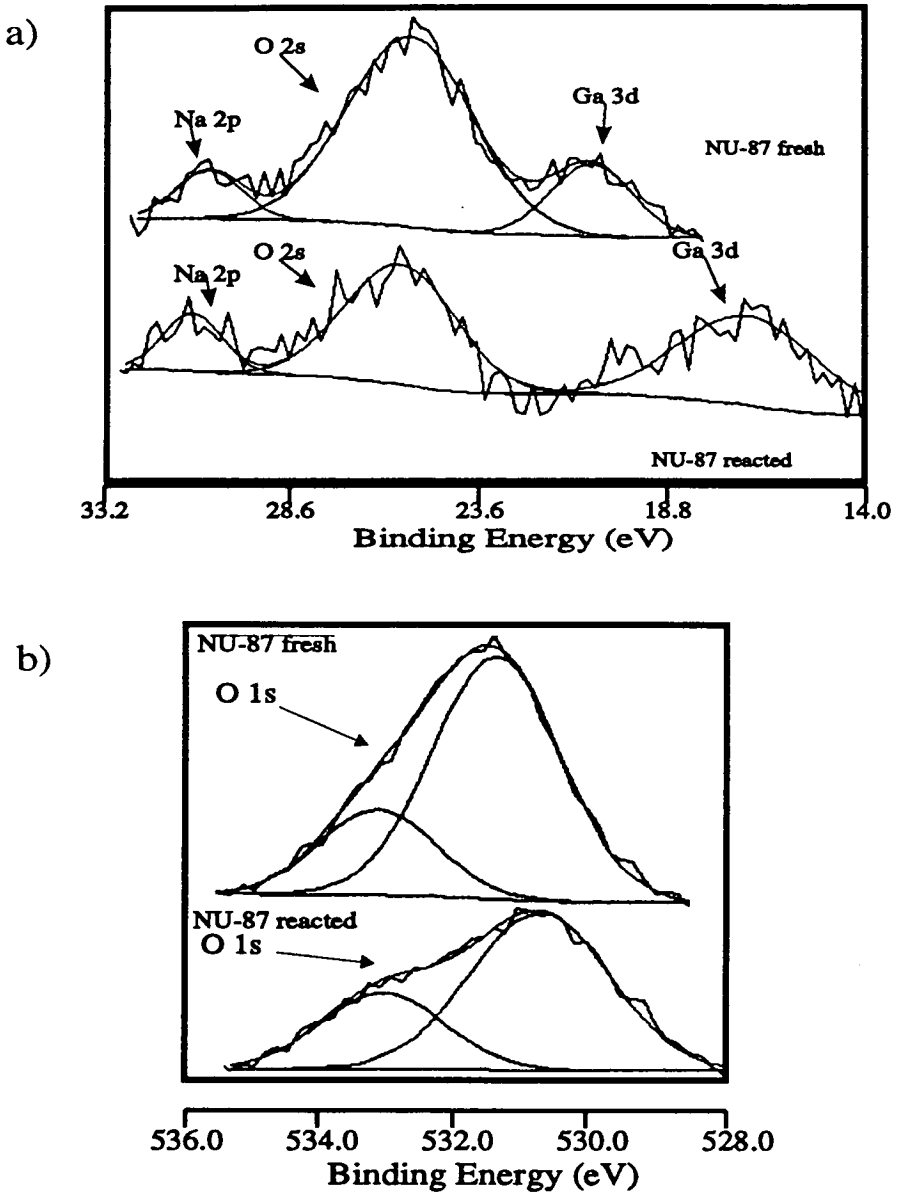

Figure 6–29: *Scan envelopes* for the a) O 2s and Ga 3d and b) O 1s regions in the fresh and reacted forms of [Ga,Si]-NU-87.

ejection of gallium from the zeotype framework. However, quantitative evaluation of these species cannot be obtained from these spectra.

Figure 6–29 a) shows the *scan envelope* which centres on the peaks used for the gallium analysis of the *near-surface.* Both analyses before and after reaction show a significant sodium level; however, it is suggested that this is simply due to surface contamination from handling rather than a quantifiable property of the material itself. It is very clear that the Ga 3d signal has a large and significant shift to lower binding energy (≈18.0 eV) which suggests that the gallium is in a reduced oxidation state. Indeed, a simple comparison to literature values suggests that the gallium species are of the form of gallium metal. It is not proposed that these gallium species exist in a truly metallic state; however, a significant degree of reduction of the oxidation state of the gallium is proposed to have occurred during the high temperature reaction under the reducing atmosphere. It has been proposed [195, 208, 209] that the magnitude of this binding energy shift can be partially accounted for by the *non-contiguous* nature of the sample *i.e.* poorly mixed. The gallium ejected from the framework, if located on the external surface of the crystallites as larger clusters, as has been suggested by this work, represents a poorly mixed system; this would result in preferential charging of the gallium species. The flood gun could preferentially charge the gallium segregated on the external surface of the crystallites such that these gallium containing clusters would not be at the same potential as the rest of the sample and so an apparent reduction in the gallium binding energy would be observed.

Figure 6–29 b) shows the oxygen component of the [Ga,Si]-NU-87R catalyst discharge to be multifa ceted. The increase in the contribution at a higher binding energy after reaction is associated with an increase in the number of OH type species formed in the hydroxyl nests after the ejection of the framework metal species. Every framework metal species ejected leaves an *hydroxyl nest* defect site which contains 4 OH groups and so a large increase in the OH concentration would be expected along with the ejection of gallium from the framework. It is likely that as gallium leaves the tetrahedral framework site it would exist as a GaO^+ species which is analogous to the AlO^+ species found in zeolites [240]. The lower binding

energy component is proposed to be associated with an oxide type species. Since there is a concomitant reduction in the oxidation state of the gallium present this suggests that there is the formation of a suboxide type species under these reaction conditions. It is likely that after ejection from the framework, the gallium species would be of the form GaO^+ which is very readily reduced to Ga_2O [101, 148]. This Ga_2O is known to be readily formed from Ga_2O_3 under a reducing atmosphere at around 773 K and has been proposed to be facilitated by an interaction with the acidic molecular sieve [104]. This Ga_2O species is also known to be extremely mobile and so it is likely to migrate to the external surface of the crystallites where sintering can readily occur.

A summary of the Ga/Si/O ratios for a range of materials which were examined in the propane conversion studies described in this Chapter are shown in Table 6–37. The full range of compositional ratios for these materials are included in Tables 6–38 to 6–42, at the end of this section. It is clear from Table 6–37 the three CEUO materials examined after exposure to a propane in diluent nitrogen feed show remarkably similar levels of gallium on the external surface of the crystallites. In their as-made form it was noted that there was an increase in surface gallium concentration with increasing bulk metal content; however, this is not the case for the reacted materials which suggests that the extreme conditions of the catalytic reaction has resulted in the ejection of some framework gallium species which have migrated and sintered on the external surface of the crystallites. From this it would be expected that if surface reactions dominated the catalytic activity observed then each of these materials should show similar levels of activity. This was observed, except for the CEUO1 material which showed slightly higher than expected activity. This has been rationalised as being associated with the relative distribution of the framework active sites, which leads to more rapid deactivation of the materials with higher metal contents.

Table 6–37 records the apparent reduction in the gallium level observed on the external surface of the [Ga,Si]-NU-87R crystallites with both the Ga $2p_{3/2}$: O 1s and Ga $2p_{3/2}$: Si 2s ratios reducing after reaction, compared to those of the fresh [Ga,Si]-NU-87F sample. There is a concomitant increase in the Ga 3d : O 2s ratio

Table 6–37: XPS analysis of catalytically examined materials.

Sample	Si 2s : O 1s	Ga $2p_{\frac{3}{2}}$: Si 2s	Ga $2p_{\frac{3}{2}}$: O 1s	Ga 3d : O 2s
NU-87F	0.306 : 0.694	0.107 : 0.893	0.046 : 0.954	0.026 : 0.974
NU-87R[a]	0.275 : 0.725	0.091 : 0.909	0.036 : 0.964	0.089 : 0.911
CEUO1R[b]	0.325 : 0.675	0.052 : 0.948	0.026 : 0.974	0.018 : 0.982
CEUO2R[b]	0.259 : 0.741	0.088 : 0.912	0.033 : 0.967	0.043 : 0.957
CEUO3R[b]	0.311 : 0.689	0.050 : 0.950	0.021 : 0.979	0.013 : 0.987
CMFI1R[b]	0.329 : 0.671	0.060 : 0.940	0.031 : 0.969	0.019 : 0.981

F = fresh, R = catalyst discharge from propane feed reactions, [a] from Flow studies, [b] from recirculating studies.

observed, which is a measure of the gallium level at a greater depth into the sample. This observation could be rationalised by a model where some gallium species are ejected from the [Ga,Si]-NU-87 framework during the reaction and rather than migrating to the external surface, where sintering can occur readily, the mobile gallium species were redistributed further into the 2-D network of channels of the [Ga,Si]-NU-87 material. However, a more likely explanation is that some gallium has been ejected from the framework and has migrated to the external surface of the crystallites and the apparent reduction in gallium content is a consequence of the extreme coking observed on the external surface of this material. The sample appeared very black after being discharged from the reactor and excessive deactivation was noted during the catalytic study of this sample (Table 6–6). This apparently thick coating of carbonaceous deposits greatly attenuates the signal and results in an apparent reduction in the external gallium content. Gallium species which have migrated to the external surface would also greatly attenuate the signal observed and so dramatically reduce the analysis volume. The Ga 3d : O 2s ratio represents an analysis deeper through this attenuating carbonaceous layer. Since this signal shows an increase in the gallium level at this depth it is proposed that any mobile gallium species, which were ejected form the [Ga,Si]-NU-87 framework (as observed by ^{71}Ga NMR), have migrated to the external surface but have been

Table 6–38: XPS analysis of reacted [Ga,Si]-NU-87R.

Sample [Ga,Si]-NU-87 after reaction					
Peak	Total area	S_f used	B.E.	Surface	Depth profile
Ga $2p_{\frac{3}{2}}$	1385	21.4	1120.3-1116.6	Ga $2p_{\frac{3}{2}}$: O 1s	Ga 3d : O 2s
O 1s	9933	2.93	536.5-533.7	0.036 : 0.964	0.089 : 0.911
Si 2s	1559	0.955	154.9	Si 2s : O 1s	Si 2p : O 2s
Ga 3d	110	1.08	18.0	0.275 : 0.725	0.610 : 0.390
O 2s	121	0.14	26.9	Ga $2p_{\frac{3}{2}}$: Si 2s	Ga 3d : Si 2p
Si 2p	1210	0.817	103.9	0.091 : 0.909	0.058 : 0.942

covered in a thick carbonaceous layer. It is therefore proposed that such carbon laydown on the external surface of catalyst discharges hinders the quantitative analysis by XPS and great care should be exercised in analysing such data.

This XPS data is of very good quality compared to that which is currently available in the open literature [209]. However, the broad signals derived from the O 1s and Ga $2p_{3/2}$ features of the catalyst discharge materials has meant that precise quantitative deconvolution has not been possible. There are, however, clear indications of the presence of gallium species with a reduced oxidation state. It is proposed that extra-framework species, of a form similar to GaO^+, which are analogous to the AlO^+ species observed in zeolites, are created after thermal treatments [240]. These species are then readily reduced to a form similar to Ga_2O, which is extremely mobile and is likely to migrate to the external surface of the crystallites. It is therefore proposed that reaction under a flow of propane with diluent nitrogen has caused the further ejection of framework gallium atoms which do not exist as stoichiometric oxide species but as some partially reduced suboxide phase, similar to Ga_2O.

Table 6–39: XPS analysis of reacted CEUO1R.

Sample CEUO1 after reaction					
Peak	Total area	S_f used	B.E.	Surface	Depth profile
Ga $2p_{\frac{3}{2}}$	2498	21.4	1119.4-1115.9	Ga $2p_{\frac{3}{2}}$: O 1s	Ga 3d : O 2s
O 1s	25394	2.93	534.5	0.026 : 0.974	0.018 : 0.982
Si 2s	4642	0.955	155.9	Si 2s : O 1s	Si 2p : O 2s
Ga 3d	126	1.08	17.3	0.325 : 0.675	0.461 : 0.539
O 2s	746	0.14	27.5	Ga $2p_{\frac{3}{2}}$: Si 2s	Ga 3d : Si 2p
Si 2p	3718	0.817	105.0	0.052 : 0.948	0.021 : 0.979

Table 6–40: XPS analysis of reacted CEUO2R.

Sample CEUO1 after reaction					
Peak	Total area	S_f used	B.E.	Surface	Depth profile
Ga $2p_{\frac{3}{2}}$	2115	21.4	1119.5-1115.6	Ga $2p_{\frac{3}{2}}$: O 1s	Ga 3d : O 2s
O 1s	16727	2.93	535.7-532.6	0.033 : 0.967	0.043 : 0.957
Si 2s	2974	0.955	155.3	Si 2s : O 1s	Si 2p : O 2s
Ga 3d	165	1.08	18.1	0.259 : 0.741	0.434 : 0.566
O 2s	392	0.14	28.1	Ga $2p_{\frac{3}{2}}$: Si 2s	Ga 3d : Si 2p
Si 2p	2102	0.817	103.9	0.088 : 0.912	0.056 : 0.944

Table 6–41: XPS analysis of reacted CEUO3R.

Sample CEUO3 after reaction					
Peak	Total area	S_f used	B.E.	Surface	Depth profile
Ga $2p_{\frac{3}{2}}$	2625	21.4	1121.7-1118.2	Ga $2p_{\frac{3}{2}}$: O 1s	Ga 3d : O 2s
O 1s	32865	2.93	535.4-534.1	0.021 : 0.979	0.013 : 0.987
Si 2s	5425	0.955	156.8	Si 2s : O 1s	Si 2p : O 2s
Ga 3d	135	1.08	16.9	0.311 : 0.689	0.438 : 0.562
O 2s	1091	0.14	27.7	Ga $2p_{\frac{3}{2}}$: Si 2s	Ga 3d : Si 2p
Si 2p	4885	0.817	105.7	0.050 : 0.950	0.018 : 0.982

Table 6–42: XPS analysis of reacted CMFI1R.

Sample CMFI1 after reaction					
Peak	Total area	S_f used	B.E.	Surface	Depth profile
Ga $2p_{\frac{3}{2}}$	2174	21.4	1120.7-1118.2	Ga $2p_{\frac{3}{2}}$: O 1s	Ga 3d : O 2s
O 1s	17762	2.93	535.4-533.7	0.031 : 0.969	0.019 : 0.981
Si 2s	2856	0.955	156.9	Si 2s : O 1s	Si 2p : O 2s
Ga 3d	92	1.08	23.0	0.329 : 0.671	0.458 : 0.542
O 2s	529	0.14	28.0	Ga $2p_{\frac{3}{2}}$: Si 2s	Ga 3d : Si 2p
Si 2p	2498	0.817	106.1	0.060 : 0.940	0.022 : 0.978

Chapter 7

Conclusions

This work has highlighted a number of interesting and exciting features. It has been shown that the preparation of gallosilicate EUO materials, with up to 8 gallium atoms per unit cell is facile and that these gallium species remained primarily in the framework, even after calcination. Gallosilicate MFI materials have also been prepared. However, there appears to be a maximum level of stabilised gallium incorporation of 4 gallium atoms per unit cell of MFI. This is proposed to be a consequence of the framework charge balancing species. The organic void filler material in MFI syntheses was TPA^+ and since a maximum of 4 TPA^+ can be occluded per unit cell, a maximum of 4 framework charges can be associated with these organic cations. At higher metal levels the framework charge is balanced by Na^+ ions and this association is proposed to result in a less stable framework metal atom. In EUO syntheses the doubly charged Hex^{2+} species was able to counter all 8 framework metals and as such was responsible for their siting within the framework structure. After ion exchange treatments in acidic conditions and subsequent catalytic investigations under reducing atmospheres, there was significant gallium ejection from both the CEUO and CMFI materials. This gallium is likely to be ejected as GaO^+, analogous to the AlO^+ extra-framework zeolite species. A detailed examination of thermal gravimetric and elemental analyses has led to the derivation of a model which predicts the location and distribution of the framework metal charges.

The XPS analysis is believed to have been based on some of the best XPS

data currently available for metal loaded molecular sieves. XPS has shown all the gallosilicate MFI materials to have a gallium rich crust with a strong gallium concentration gradient into the crystallites with a siliceous core. More gallium was detected on the external surface of the gallosilicate MFI materials than could be incorporated into the MFI framework, hence there are extra-framework gallium species present in these materials. This, however, was not detected by ^{71}Ga NMR. The external surfaces of these CMFI crystallites are effectively equivalent. The gallosilicate EUO materials also showed a slight gallium enrichment of the external surfaces, but not as marked as that of the MFI materials. This suggests a more homogeneous distribution of gallium throughout the gallosilicate EUO materials.

To reduce the complex propane aromatisation reaction, into simpler and more manageable parts, a range of materials were prepared which allowed an investigation of each of the features thought to be required for a successful aromatisation catalyst.

Gallium, or some other dehydrogenation component, is an essential component for this propane conversion and a range of gallium doping techniques were examined. Gallium loading by either incipient wetness (IW) or ion exchange (IE) have been found to be essentially equivalent for loading these high silica molecular sieves and can be regarded as deposition techniques. While the use of volatile organometallic precursors was investigated, their instability in the zeolitic environments resulted in a lack of control over this doping technique; however, this avenue is still worthy of further investigation as it potentially offers a route to perfectly dispersed metal species. Improvement of the dispersion of gallium species supported within the acidic zeolite porous environment, was achieved by direct substitution of aluminium by gallium in the synthesis gel, as described above. This has led to the crystallisation of gallosilicate materials which are analogous to the EU-1 and ZSM-5 zeolites.

The Ga-ZSM-5 material, currently used industrially in this process, is an excellent catalyst for propane aromatisation, with its remarkable resistance to deactivation by coking proving to be a huge advantage. The dimensionality of the molecular sieve catalysts was examined, with the order of catalyst lifetimes directly

following the degree of interconnectivity of the channel structure. The nature of the framework topology and channel structure are important for a successful aromatisation catalyst. The unidimensional EUO materials and the 2-D NU-87 were both rapidly deactivated in propane aromatisation studies and so it is proposed that a multidimensional network of channels, without large voids or cavities, which is resistant to pore blockage, is essential for this conversion. A simple model has been derived which allows prediction of the product distribution for aromatisation, with or without catalyst coking.

The acidic nature of the molecular sieves is also of fundamental importance in this process. The acid strength of the aluminosilicate sieves is required for this conversion, rather than the weaker Brönsted sites created by the substitution of gallium into the framework. However, it is not simply the number of acid sites, but their location which is critical. It is believed that a level of ≤ 4 such acid sites per unit cell of either EUO or the MFI structures would provide a better catalyst than the materials which have up to 8 such framework acid sites per unit cell. This optimum level has sufficient activity to allow successful conversions, yet, the acid sites are sufficiently dispersed to prevent excessive oligomerisation which would lead to pore blockage and deactivation.

The nature of the dehydrogenation species is also crucial for the preparation of a successful aromatisation catalyst and it is likely that some partial reduction of the oxidation state of the extra-framework gallium species is required for the most successful conversions. The maximum level of activity, for the Ga-ZSM-5 material, was not observed until after a few hours on stream. This induction time is likely to be associated with the formation of the active gallium species. XPS analysis of catalyst discharges supports this observation of reduction in the oxidation state of the gallium. These species are believed to be of the form Ga_2O.

A potentially successful catalyst could be prepared by the incorporation of both gallium and aluminium into the framework of a molecular sieve. This could then be activated by thermal treatments with preferential ejection of the gallium species which would be retained into the microporous structure which still retains the intrinsic acidity afforded by the aluminosilicate framework.

Based on this work it may be reasoned that the ideal catalyst requires several key features. Of greatest importance is a low coking tendency (for fixed bed applications), well dispersed gallium-oxy species (of a form similar to Ga_2O) and moderate to strong acidity, and these acid sites should also be well dispersed. Based on this an MFI material prepared from the galloaluminosilicate system would seem to offer the best combination of properties and indeed such syntheses were attempted but the studies could not be completed as described in Chapter 2. The study of such mixed metal molecular sieves could prove to be extremely valuable and an interesting avenue to explore further. By a similar reasoning it may be argued that a study of the MEL structure type may also be of considerable value.

References

[1] W. Lowenstein. *Am. Mineral.*, 39:92–95, 1954.

[2] J.W. McBain. *The Sorption of Gases and Vapors by Solids.* Rutledge and Sons., 1932.

[3] R. Szostak. *Molecular Sieves, Principles of Synthesis and Identification.* Van Nostrand Reinhold, 1989.

[4] E.M. Flanigen. *Pure Appl. Chem.*, 52:2192, 1980.

[5] A.F. Cronstedt. *Akad. Handl. Stockholm*, 17:120, 1756.

[6] Z Gabelica. *I.Z.C. Summer School*, Wildbrad Kreuth, 1994.

[7] D.W. Breck. *Zeolite Molecular Sieves.* Wiley, 1974.

[8] R.M. Barrer. *J. Chem. Soc.*, page 127, 1948.

[9] R.M. Milton. *U.S. patent*, 2 882 243, 1959.

[10] R.M. Milton. *U.S. patent*, 2 882 244, 1959.

[11] D.W. Breck. *U.S. patent*, 3 130 007, 1964.

[12] S.T. Wilson, B.M. Lok, C.A. Messina, T.R. Cannan, and E.M. Flanigen. *J. Am. Chem. Soc.*, 104:1146, 1982.

[13] A. Dyer. *An Introduction to Zeolite Molecular Sieves.* Wiley, 1988.

[14] F. Liebau. *Zeolites*, 3(2):191, 1983.

[15] J.V. Smith. *Zeolites*, 4(4):309–310, 1984.

[16] M.E. Davis and D. Young. *Stud. Surf. Sci. Catal.*, 60:53–62, 1991.

[17] M.E. Davis, C. Montes, P.E. Hathaway, and J.M. Garces. *Stud. Surf. Sci. Catal.*, 49A:199–214, 1989.

[18] S.M. Csicsery. *Chem. Br.*, 21:473, 1985.

[19] B.M. Lowe. *Education in Chem.*, Jan.:15–18, 1992.

[20] W.M. Meier. *Molecular Sieves, Soc. Chem. Ind.*, page 10, 1968.

[21] R.M. Barrer. *Chem. Ind.*, 64:130, 1945.

[22] J.A. Martens, M. Tielen, P.A. Jacobs, and J. Weitkamp. *Zeolites*, 4:98, 1984.

[23] W.M. Meier and D.H. Olsen. *Atlas of Zeolite Structure Types.* Butterworth-Heinemann, 1992.

[24] R. Townsend. *Chem. Ind.*, 241, 1984.

[25] R. Townsend. *Zeolites*, 4:191, 1984.

[26] A. Dyer. *Chem. Ind.*, 246, 1984.

[27] A. Dyer. *Zeolites*, 4:215, 1984.

[28] R.W. Grose and E.M. Flanigen. *U.S. patent*, 4 061 724, 1977.

[29] G.J. Wanless. *G.B. patent*, 1 433 416, 1976.

[30] P.M. Florack. *European patent Appl.*, 6 665, 1980.

[31] M. Seko, T. Mujake, and K. Indana. *Hydrocarbon Processing*, Jan:133, 1980.

[32] G. Ozin, A. Kuperman, and A. Stein. *Angew. Chem. Int. Ed. Eng.*, 28(3):359–376, 1989.

[33] G. Schulz-Ekloff. In *Zeolite Chemistry and Catalysis*, pages 65–78. Elsevier Sci. Pub., Amsterdam, 1991.

[34] W.F. Hoelderich. In *Zeolites: Facts, Figures, Future*, page 69. 1989.

[35] T. Bein and P. Enzel. *Ang. Chem. Int. Ed. Eng.*, 28(12):1692–1694, 1989.

[36] Q. Huo, R. Xu, S. Li, Z. Ma, J.M. Thomas, R.H. Jones, and A.M. Chippendale. *J. Chem. Soc. Chem. Comm.*, pages 875–876, 1992.

[37] M.E. Davis, C. Montes, and Garces J.M. *ACS Symp. Ser.*, 398:291–304, 1989.

[38] A. Merrouche, J. Patarin, H. Kessler, M. Soulard, L. Delmotte, J.L. Guth, and J.F. Joly. *Zeolites*, 12(3):226–232, 1992.

[39] C.T. Kresge, M.E. Leonowicz, W.J. Roth, J.C. Vartuli, and J.S. Beck. *Nature*, 359:710–712, 1992.

[40] J.S. Beck, J.C. Vartuli, W.J. Roth, M.E. Leonowicz, C.T. Kresge, K.D. Schmitt, C.T.W. Chu, D.H. Olsen, E.W. Sheppard, S.B. McCullen, J.B. Higgins, and J.L. Schlenker. *J. Am. Chem. Soc.*, 114:10835–10843, 1992.

[41] C-Y Chen, S.L. Burkett, H-X Lia, and M.E. Davis. *Microporous Materials*, 2:27, 1993.

[42] C-Y Chen, S.L. Burkett, H-X Lia, and M.E. Davis. *Microporous Materials*, 2:17, 1993.

[43] R.M. Barrer. *Hydrothermal Chemistry of Zeolites.* Academic Press, New York, 1982.

[44] V.P. Shiralker, P.N. Joshi, M.J. Eapen, and B.S. Rao. *Zeolites*, 11:511, 1991.

[45] L.D. Rollman. In *6th IZC (Reno)*, page 109. Butterworths, London, 1983.

[46] R. Aiello and R.M. Barrer. *J. Chem. Soc. (A)*, page 1470, 1970.

[47] B.M. Lok, T.R. Cannan, and C.A. Messina. *Zeolites*, 3:282–291, 1983.

[48] E.M. Flanigen. In W.M. Meier and J.B. Uytterhoeven, editors, *Molecular Sieves*, pages 119–139. ACS, 1973.

[49] J.L. Casci, T.V. Whittam, and B.M. Lowe. *European patent*, 0 042 226, 1981.

[50] B.M. Lowe and A. Araya. *Zeolites*, 6:111, 1986.

[51] B.M Lowe, J.R.D. Nee, and J.L. Casci. *Zeolites*, in press, 1994.

[52] R.M. Barrer and Denny P.J. *J. Chem. Soc.*, page 971, 1961.

[53] M.E. Davis and R.F. Lobo. *Chem. Mater.*, 4:756–768, 1992.

[54] B.M. Lowe. In *Innovation in Zeolite Materials Science*, volume 37, page 1. 1988.

[55] A. Araya and B.M. Lowe. *J. Chem. Res.*, S:192, 1985.

[56] McDaniels and Meher. *Molecular Sieves, Soc. Chem. Ind.*, page 186, 1968.

[57] G.T. Kerr. In *Molecular Sieves*, pages 219–229. ACS, 1973.

[58] J.C. McAteer and J.J. Rooney. In *Molecular Sieves*, pages 258–265. ACS, 1973.

[59] G.N. Rao, P.N. Joshi, A.N. Kotosthane, and P. Ratnasamy. *Zeolites*, 9:483–490, 1989.

[60] G.W. Dodwell, R.P. Denkewicz, and L.B. Sand. *Zeolites*, 5:153–157, 1985.

[61] J.R.D. Nee. PhD thesis, University of Edinburgh, 1993.

[62] N.A. Briscoe, D.W. Johnson, M.D. Shannon, G.T. Kokotailo, and L.B. McCusker. *Zeolites*, 8:74–76, 1988.

[63] J.L. Casci, M.P. Shannon, P.A. Cox, and S.J. Andrews. *Synthesis of Microporous Materials*, 1992.

[64] J.L. Casci, M.D. Shannon, and I.J.L. Lake. *European patent*, 0 462 745, 1991.

[65] S. Parsons, 1994. Personnal communication.

[66] J.L. Casci, T.V. Whittam, and B.M. Lowe. In *Proc. 6th Int. Zeo. Conf., Reno*, pages 894–904, 1983.

[67] S.D. Pickett, A.K. Nowak, J.M. Thomas, and A.K. Cheetham. *Zeolites*, 9:123–128, 1989.

[68] A.R. Pradhan, A.N. Kotasthane, and B.S. Rao. *Appl.Catal.*, 72:311, 1986.

[69] R.J. Argauer and G.R. Landholt. *U.S. patent*, 3,702,886, 1972.

[70] J.L. Casci, 1993. Personnal communication.

[71] E.M. Flanigen, J.M. Bennett, R.W. Grose, J.P. Cohen, R.L. Patton, R.M. Kirchner, and J.V. Smith. *Nature*, 271:512, 1978.

[72] G.P. Babu, S.G. Hegde, S.B. Kulkarni, and P. Ratansamy. *J. Catal.*, 81:471–477, 1983.

[73] J.J. Berzelius. *Edinburgh New Philosophical Journal*, XXI:223, 1836.

[74] C. Naccache and Y.B. Taarit. *Pure Appl. Chem.*, 52:2175, 1980.

[75] M. Minachev, Kh. and I. Isakov, Ya. In *Molecular Sieves*, pages 451–460. ACS, 1973.

[76] P.R. Pujado, J.A. Rabo, G.T. Antos, and S.A. Gembicki. *Catal. Today*, 13:113–141, 1991.

[77] B. Hampson. PhD thesis, University of Edinburgh, 1991.

[78] H.G. Karge, V. Mavrodinova, Z. Zheng, and H.K. Beyer. In *Guidlines for Mastering the Properties of Molecular Sieves*, page 157. Plenum Press, New York, 1990.

[79] H.K. Beyer, H.G. Karge, and G. Borbely. *Zeolites*, 8:79, 1988.

[80] G. Borbely, H.K. Beyer, H.G. Karge, L. Radics, and P. Sandor. *Zeolites*, 9:428, 1989.

[81] R.M. Barrer. In 6^{th} *IZC (Reno)*, page 870. Butterworths, London, 1983.

[82] C.D. Chang, C.T-W. Chu, J.N. Miale, R.F. Bridger, and R.B. Calvert. *J. Am. Chem. Soc.*, 106:8143–8146, 1984.

[83] N.Y. Chen, C.T-W. Chu, C.D. Chang, T.F.Jr. Degnan, and S.B. McCullen. *European patent*, 0 317 227, 1989.

[84] M. Nemet-Mavrodin. *U.S. patent*, 4 861 933, 1989.

[85] S.A.I. Barri and D. Young. *European patent*, 0 106 478, 1984.

[86] S.A.I. Barri and D. Young. *European patent*, 0 130 013, 1985.

[87] C.T-W Chu and G.T. Kerr. *European patent*, 0 134 849, 1985.

[88] H. Diaz. *European patent*, 0 283 212, 1988.

[89] C.T-W. Chu and S. Han. *European patent*, 0 327 189, 1989.

[90] M.T. Barlow and J. Harry. *International patent*, WO 84/03879, 1984.

[91] Z.G. Zulfugarov, A.S. Suleimanov, and Ch. R. Samedov. *Structure*, 19.

[92] E.E. Senderov, A.M. Bychkov, I.V. Mishin, A.L. Klyachko, and H.K. Beyer. In *Zeolites: Facts, Figures, Future*, page 355. 1989.

[93] I.S. Dring, D.H. Hall, R.J. Oldman, J.L. Casci, W.N.E. Meredith, and R.P. Tooze. In V^{th} *Int. Conf. X-ray Absorption Fine Structure, Seattle*, 1988.

[94] C.T-W. Chu and C.D. Chang. *J. Phys. Chem.*, 89:1569–1571, 1985.

[95] J. Kanai and N. Kawata. *Appl. Catal.*, 55:115–122, 1989.

[96] X. Liu and J. Klinowski. *J. Phys. Chem.*, 96:3403–3408, 1992.

[97] H. Kosslick, V.A. Tuan, B. Parlitz, R. Fricke, C. Peuker, and W. Storek. *J. Chem. Soc., Faraday Trans.*, 89(7):1131–1138, 1993.

[98] R. Monque, A. Parisi, S. Gonzalez, and G. Giannetto. *Zeolites*, 12:806–809, 1992.

[99] H. Kosslick, V.A. Tuan, and R. Fricke. *Cryst. Res. Technol.*, 26:K64–67, 1991.

[100] J. Bandiera and Y. Ben Taarit. *Appl. Catal.*, 76:199–208, 1991.

[101] P. Meriaudeau and C. Naccache. *Appl. Spect.*, 73:L13–18, 1991.

[102] P. Meriaudeau and C. Naccache. In *Catalyst Deactivation*, pages 767–772. Elsevier Sci. Pub., Amsterdam, 1991.

[103] S. Nagamatsu, M. Inomata, and K. Imura. *Sekiyu Gakkaishi*, 35:50–55, 1992.

[104] V. Kanazirev, G.L. Price, and K.M. Dooley. In *Zeolite Chemistry and Catalysis*, pages 277–285. Elsevier Sci. Pub., Amsterdam, 1991.

[105] R.M. Dessau. *Canadian patent*, 1 209 118, 1986.

[106] C.R. Bayense, J.H.C. van Hoof, J.W. de Haan, L.J.M. van de Ven, and A.P.M. Kentgens. *Catal. Lett.*, 17:349–361, 1993.

[107] S.B. Hong, E. Mielczarski, R.J. Davis, and M.E. Davis. *J. Catal.*, 134:349–369, 1992.

[108] M. Guisnet and P. Magnoux. *Appl. Catal.*, 54:1–27, 1989.

[109] P. Magnoux and M. Guisnet. *Zeolites*, 9:329–335, 1989.

[110] J. Kanai and N. Kawata. *Appl. Catal.*, 62:141–150, 1990.

[111] C.J. Plank, E.J. Rosinski, and A.B. Schwartz. *European patent*, 1 402 981, 1975.

[112] J.R.D. Nee, 1994. Personnal communication.

[113] T. Inui, Y. Makino, F. Okazumi, S. Nagano, and A. Miyamoto. *Ind. Eng. Chem. Res.*, 26:647–651, 1987.

[114] T. Inui, Y. Makino, F. Okazumi, and A. Miyamoto. *J. Chem. Soc., Chem. Comm.*, 1:571–572, 1986.

[115] A.Yu. Khodakov, L.M. Kustov, T.N. Bondarenko, A.A. Dergachev, V.B. Kazansky, Kh.M. Minachev, G. Borbely, and H.K. Beyer. *Zeolites*, 10:603–607, 1990.

[116] P.A. Jacobs. In *Studies in Surface Science and Catalysis*, pages 71–85. Elsevier Sci. Pub. Coy., 1982.

[117] V. Kanazirev, G.L. Price, and G. Tyuliev. *Zeolites*, 12:846–850, 1992.

[118] E.E. Davis and A.J. Kolombos. *European patent*, 1 561 590, 1977.

[119] J.R. Mowry, R.F. Anderson, and J.A. Johnson. *Oil & Gas J.*, Tech.:128–131, 1988.

[120] M. Guisnet, N.S. Gnep, and F. Alario. *Appl. Catal.*, 89:1–30, 1992.

[121] N.Y. Chen and T.Y. Yan. *Ind. Eng. Chem. Process Des. Dev.*, 35:151, 1986.

[122] L. Mank, A. Minkkinen, and R. Shaddick. *Hydrocarbon Technol. Int.*, 69, 1992.

[123] N.S. Gnep, J.Y. Doyemet, A.M. Seco, F.R. Ribeiro, and M. Guisnet. *Appl. Catal.*, 35:93, 1987.

[124] H. Kitagawa, Y. Sendoda, and Y. Ono. *J. Catal.*, 101:12–18, 1986.

[125] P. Meriaudeau and C. Naccache. *J. Molec. Catal.*, 50:L7–10, 1989.

[126] C.T-W. Chu. *European patent*, 0 259 954, 1988.

[127] Y. Ono and K. Kanae. *J. Chem. Soc., Faraday Trans.*, 87(4):669–675, 1991.

[128] G. Sirokman, Y. Sendoda, and Y. Ono. *Zeolites*, 6:299–303, 1986.

[129] K. Fujimoto, I. Nakamura, and K. Yokota. *Zeolites*, 9:120–122, 1989.

[130] K. Fujimoto, I. Nakamura, and K. Yokota. *Chem. Lett.*, 1:681–682, 1989.

[131] G. Buckles, G.J. Hutchings, and C.D. Williams. *Catal. Lett.*, 11:89–94, 1991.

[132] P. Meriaudeau and C. Naccache. In *Zeolite Chemistry and Catalysis*, pages 405–408. 1991.

[133] A. Corma, C. Goberna, J.H. Lopez Nieto, N. Paredes, and M. Perez. In *Zeolite Chemistry and Catalysis*, pages 409–416. Elsevier Sci. Pub., Amsterdam, 1991.

[134] L. Petit, J.P. Bournville, and F. Raatz. In *Zeolites, Facts Figures Future*, pages 1163–1171. Elsevier Sci. Pub., Amsterdam, 1989.

[135] C.R. Bayense, A.J.H.P. van der Pol, and J.H.C. van Hooff. *Appl. Catal.*, 72:81–98, 1991.

[136] V.I. Yakerson, T.V. Vasina, L.I. Lafer, V.P. Sytnyk, G.L. Dykh, A.V. Mokhov, O.V. Bragin, and Kh.M. Minachev. *Catal. Lett.*, 3:339–346, 1989.

[137] G.L. Price and V. Kanazirev. *J. Molec. Catal.*, 66:115–120, 1991.

[138] G. Buckles, G.J. Hutchings, and C.D. Williams. *Catal. Lett.*, 8:115–124, 1991.

[139] C.R. Bayense and J.H.C. van Hooff. *Appl. Catal.*, 79:127–140, 1991.

[140] R. Le Van Mao and J. Yao. *Appl. Catal.*, 79:77–87, 1991.

[141] Yu.A. Khodakov, L.M. Kustov, T.N. Bondarenko, A.A. Dergachev, V.B. Kazansky, Kh.M. Minachev, G. Borbely, and H.K. Beyer. *Zeolites*, 10:603–607, 1990.

[142] G. Giannetto, J.A. Perez, R. Sciamanna, L. Garcia, R. Gallasso, and R. Monque. In *Symp. Alkylation, Aromatization, Oligomerization and Isomerization of Short Chain Hydrocarbons Over Heterogeneous Catalysts*, pages 659–667. ACS, New York, 1991.

[143] J.M. Thomas and L. Xin-Sheng. *J. Phys. Chem.*, 90:4843–4847, 1986.

[144] N.S. Gnep, J.Y. Doyemet, and M. Guisnet. In *Zeolites as Catalysts, Sorbents and Detergent builders*, volume 46, page 153. Elsevier, Amsterdam, 1989.

[145] K. Fujimoto, I. Nakamura, K. Yokota, and K. Aimoto. *Bull. Chem. Soc. Jpn.*, 64:2275–2280, 1991.

[146] C.T-W. Chu and C.D. Chang. *J. Phys. Chem.*, 89:1569–1571, 1985.

[147] R. Challor, R.K. Harris, S.A.I. Barri, and M.J. Taylor. *Zeolites*, 11:827–831, 1991.

[148] A. Sheka, I.S. Chaus, and T.T. Mityureva. *The Chemistry of Gallium.* Elsevier Sci. Pub., Amsterdam, 1966.

[149] D. Seddon. *Catal. Today*, 6:351–372, 1990.

[150] M. Pemmble, 1993. Private communication.

[151] R. von Ballmoos and J.B. Higgins. *Collection of Simulated XRD Powder Patterns for Zeolites.* Butterworth-Heinemann, 1990 (published as *Zeolites*, 10(5), 1990).

[152] H.P. Klug and L.E. Alexander. *X-ray Diffraction Procedures.* Wiley-Interscience, 1974.

[153] J.L. Casci and B.M. Lowe. *Zeolites*, 3:186, 1983.

[154] K.R. Franklin and B.M. Lowe. *Thermochimica Acta*, 136:307, 1988.

[155] I.C. Norrish and B.W. Chappell. *Physical Methods in Determinative Mineralogy.* Academic Press, 1977.

[156] D.A. Skoog. *Principles of Instrumental Analysis.* Saunders College Publishing, 1985.

[157] N.A. Norrish and G. Hutton. *Geochim. cosmochim. Acta*, 33:431, 1969.

[158] B.M. Lowe, 1991. Private communication.

[159] J.W. Akitt. *N.M.R. and Chemistry.* Chapman and Hall, 1973.

[160] K.F.M.G.J. Scholle. *Investigation of Zeolites by Solid State NMR.* krips repro meppel, 1985.

[161] A.R. West. *Solid State Chemistry and its Applications.* J. Wiley and Sons, 1984.

[162] W. Kemp. *NMR in Chemistry, a Multinuclear Approach.* Macmillan, 1986.

[163] G. Engelhardt and D. Michel. *High Resolution Solid State NMR of Silicates and Zeolites.* Wiley, 1987.

[164] C.R. Bayense, A.R.M. Kentgens, J.W. de Haan, L.J.M. van de Ven, and J.H.C. van Hooff. *J. Phys. Chem.*, 96:775–782, 1992.

[165] S.A. Axon, K. Huddersman, and J. Klinowski. *Chem. Phys. Lett.*, 172:398–404, 1990.

[166] H. Kyung, C. Timlen, and E. Oldfield. *J. Am. Chem. Soc.*, 109:7669–7673, 1987.

[167] C.R. Bayense, J.H.C. van Hooff, A.R.M. Kentgens, J.W. de Haan, and L.J.M. van de Ven. *J. Chem. Soc., Chem. Comm.*, pages 1292–1293, 1989.

[168] Z. Yin-Xing, A. Tuel, Y. Ben Taarit, and C. Naccache. *Zeolites*, 12:138–141, 1992.

[169] B. Gore, 1994. Personnal communication.

[170] J.M. Thomas. *Sci. Am.*, 4:82–88, 1992.

[171] J.A. Rabo and G.J. Gajda. *Catal. Rev. Sci. Eng.*, 31(4):385–430, 1989.

[172] R.J. Cventanovic and Y. Amenomiya. *Adv. Catal.*, 1:103–149, 1967.

[173] N-Y. Topsoe, K. Pedersen, and E. Derouane. *J. Catal.*, 70:41–52, 1981.

[174] H. Stach, M. Hunger, J. Janchen, H-G Jerschewitz, U. Lohse, and B. Parlitz. *J. Phys. Chem.*, 96:8480–8485, 1992.

[175] R.B. Borade, A. Adnot, and S. Kallaguine. *J. Catal.*, 126:26–30, 1990.

[176] A. Corma, V. Fornes, F.V. Melo, and J. Herrero. *Zeolites*, 7:559–563, 1987.

[177] J.G. Post and J.H.C. van Hooff. *Zeolites*, 4:9–14, 1984.

[178] R.M. Roberts. *J. Chem. Soc., Chem. Comm.*, 63:1400–1403, 1959.

[179] J.W. Hightower and W.K. Hall. *J. Am. Chem. Soc.*, 90:851–858, 1968.

[180] L.M. Parker, D.M. Bibby, and R.H. Meinhold. *Zeolites*, 5:384–388, 1985.

[181] L. Forni, P. Francesco, F.P. Vatti, and E. Ortoleva. *Zeolites*, 12:101–106, 1992.

[182] A.K. Ghosh, N.G. Keats, and G. Curthoys. *J. Catal.*, 96:288–291, 1985.

[183] A. Martin, B. Parlitz, and S. Peter. *React. Kinet. Catal. Lett.*, 46:11–16, 1992.

[184] L. Forni, E. Magni, E. Ortoleva, R. Monaci, and V. Solinas. *J. Catal.*, 112:444–452, 1988.

[185] C.V. Hidalgo, H. Itoh, T. Hattor, M. Niwa, and Y. Murakami. *J. Catal.*, 85:362–369, 1884.

[186] L. Forni and E. Magni. *J. Catal.*, 112:112, 1988.

[187] M. Sawa, M. Niwa, and Y. Murakami. *Zeolites*, 10:307, 1990.

[188] P.A. Redhead. *Vacuum*, 12:203, 1962.

[189] K. Chao, B. Chiou, C. Cho, and J. Shiow. *Zeolites*, 4:2–4, 1984.

[190] A. Dolan. PhD thesis, University of Edinburgh, 1994.

[191] K. Siegbahn. *ESCA, Molecular and Solid State Structure Studied by Means of Electron Microscopy.* Almquist and Wiksells, 1965.

[192] H. Hertz. *Wiedemannische Annal.Phys.*, 31:982, 1887.

[193] A. Einstein. *Annal. Phys.*, 17:132, 1905.

[194] C.D. Wagner, W.M. Riggs, L.E. Davis, J.F. Moulder, and G.E. Muilenberg. *Handbook of X-ray Photoelectron Spectroscopy.* Perkin-Elmer Corp., 1979.

[195] D. Briggs and M.P. Seah. *Auger and X-ray Photoelectron Spectroscopy.* Wiley Publishers, 1985.

[196] K. Siegbahn, C. Nordling, A. Fahlman, R. Nordberg, K. Hamrin, J. Hedman, G. Johansson, T. Bergmark, S. Karlson, I. Lindgren, and B. Lindberg. *ESCA, Atomic, Molecular and Solid State Structure Studied by Means of Electron Spectroscopy.* Almqvist and Wilksells Boktryckeri AB, 1967.

[197] M.P. Seah and W.A. Dench. *Surf. Interface Anal.*, 1:2, 1979.

[198] S. Tanuma, C.J. Powell, and D.R. Penn. *Surface and Interface Analysis*, 20:77–89, 1993.

[199] J.E. Fulgham, R. Stokell, G. McGuire, B. Patnaik, N. Yu, Y.J. Zhao, and N. Parikh. *J. Electron Spec.*, 60:117–125, 1992.

[200] H. Ebel, M.F. Ebel, R. Svargera, and A. Hofmann. *Surface and Interface Analysis*, 18:821–823, 1992.

[201] R. Nix. *Chemistry Teaching Aid*, Edinburgh University, 1994.

[202] C.D. Wagner, L.E. Davis, M.V. Zeller, J.A. Taylor, R.H. Raymond, and L.H. Gale. *Surf. Interface Anal.*, 3:211, 1981.

[203] R.T. Poole, P.C. Kemeny, J. Liesegang, J.G. Jenkin, and R.C.G. Leckey. *J. Phys. F: Metal Phys.*, 3:L46–L48, 1973.

[204] G. Schon. *J. Elec. Spec. Rel. Phenom.*, 2:75–86, 1973.

[205] J.H. Scofield. *J. Elec. Spec. Rel. Phenom.*, 8:129–137, 1976.

[206] W. Grunert, R. Schlogi, and H.G. Karge. *J. Phys. Chem.*, 97:8638–8645, 1993.

[207] R. Carli, C.L. Bianchi, R. Giannantonio, and V. Ragaini. *J. Molec. Catal.*, 83:379–389, 1993.

[208] S. Bailey, 1994. Personnal communication.

[209] D. Creaser, 1994. Personnal communication.

[210] C.D. Wagner, W.M. Riggs, L.E. Davies, J.F. Moulder, and G.E. Muilenberg. *Hanbook of X-ray Photoelectron Spectroscopy.* Perkin Elmer Corp., 1985.

[211] A.F. Carley and M.W. Roberts. *Proc. Royal Soc.*, A363:403, 1978.

[212] M.W. Roberts, C.R. Brundle, D. Latham, and K. Yates. *J. Elec. Spec. Rel. Phenom.*, 3:241, 1974.

[213] R.F. Feilman, A. Msezane, and S.T. Mason. *J. Elec. Spect. Rel. Phenom.*, 8:389, 1976.

[214] C.S. Fadley, R.J. Baird, W. Wiekhaus, T. Nankov, and S.A.L. Bergshin. *J. Elec. Spect. Rel. Phenom.*, 4:93, 1974.

[215] J.L. Casci, 1994. Personnal communication.

[216] J.L. Casci, 1992. Personnal communication.

[217] A.N. Kosthane and V.P. Shiralkar. *Thermchim. Acta.*, 102:37, 1986.

[218] M. Padovan, G. Leofant, M. Solari, and E. Moretti. *Zeolites*, 4:295, 1984.

[219] K.R. Franklin and B.M. Lowe. *Thermochim. Acta.*, 127:319, 1988.

[220] P. Cox, 1994. Personnal communication.

[221] E.G. Derouane, S. Detremmerie, Z. Gabelica, and N. Blom. *Appl. Catal.*, 1:20, 1981.

[222] H. Kosslick, V.A. Tuan, R. Fricke, J. Jedamzik, and H.P. Lanh. *J. Thermal Analysis*, 37:2631–2641, 1991.

[223] D.M. Bibby, L.A. Aldridge, and N.B. Milestone. *J. Cats.*, 72:373, 1981.

[224] D.M. Bibby, L. P. Aldridge, and N. B. Milestone. *J. Cats*, 72:373, 1981.

[225] R. Szostak, V. Nair, D.C. Shieh, D.K. Simmons, T.L. Thomas, R. Kuvadia, and B. Dunson. In *Int. Symp. Innovation in Zeolite Material Science*, page 403. Butterworths, London, 1987.

[226] R. Brown, 1994. Personnal communication.

[227] P.D. Holmes. PhD thesis, University of Edinburgh, 1993.

[228] L.V.C. Rees and T.C. Watling. *Zeolites*, in press, 1994.

[229] L.V.C. Rees and T.C. Watling. *Zeolites*, in press, 1994.

[230] C.D. Chang and A.J. Silvestri. *J. Catal.*, 47:249, 1977.

[231] E.G. Derouane, P. Dejaifive, Z. Gabelica, and J.C. Vedrine. *Disc. Faraday Soc.*, 72:331, 1981.

[232] E. Lalik, X. Lui, and J. Klinowski. *J. Phys. Chem.*, 96:805–809, 1992.

[233] S.L. Meisel, J.P. McCullough, C.H. Lechthaler, and P.B. Weisz. *Chemtech*, Feb.:86–89, 1976.

[234] K.A. Martin and L. Zabransky. *Appl. Spect.*, 45:68–72, 1991.

[235] A.Yu. Stakheev, A.Yu. Khodakov, L.M. Kustova, V.B. Kazansky, and Kh.M. Minachev. *Zeolites*, 12:866–869, 1992.

[236] G.L. Price. *J. Catal.*, 130:611–615, 1991.

[237] R. Brown, 1984.

[238] W.A. Dietz. *J. Gas Chromatography*, Feb.:68–71, 1967.

[239] E.S. Shpiro, D.P. Shevchenko, M.S. Kharson, A.A. Dergachev, and Kh.M. Minachev. *Zeolites*, 12:670–673, 1992.

[240] J. Klinowski, J.M. Thomas, C.A. Fyfe, and G.C. Gobbi. *Nature*, 296:533, 1982.